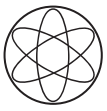

Technische Universität München

Phenomenology of the radiative E1 heavy quarkonium decay

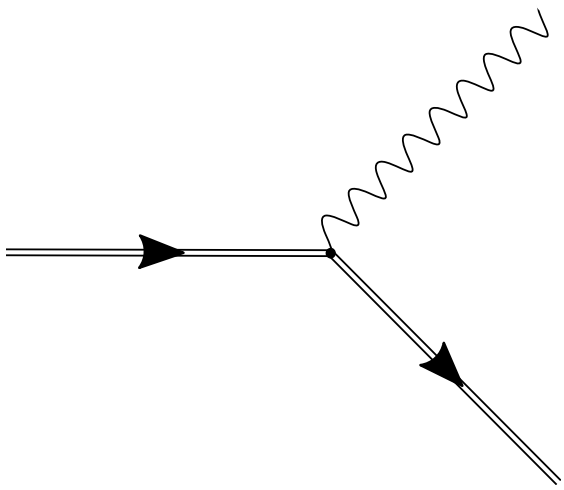

Héctor Eduardo Martínez Neira

TECHNISCHE UNIVERSITÄT MÜNCHEN
Physik Department T30f

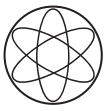

Technische Universität München

TECHNISCHE UNIVERSITÄT MÜNCHEN
Physik Department T30f

Phenomenology of the radiative E1 heavy quarkonium decay

Héctor Eduardo Martínez Neira

Vollständiger Abdruck der von der Fakultät für Physik der Technischen Universität München zur Erlangung des akademischen Grades eines

Doktors der Naturwissenschaften (Dr. rer. nat.)

genehmigten Dissertation.

Vorsitzender:		Prof. Dr. Bastian Märkisch
Prüfer der Dissertation:	1.	Prof. Dr. Nora Brambilla
	2.	Prof. Dr. Norbert Kaiser

Die Dissertation wurde am 20.03.2017 bei der Technischen Universität München eingereicht und durch die Fakultät für Physik am 26.04.2017 angenommen.

To my parents Eliana and Héctor

Acknowledgments

I would like to thank professors Nora Brambilla and Antonio Vairo for giving me the opportunity to do my PhD at TUM and to professors Marcelo Loewe and Gorazd Cvetič in Chile who helped me in my move to Germany. I am also grateful of my friends and colleagues who directly or indirectly contributed to the realization of this thesis: Matthias, Esteban, Sungmin, Vladyslav and all the other people at the T30f group.
Finally, I want to thank my family: my parents, my sister Alejandra and especially Slađana, who has been a constant support during the process that led to the completion of this document, thank you.

Munich, July of 2016

Zusammenfassung

Wir verwenden den vollständigen Ausdruck für die $O(1/m^2)$ Korrekturen, wobei m die Quarkmasse bezeichnet, zum Quark-Antiquark-Potenzial, welcher sich durch Erwartungswerte von Wilson-Loops aus der QCD ableiten lässt, sowie eine Abbildung, welche diese Wilson-Loop-Erwartungswerte für große Abstände zu Korrelatoren in der Effektiven String Theorie (EST) in Beziehung setzt, um alle $O(1/m^2)$ Potenziale bei großen Abständen zu berechnen. Insbesondere präsentieren wir zuvor unbekannte Ergebnisse für den spin- und impulsunabhängigen Teil des Potenzials und bestätigen die bereits bekannten Ergebnisse für die Anteile des Potenzials, die von Spin und Impuls abhängen. Wir berechnen die Korrekturen zum String-Spektrum, welche durch die neuen Potenziale induziert werden.
Indem wir die EST Beiträge für große Distanzen zur Vervollständigung im Infraroten verwenden, konstruieren wir das Quark-Antiquark-Potenzial auf dem ganzen Bereich. Wir bestimmen die freien Parameter durch Abgleich mit Experimenten und Gitter-QCD. Das Power-Counting und die numerische Größe der einzelnen Beiträge werden analysiert. Wir berechnen die Korrekturen zur Wellen-Funktion von schwerem Quarkonium, welche durch das Potenzial auf dem ganzen Bereich induziert werden. Schließlich ermitteln wir die elektrischen Dipol-Übergagnsraten (E1) von schwerem Quarkonium unter Berücksichtigung dieser Korrekturen bis zu $O(v^2)$ in der nicht-relativistischen Entwicklung. Unsere Ergebnisse sind in Übereinstimmung mit Experimenten und liefern Vorhersagen für die Raten, für die noch keine experimentellen Werten vorliegen.

Abstract

We use the complete expression for the $O(1/m^2)$ corrections to the quark-antiquark potential, where m is the quark mass, derived from QCD in terms of Wilson loop expectation values, and a mapping, valid at large distances, between those Wilson loop expectation values and correlators evaluated in the Effective String Theory (EST), to compute all $O(1/m^2)$ potentials at large distances. In particular, we present previously unknown results for the spin and momentum independent part of the potential and confirm known results for the spin and momentum dependent parts. We calculate the relativistic corrections induced by the newly calculated potentials to the string spectrum.
Using the EST long-distance contributions as the infrared completion, we construct the full-range quark-antiquark potential. We fix the free parameters of this potential using input from the experiment and lattice QCD. The power counting and numerical size of the different contributions are analysed. We calculate the corrections induced by the full-range potential to the heavy quarkonium wavefunction. Finally, considering these corrections, we evaluate the heavy quarkonium electric dipole (E1) transition rates at $O(v^2)$ in the non-relativistic expansion. Our results compare favorably with the experiment and provide predictions for the rates for which no experimental data is yet available.

Contents

Chapter 1

Introduction

The existence of phenomena at different energy scales is an intrinsic property of Nature. Our perception of these phenomena has driven the development of modern science and through it our understanding of Nature. At first, our understanding was limited to explain phenomena perceptible only at human scales. Due to the development of the experimental sciences we were often in presence of phenomena that could not be understood in terms of the, by that time, accepted theories. This cycle of empirical discovery and later theoretical understanding has been essential for the development of Physics. A classical example of this cycle is how our understanding of Gravity has changed since the times of Newton to the present day. In the *Principia* [1] Newton was able to explain Kepler's empirical laws for the movement of celestial bodies with the same simple formula that explained the effect of Gravity on the surface of Earth. Centuries had to pass until Einstein came up with a *more universal* theory of Gravity [2] that explained, among other phenomena, the precession of the orbit of Mercury, something that Newton's theory had failed to explain. The universality of Einstein's theory implied that when studying phenomena at the scales in which Newton's theory was applicable both theories yielded the same results. In a modern language we may think of Newton's theory as an *effective theory* of Einstein's General Relativity[1].

Another example where the concept of effective theory arises comes from the relation between Quantum Mechanics and Chemistry. We know that the interactions between the atomic nucleus and electrons are explained by the laws and principles of Quantum Mechanics, however, the study of the composition and change of matter at the molecular level are better studied by means of the *effective* rules of Chemistry.

In a more speculative way we could think that the theory that *explains* three of the four known fundamental interactions, the Standard Model [3–5], is an effective theory of a yet-unknown fundamental theory.

In Particle Physics the modern realisation of the idea that physical processes or phenomena can be better studied with a set of effective rules valid only for a given energy scale is through the construction of *effective field theories* (EFTs).

[1] This terminology is usually avoided because of the historical importance of Newton and the fact that Newton's theory precedes Einstein's work by more than two hundred years.

In contrast to the examples of Gravity and Atomic Physics, in which the development of what we might call effective theories was done mostly independently from what is understood as their respective *fundamental* theories, we will focus on theories constructed with a *top-to-bottom* approach, i.e., effective theories constructed starting from a known *fundamental theory*.

Our object of study will be quarkonium, a bound state formed by a quark and its antiquark[2]. Since the discovery of the first quarkonium state, the J/Ψ meson in November of 1974, the so-called *November revolution* [6], quarkonia have played an important role in the development of QCD.

There are two main properties of quarkonium that have driven our theoretical understanding of it. The first one is that, since the relative velocity between the quark and the antiquark, v, is small compared to the speed of light, c, the system appears to be suitable for a non-relativistic description. This observation has motivated the modeling of the quark-antiquark interaction inside the bound system by means of non-relativistic potentials. This effective approach, that we will call *potential models*, proved to be successful at reproducing the values of the quarkonium masses, for a review of these approaches see [7, 8].

The other important property of quarkonium is a consequence of the non-relativistic nature of the system. If v is such that $v \ll c$, then quarkonium is a *multi-scale system* with the following hierarchy among the quark mass m (*hard*), relative momentum p (*soft*), and energy E (*ultrasoft*) scales,

$$m \gg p \sim mv \gg E \sim mv^2.$$

This separation of energy scales is used to construct EFTs in which the degrees of freedom with energies that are not relevant for studying some phenomena are integrated out. In particular the EFT that is obtained after integrating out from QCD the degrees of freedom with energies of order m is called non-relativistic QCD (NRQCD) [9, 10]. If we go further and now from NRQCD we integrate out the degrees of freedom with energies that scale like mv, we obtain the EFT called potential non-relativistic QCD (pNRQCD) [11, 12]. This last theory is closer to a quantum-mechanical description of the bound state with some similarities to the potential models, however, in contrast to these models in which the shape of the potential was a matter of guessing, pNRQCD is by construction fully equivalent to QCD when studying the same energy region.

Depending on how the energy scale of hadronic physics, $\Lambda_{\rm QCD}$, compares to the other scales of the system, the construction of the EFT may or may not be done using perturbative methods. In the latter case, some input from experiment or lattice QCD (in which Green functions are computed numerically) is needed in order to fully determine the effective theory. One of the advantageous features of the EFTs of QCD is that they allow us to separate the perturbative and non-perturbative physics in a systematic way.

[2]From here on we will understand quarkonium only as the bound state formed by heavy quarks: charmonium and bottomonium. A possible bound state formed by top and antitop, *toponium*, does not exist since, due to its large mass, the top quark decays through electroweak interactions before forming a bound state.

These effective theories, NRQCD and pNRQCD, are currently one of the most important theoretical tools for the study of quarkonium, more details about them are given in the next chapter.

Among the present-day experiments involved in the study of quarkonium and quarkonium-like systems we can mention BES at IHEP in Beijing, BELLE at KEK in Japan, BaBar at SLAC in California and the quarkonium physics programs of the LHC experiments: ATLAS, CMS, ALICE and LHCb[3]. The amount and the increasing quality of the experimental data coming from these and other experiments, make quarkonium physics an exciting research field. Some of the topics that currently garner attention from the quarkonium community are the study of the so-called *exotic states*, the properties of quarkonia in media and quarkonium decays. The first topic refers to the study of quarkonium-like states with masses larger than the threshold where other mesons may appear. The interpretation of these states in terms of mesonic molecules, quarkonium hybrids or other configurations is a matter of intensive debate among the community. A notable example of such debates is the interpretation of the charmonium-like resonance with a mass of 4.45 GeV, whose Pentaquark interpretation claimed by LHCb [15] has been challenged by some theoreticians [16].

The interest in the study of quarkonium in media is in part motivated by the proposal that the melting of quarkonium states within a hot medium could be used to probe the formation of *quark-gluon plasma* (QGP) [17], a state of matter formed by *free* quarks and gluons believed to have been present in the early universe. This plasma can be produced in heavy ion collision experiments at RHIC at Brookhaven and the LHC at CERN. The study of QGP through different experimental probes is a very active research field not only among the quarkonium community but also among the QCD community at large.

Regarding quarkonium decays we have that, depending on the final state, these can be grossly divided into hadronic and radiative. Many of these decays have been observed for the first time only in recent years. Also the precision of measurements has improved considerably in modern experiments, posing a challenge to the theory.

The aim of this thesis is to apply the results of the EFTs of QCD to the evaluation of the quarkonium electromagnetic dipole (E1) transition rates. This transition is characterised by the decay of quarkonium into a photon and a lighter quarkonium state that has an angular momentum quantum number that differs by one with respect to the initial state. This and other radiative transitions have been studied in the past using potential models, we intend to give a fresh look to these decays using the modern approach of the EFTs of QCD.

One of the fundamental objects in our evaluation will be the quark-antiquark potential including $O(1/m^2)$ relativistic corrections that has been obtained using pNRQCD [18, 19]. In contrast to the potential models, the expression obtained from pNRQCD is fully equivalent to QCD in the non-relativistic limit. The relativistic corrections are organized as an expansion in powers of $1/m$ where the coefficients of the expansion correspond to expectation values of the rectangular Wilson loop with gluonic field insertions.

[3]For a review on the experimental findings relevant for quarkonium physics of these and other experiments see the relevant sections of Refs. [13] and [14].

The way these correlators are evaluated will depend on the distance regime that is being considered. At short distances the correlators can be evaluated using perturbative methods. In the long-distance regime they must be computed on the lattice, however, a lattice determination of all relevant correlators is still missing. In order to evaluate the long-distance limit of the potential we will assume the hypothesis that at long distances the quark-antiquark interaction may be modeled as a string with fixed ends [20]. The string hypothesis will allow us to get a compact expression for the long-range potential. The other key piece we will need are the expressions for the E1 decay rates up to $O(v^2)$ relativistic corrections [21]. These formulas are completely model-independent, however, we will see that in order to evaluate them we need the quark-antiquark potential in the whole distance regime as an input. The construction of this potential will occupy a large portion of this thesis.

The rest of the text is organized as follows; in Chapter 2 we give an introduction to the EFTs for the study of heavy quarkonium. In Chapter 3 we present the expressions of the $O(1/m^2)$ relativistic corrections to the quark-antiquark potential obtained within the framework of pNRQCD. We give details of the derivation of the $1/m$-suppressed correction. In Chapter 4 we compute the long-range potential assuming the string hypothesis to evaluate the correlators of Chapter 3. We also evaluate the effect of the relativistic corrections to the string spectrum. In Chapter 5 we construct the potential that we will use in the evaluation of the decay rates. Once the potential is fixed, it determines the explicit formulas that need to be evaluated in order to compute the E1 rates, these formulas are derived in Chapter 6. In Chapter 7 we give details about the numerical evaluation of the formulas of Chapter 6 and some of the numerical aspects regarding the construction of the potential. In Chapter 8 we present the partial results of the evaluation of the E1 decay rates. Based on these results in Chapter 9 we present our final results for the rates. Using these results together with experimental input we estimate some branching fractions and total widths. In this chapter we also compare our results with the available experimental data. Finally Chapter 10 presents our conclusions and outlook to related future research. Many of the technical details and intermediate numerical results emerging along the thesis have been left for the Appendix that is included after Chapter 10.

Chapter 2

Effective field theories for heavy quarkonium

In this chapter we present a brief introduction to the effective theories that are relevant for the study of heavy quarkonium. We start giving a gross description of the most relevant aspects of QCD, to later proceed to give the recipe to construct EFTs starting from a *fundamental theory*. Following this recipe we show how NRQCD is obtained from QCD once the *hard scale* is integrated out. We close the chapter describing the physical picture of pNRQCD, the effective theory that results from integrating out the *soft scale* from NRQCD. This theory will be the central subject of the next chapter. We will follow closely [22], to which we refer for a more comprehensive introduction to NRQCD and pNRQCD.[1]

2.1 Quantum Chromodynamics

It is our current understanding that Quantum Chromodynamics (QCD) [24, 25] is the quantum field theory describing the strong interaction. It corresponds to a non-Abelian SU(3) gauge theory coupled to fermions called quarks which carry a *color charge*. The QCD Lagrangian reads

$$\mathcal{L}_{\rm QCD} = \sum_{i=1}^{N_f} \bar{q}_i (i\not{D} - m_i) q_i - \frac{1}{4} G^{\mu\nu\,a} G^a_{\mu\nu}, \tag{2.1}$$

where $N_f = 6$ is the number of quark flavors (up, down, charm, strange, top, bottom), $D_\mu = \partial_\mu + igA_\mu$, $igG_{\mu\nu} = [D_\mu, D_\nu]$, q_i are the quark fields, m_i their (bare) masses, A_μ are the gauge fields, called gluons, mediating the color interactions and g is the bare coupling. We have used the definition $A_\mu \equiv T^a A^a_\mu$, where T^a, with $a = 1, ..., 8$, are the generators of the SU(3) gauge group in the fundamental representation. These

[1] For an introduction to EFTs of QCD relevant to other contexts see [23].

correspond to Hermitian, traceless 3× 3 matrices that fulfill

$$[T^a, T^b] = if^{abc}T^c, \tag{2.2}$$
$$\mathrm{Tr}\{T^a T^b\} = T_F \delta^{ab}, \tag{2.3}$$

where f^{abc} are the *structure constants* of the gauge group; an explicit representation of these matrices can be found in [26]. Together with the SU(3) gauge symmetry and Poincaré invariance, in QCD each of the discrete charge conjugation, parity and time reversal (CPT) symmetries is realized. These are the five symmetries that, in principle, must be realized in any EFT derived from QCD.
For the $\mathrm{SU(N_c)}$ gauge group the following identities for the quadratic Casimir operators of the fundamental, C_F, and adjoint, C_A, representations hold

$$C_F = \frac{T_F}{N_c}(N_c^2 - 1), \tag{2.4}$$
$$C_A = 2T_F N_c. \tag{2.5}$$

For the fundamental representation of the matrices T^a we will use the convention that fixes $T_F = 1/2$. Using this convention and the fact that in QCD $N_c = 3$ (the number of colors) we have $C_F = 4/3$ and $C_A = 3$. A derivation of these identities can be found in [26].
After quantizing QCD, divergences appear in the computation of loop integrals. The procedure to absorb these divergences introduces an energy scale, μ, called the *renormalization scale*. The bare parameters (coupling and masses) of the Lagrangian must be replaced with the *renormalized* parameters measured at the scale μ. The condition that observables must be independent of the renormalization scale ultimately settles how these parameters depend on μ. The explicit dependence on the energy scale is given through the *renormalization group equations* (RGE). In the case of the coupling, defining $\alpha_\mathrm{s} \equiv g^2/4\pi$, its RGE is given by

$$Q^2 \frac{\partial}{\partial Q^2}\alpha_\mathrm{s}(Q^2) = \beta(\alpha_\mathrm{s}(Q^2)), \tag{2.6}$$

where we assume that the coupling is known at a given energy scale Q^2. The function $\beta(\alpha_\mathrm{s}(Q^2))$ is called the *Beta function* and it is implicitly defined by the previous equation, it can be organized as an expansion in the coupling

$$\beta(\alpha_\mathrm{s}) = -\alpha_\mathrm{s}\left(\frac{\alpha_\mathrm{s}}{4\pi}\beta_0 + \frac{\alpha_\mathrm{s}^2}{(4\pi)^2}\beta_1 + ...\right), \tag{2.7}$$

where the coefficients of the expansion, β_i, are obtained calculating relevant Green functions. Currently these coefficients are known up to $i = 4$ [27–30]. In general the β_i coefficients depend on the gauge and the scheme that is chosen to regularize the divergences. It can be proven that in mass-independent schemes like MS or $\overline{\mathrm{MS}}$, however, the

Beta function is gauge-independent. Moreover, it turns out that the first two coefficients β_0 and β_1 are scheme-independent. The first coefficient is given by [31, 32]

$$\beta_0 = \left(\frac{11}{3}C_A - \frac{2}{3}n_f\right), \tag{2.8}$$

where n_f is the number of active quark flavors that is being considered at some given scale[2]. If we consider just this first coefficient in the Beta function, Eq. (2.7) can be solved exactly and one obtains

$$\alpha_{\rm s}(Q^2) = \frac{\alpha_{\rm s}(\mu^2)}{1 + \beta_0 \frac{\alpha_{\rm s}(\mu^2)}{4\pi} \ln \frac{Q^2}{\mu^2}}. \tag{2.9}$$

Defining $\Lambda_{\rm QCD}$ as the scale in which $\alpha_{\rm s}(Q^2)$ diverges, we can write

$$\alpha_{\rm s}(\mu) = \frac{2\pi}{\beta_0 \ln(\mu/\Lambda_{\rm QCD})}. \tag{2.10}$$

From Eq. (2.10) we can infer one of the characteristics of QCD calculations: to compute the amplitude of a QCD process that occurs at a given energy scale E, the QCD coupling $\alpha_{\rm s}$ can be used as the expansion parameter of the perturbative series only if $E \gg \Lambda_{\rm QCD}$ [31, 32]. To compute amplitudes of processes that occur at a scale $E \sim \Lambda_{\rm QCD}$ we must rely on so-called *non-perturbative approaches* to QCD. The scale $\Lambda_{\rm QCD} \approx 200\,\text{MeV}$ [34] is the typical scale of hadronic physics, which implies that some phenomena in quarkonium physics cannot be studied purely with perturbative methods.

One of the non-perturbative approaches to QCD is lattice QCD. In this approach the functional integrals of the Green functions are calculated numerically over a lattice of points in space-time. The precision of the calculation is constrained by the size of the lattice and the separation among its nodes, called the *lattice spacing*. The larger the lattice and smaller the lattice spacing is, the more precise but also more expensive the calculation gets. The development of more efficient algorithms and dropping computing costs have improved the precision of lattice calculations in recent years, for a review of the current status of lattice QCD studies in quarkonium see the chapters dedicated to the topic in Ref. [14].

One of the advantages of using EFTs to study quarkonium is that they allow us to factorize the contributions of physics coming from different energy scales. In particular, they allow us to factorize the non-perturbative contributions that can later be computed on the lattice or extracted from experimental data. In the next section we review the general recipe for constructing EFTs.

2.2 A very brief introduction to Effective Field Theories

Let us assume that we are interested in studying physics at an energy scale E that is much smaller than another energy scale Λ. Let us assume also that there exists a *funda-*

[2]Usually $\alpha_{\rm s}$ is evaluated at a scale where the active quarks can be treated as massless. See also the decoupling theorem [33].

mental theory that is valid for both, the scale E and the scale Λ.
The first step to construct the EFT is to identify the symmetries of the fundamental theory that are preserved at the scale E. The Lagrangian of the EFT is then constructed including all the allowed operators consistent with this subset of symmetries. The Lagrangian can be conveniently organized as an expansion of operators of increasing dimensionality, in four spacetime dimensions we have

$$\mathcal{L}_{\rm EFT} = \sum_i c_i \left(\frac{\mu}{\Lambda}\right) \frac{O_i}{\Lambda^{d_i-4}} \tag{2.11}$$

where d_i is the mass dimension of the operator O_i and μ is the renormalization scale. The (undetermined) coefficients $c_i(\mu/\Lambda)$ are called the *Wilson (or matching) coefficients*, they encode the physics of the degrees of freedom with energy Λ that have being *integrated out*, that is, that are not present in the theory anymore.
In order to reduce the (infinite) number of terms in $\mathcal{L}_{\rm EFT}$ we must define the *power counting* that will determine the relative importance of the terms in the Lagrangian. This power counting is based on the hierarchy among the relevant energy scales, for instance, derivatives will count as the momentum of the degrees of freedom that are present in the effective theory. How the momentum compares to E will then define the relative size of operators containing derivatives. In the next section, in which we will review NRQCD, we will see an explicit example of a power counting.
Once we have specified the power counting and the size of the operators O_i in terms of E is known, we must define the accuracy of the theory. Usually the accuracy, A, is defined as $A \equiv (E/\Lambda)^n$ where $n > 0$. To reach a given accuracy A, one has to include in the Lagrangian all possible terms whose size is equal to or smaller than A.
The number of independent Wilson coefficients can be reduced by imposing the constraints coming from Poincaré invariance. These constraints originate from the fact that, although the Lagrangian of the EFT is not explicitly Poincaré invariant, we can impose the Poincaré algebra on the Poincaré generators of the EFT. This procedure provides relations among the coefficients [35, 36] effectively reducing the number of independent ones.
The remaining set of Wilson coefficients now needs to be calculated. The method to compute these coefficients is called *matching*; it consists in determining the coefficients c_i by comparing the results, usually Green functions, obtained from the fundamental theory and the EFT at a certain scale ν that fulfills $E \sim \nu < \Lambda$. In EFTs derived from QCD the nature of the matching procedure is defined by how the scales E, ν, Λ compare to $\Lambda_{\rm QCD}$. If $\nu \gg \Lambda_{\rm QCD}$, the matching procedure is carried out perturbatively leading to Wilson coefficients that are organized as an expansion in powers of $\alpha_{\rm s}$. In the case when $\nu \sim \Lambda_{\rm QCD}$ the matching is done using non-perturbative methods. We will give some details about the matching procedure in the next two sections, when we review the main features of NRQCD and pNRQCD, and in Chapter 3, where an overview of the calculation of the $1/m$-suppressed relativistic correction to the quark-antiquark potential will be given.
From Eq. (2.11) we see that the effective theory is in principle not renormalizable be-

cause the Lagrangian may contain operators of dimension $d_i > 4$. This is not a problem since the EFT can be made finite order by order in the expansion in powers of $1/\Lambda$; actually, much of the physical information of the theory is contained in terms that are proportional to these operators. For more details about the renormalizability of EFTs we refer the reader to the discussion presented in [23].
With the accuracy of the theory defined and the independent Wilson coefficients calculated, we are left with an EFT that fulfills the following properties:

- It has the same infra-red (IR) behavior as the fundamental theory but a different ultra-violet (UV) one.

- Its Lagrangian has only the degrees of freedom relevant to study the phenomena at the scale E or lower.

- Its predictability can be improved systematically according to the power counting by increasing the power n of the accuracy.

- For EFTs derived from QCD, if the Wilson coefficients have been obtained from a perturbative matching, the precision in the predictability of the theory can also be improved by increasing the order in perturbation theory at which the coefficients are calculated.

Before concluding this section, let us consider a physical system that has the following energy scale hierarchy

$$E \ll \Lambda_2 \ll \Lambda_1, \tag{2.12}$$

which is described in all energy regions by what we will call the *full theory*. Integrating out the scale Λ_1 from this theory, we may obtain an EFT that describes the physics of scales E and Λ_2; let us call this theory EFT_1. Then we may consider EFT_1 as the fundamental theory to integrate out from it degrees of freedom that scale like Λ_2 and construct another theory, EFT_2. This last EFT will be suitable to study the physics of the scale E. Since by construction each EFT is equivalent to its parent (fundamental) theory when describing the same energy region, EFT_1 and EFT_2 will be equivalent to the full theory when describing their respective energy regions. This equivalence is manifest in the Wilson coefficients of each theory; in particular, the Wilson coefficients of EFT_2 will depend on the Wilson coefficients of EFT_1 that in turn encode the dynamics of the degrees of freedom of energy Λ_1 described by the full theory.
As we mentioned in Chapter 1, an energy scale hierarchy like the one of Eq. (2.12) is present in quarkonium, where naturally, the full theory corresponds to QCD. The scale Λ_1 is identified as the heavy quark mass and Λ_2 as the relative momentum. After integrating out the mass scale one obtains NRQCD, integrating out from NRQCD the momentum we obtain pNRQCD. In the following sections we present an overview of these two theories.

2.3 Non-relativistic QCD

For convenience let us start by recalling one more time the hierarchy of energy scales present in quarkonium

$$m \gg mv \gg mv^2, \tag{2.13}$$

where m is the heavy quark mass and v is the relative velocity between quark and antiquark. Following the method described in the previous section, the Lagrangian of NRQCD is organized as an expansion in powers of $1/m$, multiplying operators of increasing dimensionality that fulfill the symmetries of QCD. The resulting $O(1/m)$ Lagrangian of the heavy quark-antiquark sector that fulfills all these conditions except Poincaré invariance (see below) is rather simple, it reads[3]

$$\mathcal{L}_{Q\bar{Q}}^{(1/m)} = \psi^\dagger \left(iD_0 + \frac{c_k}{2m}\mathbf{D}^2 \right) \psi + \chi^\dagger \left(iD_0 - \frac{c_k}{2m}\mathbf{D}^2 \right) \chi, \tag{2.14}$$

where $\psi(x)$ is a Pauli spinor field that annihilates a quark and $\chi(x)$ is the spinor that creates an antiquark. Both spinors transform in the fundamental representation of SU(3). In Eq. (2.14) in order to write the same Wilson coefficient, c_k, for both quark and antiquark fields, we have used the fact that the NRQCD Lagrangian, as the QCD one, must be invariant under charge conjugation. By design NRQCD describes the physics of heavy quarks at energy scales much smaller than m, so heavy quark-antiquark pairs can no more be created; apart from this feature the light degrees of freedom are the same ones as in QCD, however, we must introduce a UV cutoff ν_{NR} that satisfies

$$E, |\mathbf{p}|, \Lambda_{\rm QCD} \ll \nu_{NR} \ll m, \tag{2.15}$$

when evaluating Green functions that contain these lighter degrees of freedom.[4]
The presence of three dynamical scales $(E, |\mathbf{p}|, \Lambda_{\rm QCD})$ in the theory implies that further assumptions on how these scales organize are necessary. The original power counting adopted in [10] reads

$$\begin{aligned} \Lambda_{\rm QCD} &\sim E \sim mv^2, \\ |\mathbf{p}| &\sim mv, \\ v &\sim \alpha_{\rm s}(mv), \end{aligned} \tag{2.16}$$

which implies that the bound state can be described by a Coulombic potential. This assumption may work well for low lying quarkonia, however, for excited states non-perturbative effects have to be included in the potential. Assuming this power counting we have that $\mathbf{D}$ acting on a heavy (anti)quark field scales as mv. Similarly D_0 acting on a heavy (anti)quark field will count as mv^2. With these two scaling rules it is trivial to check

[3] NRQCD can describe heavy quarks of different flavor, however, for simplicity in the present discussion we will consider the heavy quark-antiquark pair to be of the same flavor, which is the relevant case for quarkonium.

[4] In general ν_{NR} correspond to the set of two cutoffs ν_s and ν_p for the energy and momentum of the light degrees of freedom respectively. For simplicity we will use the same cutoff for both quantities.

that the $O(1/m)$ Lagrangian in Eq. (2.14) scales homogeneously as mv^2. The scaling implies that the accuracy of the calculations performed with the $O(1/m)$ Lagrangian is $mv^2 \times \alpha_{\rm s}^n$ where $n = 0, 1, 2, \ldots$ indicates the precision at which the matching coefficients are calculated. The scaling rules for the rest of the operators of the NRQCD Lagrangian (see below) based on this power counting can be found in [10]. For the time being let us proceed to describe the NRQCD Lagrangian beyond the leading order.
Up to $\mathcal{O}(1/m^2)$ the heavy quark sector of the NRQCD Lagrangian reads [9, 10, 37, 38]

$$\begin{aligned}
\mathcal{L}_{Q\bar{Q}} &= \psi^\dagger \Big\{ iD_0 + \frac{c_k}{2m}\mathbf{D}^2 + \frac{c_F}{2m}\boldsymbol{\sigma}\cdot g\mathbf{B} + \frac{c_D}{8m^2}(\mathbf{D}\cdot g\mathbf{E} - g\mathbf{E}\cdot\mathbf{D}) \\
&+ i\frac{c_S}{8m^2}\boldsymbol{\sigma}\cdot(\mathbf{D}\times g\mathbf{E} - g\mathbf{E}\times\mathbf{D})\Big\}\psi \\
&+ \chi^\dagger \Big\{ iD_0 - \frac{c_k}{2m}\mathbf{D}^2 - \frac{c_F}{2m}\boldsymbol{\sigma}\cdot g\mathbf{B} + \frac{c_D}{8m^2}(\mathbf{D}\cdot g\mathbf{E} - g\mathbf{E}\cdot\mathbf{D}) \\
&+ i\frac{c_S}{8m^2}\boldsymbol{\sigma}\cdot(\mathbf{D}\times g\mathbf{E} - g\mathbf{E}\times\mathbf{D})\Big\}\chi, \qquad (2.17)
\end{aligned}$$

where c_k, c_F, c_D, c_S are Wilson coefficients, $\boldsymbol{\sigma}$ are the Pauli matrices, $\mathbf{E} = \mathbf{E}^i = G^{i0}$, $\mathbf{B}^i = -\epsilon_{ijk}G^{jk}/2$ with ϵ^{ijk} being the three-dimensional antisymmetric tensor. The gluonic part of the Lagrangian at the same order is given by

$$\mathcal{L}_g = -\frac{1}{4}G^{\mu\nu a}G^a_{\mu\nu} + \frac{c_1^g}{4m^2}g f_{abc}G^a_{\mu\nu}G^{\mu b}_{\alpha}G^{\nu\alpha c}. \qquad (2.18)$$

Another part of the Lagrangian relevant for the following discussion contains the four fermion operators, explicitly at $\mathcal{O}(1/m^2)$ they read [10]

$$\mathcal{L}_{\psi\chi} = \frac{f_1(^1S_0)}{m^2}O_1(^1S_0) + \frac{f_1(^3S_1)}{m^2}O_1(^3S_1) + \frac{f_8(^1S_0)}{m^2}O_8(^1S_0) + \frac{f_8(^3S_1)}{m^2}O_8(^3S_1), \quad (2.19)$$

where

$$\begin{aligned}
O_1(^1S_0) &= \psi^\dagger\chi\chi^\dagger\psi, \\
O_1(^3S_1) &= \psi^\dagger\boldsymbol{\sigma}\chi\cdot\chi^\dagger\boldsymbol{\sigma}\psi, \\
O_8(^1S_0) &= \psi^\dagger T^a\chi\chi^\dagger T^a\psi, \\
O_8(^3S_1) &= \psi^\dagger T^a\boldsymbol{\sigma}\chi\cdot\chi^\dagger T^a\boldsymbol{\sigma}\psi, \qquad (2.20)
\end{aligned}$$

and the coefficients $f_{1,8}$ are (singlet or octet) Wilson coefficients. The NRQCD Lagrangian is then given by

$$\mathcal{L}_{\rm NRQCD} = \mathcal{L}_{Q\bar{Q}} + \mathcal{L}_g + \mathcal{L}_{\psi\chi} + \Delta\mathcal{L}_{\rm light}, \qquad (2.21)$$

where $\Delta\mathcal{L}_{\rm light}$ accounts for light quark operators and light-heavy quark interactions; for an explicit expression of this term we refer the reader to [22]. Many other possible operators that may appear at order $1/m^2$ have been neglected since they can be eliminated through *field redefinitions*, for details see [22].
In the case when the theory is coupled to electromagnetism we must add the photon field

to the covariant derivatives, i.e., $D_\mu = \partial_\mu + igA_\mu + iee_Q A_\mu^{\rm em}$, add $\mathcal{L}_\gamma^{\rm em} = (-1/4)F^{\mu\nu}F_{\mu\nu}$ to the light sector and augment the heavy quark sector Lagrangian by

$$\begin{aligned}
\Delta\mathcal{L}_{Q\bar{Q}}^{\rm em} &= \psi^\dagger \left\{ \frac{c_F^{\rm em}}{2m}\boldsymbol{\sigma}\cdot ee_Q\mathbf{B}^{\rm em} + \frac{c_D^{\rm em}}{8m^2}(\mathbf{D}\cdot ee_Q\mathbf{E}^{\rm em} - ee_Q\mathbf{E}^{\rm em}\cdot\mathbf{D}) \right. \\
&+ \left. i\frac{c_S^{\rm em}}{8m^2}\boldsymbol{\sigma}\cdot(\mathbf{D}\times ee_Q\mathbf{E}^{\rm em} - ee_Q\mathbf{E}^{\rm em}\times\mathbf{D}) \right\}\psi \\
&+ \chi^\dagger \left\{ -\frac{c_F^{\rm em}}{2m}\boldsymbol{\sigma}\cdot ee_Q\mathbf{B}^{\rm em} + \frac{c_D^{\rm em}}{8m^2}(\mathbf{D}\cdot ee_Q\mathbf{E}^{\rm em} - ee_Q\mathbf{E}^{\rm em}\cdot\mathbf{D}) \right. \\
&+ \left. i\frac{c_S^{\rm em}}{8m^2}\boldsymbol{\sigma}\cdot(\mathbf{D}\times ee_Q\mathbf{E}^{\rm em} - ee_Q\mathbf{E}^{\rm em}\times\mathbf{D}) \right\}\chi, \qquad (2.22)
\end{aligned}$$

where e is the electron charge, e_Q is the quark electric charge ($e_b = -1/3$, $e_c = 2/3$), $\mathbf{E}^{i\,\rm em} = F^{i0}$, $\mathbf{B}^{i\,\rm em} = -\epsilon_{ijk}F^{jk}/2$ and $F_{\mu\nu} = \partial_\mu A_\nu^{\rm em} - \partial_\nu A_\mu^{\rm em}$ is the electromagnetic field tensor. In this case the coefficients $c_i^{\rm em}$ must be obtained matching NRQCD to QCD coupled to electromagnetism.
As we pointed out in the previous section, the number of independent Wilson coefficients of the theory can be reduced by imposing the Poincaré algebra on the generators of the theory; for instance, the coefficients c_k, c_F and c_S are constrained through [36]

$$\begin{aligned}
c_k &= 1, \\
2c_F - c_S - 1 &= 0.
\end{aligned}$$

An alternative derivation of these relations has been obtained also in [37, 39] using the method called *reparametrization invariance* of the Heavy Quark Effective Theory (HQET), which coincides with NRQCD in the heavy quark sector of the Lagrangian. Recent developments on this approach for reducing the number of matching coefficients of EFTs can be found in [40] and [41].

The details of an NRQCD matching calculation are beyond the scope of this thesis, however, we can grossly summarize the method in the following steps

- The matching is carried out by requiring suitable renormalized Green functions of QCD and NRQCD to be equal at an energy scale below ν_{NR} at the desired order in $\alpha_{\rm s}$ and $1/m$. The same renormalization scheme should be used in both theories. This procedure leads to Wilson coefficients that are valid for this specific scheme.
- IR divergences may arise in the QCD and NRQCD Green functions. Since the theories share the same IR behavior, the same regulator must be used to regularize these divergences in both theories.
- In dimensional regularization, NRQCD loop integrals are scaleless so they may be set to zero, for details see the discussion in [22] and [37].
- NRQCD and QCD are gauge-invariant, so the calculations can be made in any gauge, however, it may be required to match gauge-dependent Green functions, in such a case the same gauge must be used in both theories.

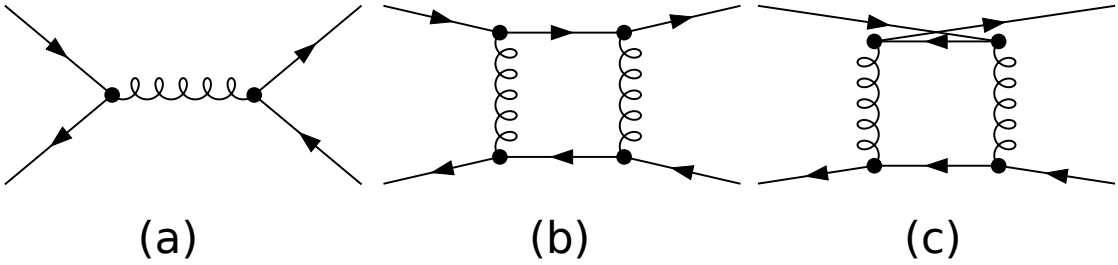

Figure 2.1: Leading QCD diagrams contributing to the Wilson coefficients of the four-fermion sector of the NRQCD Lagrangian. In the case of unequal heavy quark masses only diagrams (b) and (c) contribute. The energy of the gluon fields in these diagrams scales like m, therefore they are not present as a degree of freedom of NRQCD, yet their physics is encoded in the Wilson coefficients. Loop corrections to the annihilation diagram (a) lead to the appearance of imaginary contributions in the Wilson coefficients of $\mathcal{L}_{\psi\chi}$. These contributions are relevant for the calculation of quarkonium inclusive decay rates, for a review on the calculations of these coefficients see [43].

The most common choice in the matching calculations of NRQCD is to use dimensional regularization and the MS (or $\overline{\text{MS}}$) scheme. In the background Feynman gauge, at leading order, the Wilson coefficients of the heavy quark sector of the Lagrangian are found to be

$$c_F = c_D = c_S = 1. \tag{2.23}$$

The expressions at order α_s can be found in [37]. In the case of the coefficients of the four-fermion sector the matching comes from calculating QCD diagrams like the ones shown in Fig. 2.1; the complete set of diagrams and expressions for the Wilson coefficients can be found in [42].
NRQCD has been successfully applied to the study of heavy quarkonium decay and production, where it allows the factorization of the contributions of the hard and soft scales. The physics of the hard scale is encoded in the Wilson coefficients (see Fig. 2.1) while the contribution of the lower scales appears as the so-called *long distance matrix elements* (LDME), which may be extracted from experiment or lattice calculations. These matrix elements are in principle universal, i.e., they are independent from the physical observable from where they are extracted. The proof of the universality of the NRQCD LDME is currently a topic of active research; for a recent review on the status of the verification of the universality of the LDME we refer to the Section 4.5 of [14]. Another successful application of NRQCD is the study of bottomonium on the lattice; for a review on the progress of these studies see [13, 44, 45] and the relevant sections of [14].

2.4 Potential non-relativistic QCD

Quarkonium phenomena like the binding and the radiative transitions occur at the ultrasoft scale $E \sim mv^2$. As we have mentioned in this chapter, the EFT suitable for the

study of the physics at this scale is potential non-relativistic QCD (pNRQCD) [11, 12]. We also mentioned that this theory is obtained from NRQCD by integrating out the soft scale, $p \equiv |\mathbf{p}| \sim mv$. We are integrating out light degrees of freedom with energies $\sim p \gg E$ and heavy quarks with energy fluctuations of the same order. Depending on how $\Lambda_{\rm QCD}$ scales with respect to p we will distinguish two cases:

- If $p \gg \Lambda_{\rm QCD}$ the integration of the soft scale can be done using perturbation theory. If also $p \gg E \gtrsim \Lambda_{\rm QCD}$ one obtains what is called *weakly-coupled* pNRQCD.
- If $p, \Lambda_{\rm QCD} \gg E$, in order to obtain pNRQCD we need to integrate out $\Lambda_{\rm QCD}$ non-perturbatively after integrating out the scale p. This theory is called *strongly-coupled* pNRQCD.

Let us discuss first weakly-coupled pNRQCD. In this case the degrees of freedom are quark-antiquark pairs and gluons with the cutoffs ν_p and ν_{us}. The cutoff ν_p is the cutoff of the relative three momentum of the heavy quarks and ν_{us} is the cutoff of the energy of the heavy quark-antiquark pair and of the four momentum of the light degrees of freedom (gluons and light quarks). These cutoffs satisfy $p \ll \nu_p \ll m$, $\frac{\mathbf{p}^2}{m} \ll \nu_{us} \ll p$. In principle the degrees of freedom of pNRQCD can be represented by the same fields as in NRQCD, the difference lies in that the Wilson coefficients in the pNRQCD Lagrangian now depend on $\mathbf{p}$, hence, non-local terms in space are generated.
Explicitly the pNRQCD Lagrangian in the weakly-coupled regime can be written as

$$L_{\rm pNRQCD} = L^{\rm US}_{\rm NRQCD} + L_{\rm pot}. \tag{2.24}$$

with

$$L_{\rm pot} = -\int d^3\mathbf{x}_1 d^3\mathbf{x}_2 \psi^\dagger(t,\mathbf{x}_1)\chi(t,\mathbf{x}_2) V(\mathbf{r},\mathbf{p}_1,\mathbf{p}_2,\mathbf{S}_1,\mathbf{S}_2) \times (\text{US gluons}) \chi^\dagger(t,\mathbf{x}_2)\psi(t,\mathbf{x}_1), \tag{2.25}$$

where $\mathbf{p}_j = -i\nabla_{\mathbf{x}_j}$ and $\mathbf{S}_j = \boldsymbol{\sigma}/2$ where $j = 1,2$ means action on the fermion or antifermion respectively, and $L^{\rm US}_{\rm NRQCD}$ should be understood as the NRQCD Lagrangian with only ultrasoft gluons.
If we write the heavy quark-antiquark bilinear as a single field

$$\begin{aligned} \Psi(\mathbf{x}_1,\mathbf{x}_2,t)_{\alpha\beta} &\sim \psi_\alpha(\mathbf{x}_1,t)\chi^\dagger_\beta(\mathbf{x}_2,t) \\ &\sim \frac{1}{N_c}\delta_{\alpha\beta}\psi_\sigma(\mathbf{x}_1,t)\chi^\dagger_\sigma(\mathbf{x}_2,t) + \frac{1}{T_F}T^a_{\alpha\beta}T^a_{\rho\sigma}\psi_\sigma(\mathbf{x}_1,t)\chi^\dagger_\rho(\mathbf{x}_2,t), \end{aligned} \tag{2.26}$$

we can decompose this field into color singlet and octet field components with homogeneous ultrasoft gauge transformations with respect to the center-of-mass coordinate; explicitly

$$\Psi(\mathbf{x}_1,\mathbf{x}_2,t) = P\left[e^{ig\int_{\mathbf{x}_2}^{\mathbf{x}_1}\mathbf{A}\cdot d\mathbf{x}}\right] S(\mathbf{r},\mathbf{R},t) + P\left[e^{ig\int_{\mathbf{R}}^{\mathbf{x}_1}\mathbf{A}\cdot d\mathbf{x}}\right] O(\mathbf{r},\mathbf{R},t) P\left[e^{ig\int_{\mathbf{x}_2}^{\mathbf{R}}\mathbf{A}\cdot d\mathbf{x}}\right], \tag{2.27}$$

where P stands for path ordered. The fields S and O transform under ultrasoft color transformations, $g(\mathbf{R},t)$, as

$$\begin{aligned} S(\mathbf{r},\mathbf{R}) &\to S(\mathbf{r},\mathbf{R}), \\ O(\mathbf{r},\mathbf{R}) &\to g(\mathbf{R},t)O(\mathbf{r},\mathbf{R},t)g^{-1}(\mathbf{R},t). \end{aligned} \tag{2.28}$$

Using the decomposition of Eq. (2.27), the pNRQCD Lagrangian can be written in a more convenient way. First the pNRQCD Hamiltonian derived from the Lagrangian of Eq. (2.24) is projected onto the Fock subspace spanned by

$$\int d^3\mathbf{x}_1 d^3\mathbf{x}_2 \Psi(\mathbf{x}_1,\mathbf{x}_2)\psi^\dagger(\mathbf{x}_1)\chi(\mathbf{x}_2)|US\rangle, \tag{2.29}$$

where $|US\rangle$ is a Fock subspace that contains no quarks or antiquarks but an arbitrary number of ultrasoft gluons. Additionally one needs to enforce that the gluon fields are ultrasoft by multipole expanding them with respect to $\mathbf{r}$. Using the decomposition of Eq. (2.27) and the following normalization with respect to color

$$\begin{aligned} S &= S\mathbf{I}_c/\sqrt{N_c}, \\ O &= O^a T^a/\sqrt{T_F}, \end{aligned} \tag{2.30}$$

one eventually arrives to

$$\begin{aligned} \mathcal{L}_{\rm pNRQCD} &= \int d^3\mathbf{r}\,{\rm Tr}\{S^\dagger[i\partial_0 - h_S(\mathbf{r},\mathbf{p},\mathbf{P_R},\mathbf{S}_1,\mathbf{S}_2)]S \\ &+ O^\dagger[iD_0 - h_O(\mathbf{r},\mathbf{p},\mathbf{P_R},\mathbf{S}_1,\mathbf{S}_2)]O\} + V_A(r){\rm Tr}\{O^\dagger\mathbf{r}\cdot g\mathbf{E}S + S^\dagger\mathbf{r}\cdot g\mathbf{E}O\} \\ &+ \frac{V_B(r)}{2}{\rm Tr}\{O^\dagger\mathbf{r}\cdot g\mathbf{E}O + O^\dagger O\mathbf{r}\cdot g\mathbf{E}\} - \frac{1}{4}G^a_{\mu\nu}G^{\mu\nu a} + \sum_{i=1}^{n_f}\bar{q}i\not{D}q + \dots\,, \end{aligned} \tag{2.31}$$

where the dots account for operators of order $\mathbf{r}^2$ or higher, $iD_0O \equiv i\partial_0 O - g[A_0(\mathbf{R},t),O]$, $\mathbf{D_R}O \equiv [\mathbf{D_R},O]$, $\mathbf{P_R} = -i\mathbf{D_R}$, $\mathbf{p} = -i\nabla_{\mathbf{r}}$ and n_f should be understood as the number of light flavors only. In Eq. (2.30) it should be understood that the S on the RHS is a scalar function and the S on the LHS is a matrix field. In the equal mass case h_S and h_O are given by

$$\begin{aligned} h_S(\mathbf{r},\mathbf{p},\mathbf{P_R},\mathbf{S}_1,\mathbf{S}_2) &= \left\{c_S^{(1,-2)}(r),\frac{\mathbf{p}^2}{2m}\right\} + c_S^{(1,0)}(r)\frac{\mathbf{P}_\mathbf{R}^2}{4m} + V_S(\mathbf{r},\mathbf{p},\mathbf{P_R},\mathbf{S}_1,\mathbf{S}_2) \\ h_O(\mathbf{r},\mathbf{p},\mathbf{P_R},\mathbf{S}_1,\mathbf{S}_2) &= \left\{c_O^{(1,-2)}(r),\frac{\mathbf{p}^2}{2m}\right\} + c_O^{(1,0)}(r)\frac{\mathbf{P}_\mathbf{R}^2}{4m} + V_O(\mathbf{r},\mathbf{p},\mathbf{P_R},\mathbf{S}_1,\mathbf{S}_2) \\ V_S &= V_S^{(0)} + \frac{V_S^{(1)}}{m} + \dots, \\ V_O &= V_O^{(0)} + \frac{V_O^{(1)}}{m} + \dots, \end{aligned} \tag{2.32}$$

where [22]

$$c_S^{(1,-2)} = c_O^{(1,-2)} = c_S^{(1,0)} = c_O^{(1,0)} = 1. \tag{2.33}$$

The other Wilson coefficients, V_S and V_O are identified as the singlet and octet quark-antiquark potential respectively; their leading contributions in the weakly-coupled regime are

$$V_S^{(0)} = -C_F \frac{\alpha_{\rm s}}{r}, \tag{2.34}$$

$$V_O^{(0)} = \frac{T}{N_c} \frac{\alpha_{\rm s}}{r}. \tag{2.35}$$

Higher order (relativistic) corrections to V_S and V_O are organized in powers of $1/m$. The calculation of the $V_S^{(1)}$ potential is shown in Chapter 3 where also explicit expressions of the $1/m^2$-suppressed corrections are presented.
Equation (2.31) provides the pNRQCD Lagrangian up to order p^3/m^2 considering the following power counting

$$\begin{aligned} \nabla_{\mathbf{r}}, \frac{1}{r} &\sim p, \\ \partial_0, \nabla_{\mathbf{R}} &\sim E. \end{aligned} \tag{2.36}$$

We shall complement the counting above with the expected size of $\alpha_{\rm s}$, which should be evaluated at the hard scale, i.e., $\alpha_{\rm s} = \alpha_{\rm s}(m)$ when it appears in terms inherited from the matching between NRQCD and QCD. When the coupling originates from matching calculations between pNRQCD and NRQCD it should be evaluated at the soft scale, thus $\alpha_{\rm s} = \alpha_{\rm s}(1/r)$. Finally if $\alpha_{\rm s}$ is associated with light degrees of freedom like ultrasoft gluons, it must be evaluated at the corresponding ultrasoft scale, i.e. $\alpha_{\rm s} = \alpha_{\rm s}(E)$. Notice that the scaling of p with respect to $\Lambda_{\rm QCD}$ determines the size of $\alpha_{\rm s}$, and therefore, its usability as an expansion parameter. In weakly-coupled pNRQCD $p \gg \Lambda_{\rm QCD}$, then $\alpha_{\rm s}(1/r) \ll 1$, so the matching between pNRQCD and NRQCD can be performed perturbatively. In the case of strongly-coupled pNRQCD $p \gtrsim \Lambda_{\rm QCD}$ so $\alpha_{\rm s}(1/r) \sim 1$, thus perturbation theory is not applicable in the matching procedure.
We have skipped the details of the derivation of Eq. (2.31), however, Chapter 3 deals with some of the steps we have left aside in this section. For a detailed derivation we refer the reader to the original papers where pNRQCD was presented and to [22].
One of the advantages of writing the pNRQCD Lagrangian as in Eq. (2.31) is that it permits us to have a clear visualization of the degrees of freedom of the theory: quark-antiquark pairs in singlet or octet configurations and ultrasoft gluons. The precision of the Lagrangian can be systematically improved by including operators proportional to higher powers of $\mathbf{r}$ that must be invariant under charge conjugation, time reversal and parity transformations. For instance, notice that the charge conjugation of the term $\int d^3\mathbf{r} \mathrm{Tr}\{O^\dagger \mathbf{r} \cdot g\mathbf{E} O\}$ is $\int d^3\mathbf{r} \mathrm{Tr}\{O^\dagger O \mathbf{r} \cdot g\mathbf{E}\}$ so the sum of the two must appear. The explicit symmetry transformations of fields of the Lagrangian can be found in [22].

Let us close this section by discussing briefly strongly-coupled pNRQCD. In this regime

$\Lambda_{\rm QCD} \gg E$ so at the scale E it is natural to expect only hadronic degrees of freedom. Consequently, in the strong coupling regime of pNRQCD only the singlet field remains as an explicit degree of freedom of the theory[5]; thus the Lagrangian reduces to

$$\mathcal{L}_{\rm pNRQCD} = \int d^3\mathbf{r} S^\dagger [i\partial_0 - h_S(\mathbf{r}, \mathbf{p}, \mathbf{P_R}, \mathbf{S}_1, \mathbf{S}_2)] S, \tag{2.37}$$

where h_S has the same shape as in weakly-coupled pNRQCD, however, in this case the potential V_S has a non-perturbative nature. We left the details of the quark-antiquark potential for Chapters 3 and 5, where it is discussed with more detail. It will be useful for later reference to give explicitly the canonical equal-time commutation relation for the singlet field, it reads

$$\left[S_{ij}(\mathbf{r}, \mathbf{R}), S^\dagger_{kl}(\mathbf{r}', \mathbf{R}')\right] = \delta_{il}\delta_{jk}\delta^{(3)}(\mathbf{r} - \mathbf{r}')\delta^{(3)}(\mathbf{R} - \mathbf{R}'), \tag{2.38}$$

where $(i, j), (k, l)$ correspond to the spin indices. This relation is also valid for the singlet field in weakly-coupled pNRQCD where it should be complemented with an analogous relation for the octet.

We will adopt the strongly-coupled regime for the computation of the quark-antiquark potential in the Effective String Theory (EST) in Chapter 4. Moreover, since most of the E1 transitions involve excited initial states, we will adopt the strong-coupling regime also in the evaluation of the decay rates. This implies that no contributions from octet fields will appear in our evaluations; nevertheless, the implications of our adoption of strongly-coupled pNRQCD for the evaluation of transitions among low-lying quarkonia are discussed in Chapter 6.

Neglecting the contribution of light quark fields, which would lead to the emergence of pseudo-Goldstone bosons in strongly-coupled pNRQCD (see footnote below); from the pNRQCD Lagrangians in Eqs. (2.31) and (2.37) we see that apart from the quark-antiquark pairs in singlet or octet configurations, in the case of weakly-coupled pNRQCD, the ultrasoft gluons, no other degrees of freedom are present in the theory. This implies that the two versions of pNRQCD that we presented are valid only to study physics below the charm and bottom open thresholds, where no other than these degrees of freedom are expected. This is a restriction that we will consider for the rest of the thesis: in the evaluation of the radiative decays we will only consider transitions in which the initial quarkonium state lies below its respective open flavor threshold.

As in the case of NRQCD, pNRQCD can be coupled to electromagnetism. In this case the pNRQCD Lagrangian is augmented by operators that couple quark-antiquark pairs to ultrasoft photon fields expressed through electric or magnetic operators. The Wilson coefficients accompanying these operators must be obtained by matching the theory to NRQCD coupled to electromagnetism. The relevant pNRQCD operators for the E1 transition will be explicitly given in Chapter 6.

[5]Also pseudo-Goldstone bosons whose masses are smaller than $\Lambda_{\rm QCD}$ are allowed. Here and in the rest of the thesis we will assume that their final contribution to observables, e.g. decay rates and masses, is small enough to be absorbed within other sources of uncertainty, so they will not be included in the pNRQCD Lagrangian.

2.5 Final remarks

We presented the two main EFTs used to study quarkonium. We skipped most of the technical details since they are not relevant for what follows in the thesis and can be found in other sources. For what concerns the current status of research in quarkonium our overview is far from complete. Notably we have left out two of the current topics of quarkonium research mentioned in the Introduction: quarkonium in a hot medium and the spectroscopy of exotic states. The construction of EFTs for quarkonium at finite temperature can be carried out systematically as in the case of zero temperature, the key difference is that now the temperature scales must be included in the hierarchy of scales present in the system. The way the temperature compares to the other scales of quarkonium and to $\Lambda_{\rm QCD}$ will determine the way the theory is constructed. Efforts to understand the physics of quarkonium in media in the framework of EFTs have been carried out, for instance, in [46–49]. A complete introduction to the topic can be found in [50].

One would expect that an EFT suitable for the study of quarkonium and quarkonium-like states above threshold should account for other possible bound states at the level of the Lagrangian. An example of such an approach can be found in [51], where an EFT of QCD for the study of quarkonium hybrids[6] has been constructed. Their results are still not conclusive in explaining the nature of the exotic states that are hybrid candidates, however, it represents a first attempt to study one of the interpretations of exotic states in the framework of the EFTs.

[6]Quarkonium hybrids are states formed by a quark-antiquark pair in an octet configuration and a gluon excitation.

Chapter 3

The quark-antiquark potential in pNRQCD

In this chapter we present the complete singlet quark-antiquark potential up to order $1/m^2$, which has been obtained within the framework of pNRQCD in [18] and [19]. Since these expressions will be important for the evaluation of the E1 decay rates, we show the derivation of the $1/m$-suppressed correction with some detail. The $1/m^2$-suppressed corrections follow from a similar calculation; for these we only give their final expressions.

3.1 The structure of the potential

We consider a heavy quark of mass m_1 located at $\mathbf{x}_1$ and a heavy antiquark of mass m_2 located at $\mathbf{x}_2$. The spin and momentum operators of the two particles are respectively $\mathbf{S}_1 \equiv \boldsymbol{\sigma}_1/2$ and $\mathbf{p}_1 \equiv -i\boldsymbol{\nabla}_{\mathbf{x}_1}$, and $\mathbf{S}_2 \equiv \boldsymbol{\sigma}_2/2$ and $\mathbf{p}_2 \equiv -i\boldsymbol{\nabla}_{\mathbf{x}_2}$. The distance between the quark and the antiquark is $\mathbf{r} \equiv \mathbf{x}_1 - \mathbf{x}_2$. In the center-of-mass frame up to order $1/m^2$ the singlet quark-antiquark potential can be written as the sum of three terms,

$$V_{Q\bar{Q}} = V^{(0)} + V^{(1/m)} + V^{(1/m^2)}\,, \tag{3.1}$$

where $V^{(0)}(r)$ is the static potential,

$$V^{(1/m)}(r) = \frac{V^{(1,0)}(r)}{m_1} + \frac{V^{(0,1)}(r)}{m_2}\,, \tag{3.2}$$

the $1/m$ potential and

$$V^{(1/m^2)} = \frac{V^{(2,0)}}{m_1^2} + \frac{V^{(0,2)}}{m_2^2} + \frac{V^{(1,1)}}{m_1 m_2}\,, \tag{3.3}$$

the $1/m^2$ potential. Invariance under charge conjugation and particle interchange implies $V^{(1,0)}(r) = V^{(0,1)}(r)$. It is useful to separate the $1/m^2$ potential into a spin-dependent

(SD) and a spin-independent (SI) part:

$$V^{(2,0)} = V_{SD}^{(2,0)} + V_{SI}^{(2,0)}\,, \tag{3.4}$$

$$V^{(0,2)} = V_{SD}^{(0,2)} + V_{SI}^{(0,2)}\,, \tag{3.5}$$

where

$$V_{SI}^{(2,0)} = \frac{1}{2}\left\{\mathbf{p}_1^2, V_{\mathbf{p}^2}^{(2,0)}(r)\right\} + \frac{V_{\mathbf{L}^2}^{(2,0)}(r)}{r^2}\mathbf{L}_1^2 + V_r^{(2,0)}(r)\,, \tag{3.6}$$

$$V_{SI}^{(0,2)} = \frac{1}{2}\left\{\mathbf{p}_2^2, V_{\mathbf{p}^2}^{(0,2)}(r)\right\} + \frac{V_{\mathbf{L}^2}^{(0,2)}(r)}{r^2}\mathbf{L}_2^2 + V_r^{(0,2)}(r)\,, \tag{3.7}$$

and $\mathbf{L}_i = \mathbf{r}\times\mathbf{p}_i$ with $i = 1, 2$. Also in this case invariance under charge conjugation and particle interchange yields

$$V_{\mathbf{p}^2}^{(2,0)}(r) = V_{\mathbf{p}^2}^{(0,2)}(r)\,, \tag{3.8}$$

$$V_{\mathbf{L}^2}^{(2,0)}(r) = V_{\mathbf{L}^2}^{(0,2)}(r)\,, \tag{3.9}$$

$$V_r^{(2,0)}(r) = V_r^{(0,2)}(r)\,. \tag{3.10}$$

For the spin-dependent part we have

$$V_{SD}^{(2,0)} = V_{LS}^{(2,0)}(r)\,\mathbf{L}_1\cdot\mathbf{S}_1\,, \tag{3.11}$$

$$V_{SD}^{(0,2)} = -V_{LS}^{(0,2)}(r)\,\mathbf{L}_2\cdot\mathbf{S}_2\,. \tag{3.12}$$

Charge conjugation and particle interchange invariance imply $V_{LS}^{(2,0)}(r) = V_{LS}^{(0,2)}(r; m_2 \leftrightarrow m_1)$. One proceeds similarly for the $V^{(1,1)}$ potential:

$$V^{(1,1)} = V_{SD}^{(1,1)} + V_{SI}^{(1,1)}\,, \tag{3.13}$$

where

$$V_{SI}^{(1,1)} = -\frac{1}{2}\left\{\mathbf{p}_1\cdot\mathbf{p}_2, V_{\mathbf{p}^2}^{(1,1)}(r)\right\} - \frac{V_{\mathbf{L}^2}^{(1,1)}(r)}{2r^2}(\mathbf{L}_1\cdot\mathbf{L}_2 + \mathbf{L}_2\cdot\mathbf{L}_1) + V_r^{(1,1)}(r)\,, \tag{3.14}$$

and

$$V_{SD}^{(1,1)} = V_{L_1S_2}^{(1,1)}(r)\mathbf{L}_1\cdot\mathbf{S}_2 - V_{L_2S_1}^{(1,1)}(r)\mathbf{L}_2\cdot\mathbf{S}_1 + V_{S^2}^{(1,1)}(r)\mathbf{S}_1\cdot\mathbf{S}_2 + V_{\mathbf{S}_{12}}^{(1,1)}(r)\mathbf{S}_{12}(\hat{\mathbf{r}}), \tag{3.15}$$

with

$$\mathbf{S}_{12}(\hat{\mathbf{r}}) \equiv 3\,\hat{\mathbf{r}}\cdot\boldsymbol{\sigma}_1\,\hat{\mathbf{r}}\cdot\boldsymbol{\sigma}_2 - \boldsymbol{\sigma}_1\cdot\boldsymbol{\sigma}_2\,, \tag{3.16}$$

and $V_{L_1S_2}^{(1,1)}(r) = V_{L_2S_1}^{(1,1)}(r; m_1 \leftrightarrow m_2)$.

This structure of the potential is dictated by the dimensional analysis of possible terms, constraints from discrete symmetries and ultimately by the matching between NRQCD and pNRQCD. The structure given here will be adopted for the rest of the thesis, however, we recall that it is not unique since it can be reshuffled by a unitary redefinition of the singlet field in the pNRQCD Lagrangian, for a discussion about the implications of such a transformation see [35] and [52].

In the next two sections we will present the explicit expressions of the $V^{(i,j)}(r)$ potentials obtained with pNRQCD.

3.2 Derivation of the $1/m$-suppressed relativistic correction

3.2.1 Set-up

In this section we sketch the derivation of the $1/m$ correction to the heavy quark-antiquark ($Q\bar{Q}$) potential obtained within the framework of pNRQCD. The original derivation has been carried out in [18], to which we will refer for details that we will omit.

The strategy is to match a relevant Green function in NRQCD and pNRQCD at order $1/m$. We do not consider any specific counting of the NRQCD operators other than their suppression in powers of $1/m$. On the pNRQCD side we will work in the strong-coupling regime, so the only degree of freedom of the Lagrangian is the singlet field. We are not considering other light degrees of freedom, their inclusion will not change the results of this section but may change some intermediate steps [18]. The derivation also assumes that we are away enough from the open flavor threshold to neglect any possible effects associated with it.

Let us start recalling the NRQCD Lagrangian[1] at order $1/m$

$$\begin{aligned}\mathcal{L}_{\rm NRQCD} &= \psi^\dagger\left(iD_0+\frac{\mathbf{D}^2}{2m_1}+gc_F^{(1)}\frac{\boldsymbol{\sigma}\cdot\mathbf{B}}{2m_1}\right)\psi+\chi^\dagger\left(iD_0-\frac{\mathbf{D}^2}{2m_2}-gc_F^{(2)}\frac{\boldsymbol{\sigma}\cdot\mathbf{B}}{2m_2}\right)\chi \\ &- \frac{1}{4}G^a_{\mu\nu}G^{\mu\nu\,a}. \end{aligned} \tag{3.17}$$

We differentiate between the Wilson coefficients $c_F^{(i)}=1+\mathcal{O}(\alpha_{\rm s})$ for the quark and antiquark. The Hamiltonian corresponding to Eq. (3.17) can be organized as

$$H=H^{(0)}+\frac{1}{m_1}H^{(1,0)}+\frac{1}{m_2}H^{(0,1)}. \tag{3.18}$$

For our calculation we will need to consider only eigenfunctions and eigenvalues of the leading order (static) Hamiltonian $H^{(0)}$ given by

$$H^{(0)}=\int d^3\mathbf{x}\,\frac{1}{2}(\mathbf{E}^a\cdot\mathbf{E}^a+\mathbf{B}^a\cdot\mathbf{B}^a) \tag{3.19}$$

The eigenfunctions and eigenvalues of this operator fulfill the following relations

$$H^{(0)}|\underline{n};\mathbf{x}_1,\mathbf{x}_2\rangle^{(0)} = E_n^{(0)}(\mathbf{x}_1,\mathbf{x}_2)|\underline{n};\mathbf{x}_1,\mathbf{x}_2\rangle^{(0)} \tag{3.20}$$

$${}^{(0)}\langle\underline{m};\mathbf{x}_1,\mathbf{x}_2|\underline{n};\mathbf{x}_1',\mathbf{x}_2'\rangle^{(0)} = \delta_{mn}\delta^{(3)}(\mathbf{x}_1-\mathbf{x}_1')\delta^{(3)}(\mathbf{x}_2-\mathbf{x}_2'). \tag{3.21}$$

Since we are interested in the one-quark one-antiquark sector of the Fock space, it will be convenient to decompose $|\underline{n};\mathbf{x}_1,\mathbf{x}_2\rangle^{(0)}$ as

$$|\underline{n};\mathbf{x}_1,\mathbf{x}_2\rangle^{(0)}\equiv\psi^\dagger(\mathbf{x}_1)\chi(\mathbf{x}_2)|n;\mathbf{x}_1,\mathbf{x}_2\rangle^{(0)} \tag{3.22}$$

[1] As in the previous section, we will consider the general case in which $m_1\neq m_2$.

where the $|n;\mathbf{x}_1,\mathbf{x}_2\rangle^{(0)}$ state encodes the gluonic content of the state; it fulfills

$$ {}^{(0)}\langle m;\mathbf{x}_1,\mathbf{x}_2|n;\mathbf{x}_1,\mathbf{x}_2\rangle^{(0)} = \delta_{mn}. \tag{3.23}$$

Since $H^{(0)}$ does not contain heavy quark fields, $|n;\mathbf{x}_1,\mathbf{x}_2\rangle$ is also an eigenstate of $H^{(0)}$ with energy $E_n^{(0)}(\mathbf{x}_1,\mathbf{x}_2)$. In Eq. (3.20) it is explicit that $\mathbf{x}_1$ and $\mathbf{x}_2$ are good quantum numbers of the state $|\underline{n};\mathbf{x}_1,\mathbf{x}_2\rangle^{(0)}$.
The static NRQCD energy $E_0^{(0)}(\mathbf{x}_1,\mathbf{x}_2)$ is associated with the static $Q\bar{Q}$ potential. Away from threshold, in the strong coupling regime of pNRQCD, only the state associated with this energy, namely $|\underline{n}=0;\mathbf{x}_1,\mathbf{x}_2\rangle^{(0)}$, is kept as degree of freedom, while states with $n\neq 0$ (*gluonic excitations*) are integrated out. This assumes that states with $n>0$ have energies much larger than mv^2.
The strongly-coupled pNRQCD Lagrangian was presented in the previous chapter for the equal mass case, in the case where $m_1\neq m_2$ it reads

$$ \mathcal{L}_{\rm pNRQCD} = \int d^3\mathbf{x}_1 d^3\mathbf{x}_2\, S^\dagger[i\partial_0 - h_S(\mathbf{x}_1,\mathbf{x}_2,\mathbf{p}_1,\mathbf{p}_2,\ldots)]S, \tag{3.24}$$

where at order $1/m$ in the center-of-mass frame

$$ h_s(\mathbf{x}_1,\mathbf{x}_2,\mathbf{p}_1,\mathbf{p}_2) = \frac{\mathbf{p}_1}{2m_1} + \frac{\mathbf{p}_2}{2m_2} + V_S. \tag{3.25}$$

with

$$ V_S = V^{(0)} + \left(\frac{1}{m_1}+\frac{1}{m_2}\right) V^{(1)}. \tag{3.26}$$

We used invariance under charge conjugation and particle interchange to define $V^{(1)} \equiv V^{(1,0)} = V^{(0,1)}$. In the language of EFTs, $V^{(0)}$ and $V^{(1)}$ are the Wilson coefficients of pNRQCD. In the next two subsections we proceed to match NRQCD and pNRQCD in order to obtain a set of equations that will fix the expressions of these two potentials.

3.2.2 Wilson loop matching

We start by writing a state that has a non-zero overlap with $|\underline{0}\rangle^{(0)}$,

$$ \psi^\dagger(\mathbf{x}_1)\phi(\mathbf{x}_1,\mathbf{x}_2)\chi(\mathbf{x}_2)|{\rm vac}\rangle, \tag{3.27}$$

where ϕ is responsible for the overlap with the ground state, for which we adopt the following ansatz

$$ \phi(\mathbf{x}_1,\mathbf{x}_2;t) \equiv {\rm P}\exp\left[ig\int_0^1 ds(\mathbf{x}_1-\mathbf{x}_2)\cdot\mathbf{A}(\mathbf{x}_2 - s(\mathbf{x}_2-\mathbf{x}_1),t)\right]. \tag{3.28}$$

For the calculation in pNRQCD we will also need the following decomposition

$$ \psi^\dagger(\mathbf{x}_1)\phi(\mathbf{x}_1,\mathbf{x}_2)\chi(\mathbf{x}_2)|{\rm vac}\rangle = \sum_n a_n(\mathbf{x}_1,\mathbf{x}_2)|\underline{n};\mathbf{x}_1,\mathbf{x}_2\rangle^{(0)}, \tag{3.29}$$

where the coefficients $a_n(\mathbf{x}_1, \mathbf{x}_2)$ are fixed in such a way that they are real.
The key identification for the matching is that since the field in Eq. (3.27) overlaps with the only degree of freedom in pNRQCD, the singlet S, there should be a non-zero Wilson coefficient Z (a *normalization constant*) such that

$$\chi^\dagger(\mathbf{x}_2, t)\phi(\mathbf{x}_2, \mathbf{x}_1; t)\psi(\mathbf{x}_1, t) = Z^{1/2}(\mathbf{x}_1, \mathbf{x}_2, \mathbf{p}_1, \mathbf{p}_2)S(\mathbf{x}_1, \mathbf{x}_2, t). \tag{3.30}$$

As with the potentials, $Z(\mathbf{x}_1, \mathbf{x}_2, \mathbf{p}_1, \mathbf{p}_2)$ can be expanded in powers of $1/m$; up to order $1/m$ the expansion reads

$$Z(\mathbf{x}_1, \mathbf{x}_2, \mathbf{p}_1, \mathbf{p}_2) = Z_0(r) + \left(\frac{1}{m_1} + \frac{1}{m_2}\right) Z_1(r) + iZ_{1p}(r)\mathbf{r} \cdot \left(\frac{\mathbf{p}_1}{m_1} - \frac{\mathbf{p}_2}{m_2}\right), \tag{3.31}$$

where constraints coming from CP and mass exchange invariances of the NRQCD and pNRQCD Lagrangians reduce the number of independent coefficients in the expansion.
We will consider the following NRQCD Green function for the matching

$$\begin{aligned} G_{\rm NRQCD} &= \langle \mathrm{vac}|\chi^\dagger(\mathbf{x}_2, T/2)\phi(\mathbf{x}_2, \mathbf{x}_1; T/2)\psi(\mathbf{x}_1, T/2) \\ &\times \psi^\dagger(\mathbf{y}_1, -T/2)\phi(\mathbf{y}_1, \mathbf{y}_2; -T/2)\chi(\mathbf{y}_2, -T/2)|\mathrm{vac}\rangle. \end{aligned} \tag{3.32}$$

In order to construct the equivalent pNRQCD Green function let us first consider that in the Heisenberg picture the time evolution of the singlet field is given by

$$S(\mathbf{x}_1, \mathbf{x}_2; t) = e^{+iH_s t} S(\mathbf{x}_1, \mathbf{x}_2; t = 0) e^{-iH_s t}, \tag{3.33}$$

where

$$H_s = \int d^3\mathbf{x}_1 d^3\mathbf{x}_2 \, \mathrm{Tr}\{S^\dagger h_s S\}. \tag{3.34}$$

Using Eqs. (3.30), (3.33) and the equal-time commutation relations of the singlet fields given in Eq. (2.38) of the previous chapter one obtains

$$G_{\rm pNRQCD} = Z^{1/2} e^{-iTh_s} Z^{\dagger\, 1/2} \delta^{(3)}(\mathbf{x}_1 - \mathbf{y}_1)\delta^{(3)}(\mathbf{x}_2 - \mathbf{y}_2). \tag{3.35}$$

What follows is to expand Eqs. (3.32) and (3.35) in powers of $1/m$ and then compare them order by order. Our aim with this procedure is to obtain a set of equations to fix $V^{(0)}$ and $V^{(1)}$ in terms of expectation values involving NRQCD operators.
In the case of the pNRQCD Green function, using (3.25), (3.31) and expanding the exponential operator, the expansion up to $1/m$ order reads [18]

$$G_{\rm pNRQCD} = G^{(0)}_{\rm pNRQCD} + \frac{1}{m_1} G^{(1,0)}_{\rm pNRQCD} + \frac{1}{m_2} G^{(0,1)}_{\rm pNRQCD} \tag{3.36}$$

with

$$
\begin{aligned}
G^{(0)}_{\rm pNRQCD} &= Z_0 e^{-iV^{(0)}T}\delta^{(3)}(\mathbf{x}_1-\mathbf{y}_1)\delta^{(3)}(\mathbf{x}_2-\mathbf{y}_2), \qquad (3.37)\\
G^{(1,0)}_{\rm pNRQCD} &= Z_0 e^{-iV^{(0)}T}\left\{\frac{{\rm Re}[Z_1]}{Z_0}-\frac{1}{2}\left(\boldsymbol{\nabla}\cdot\mathbf{r}\frac{Z_{1p}}{Z_0}\right)-\frac{i}{2}T(\boldsymbol{\nabla}V^{(0)})\cdot\mathbf{r}\frac{Z_{1p}}{Z_0}\right.\\
&+ iT\frac{\boldsymbol{\nabla}^2_{\mathbf{x}_1}}{2}-iTV^{(1)}+\frac{iT}{8}\left(4\frac{(\boldsymbol{\nabla}Z_0}{Z_0}\cdot\boldsymbol{\nabla}_{\mathbf{x}_1}+2\frac{\boldsymbol{\nabla}^2Z_0}{Z_0}-\frac{\boldsymbol{\nabla}Z_0)^2}{Z_0}\right)\\
&+ \frac{T^2}{4}\left(2(\boldsymbol{\nabla}V^{(0)})\cdot\boldsymbol{\nabla}_{\mathbf{x}_1}+\frac{\boldsymbol{\nabla}Z_0}{Z_0}\cdot(\boldsymbol{\nabla}V^{(0)})+\boldsymbol{\nabla}^2V^{(0)}\right)\\
&- \left.\frac{iT^3}{6}(\boldsymbol{\nabla}V^{(0)})^2\right\}\delta^{(3)}(\mathbf{x}_1-\mathbf{y}_1)\delta^{(3)}(\mathbf{x}_2-\mathbf{y}_2), \qquad (3.38)
\end{aligned}
$$

where $\boldsymbol{\nabla}=\boldsymbol{\nabla}_{\mathbf{r}}$ with $\mathbf{r}$ being the quark-antiquark separation vector $\mathbf{r}=\mathbf{x}_1-\mathbf{x}_2$. We skipped the analogous expression for $G^{(0,1)}_{\rm pNRQCD}$.
The computation of the NRQCD Green functions is a bit more elaborate. First let us expand the NRQCD Green function as we did for the pNRQCD one

$$
G_{\rm NRQCD}=G^{(0)}_{\rm NRQCD}+\frac{1}{m_1}G^{(1,0)}_{\rm NRQCD}+\frac{1}{m_2}G^{(0,1)}_{\rm NRQCD}. \qquad (3.39)
$$

After integrating out the heavy quark fields one obtains [18]

$$
\begin{aligned}
G^{(0)}_{\rm NRQCD} &= \langle W_\Box\rangle\delta^{(3)}(\mathbf{x}_1-\mathbf{y}_1)\delta^{(3)}(\mathbf{x}_2-\mathbf{y}_2), \qquad (3.40)\\
G^{(1,0)}_{\rm NRQCD} &= \frac{i}{2}\int_{-T/2}^{T/2}dt\langle\mathbf{D}^2(\mathbf{x}_1,t)\rangle_\Box\delta^{(3)}(\mathbf{x}_1-\mathbf{y}_1)\delta^{(3)}(\mathbf{x}_2-\mathbf{y}_2), \qquad (3.41)
\end{aligned}
$$

where the average is over the pure Yang-Mills action and

$$
W_\Box\equiv{\rm P}\exp\left\{-ig\oint_{r\times T}dz^\mu\,A_\mu(z)\right\}, \qquad (3.42)
$$

is the rectangular Wilson loop. We have introduced the notation $\langle ...\rangle_\Box\equiv\langle ...W_\Box\rangle$. Using identities of the covariant derivatives acting on Schwinger lines and symmetry arguments (see [18] and [53]) Eq. (3.41) can be rewritten as

$$
\begin{aligned}
G^{(1,0)}_{\rm NRQCD} &= \frac{i}{2}\left\{\frac{T}{2}\boldsymbol{\nabla}^2_{\mathbf{x}_1}\langle W_\Box\rangle+\frac{T}{2}\langle W_\Box\rangle\boldsymbol{\nabla}^2_{\mathbf{x}_1}+T\langle\mathbf{O}_2(T/2)\cdot\mathbf{O}_1(-T/2)\rangle_\Box\right.\\
&+ ig\int_{-T/2}^{T/2}dt\left(\frac{T}{2}-t\right)\langle\mathbf{O}_2(T/2)\cdot\mathbf{E}(\mathbf{x}_1,t)\rangle_\Box\\
&- ig\int_{T/2}^{T/2}dt\left(\frac{T}{2}+t\right)\langle\mathbf{E}(\mathbf{x}_1,t)\cdot\mathbf{O}_1(-T/2)\rangle_\Box\\
&+ \left.\int_{-T/2}^{T/2}dt\int_{-T/2}^{T/2}dt'|t-t'|\langle\mathbf{E}(\mathbf{x}_1,t)\cdot\mathbf{E}(\mathbf{x}_1,t')\rangle_\Box\right\}\delta^{(3)}(\mathbf{x}_1-\mathbf{y}_1)\delta^{(3)}(\mathbf{x}_2-\mathbf{y}_2),
\end{aligned}
\qquad (3.43)
$$

where

$$\mathbf{O}_1(t) = ig\mathbf{r}\times\int_0^1 ds\, s\phi(\mathbf{x}_1,\mathbf{x}'(s);t)\mathbf{B}(\mathbf{x}'(s),t)\phi(\mathbf{x}'(s),\mathbf{x}_2;t), \tag{3.44}$$

$$\mathbf{O}_2(t) = ig\mathbf{r}\times\int_0^1 ds(1-s)\phi(\mathbf{x}_2,\mathbf{x}''(s);t)\mathbf{B}(\mathbf{x}''(s),t)\phi(\mathbf{x}''(s),\mathbf{x}_1;t), \tag{3.45}$$

with

$$\mathbf{x}'(s) = \mathbf{x}_2 + s\mathbf{r}, \tag{3.46}$$

$$\mathbf{x}''(s) = \mathbf{x}_1 - s\mathbf{r}. \tag{3.47}$$

$$\tag{3.48}$$

Now we can proceed to match order by order in $1/m$. Comparing Eq. (3.37) with (3.40) and taking the $T\to\infty$ limit, we get the familiar expression of the LO potential in terms of the expectation value of the Wilson loop:

$$V^{(0)} = \lim_{T\to\infty}\frac{i}{T}\ln\langle W_\square\rangle. \tag{3.49}$$

At order $1/m$ comparing Eq. (3.38) with Eq. (3.43) we obtain

$$\begin{aligned} V^{(1)} + \frac{1}{2}(\boldsymbol{\nabla}V^{(0)})\cdot\mathbf{r}\frac{Z_{1p}}{Z_0} = \lim_{T\to\infty}\Bigg(&-\frac{1}{8}\left(\frac{(\boldsymbol{\nabla}Z_0)}{Z_0}\right)^2 + i\frac{T}{4}\frac{(\boldsymbol{\nabla}Z_0)}{Z_0}\cdot(\boldsymbol{\nabla}V^{(0)}) + \frac{T^2}{12}(\boldsymbol{\nabla}V^{(0)})^2 \\ &- \frac{g}{4}\int_{-T/2}^{T/2}dt\Bigg\{\left(1-\frac{2t}{T}\right)\langle\!\langle\mathbf{O}_2(T/2)\cdot\mathbf{E}(\mathbf{x}_1,t)\rangle\!\rangle \\ &- \left(1+\frac{2t}{T}\right)\langle\!\langle\mathbf{E}(\mathbf{x}_1,t)\cdot\mathbf{O}_1(-T/2)\rangle\!\rangle\Bigg\} - \frac{1}{2}\langle\!\langle\mathbf{O}_2(T/2)\cdot\mathbf{O}_1(-T/2)\rangle\!\rangle \\ &- \frac{g^2}{4T}\int_{-T/2}^{T/2}dt'|t-t'|\langle\!\langle\mathbf{E}(\mathbf{x}_1,t)\cdot\mathbf{E}(\mathbf{x}_1,t')\rangle\!\rangle\Bigg). \end{aligned} \tag{3.50}$$

In the equation above we have defined the notation $\langle\!\langle\ldots\rangle\!\rangle \equiv \langle\ldots\rangle_\square/\langle W_\square\rangle$. The matching conditions (3.49) and (3.50) can be further simplified by writing the Wilson loop average as

$$\langle W_\square\rangle = \sum_n e^{-iE_n^{(0)}T}a_n^2. \tag{3.51}$$

Using this decomposition at leading order one gets

$$V^{(0)} = E_0^{(0)}, \tag{3.52}$$

and for the $1/m$ matching condition the result yields

$$V^{(1)} + \frac{1}{2}(\boldsymbol{\nabla}V^{(0)})\cdot\mathbf{r}\frac{Z_{1p}}{Z_0} = \frac{1}{2}\sum_{n\neq 0}\left|\frac{{}^{(0)}\langle n|g\mathbf{E}(\mathbf{x}_1)|0\rangle^{(0)}}{E_0^{(0)}-E_n^{(0)}}\right|^2 + (\boldsymbol{\nabla}E_0^{(0)})\sum_{n\neq 0}\frac{a_n}{a_0}\frac{{}^{(0)}\langle n|g\mathbf{E}(\mathbf{x}_1)|0\rangle^{(0)}}{(E_0^{(0)}-E_n^{(0)})^2}. \tag{3.53}$$

The last two equations have been obtained after taking the limit for large T; more details about their derivation are found in Appendix A. Notice that Eq. (3.52) verifies our identification of the ground state energy with the leading order potential $V^{(0)}$. Our final goal is to obtain an expression analogous to the one obtained for $V^{(0)}$ in Eq. (3.49) also for the $V^{(1)}$ potential, that is, we want to find an expression for $V^{(1)}$ written in terms of the expectation value of the rectangular Wilson loop that does not depend on the coefficients of the expansion of the normalization constant. For this purpose we need to find new equations in order to eliminate the coefficients from Eqs. (3.50) and (3.53). In the next section we take another approach for the matching that will provide us with these equations.

3.2.3 Quantum mechanical matching

Instead of comparing Green functions, in this approach we will compare states and matrix elements in a calculation that has some similarities to perturbative calculations in Quantum Mechanics.
Let us consider the eigenstates $|\underline{n};\mathbf{x}_1,\mathbf{x}_2\rangle$ of the full $O(1/m)$ NRQCD Hamiltonian H, they fulfill

$$\begin{aligned}\langle\underline{m};\mathbf{x}_1,\mathbf{x}_2|H|\underline{n};\mathbf{x}_1',\mathbf{x}_2'\rangle &= \delta_{mn}E_n(\mathbf{x}_1,\mathbf{x}_2,\mathbf{p}_1,\mathbf{p}_2)\delta^{(3)}(\mathbf{x}_1-\mathbf{x}_1')\delta^{(3)}(\mathbf{x}_2-\mathbf{x}_2'), &(3.54)\\ \langle\underline{m};\mathbf{x}_1,\mathbf{x}_2|\underline{n};\mathbf{x}_1',\mathbf{x}_2'\rangle &= \delta_{mn}\delta^{(3)}(\mathbf{x}_1-\mathbf{x}_1')\delta^{(3)}(\mathbf{x}_2-\mathbf{x}_2'). &(3.55)\end{aligned}$$

The equations above imply that

$$H|\underline{n};\mathbf{y}_1,\mathbf{y}_2\rangle=\int d^3\mathbf{x}_1d^3\mathbf{x}_2|\underline{n};\mathbf{x}_1,\mathbf{x}_2\rangle E_n(\mathbf{x}_1,\mathbf{x}_2,\mathbf{p}_1,\mathbf{p}_2)\delta^{(3)}(\mathbf{x}_1-\mathbf{y}_1)\delta^{(3)}(\mathbf{x}_2-\mathbf{y}_2). \quad (3.56)$$

In analogy to quantum mechanical perturbation theory, we can expand the states and energies in powers of $1/m$, thus

$$\begin{aligned}|\underline{n}\rangle &= |\underline{n}\rangle^{(0)}+\frac{1}{m_1}|\underline{n}\rangle^{(1,0)}+\frac{1}{m_2}|\underline{n}\rangle^{(0,1)}+\ldots, &(3.57)\\ E_n &= E_n^{(0)}+\frac{1}{m_1}E_n^{(1,0)}+\frac{1}{m_2}E_n^{(0,1)}+\ldots, &(3.58)\end{aligned}$$

for the state and energy $n=0$ we have [18]

$$\begin{aligned}|\underline{0}\rangle^{(1,0)} &= \frac{1}{E_0^{(0)}-H^{(0)}}\sum_{n\neq0}\int d^3\mathbf{x}_1'd^3\mathbf{x}_2'|\underline{n};\mathbf{x}_1',\mathbf{x}_2'\rangle^{(0)\,(0)}\langle\underline{n};\mathbf{x}_1',\mathbf{x}_2'|H^{(1,0)}|\underline{0}\rangle^{(0)}\\ &= -\frac{1}{E_0^{(0)}-H^{(0)}}\sum_{n\neq0}\left\{\frac{{}^{(0)}\langle n|g\mathbf{E}(\mathbf{x}_1)|0\rangle^{(0)}}{E_0^{(0)}-E_n^{(0)}}\cdot\boldsymbol{\nabla}_{\mathbf{x}_1}+\frac{1}{2}\left(\boldsymbol{\nabla}_{\mathbf{x}_1}\cdot\frac{{}^{(0)}\langle n|g\mathbf{E}(\mathbf{x}_1)|0\rangle^{(0)}}{E_0^{(0)}-E_n^{(0)}}\right)\right.\\ &\left.-\frac{1}{2}\sum_{j\neq0,n}\frac{{}^{(0)}\langle n|g\mathbf{E}(\mathbf{x}_1)|j\rangle^{(0)}\,{}^{(0)}\langle j|g\mathbf{E}(\mathbf{x}_1)|0\rangle^{(0)}}{(E_j^{(0)}-E_n^{(0)})(E_j^{(0)}-E_0^{(0)})}\right\}|\underline{n}\rangle^{(0)},\end{aligned} \quad (3.59)$$

$$E_0^{(1,0)}\delta^{(3)}(\mathbf{x}_1-\mathbf{y}_1)\delta^{(3)}(\mathbf{x}_2-\mathbf{y}_2) =^{(0)} \langle \underline{0}|H^{(1,0)}|\underline{0}\rangle^{(0)}$$
$$= \left(-\frac{\boldsymbol{\nabla}^2_{\mathbf{x}_1}}{2}+\frac{1}{2}\sum_{n\neq 0}\left|\frac{^{(0)}\langle n|g\mathbf{E}(\mathbf{x}_1)|0\rangle^{(0)}}{E^{(0)}-E_m^{(0)}}\right|^2\right)\delta^{(3)}(\mathbf{x}_1-\mathbf{y}_1)\delta^{(3)}(\mathbf{x}_2-\mathbf{y}_2). \tag{3.60}$$

Since the only degree of freedom of pNRQCD is identified as $|\underline{0}\rangle$ the matching conditions in this approach read

$$|\underline{0}\rangle = S^\dagger|\mathrm{vac}\rangle, \tag{3.61}$$
$$E_0(\mathbf{x}_1,\mathbf{x}_2,\mathbf{p}_1,\mathbf{p}_2) = h_s(\mathbf{x}_1,\mathbf{x}_2,\mathbf{p}_1,\mathbf{p}_2). \tag{3.62}$$

Using this last equation together Eq. (3.30) we obtain a matching condition for the normalization constant

$$Z^{1/2}(\mathbf{x}_1,\mathbf{x}_2,\mathbf{p}_1,\mathbf{p}_2)\delta^{(3)}(\mathbf{x}_1-\mathbf{y}_1)\delta^{(3)}(\mathbf{x}_2-\mathbf{y}_2) = \langle \mathrm{vac}|\chi^\dagger(\mathbf{x}_2)\phi(\mathbf{x}_2,\mathbf{x}_1)\psi(\mathbf{x}_1)|\underline{0};\mathbf{y}_1,\mathbf{y}_2\rangle. \tag{3.63}$$

Notice that this matching condition is valid at any order in $1/m$.
Combining Eqs. (3.59) and (3.63) together with the expansions (3.31) and (3.29) we get at order $1/m$

$$Z_0^{1/2} = a_0, \tag{3.64}$$
$$\frac{Z_1}{Z_0^{1/2}} = \sum_{n\neq 0}\frac{a_n}{E_0^{(0)}-E_n^{(0)}}\left\{\left(\boldsymbol{\nabla}_{\mathbf{x}_1}\cdot\frac{^{(0)}\langle n|g\mathbf{E}(\mathbf{x}_1)|0\rangle^{(0)}}{E_0^{(0)}-E_n^{(0)}}\right)\right.$$
$$- 2\left(\frac{^{(0)}\langle n|g\mathbf{E}(\mathbf{x}_1)|0\rangle^{(0)}}{(E_0^{(0)}-E_n^{(0)})^2}\right)\cdot(\boldsymbol{\nabla}_{\mathbf{x}_1}E_0^{(0)})$$
$$\left.+ \sum_{j\neq 0,n}\frac{^{(0)}\langle n|g\mathbf{E}(\mathbf{x}_1)|j\rangle^{(0)}\,{}^{(0)}\langle j|g\mathbf{E}(\mathbf{x}_1)|0\rangle^{(0)}}{(E_j^{(0)}-E_n^{(0)})(E_j^{(0)}-E_0^{(0)})}\right\}, \tag{3.65}$$
$$\frac{Z_{1p}\mathbf{r}}{Z_0^{1/2}} = 2\sum_{n\neq 0}a_n\frac{^{(0)}\langle n|g\mathbf{E}(\mathbf{x}_1)|0\rangle^{(0)}}{(E_0^{(0)}-E_n^{(0)})^2}. \tag{3.66}$$

Replacing Eqs. (3.52) and (3.66) into (3.53) one obtains

$$V^{(1)} = \frac{1}{2}\sum_{n\neq 0}\left|\frac{^{(0)}\langle n|g\mathbf{E}(\mathbf{x}_1)|0\rangle^{(0)}}{E_0^{(0)}-E_n^{(0)}}\right|^2. \tag{3.67}$$

The previous equation fully determines the $O(1/m)$ correction. Applying the same procedure used in going from Eq. (3.50) to Eq. (3.53) it can be shown that

$$V^{(1)} = \lim_{T\to\infty}\frac{g^2}{4T}\int_{-T/2}^{T/2}dt\int_{-T/2}^{T/2}dt'|t-t'|\left[\langle\!\langle\mathbf{E}(\mathbf{x}_1,t)\cdot\mathbf{E}(\mathbf{x}_1,t')\rangle\!\rangle\right.$$
$$\left.-\langle\!\langle\mathbf{E}(\mathbf{x}_1,t)\rangle\!\rangle\cdot\langle\!\langle\mathbf{E}(\mathbf{x}_1,t')\rangle\!\rangle\right] \tag{3.68}$$

is equivalent to Eq. (3.67). The steps of the method to obtain (3.67) from Eq. (3.68) are listed in Appendix A.
The potential $V^{(1)}$ can be written in a more compact way [19]

$$V^{(1)} = -\frac{1}{2} \lim_{T\to\infty} \int_0^T dt\, t\, \langle\!\langle g\mathbf{E}_1(t) \cdot g\mathbf{E}_1(0) \rangle\!\rangle_c, \tag{3.69}$$

with

$$\langle\!\langle O_1(t_1) O_2(t_2) \rangle\!\rangle_c = \langle\!\langle O_1(t_1) O_2(t_2) \rangle\!\rangle - \langle\!\langle O_1(t_1) \rangle\!\rangle \langle\!\langle O_2(t_2) \rangle\!\rangle. \tag{3.70}$$

The index i in $\mathbf{E}_i$ indicates that the operator is evaluated at $\mathbf{x}_i$. The $V^{(0)}$ and $V^{(1)}$ potentials written as in Eqs. (3.49) and (3.69) respectively are the main results of this section. The expression of $V^{(1)}$ in terms of field insertions in the Wilson loop expectation value was, by the time Ref. [18] was published, a novel result obtained for the first time within the framework of pNRQCD. For our purposes it is important to recall that Eq. (3.69) holds for the whole distance regime of the potential. In [18] it was shown that at short distances, where perturbation theory can be used, $V^{(1)}$ reduces to

$$V^{(1)}_{\rm pert} = -C_F C_A \frac{\alpha_{\rm s}^2}{4r^2}, \tag{3.71}$$

which coincides with previously known perturbative calculations [54, 55]. In the next section we list the expressions of all $1/m^2$ corrections to the potential obtained by following a similar matching procedure as the one we have described here.

3.3 The $1/m^2$-suppressed corrections

Going to order $1/m^2$ in the matching between NRQCD and pNRQCD, the $1/m^2$-suppressed relativistic corrections to the potential can be obtained. The matching has been performed in [19], to which refer for the details of the calculation. Using the same notation

as in the previous section, the potentials obtained in [19] read

$$V_{\mathbf{p}^2}^{(2,0)}(r) = \frac{i}{2}\hat{\mathbf{r}}^i\hat{\mathbf{r}}^j \int_0^\infty dt\, t^2 \langle\!\langle g\mathbf{E}_1^i(t) g\mathbf{E}_1^j(0)\rangle\!\rangle_c \,, \tag{3.72}$$

$$V_{\mathbf{L}^2}^{(2,0)}(r) = \frac{i}{4}\left(\delta^{ij} - 3\hat{\mathbf{r}}^i\hat{\mathbf{r}}^j\right) \int_0^\infty dt\, t^2 \langle\!\langle g\mathbf{E}_1^i(t) g\mathbf{E}_1^j(0)\rangle\!\rangle_c \,, \tag{3.73}$$

$$V_{LS}^{(2,0)}(r) = -\frac{c_F^{(1)}}{r^2} i\mathbf{r}\cdot \int_0^\infty dt\, t\, \langle\!\langle g\mathbf{B}_1(t) \times g\mathbf{E}_1(0)\rangle\!\rangle + \frac{c_S^{(1)}}{2r^2}\mathbf{r}\cdot\left(\boldsymbol{\nabla}_r V^{(0)}\right) \,, \tag{3.74}$$

$$V_{\mathbf{p}^2}^{(1,1)}(r) = i\hat{\mathbf{r}}^i\hat{\mathbf{r}}^j \int_0^\infty dt\, t^2 \langle\!\langle g\mathbf{E}_1^i(t) g\mathbf{E}_2^j(0)\rangle\!\rangle_c \,, \tag{3.75}$$

$$V_{\mathbf{L}^2}^{(1,1)}(r) = \frac{i}{2}\left(\delta^{ij} - 3\hat{\mathbf{r}}^i\hat{\mathbf{r}}^j\right) \int_0^\infty dt\, t^2 \langle\!\langle g\mathbf{E}_1^i(t) g\mathbf{E}_2^j(0)\rangle\!\rangle_c \,, \tag{3.76}$$

$$V_{L_2S_1}^{(1,1)}(r) = -\frac{c_F^{(1)}}{r^2} i\mathbf{r}\cdot \int_0^\infty dt\, t\, \langle\!\langle g\mathbf{B}_1(t) \times g\mathbf{E}_2(0)\rangle\!\rangle \,, \tag{3.77}$$

$$V_{S^2}^{(1,1)}(r) = \frac{2c_F^{(1)}c_F^{(2)}}{3} i \int_0^\infty dt\, \langle\!\langle g\mathbf{B}_1(t)\cdot g\mathbf{B}_2(0)\rangle\!\rangle - 4(d_{sv} + d_{vv}C_F)\,\delta^{(3)}(\mathbf{r}) \,, \tag{3.78}$$

$$V_{\mathbf{S}_{12}}^{(1,1)}(r) = \frac{c_F^{(1)}c_F^{(2)}}{4} i\hat{\mathbf{r}}^i\hat{\mathbf{r}}^j \int_0^\infty dt\, \left[\langle\!\langle g\mathbf{B}_1^i(t) g\mathbf{B}_2^j(0)\rangle\!\rangle - \frac{\delta^{ij}}{3}\langle\!\langle g\mathbf{B}_1(t)\cdot g\mathbf{B}_2(0)\rangle\!\rangle\right] \tag{3.79}$$

$$\begin{aligned}
&V_r^{(2,0)}(r) = \frac{\pi C_F \alpha_s c_D^{(1)\prime}}{2}\delta^{(3)}(\mathbf{x}_1 - \mathbf{x}_2) \\
&-\frac{ic_F^{(1)\,2}}{4}\int_0^\infty dt \langle\!\langle g\mathbf{B}_1(t)\cdot g\mathbf{B}_1(0)\rangle\!\rangle_c + \frac{1}{2}(\boldsymbol{\nabla}_r^2 V_{\mathbf{p}^2}^{(2,0)}) \\
&-\frac{i}{2}\int_0^\infty dt_1 \int_0^{t_1} dt_2 \int_0^{t_2} dt_3\, (t_2 - t_3)^2 \langle\!\langle g\mathbf{E}_1(t_1)\cdot g\mathbf{E}_1(t_2) g\mathbf{E}_1(t_3)\cdot g\mathbf{E}_1(0)\rangle\!\rangle_c \\
&+\frac{1}{2}\left(\boldsymbol{\nabla}_r^i \int_0^\infty dt_1 \int_0^{t_1} dt_2\, (t_1 - t_2)^2 \langle\!\langle g\mathbf{E}_1^i(t_1) g\mathbf{E}_1(t_2)\cdot g\mathbf{E}_1(0)\rangle\!\rangle_c\right) \\
&-\frac{i}{2}\left(\boldsymbol{\nabla}_r^i V^{(0)}\right)\int_0^\infty dt_1 \int_0^{t_1} dt_2\, (t_1 - t_2)^3 \langle\!\langle g\mathbf{E}_1^i(t_1) g\mathbf{E}_1(t_2)\cdot g\mathbf{E}_1(0)\rangle\!\rangle_c \\
&+\frac{1}{4}\left(\boldsymbol{\nabla}_r^i \int_0^\infty dt\, t^3 \langle\!\langle g\mathbf{E}_1^i(t) g\mathbf{E}_1^j(0)\rangle\!\rangle_c (\boldsymbol{\nabla}_r^j V^{(0)})\right) \\
&-\frac{i}{12}\int_0^\infty dt\, t^4 \langle\!\langle g\mathbf{E}_1^i(t) g\mathbf{E}_1^j(0)\rangle\!\rangle_c (\boldsymbol{\nabla}_r^i V^{(0)})(\boldsymbol{\nabla}_r^j V^{(0)}) \\
&-d_3^{(1)\prime} f_{abc}\int d^3\mathbf{x} \lim_{T\to\infty} g\langle\!\langle G_{\mu\nu}^a(x) G_{\mu\alpha}^b(x) G_{\nu\alpha}^c(x)\rangle\!\rangle \,,
\end{aligned} \tag{3.80}$$

$$
\begin{aligned}
V_r^{(1,1)}(r) &= -\frac{1}{2}(\boldsymbol{\nabla}_r^2 V_{\mathbf{p}^2}^{(1,1)}) \qquad (3.81)\\
&-i\int_0^\infty dt_1\int_0^{t_1} dt_2\int_0^{t_2} dt_3\,(t_2-t_3)^2\langle\!\langle g\mathbf{E}_1(t_1)\cdot g\mathbf{E}_1(t_2) g\mathbf{E}_2(t_3)\cdot g\mathbf{E}_2(0)\rangle\!\rangle_c\\
&+\frac{1}{2}\left(\boldsymbol{\nabla}_r^i\int_0^\infty dt_1\int_0^{t_1} dt_2(t_1-t_2)^2\langle\!\langle g\mathbf{E}_1^i(t_1) g\mathbf{E}_2(t_2)\cdot g\mathbf{E}_2(0)\rangle\!\rangle_c\right)\\
&+\frac{1}{2}\left(\boldsymbol{\nabla}_r^i\int_0^\infty dt_1\int_0^{t_1} dt_2(t_1-t_2)^2\langle\!\langle g\mathbf{E}_2^i(t_1) g\mathbf{E}_1(t_2)\cdot g\mathbf{E}_1(0)\rangle\!\rangle_c\right)\\
&-\frac{i}{2}\left(\boldsymbol{\nabla}_r^i V^{(0)}\right)\int_0^\infty dt_1\int_0^{t_1} dt_2(t_1-t_2)^3\langle\!\langle g\mathbf{E}_1^i(t_1) g\mathbf{E}_2(t_2)\cdot g\mathbf{E}_2(0)\rangle\!\rangle_c\\
&-\frac{i}{2}\left(\boldsymbol{\nabla}_r^i V^{(0)}\right)\int_0^\infty dt_1\int_0^{t_1} dt_2(t_1-t_2)^3\langle\!\langle g\mathbf{E}_2^i(t_1) g\mathbf{E}_1(t_2)\cdot g\mathbf{E}_1(0)\rangle\!\rangle_c\\
&+\frac{1}{4}\left(\boldsymbol{\nabla}_r^i\int_0^\infty dt\,t^3\left\{\langle\!\langle g\mathbf{E}_1^i(t) g\mathbf{E}_2^j(0)\rangle\!\rangle_c+\langle\!\langle g\mathbf{E}_2^i(t) g\mathbf{E}_1^j(0)\rangle\!\rangle_c\right\}(\boldsymbol{\nabla}_r^j V^{(0)})\right)\\
&-\frac{i}{6}\int_0^\infty dt\,t^4\langle\!\langle g\mathbf{E}_1^i(t) g\mathbf{E}_2^j(0)\rangle\!\rangle_c(\boldsymbol{\nabla}_r^i V^{(0)})(\boldsymbol{\nabla}_r^j V^{(0)})+(d_{ss}+d_{vs}C_F)\,\delta^{(3)}(\mathbf{x}_1-\mathbf{x}_2).
\end{aligned}
$$

In the above expressions where the average over the Wilson loop is not connected, it means that it is the same as connected. The coefficients $c_F^{(i)}=1+\mathcal{O}(\alpha_{\rm s})$, $c_S^{(i)}=2c_F^{(i)}-1$, $c_D^{(i)\prime}=1+\mathcal{O}(\alpha_{\rm s})$, $d_3^{(1)\prime}=\alpha_{\rm s}/(720\pi)+\mathcal{O}(\alpha_{\rm s}^2)$ [37], and d_{sv}, d_{vv}, d_{ss}, d_{vs}, which are such that $(d_{sv}+d_{vv}C_F)=\mathcal{O}(\alpha_{\rm s}^2)$ and $(d_{ss}+d_{vs}C_F)=\mathcal{O}(\alpha_{\rm s}^2)$ [42], are Wilson coefficients of NRQCD. The natural scale of $\alpha_{\rm s}$ in these coefficients is of the order of the heavy-quark mass, hence we may expect $\alpha_{\rm s}$ to be a fairly small number.

3.4 Final remarks

As in the case of the $1/m$ correction, the expressions for the $1/m^2$-suppressed potentials obtained from pNRQCD are valid in the whole distance regime. The short-distance limit can be computed using perturbation theory whereas the long-distance limit must be studied with non-perturbative methods. In particular, the fact that the potentials are expressed in terms of correlators of the rectangular Wilson loop makes them suitable for an evaluation on the lattice, however, such an evaluation is missing for most of them. In the next chapter we will adopt the Effective String Theory hypothesis to compute the Wilson loop correlators in the large r limit. These results will be used later to construct the full-range potential (Chapter 5), which we will use in the evaluation of the E1 decay rates.

Chapter 4

The quark-antiquark potential in the Effective String Theory

Here we derive the Effective String Theory (EST) expressions of the QCD correlators presented in Chapter 3. We use a mapping that relates the QCD operator insertions into the rectangular Wilson loop with the EST degrees of freedom. This mapping has been proposed in [56] and [57] assuming that the $Q\bar{Q}$ system has the same symmetry properties in both theories. Using the EST expressions for the correlators we construct the *string potential*. Using this potential, in the last part of the chapter we compute the *string spectrum* at $O(1/m^2)$. The findings of this chapter have also been published in [58].

4.1 The Effective String Theory

In the previous chapter we obtained the following expression for the static potential in terms of the rectangular Wilson loop

$$V^{(0)}(r) = \lim_{T\to\infty} \frac{i}{T} \ln\langle W_\Box \rangle \,, \tag{4.1}$$

where

$$W_\Box \equiv \mathrm{P} \exp\left\{ -ig \oint_{r\times T} dz^\mu \, A_\mu(z) \right\} . \tag{4.2}$$

In the strong coupling limit, which is the expected coupling regime for large quark-antiquark separation, this relation leads to a potential with a linear dependence on r

$$V^{(0)}(r \to \infty) \propto r.$$

Another example of a system with a constant force along the interaction line, as the one described by Eq. (4.1), is a string with fixed ends. Moreover, it has been proposed[1] that the gluonic interaction between a quark and an antiquark at long distances form a

[1] See Ref. [59] for new developments based on this hypothesis.

flux tube (Fig. 4.1). Considering the picture of this flux tube we can get a qualitative motivation for the string hypothesis: if the separation between the quarks is large enough compared to the width of the tube, it may be expected that the $Q\bar{Q}$ interaction behaves like a string with fixed ends. This observation was quantified already in [20], where it was shown that the Wilson line $U = \mathrm{P}\exp\left\{-ig\int_\Sigma dz^\mu\, A_\mu(z)\right\}$ fulfills the equation of a quantized string. In our evaluation of the long-range $Q\bar{Q}$ potential we will adopt the EST hypothesis, which states that in pure gluodynamics and in the long-distance regime, $r\Lambda_{\mathrm{QCD}} \gg 1$, the expectation value of the rectangular Wilson loop can be expressed in terms of a string action:

$$\lim_{T\to\infty}\langle W_\square\rangle = Z\int \mathcal{D}\xi^1\mathcal{D}\xi^2\, e^{iS_{\mathrm{string}}(\xi^1,\xi^2)}\,, \tag{4.3}$$

where Z is a constant. For $r\Lambda_{\mathrm{QCD}} \gg 1$ the string action, S_{string}, can be expanded in a series whose terms involve an increasing number of derivatives acting on the transverse string coordinates $\xi^l = \xi^l(t,z)$ $(l = 1,2)$ [60]. The coordinates ξ^l count like $1/\Lambda_{\mathrm{QCD}}$, whereas derivatives in t and z acting on them count like $1/r$. Hence, terms in S_{string} are suppressed in the long range by powers of $1/(r\Lambda_{\mathrm{QCD}})$. Up to terms with only two derivatives, the string action reads

$$S_{\mathrm{string}} = -\kappa\int dt\, dz\, \left(1 - \frac{1}{2}\partial_\mu\xi^l\partial^\mu\xi^l\right). \tag{4.4}$$

This effective action corresponds to the leading order of the long wavelength limit of the Nambu-Goto action, which in turn corresponds to the surface spanned by a string propagating in spacetime [61]. Studies constraining the form of the higher-order terms, also by Lorentz invariance, are found in [62–66]. The next terms in the expansion turn out to involve at least four derivatives, so they are suppressed by $1/(r\Lambda_{\mathrm{QCD}})^2$ with respect to the kinetic term in (4.4). Such terms and subleading ones do not affect the results presented here and will be neglected in the rest of this chapter. Since the string has fixed ends at $z = -r/2$ and $z = r/2$, the transverse coordinates ξ^l satisfy the boundary conditions $\xi^l(t,-r/2) = \xi^l(t,r/2) = 0$. The constant κ, which is of order Λ^2_{QCD}, is the string tension; its numerical value is known from lattice QCD determinations [67][2]

$$\kappa_{\mathrm{lattice}} \approx 0.21\,[\mathrm{GeV}^2]. \tag{4.5}$$

From (4.1), (4.3) and (4.4) it follows that [60, 69]

$$V^{(0)}(r) = \kappa r + \mu - \frac{\pi}{12r} \approx \kappa r\,, \tag{4.6}$$

where μ is an unknown regularization-dependent constant and the term $-\pi/(12r)$ is a universal quantum correction known as the Lüscher term.[3] The last approximation holds in the large distance limit when the Lüscher term may be neglected.

[2]This value corresponds to a *quenched* lattice determination in which loop of fermions are neglected. Unquenched studies of the QCD flux tube can be found, for instance, in [68].

[3] The Lüscher term does depend on the dimension of spacetime. In d dimensions it reads $-\pi(d-2)/(24\,r)$. Equation (4.6) holds for $d = 4$.

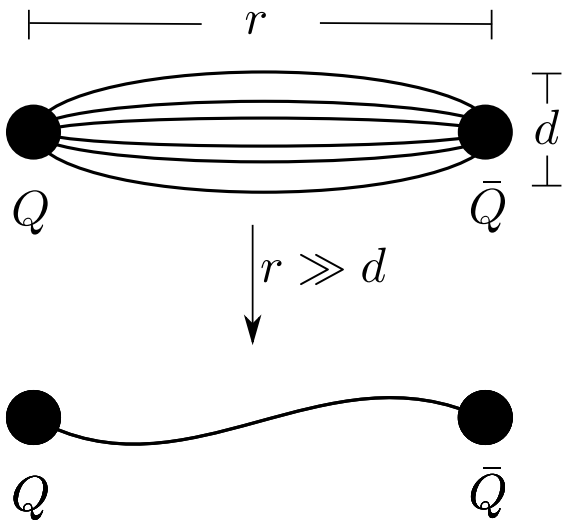

Figure 4.1: The flux tube hypothesis provides us with a graphic motivation to introduce the EST: if the separation between the quark and the antiquark, r, is much larger than the width of the flux tube, d, the gluonic exchange among the quarks in the long distance limit may behave as a string with fixed ends.

The mapping between QCD and EST correlators that we will present in the next section was constructed assuming the same symmetry transformations of the correlators in both theories. Explicitly for the string coordinates $\xi^i(t,z)$ (with $\xi^3 = z$) the symmetry transformations are [57]

- rotations with respect to the z axis:

$$\xi^i(t,z) \to R^{ij}\xi^j(t,z), \tag{4.7}$$

- reflection with respect to the zx plane:

$$\xi^i(t,z) \to \rho^{ij}\xi^j(t,z), \tag{4.8}$$

- charge conjugation and parity (CP):

$$\xi^i(t,z) \to -\xi^i(t,-z), \tag{4.9}$$

- time-reversal (T):

$$\xi^i(t,z) \to \xi^i(-t,z) \tag{4.10}$$

where R^{ij} is the rotation matrix and $\rho^{ij} = \mathrm{diag}(1,-1,1)$.
Later we will need the explicit expression of the correlator of two string coordinates. Considering (4.4) and the string boundary conditions, the two-field correlator of the EST in euclidean time is given by [57]

$$\langle \xi^l(it,z)\xi^m(it',z')\rangle = \frac{\delta^{lm}}{4\pi\kappa}\ \ln\left(\frac{\cosh[(t-t')\,\pi/r] + \cos[(z+z')\,\pi/r]}{\cosh[(t-t')\,\pi/r] - \cos[(z-z')\,\pi/r]}\right). \tag{4.11}$$

A derivation of this expression is available in Appendix B.

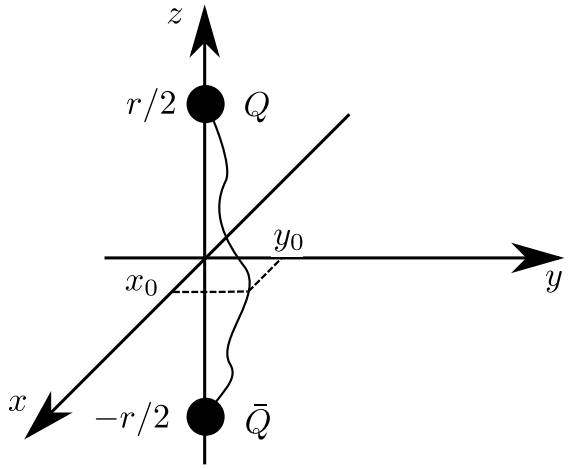

Figure 4.2: Reference frame set-up for the string in the EST. The vibration of the string implies a variation of its transverse coordinates, here x and y, which correspond to the degrees of freedom of the theory. In the figure we show the value of the coordinates $\xi^1(t_0, z = 0) = x_0$ and $\xi^2(t_0, z = 0) = y_0$ for a given time t_0.

4.2 The long-range potential in the EST

4.2.1 Mapping

In [56] it was proposed that the equivalence (4.3) could be extended to relate Wilson loops with field strength tensor insertions, like the ones appearing in the relativistic corrections, to correlators of the string fields ξ^l. This would allow one to compute in the EST the potentials listed in Chapter 3 in the long-distance regime.
Requiring the same symmetry properties for the transverse string coordinates and the operators inserted in the Wilson loop, a program to expand the mapping of Eq. (4.3) was first started in [56] and then extended in [57]; we follow the method specified in the latter to show the construction of the mapping. The transformations with respect to the generators of the symmetry group of the string transverse coordinates were listed in Eqs. (4.7)-(4.10); for the field insertions in the Wilson loop the same transformations read

- rotations with respect to the z axis:

$$\begin{aligned} \mathbf{E}^i(t, \mathbf{z}) &\rightarrow R^{ij}\mathbf{E}^j(t, \mathbf{z}), \\ \mathbf{B}^i(t, \mathbf{z}) &\rightarrow R^{ij}\mathbf{B}^j(t, \mathbf{z}), \end{aligned} \tag{4.12}$$

- reflection with respect to the zx plane:

$$\begin{aligned}\mathbf{E}^i(t,\mathbf{z}) &\to \rho^{ij}\mathbf{E}^j(t,\mathbf{z}),\\ \mathbf{B}^i(t,\mathbf{z}) &\to -\rho^{ij}\mathbf{B}^j(t,\mathbf{z}),\end{aligned} \tag{4.13}$$

- charge conjugation and parity (CP):

$$\begin{aligned}\mathbf{E}^i(t,\mathbf{z}) &\to (\mathbf{E}^i)^T(t,-\mathbf{z}),\\ \mathbf{B}^i(t,\mathbf{z}) &\to -(\mathbf{B}^i)^T(t,-\mathbf{z}),\end{aligned} \tag{4.14}$$

- time-reversal (T):

$$\begin{aligned}\mathbf{E}^i(t,\mathbf{z}) &\to \mathbf{E}^i(-t,\mathbf{z}),\\ \mathbf{B}^i(t,\mathbf{z}) &\to -\mathbf{B}^i(-t,\mathbf{z}),\end{aligned} \tag{4.15}$$

The superscript T stands for transpose, $\mathbf{z} = (0,0,z)$ and as before R^{ij} is the rotation matrix and $\rho^{ij} = \mathrm{diag}(1,-1,1)$.
In [56, 57] a mapping that satisfies the transformation properties (4.7)-(4.10) and (4.12)-(4.15) was found to be

$$\begin{aligned}\langle\!\langle \dots \mathbf{E}_1^l(t) \dots \rangle\!\rangle &= \langle \dots \Lambda^2 \partial_z \xi^l(t, r/2) \dots \rangle\,,\\ \langle\!\langle \dots \mathbf{E}_2^l(t) \dots \rangle\!\rangle &= \langle \dots \Lambda^2 \partial_z \xi^l(t, -r/2) \dots \rangle\,,\\ \langle\!\langle \dots \mathbf{B}_1^l(t) \dots \rangle\!\rangle &= \langle \dots \Lambda' \epsilon^{lm} \partial_t \partial_z \xi^m(t, r/2) \dots \rangle\,,\\ \langle\!\langle \dots \mathbf{B}_2^l(t) \dots \rangle\!\rangle &= \langle \dots - \Lambda' \epsilon^{lm} \partial_t \partial_z \xi^m(t, -r/2) \dots \rangle\,,\\ \langle\!\langle \dots \mathbf{E}_1^3(t) \dots \rangle\!\rangle &= \langle \dots \Lambda''^2 \dots \rangle\,,\\ \langle\!\langle \dots \mathbf{E}_2^3(t) \dots \rangle\!\rangle &= \langle \dots \Lambda''^2 \dots \rangle\,,\\ \langle\!\langle \dots \mathbf{B}_1^3(t) \dots \rangle\!\rangle &= \langle \dots \Lambda''' \epsilon^{lm} \partial_t \partial_z \xi^l(t, r/2) \partial_z \xi^m(t, r/2) \dots \rangle\,,\\ \langle\!\langle \dots \mathbf{B}_2^3(t) \dots \rangle\!\rangle &= \langle \dots - \Lambda''' \epsilon^{lm} \partial_t \partial_z \xi^l(t, -r/2) \partial_z \xi^m(t, -r/2) \dots \rangle\,,\end{aligned} \tag{4.16}$$

where the indices l and m label the transverse coordinates: $l, m = 1, 2$. The tensor ϵ^{lm} is such that $\epsilon^{12} = 1$ and $\epsilon^{lm} = -\epsilon^{ml}$. In the Wilson-loop part of the mapping the heavy quark is located at $\mathbf{x}_1 = (0,0,r/2)$ and the heavy antiquark at $\mathbf{x}_2 = (0,0,-r/2)$, which implies $\mathbf{r} = (0,0,r)$, see Fig. 4.2. The constants Λ, Λ', Λ'' and Λ''' are unknown constants of mass dimension one and of order Λ_{QCD}.
The mapping (4.16) is valid up to corrections that are subleading in the long range in the EST counting. For the calculation of the long-range potential in the EST we will assume the mapping (4.16) to be exact. The impact of subleading corrections will be discussed in section 4.2.5.
The right-hand side of (4.16) consists of correlators of string coordinates ξ^l. The functional integral over the string coordinates is Gaussian (see the string action (4.4)). So we have that correlators of more than two string fields ξ^l break up into products of two-field correlators and derivatives of them, and that two-field correlators are given by Eq. (4.11).

4.2.2 String representation of the QCD correlators

Provided with the mapping (4.16) we can evaluate in the long-range the Wilson loop expectation values that were given in Chapter 3. Correlators involving more than two string fields, which come from mapping Wilson loops with $\mathbf{B}^3$ fields or more than two chromoelectric field insertions, decompose into the product of two string field correlators due to the Gaussian string action. Gaussianity also implies that correlators with an odd number of string fields vanish. The Wilson loop expectation values appearing in the $1/m$ suppressed corrections for $r\Lambda_{\rm QCD} \gg 1$ map into the following expressions:

$$\langle\!\langle \mathbf{E}_1^i(it)\mathbf{E}_1^j(0)\rangle\!\rangle_c = \tilde{\delta}^{ij}\frac{\pi\Lambda^4}{4\kappa r^2}\sinh^{-2}\left(\frac{\pi t}{2r}\right), \tag{4.17}$$

$$\langle\!\langle \mathbf{E}_1^i(it)\mathbf{E}_2^j(0)\rangle\!\rangle_c = -\tilde{\delta}^{ij}\frac{\pi\Lambda^4}{4\kappa r^2}\cosh^{-2}\left(\frac{\pi t}{2r}\right), \tag{4.18}$$

$$\mathbf{r}\cdot\langle\!\langle \mathbf{B}_1(it)\times\mathbf{E}_1(0)\rangle\!\rangle = \frac{i\pi^2\Lambda^2\Lambda'}{2\kappa r^2}\cosh\left(\frac{\pi t}{2r}\right)\sinh^{-3}\left(\frac{\pi t}{2r}\right), \tag{4.19}$$

$$\mathbf{r}\cdot\langle\!\langle \mathbf{B}_1(it)\times\mathbf{E}_2(0)\rangle\!\rangle = -\frac{i\pi^2\Lambda^2\Lambda'}{2\kappa r^2}\sinh\left(\frac{\pi t}{2r}\right)\cosh^{-3}\left(\frac{\pi t}{2r}\right), \tag{4.20}$$

$$\sum_{l=1}^{2}\langle\!\langle \mathbf{B}_1^l(it)\mathbf{B}_1^l(0)\rangle\!\rangle_c = \frac{\pi^3\Lambda'^2}{4\kappa r^4}\sinh^{-4}\left(\frac{\pi t}{2r}\right)\left[2+\cosh\left(\frac{\pi t}{r}\right)\right], \tag{4.21}$$

$$\sum_{l=1}^{2}\langle\!\langle \mathbf{B}_1^l(it)\mathbf{B}_2^l(0)\rangle\!\rangle_c = -\frac{\pi^3\Lambda'^2}{4\kappa r^4}\cosh^{-4}\left(\frac{\pi t}{2r}\right)\left[2-\cosh\left(\frac{\pi t}{r}\right)\right], \tag{4.22}$$

$$\langle\!\langle \mathbf{B}_1^3(it)\mathbf{B}_1^3(0)\rangle\!\rangle_c = \frac{\pi^4\Lambda'''^2}{16\kappa^2 r^6}\sinh^{-6}\left(\frac{\pi t}{2r}\right), \tag{4.23}$$

$$\langle\!\langle \mathbf{B}_1^3(it)\mathbf{B}_2^3(0)\rangle\!\rangle_c = \frac{\pi^4\Lambda'''^2}{16\kappa^2 r^6}\cosh^{-6}\left(\frac{\pi t}{2r}\right), \tag{4.24}$$

$$\begin{aligned}\langle\!\langle \mathbf{E}_1(it_1)\cdot\mathbf{E}_1(it_2)\mathbf{E}_1(it_3)\cdot\mathbf{E}_1(0)\rangle\!\rangle_c = \frac{\pi^2\Lambda^8}{8\kappa^2 r^4}\Bigg[&\sinh^{-2}\left(\frac{\pi t_2}{2r}\right)\sinh^{-2}\left(\frac{\pi(t_1-t_3)}{2r}\right)\\ &+\sinh^{-2}\left(\frac{\pi t_1}{2r}\right)\sinh^{-2}\left(\frac{\pi(t_2-t_3)}{2r}\right)\Bigg],\end{aligned} \tag{4.25}$$

$$\begin{aligned}\langle\!\langle \mathbf{E}_1(it_1)\cdot\mathbf{E}_1(it_2)\mathbf{E}_2(it_3)\cdot\mathbf{E}_2(0)\rangle\!\rangle_c = \frac{\pi^2\Lambda^8}{8\kappa^2 r^4}\Bigg[&\cosh^{-2}\left(\frac{\pi t_2}{2r}\right)\cosh^{-2}\left(\frac{\pi(t_1-t_3)}{2r}\right)\\ &+\cosh^{-2}\left(\frac{\pi t_1}{2r}\right)\cosh^{-2}\left(\frac{\pi(t_2-t_3)}{2r}\right)\Bigg],\end{aligned} \tag{4.26}$$

where $\tilde{\delta}^{ij}=0$ for i or $j=3$ and $\tilde{\delta}^{ij}=\delta^{ij}$ for $i,j=1,2$. Terms of the type $\langle\!\langle \mathbf{E}^i(t_1)\mathbf{E}(t_2)\cdot\mathbf{E}(0)\rangle\!\rangle_c$ vanish after (4.16) regardless of the quark line where the chromoelectric fields

are located. This is due to Gaussianity and to the subtraction of the disconnected parts. It is also a specific feature of $\langle\!\langle \mathbf{E}^i(t_1)\mathbf{E}(t_2)\cdot\mathbf{E}(0)\rangle\!\rangle_c$, which is the only type of three-field correlator appearing in the heavy quark-antiquark potential up to order $1/m^2$. For example, a term like $\langle\!\langle \mathbf{E}^j(t_1)\mathbf{E}^3(t_2)\mathbf{E}^j(0)\rangle\!\rangle_c$ would not vanish after (4.16). Finally terms involving four chromoelectric fields contribute in the EST through two two-field correlators that are connected.

4.2.3 The relativistic corrections to the $Q\bar{Q}$ potential in the EST

Once we are provided with the mapping of the correlators into the EST the calculation of the long-range relativistic corrections to the $Q\bar{Q}$ potential follows straightforwardly. Substituting (4.17)-(4.26) in the expressions of the potentials, we obtain

$$V^{(1,0)}(r) = \frac{g^2\Lambda^4}{2\pi\kappa}\ln\left(\kappa r^2\right)+\mu_1\,, \tag{4.27}$$

$$V^{(2,0)}_{\mathbf{p}^2}(r) = 0\,, \tag{4.28}$$

$$V^{(2,0)}_{\mathbf{L}^2}(r) = -\frac{g^2\Lambda^4\, r}{6\kappa}\,, \tag{4.29}$$

$$V^{(2,0)}_{LS}(r) = -\frac{\mu_2}{r}-\frac{c_F^{(1)}g^2\Lambda^2\Lambda'}{\kappa\, r^2}\,, \tag{4.30}$$

$$V^{(1,1)}_{\mathbf{p}^2}(r) = 0\,, \tag{4.31}$$

$$V^{(1,1)}_{\mathbf{L}^2}(r) = \frac{g^2\Lambda^4\, r}{6\kappa}\,, \tag{4.32}$$

$$V^{(1,1)}_{L_2\,S_1}(r) = -\frac{c_F^{(1)}g^2\Lambda^2\Lambda'}{\kappa\, r^2}\,, \tag{4.33}$$

$$V^{(1,1)}_{S^2}(r) = \frac{2\pi^3 c_F^{(1)}c_F^{(2)}g^2\Lambda'''^2}{45\kappa^2\, r^5}-4(d_{sv}+d_{vv}C_F)\delta^{(3)}(\mathbf{r})\,, \tag{4.34}$$

$$V^{(1,1)}_{\mathbf{S}_{12}}(r) = \frac{\pi^3 c_F^{(1)}c_F^{(2)}g^2\Lambda'''^2}{90\kappa^2\, r^5}\,, \tag{4.35}$$

$$\begin{aligned} V_r^{(2,0)}(r) &= -\frac{2\,\zeta_3\, g^4\Lambda^8 r}{\pi^3\kappa^2}+\mu_3+\frac{\mu_4}{r^2}+\frac{\mu_5}{r^4}+\frac{\pi^3 c_F^{(1)\,2}g^2\Lambda'''^2}{60\kappa^2 r^5} \\ &\quad +\frac{\pi C_F\alpha_{\rm s}c_D^{(1)\prime}}{2}\delta^{(3)}(\mathbf{r})-d_3^{(1)\prime}f_{abc}\int d^3\mathbf{x}\lim_{T\to\infty} g\langle\!\langle G^a_{\mu\nu}(x)G^b_{\mu\alpha}(x)G^c_{\nu\alpha}(x)\rangle\!\rangle\,, \end{aligned} \tag{4.36}$$

$$V_r^{(1,1)}(r) = -\frac{\zeta_3\, g^4\Lambda^8 r}{2\pi^3\kappa^2}+(d_{ss}+d_{vs}C_F)\,\delta^{(3)}(\mathbf{r})\,, \tag{4.37}$$

where $\zeta_3 = 1.2020569...$ is the Riemann zeta function of argument three and μ_i are renormalization constants that appear after introducing a UV cutoff for small times in the integrals of the correlators. The expressions for the potentials (4.27)-(4.33) agree

with those in [57]. The spin-spin potentials (4.34) and (4.35) are of order $1/r^5$. The $1/r^5$ behaviour comes from the subleading correlator (4.24), for the long-range leading contribution coming from the correlator (4.22), which would be of order $1/r^3$, vanishes in the integrals of (3.78) and (3.79) (the result is independent of the specific form of the string action). This contrasts with the result of [56], where the correlator (4.24) is not taken into account and the leading spin-spin potentials shows up only at order $1/m^4$. The explicit expressions of the potentials in Eqs. (4.34), (4.35), (4.36) and (4.37) are new (first reported in [58]). We observe that correlators of two chromoelectric fields contracted with $\mathbf{r} = (0, 0, r)$ vanish because of $\mathbf{r}^i \tilde{\delta}^{ij} = 0$, and that we do not have a mapping prescription into the EST for the matrix element $\langle\langle G^a_{\mu\nu}(x) G^b_{\mu\alpha}(x) G^c_{\nu\alpha}(x) \rangle\rangle$ involving three gluon fields located at an arbitrary point x of spacetime.

4.2.4 Constraints from Poincaré invariance

As pointed out in [57], Poincaré invariance fixes some of the renormalization constants μ_i and field normalization constants, Λ, Λ', ..., because it requires some equations to be exactly fulfilled by the potentials (see [35, 36]). One of these equations is the Gromes relation that relates the spin-orbit potentials with the static potential [70]:

$$\frac{1}{2r}\frac{dV^{(0)}}{dr} + V^{(2,0)}_{LS} - V^{(1,1)}_{L_2 S_1} = 0\,. \tag{4.38}$$

This equation is fulfilled in the EST only if

$$\mu_2 = \frac{\kappa}{2}\,. \tag{4.39}$$

Another equation relates the momentum-dependent potentials with the static potential [71]:

$$\frac{r}{2}\frac{dV^{(0)}}{dr} + 2V^{(2,0)}_{\mathbf{L}^2} - V^{(1,1)}_{\mathbf{L}^2} = 0\,. \tag{4.40}$$

This equation is fulfilled in the EST only if

$$g\Lambda^2 = \kappa\,. \tag{4.41}$$

In [35, 71] also the exact relation

$$-4V^{(2,0)}_{\mathbf{p}^2} + 2V^{(1,1)}_{\mathbf{p}^2} - V^{(0)} + r\frac{dV^{(0)}}{dr} = 0\,,$$

was derived. This relation is automatically fulfilled by the potentials (4.6), (4.28) and (4.31) in the long range, i.e., neglecting μ and the Lüscher term in $V^{(0)}$, and does not provide further constraints.
A similar relation holds for Λ'' and follows from the equation $-\boldsymbol{\nabla}_1 V^{(0)} = \langle\langle g\mathbf{E}_1 \rangle\rangle$ valid for $T \to \infty$ derived in [18]. The equation is fulfilled in the EST only if

$$g\Lambda''^2 = -\kappa\,. \tag{4.42}$$

Equations (4.41) and (4.42) are remarkable, for they completely determine the long-range mapping of the chromoelectric field in the EST. Finally, we note that the equations induced by Poincaré invariance would require the inclusion of subleading corrections to the action (4.4) and the mapping (4.16) in order to be fulfilled beyond leading order in the long-range limit.

Taking the potentials (4.27)-(4.37) at leading order in the long-range limit, using the constraints (4.39) and (4.41), and dropping terms suppressed by powers of $\alpha_{\rm s}$, like the term proportional to $\langle\!\langle G^a_{\mu\nu}(x) G^b_{\mu\alpha}(x) G^c_{\nu\alpha}(x) \rangle\!\rangle$, we obtain

$$V^{(1,0)}(r) = \frac{\kappa}{2\pi} \ln\left(\kappa r^2\right) + \mu_1 \,, \tag{4.43}$$

$$V^{(2,0)}_{\mathbf{p}^2}(r) = 0 \,, \tag{4.44}$$

$$V^{(2,0)}_{\mathbf{L}^2}(r) = -\frac{\kappa\, r}{6} \,, \tag{4.45}$$

$$V^{(2,0)}_{LS}(r) = -\frac{\kappa}{2\, r} - \frac{c_F^{(1)} g \Lambda'}{r^2} \,, \tag{4.46}$$

$$V^{(1,1)}_{\mathbf{p}^2}(r) = 0 \,, \tag{4.47}$$

$$V^{(1,1)}_{\mathbf{L}^2}(r) = \frac{\kappa\, r}{6} \,, \tag{4.48}$$

$$V^{(1,1)}_{L_2\, S_1}(r) = -\frac{c_F^{(1)} g \Lambda'}{r^2} \,, \tag{4.49}$$

$$V^{(1,1)}_{S^2}(r) = \frac{2\pi^3 c_F^{(1)} c_F^{(2)} g^2 \Lambda'''^2}{45 \kappa^2\, r^5} \,, \tag{4.50}$$

$$V^{(1,1)}_{\mathbf{S}_{12}}(r) = \frac{\pi^3 c_F^{(1)} c_F^{(2)} g^2 \Lambda'''^2}{90 \kappa^2\, r^5} \,, \tag{4.51}$$

$$V^{(2,0)}_{r}(r) = -\frac{2\, \zeta_3\, \kappa^2 r}{\pi^3} \,, \tag{4.52}$$

$$V^{(1,1)}_{r}(r) = -\frac{\zeta_3\, \kappa^2 r}{2\pi^3} \,. \tag{4.53}$$

We have kept the subleading term proportional to $1/r^2$ in (4.46), because (4.6) and (4.49) together with (4.38) guarantee that there cannot be any other term proportional to $1/r^2$ contributing to $V^{(2,0)}_{LS}$.

4.2.5 On the subleading contributions to the mapping

Equations (4.43)-(4.53) provide the EST expressions for the heavy quark-antiquark potential in the long range following from the exact mapping (4.16). Subleading corrections to the mapping will not change the functional dependence of the potential but may affect some of the numerical coefficients. For instance, in the case of the $V^{(2,0)}_r(r)$ and $V^{(1,1)}_r(r)$ potentials, which at order r may be affected by subleading contributions to the mapping of $\mathbf{E}^3$ given by

$$\langle\!\langle \ldots \mathbf{E}^3(t) \ldots \rangle\!\rangle = \langle \ldots \Lambda''^2 + (\partial_z \xi)^2 \ldots \rangle \,,$$

all possible terms proportional to $\Lambda''^8 r^5$, $\Lambda''^6 r^3$ and $\Lambda''^4 \left(\Lambda^4/\kappa\right) r^3$ vanish after subtraction of the disconnected parts of the correlators, so altering the coefficient of the term proportional to r is the largest contribution of the subleading mapping. A similar situation can be checked in the case of spin-spin potentials at order $1/r^5$, which may be affected by subleading contributions proportional to two string fields in the mapping of $\mathbf{B}^l$, however, no terms larger than $1/r^5$ will contribute to the potential. In all other cases, subleading contributions to the mapping and action will lead to subleading contributions to the potentials.

4.3 Spectrum of the LO EST potential

In order to illustrate the impact on the spectrum of the new long-range potentials derived in the previous section, we consider the following model: a quark-antiquark pair both of mass m bound by the potential given in (4.43)-(4.53). In the center-of-mass frame, the Hamiltonian of the system is $H = \mathbf{p}^2/m + V$. The potential, V, reads

$$\begin{aligned} V(r) &= V^{(0)}(r) + \frac{2}{m} V^{(1,0)}(r) + \frac{1}{m^2}\Bigg\{ \left[2\frac{V^{(2,0)}_{\mathbf{L}^2}(r)}{r^2} + \frac{V^{(1,1)}_{\mathbf{L}^2}(r)}{r^2} \right] \mathbf{L}^2 \\ &\quad + \left[V^{(2,0)}_{LS}(r) + V^{(1,1)}_{L_2 S_1}(r) \right] \mathbf{L}\cdot\mathbf{S} + V^{(1,1)}_{S^2}(r) \left(\frac{\mathbf{S}^2}{2} - \frac{3}{4} \right) + V^{(1,1)}_{\mathbf{S}_{12}}(r) \mathbf{S}_{12}(\hat{\mathbf{r}}) \\ &\quad + 2V^{(2,0)}_r(r) + V^{(1,1)}_r(r) \Bigg\} \\ &\approx \kappa r + \frac{1}{m}\frac{\kappa}{\pi} \ln\left(\kappa r^2\right) + \frac{1}{m^2}\left(-\frac{\kappa}{6r}\mathbf{L}^2 - \frac{\kappa}{2r}\mathbf{L}\cdot\mathbf{S} - \frac{9\,\zeta_3\,\kappa^2 r}{2\pi^3} \right), \end{aligned} \tag{4.54}$$

where $\mathbf{L} = \mathbf{r} \times \mathbf{p}$ and $\mathbf{S}$ is the total spin of the system. In the last line we have dropped contributions to the static and spin-orbit potentials that are subleading in the long range, and the spin-spin potentials, which fall off sharply like $1/r^5$. The constants in the static and $1/m$ potentials do not contribute to the energy level splittings; hence we do not display them. The model has the advantage of depending only on two parameters: the mass m and the string tension κ. We compute the energy levels by including contributions from the potential that are first order in $1/m^2$ and up to second order in $1/m$. We call $E^{(0)}_{nl}$ the eigenvalues of the zeroth-order Hamiltonian $\mathbf{p}^2/m + \kappa r$. The eigenstates of the zeroth-order Hamiltonian, $|nljs\rangle$, may be chosen to be simultaneously eigenstates of the angular momenta and spin. They are labeled by n, l, j and s, which are the principal, orbital angular momentum, total angular momentum and spin quantum numbers. The state $|nl\rangle$ stands for $|nljs\rangle$ when acting on an operator that does not depend on spin. The energy levels read

$$E_{nljs} = E^{(0)}_{nl} + \langle nl|V^{(1/m)}|nl\rangle + \sum_{(n',l')\neq(n,l)} \frac{|\langle nl|V^{(1/m)}|n'l'\rangle|^2}{E^{(0)}_{nl} - E^{(0)}_{n'l'}} + \langle nljs|V^{(1/m^2)}|nljs\rangle\,. \tag{4.55}$$

The results for the spectrum are summarized in the Tables 4.1 and 4.2, which refer to the cases $m = 3\sqrt{\kappa}$ and $m = 10\sqrt{\kappa}$ respectively. We choose these values because if $\kappa = 0.21$ GeV^2, then $m = 3\sqrt{\kappa}$ corresponds approximately to the charm mass and $m = 10\sqrt{\kappa}$ to the bottom mass.
The tables show all levels up to $n = 3$ and all S-wave levels up to $n = 6$. S-wave levels are degenerate in spin because the last line of (4.54) does not contain a spin-spin interaction. For some states, the $1/m$ potential turns out to give a smaller contribution than the $1/m^2$ potentials. It happens when $\sqrt{\kappa}\,\langle nl|r|nl\rangle$ is close to 1, and the logarithm in the $1/m$ potential vanishes. This is the case for the $1S$ state when $m = 3\sqrt{\kappa}$: $\sqrt{\kappa}\,\langle 1S|r|1S\rangle \approx 1.08$, and for the $1P$ states when $m = 10\sqrt{\kappa}$: $\sqrt{\kappa}\,\langle 1P|r|1P\rangle \approx 1.04$. For the other states, and in particular for higher states, the contributions of the different potentials scale naturally. All $1/m^2$ corrections are of similar size. This holds also for the newly calculated corrections, which are listed in the column labeled V_r, showing the relevance of the spin and momentum-independent potentials.
In Fig. 4.3 we show graphically the effects of the relativistic corrections to the energy levels for the $1S$, 1^3P_J and 2^3P_J states in the cases $m = 3\sqrt{\kappa}$ and $m = 10\sqrt{\kappa}$. In Fig. 4.4 we summarize in one plot the effect of these corrections on the whole spectrum for the case $m = 3\sqrt{\kappa}$.

Levels	$E^{(0)}$	$V^{(1/m)}$	$V^{(1/m)}_{\text{2nd order}}$	$V_{\mathbf{L}^2}$	V_{LS}	V_r	E
$1S$	1.621	-0.007	-0.007	0	0	-0.021	1.586
1^1P_1	2.331	0.080	-0.005	-0.027	0	-0.030	2.349
1^3P_0	2.331	0.080	-0.005	-0.027	0.082	-0.030	2.431
1^3P_1	2.331	0.080	-0.005	-0.027	0.041	-0.030	2.390
1^3P_2	2.331	0.080	-0.005	-0.027	-0.041	-0.030	2.308
$2S$	2.834	0.100	-0.004	0	0	-0.037	2.893
1^1D_2	2.946	0.134	-0.004	-0.062	0	-0.038	2.976
1^3D_1	2.946	0.134	-0.004	-0.062	0.093	-0.038	3.069
1^3D_2	2.946	0.134	-0.004	-0.062	0.031	-0.038	3.007
1^3D_3	2.946	0.134	-0.004	-0.062	-0.062	-0.038	2.914
2^1P_1	3.387	0.147	-0.003	-0.022	0	-0.044	3.465
2^3P_0	3.387	0.147	-0.003	-0.022	0.066	-0.044	3.531
2^3P_1	3.387	0.147	-0.003	-0.022	0.033	-0.044	3.498
2^3P_2	3.387	0.147	-0.003	-0.022	-0.033	-0.044	3.432
$3S$	3.828	0.161	-0.003	0	0	-0.049	3.937
$4S$	4.706	0.203	-0.002	0	0	-0.061	4.846
$5S$	5.508	0.235	-0.002	0	0	-0.071	5.670
$6S$	6.256	0.262	-0.002	0	0	-0.081	6.435

Table 4.1: Spectrum in the case $m = 3\sqrt{\kappa}$. All energies are expressed in units of $\sqrt{\kappa}$. The column $E^{(0)}$ lists the zeroth-order energy levels, which for S waves are related to the zeros of the Airy function [7]. The column $V^{(1/m)}$ lists the matrix element of $\kappa \ln\left(\kappa r^2\right)/(\pi m)$. The columns $V^{(1/m)}_{\text{2nd order}}$, $V_{\mathbf{L}^2}$, V_{LS} and V_r list the matrix elements of the second-order contribution of the $1/m$ potential and the matrix elements of $-\kappa\mathbf{L}^2/(6m^2r)$, $-\kappa\mathbf{L}\cdot\mathbf{S}/(2m^2r)$ and $-9\,\zeta_3\,\kappa^2 r/(2\pi^3 m^2)$ respectively. The column E gives the total energy levels according to (4.55).

Levels	$E^{(0)}$	$V^{(1/m)}$	$V^{(1/m)}_{\text{2nd order}}$	$V_{\mathbf{L}^2}$	V_{LS}	V_r	E
$1S$	1.085	-0.028	-0.001	0	0	-0.001	1.055
1^1P_1	1.560	-0.0015	-0.0007	-0.004	0	-0.002	1.552
1^3P_0	1.560	-0.0015	-0.0007	-0.004	0.011	-0.002	1.563
1^3P_1	1.560	-0.0015	-0.0007	-0.004	0.006	-0.002	1.558
1^3P_2	1.560	-0.0015	-0.0007	-0.004	-0.006	-0.002	1.546
$2S$	1.897	0.004	-0.0005	0	0	-0.002	1.899
1^1D_2	1.972	0.015	-0.0005	-0.008	0	-0.002	1.977
1^3D_1	1.972	0.015	-0.0005	-0.008	0.013	-0.002	1.990
1^3D_2	1.972	0.015	-0.0005	-0.008	0.004	-0.002	1.981
1^3D_3	1.972	0.015	-0.0005	-0.008	-0.008	-0.002	1.969
2^1P_1	2.267	0.019	-0.0005	-0.003	0	-0.003	2.280
2^3P_0	2.267	0.019	-0.0005	-0.003	0.009	-0.003	2.289
2^3P_1	2.267	0.019	-0.0005	-0.003	0.004	-0.003	2.284
2^3P_2	2.267	0.019	-0.0005	-0.003	-0.004	-0.003	2.276
$3S$	2.562	0.023	-0.0004	0	0	-0.003	2.582
$4S$	3.150	0.035	-0.0003	0	0	-0.004	3.181
$5S$	3.687	0.045	-0.0002	0	0	-0.004	3.728
$6S$	4.188	0.053	-0.0002	0	0	-0.005	4.236

Table 4.2: Spectrum in the case $m = 10\sqrt{\kappa}$, columns are like those in Table 4.1.

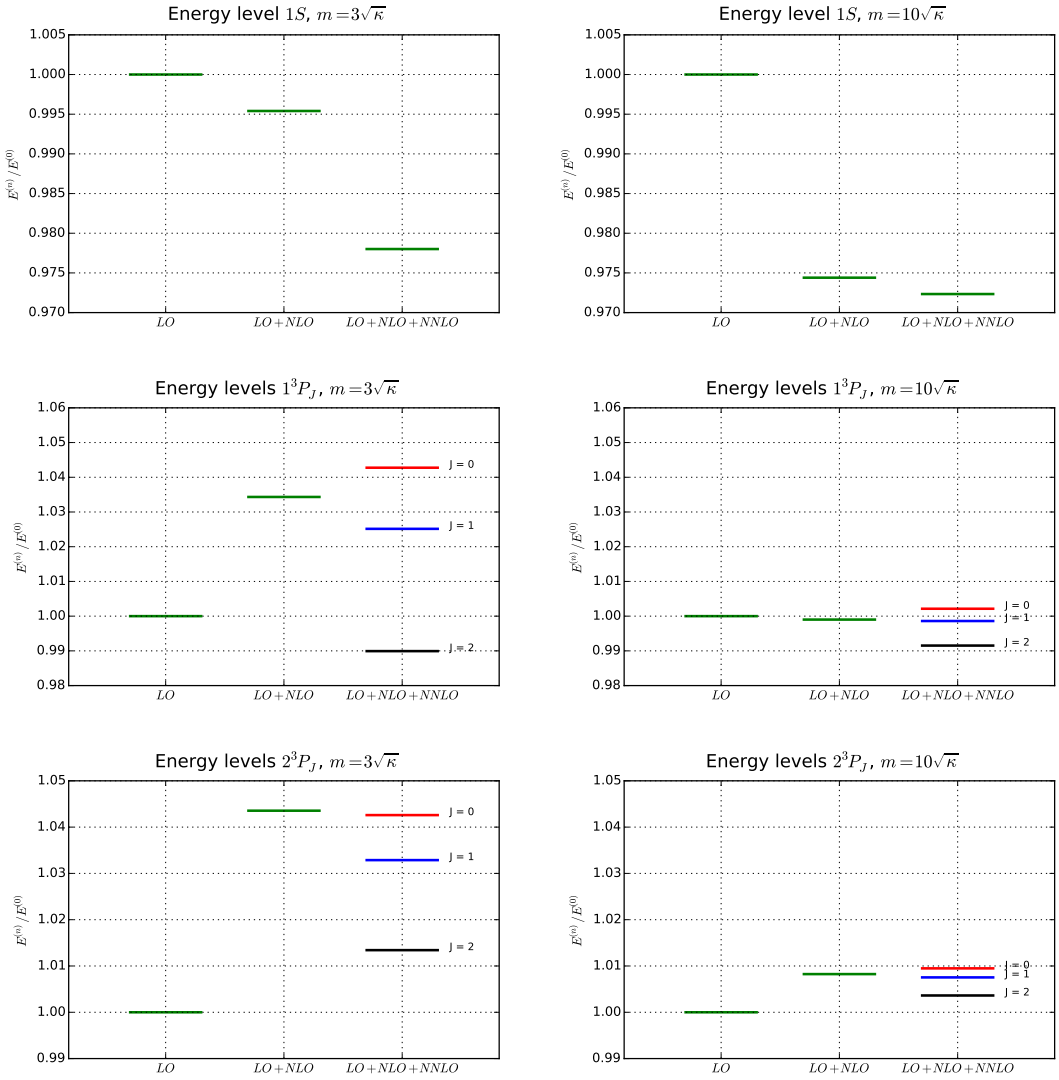

Figure 4.3: Energy levels for the states $1S$, 1^3P_J and 2^3P_J normalized with respect to $E^{(0)}_{1S}$, $E^{(0)}_{1P}$ and $E^{(0)}_{2P}$ respectively. The left plots refer to the case $m = 3\sqrt{\kappa}$, the right ones to the case $m = 10\sqrt{\kappa}$. The leading order (LO) levels correspond to $E^{(0)}_{nl}$, the next-to-leading-order (NLO) corrections to $\langle nl|V^{(1/m)}|nl\rangle$ and the next-to-next-to-leading-order (NNLO) ones to the remaining two terms shown in the right-hand side of Eq. (4.55).

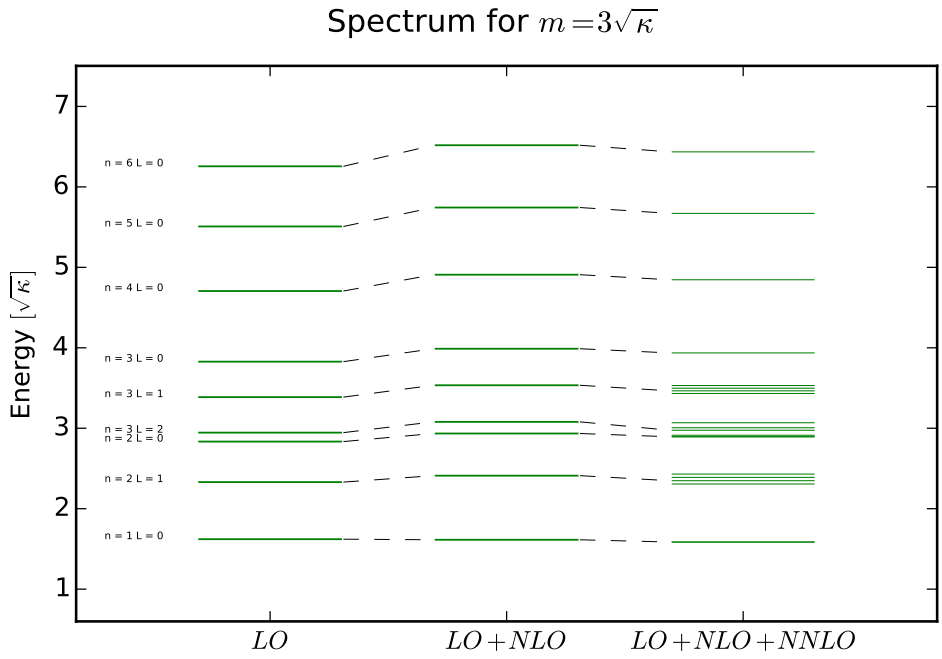

Figure 4.4: Spectrum of all states up to $n = 3$ and of all S-wave states up to $n = 6$ in the case $m = 3\sqrt{\kappa}$. Energies are expressed in units of $\sqrt{\kappa}$.

4.4 Summary

In this chapter we have computed all $1/m^2$ EST potentials, in particular we found novel expressions for the momentum and spin-independent $1/m^2$ potentials. These expressions show a linearly rising behaviour with the distance and may be interpreted as a sort of relativistic correction to the static potential. This is a sharp prediction of the EST that can be checked against data from lattice, once calculations of Wilson loop expectation values with four chromoelectric field insertions are performed.
Under the assumption that the mapping (4.16) is exact, the expressions of the potentials are given in (4.52) and (4.53). The net effect of these potentials in the equal mass case is to reduce the string tension by an amount $9\,\zeta_3\,\kappa^2/(2\pi^3 m^2)$.
We will give more general conclusions about the findings of this chapter in Chapter 10. What will be immediately important for the construction of the potential in the next chapter is Eq. (4.54) since that is the expression we will use to parametrize the long-range (non-perturbative) part of the full $Q\bar{Q}$ potential.

Chapter 5

The full-range $Q\bar{Q}$ potential

As we will see in Chapter 6, the evaluation of the E1 decay rates requires as input the $Q\bar{Q}$ potential for the whole distance regime. In the present chapter, we construct such a potential using the results of the perturbative evaluation of the QCD correlators of Chapter 3 for the short distance limit and the EST evaluation of these correlators for the long distance limit. To fit its free parameters we use state-of-the-art input from experiment and lattice QCD.

5.1 Construction of the potential

Here and for the rest of the thesis we will assume the string hypothesis as valid, namely, that the evaluation of the QCD correlators of Chapter 3 in the EST leads to the right dependence of the $Q\bar{Q}$ potential on r for $r\Lambda_{\rm QCD} \gg 1$. In the limit $r \to 0$, the potential is determined by the perturbative evaluation of these QCD correlators (see below). Even if both limits are known, the problem of the transition zone between the perturbative and non-perturbative regimes remains. To construct the full-range potential we will adopt the simplest approach of adding the expressions for the short and long distance limits. In this way, the full $Q\bar{Q}$ potential will have the right dependence on r in both limits and a smooth transition between the perturbative and non-perturbative regimes. The main inconvenience of this approach is that in both regimes the potential will still receive *artificial* contributions from either short or long range potentials[1]. This problem is especially critical for the perturbative contributions going into the non-perturbative regime, where, due to their dependence on $\alpha_{\rm s}$, they will present a singularity at $r = \Lambda_{\rm QCD}^{-1}$. In order to avoid this issue, in the perturbative expressions we will replace the running coupling by a free parameter a that needs to be fixed. We do the same with the mass m, that we will treat as a free parameter of the potential.
For the long-distance contribution, we consider the LO EST potential given in Eq. (4.54)

[1]By the *right dependence on r in the limit* we mean that artificial contributions will vanish *faster* in the limit. For instance, we may have a non-perturbative contribution $\sim 1/r$ and a perturbative contribution proportional to the same operator that scales as $\sim 1/r^3$, but in the limit $r\Lambda_{\rm QCD} \gg 1$ the non-perturbative contribution will be dominant compared to the perturbative one.

that for convenience we recall here introducing notation that we will use later on

$$V^{\rm long-range}(r) = \kappa r + V^{\rm EST}_{(1/m)}(r) + V^{\rm EST}_{L^2}(r)\mathbf{L}^2 + V^{\rm EST}_{LS}(r)\mathbf{L}\cdot\mathbf{S} + V^{\rm EST}_{(1/m^2)}(r)\,, \qquad (5.1)$$

where

$$\begin{aligned} V^{\rm EST}_{(1/m)}(r) &= \frac{\kappa \ln\left(\kappa r^2\right)}{m\pi}, & (5.2)\\ V^{\rm EST}_{L^2}(r) &= -\frac{\kappa}{6m^2 r}, & (5.3)\\ V^{\rm EST}_{LS}(r) &= -\frac{\kappa}{2m^2 r}, & (5.4)\\ V^{\rm EST}_{(1/m^2)}(r) &= -\frac{9\,\zeta_3\,\kappa^2 r}{2m^2\pi^3}. & (5.5) \end{aligned}$$

In the case of the perturbative potential, its structure is given by the expressions of Sec. 3.1 in the equal mass case, explicitly

$$\begin{aligned} V^{\rm pert.}(r) &= V_{\rm Coul.}(r) + V^{\rm pert.}_{(1/m)}(r) + V^{\rm pert.}_{L^2}(r)\mathbf{L}^2 + V^{\rm pert.}_{LS}(r)\mathbf{L}\cdot\mathbf{S} + V_{S^2}(r)\mathbf{S}^2 \\ &+ V_{S_{12}}(r)\mathbf{S}_{12} + V_{\delta(r)}(r), \qquad (5.6) \end{aligned}$$

where $\mathbf{S}_{12}$ is given in Eq. (3.16). Following this notation, the perturbative expressions of the short distance potentials are given by [72–76]

$$\begin{aligned} V_{\rm Coul.}(r) &= -C_F\frac{\alpha_{\rm s}(r)}{r}, & (5.7)\\ V^{\rm pert.}_{(1/m)}(r) &= -\frac{C_F C_A \alpha_{\rm s}(r)^2}{2mr^2}, & (5.8)\\ V_{p^2}(r) &= -\frac{C_F\alpha_{\rm s}(r)}{m^2 r}, & (5.9)\\ V^{\rm pert.}_{L^2}(r) &= \frac{C_F\alpha_{\rm s}(r)}{2m^2 r^3}, & (5.10)\\ V_{\delta(r)}(r) &= \pi C_F\frac{\alpha_{\rm s}(r)\delta^{(3)}(\mathbf{r})}{m^2}, & (5.11)\\ V_{S^2}(r) &= \frac{4\pi C_F\alpha_{\rm s}(r)}{3m^2}\delta^{(3)}(\mathbf{r}), & (5.12)\\ V^{\rm pert.}_{LS}(r) &= \frac{3C_F\alpha_{\rm s}(r)}{2m^2 r^3}, & (5.13)\\ V_{S_{12}}(r) &= \frac{C_F\alpha_{\rm s}(r)}{4m^2 r^3}. & (5.14) \end{aligned}$$

These expressions can be re-obtained by computing the correlators of Chapter 3 in the short-distance limit.
Replacing $\alpha_{\rm s}(r)$ by the parameter a in Eqs.(5.7)-(5.14) and adding the long-range potential we get

$$V_{Q\bar{Q}} = V^{(0)} + V^{(1/m)} + V^{(1/m^2)} - \frac{\mathbf{p}^4}{4m^3} \qquad (5.15)$$

where

$$V^{(0)}(r) = -C_F\frac{a}{r} + \kappa r, \tag{5.16}$$

$$V^{(1/m)}(r) = \frac{2\kappa}{m\pi}\log(\sqrt{\kappa}r) - \frac{C_F C_A a^2}{2mr^2}, \tag{5.17}$$

$$\begin{aligned} V^{(1/m^2)}(r,\mathbf{p},\mathbf{L},\mathbf{S}) &= \frac{1}{m^2}\left\{\frac{1}{2}\left\{\mathbf{p}^2, -\frac{C_F a}{r}\right\} + \left(\frac{C_F a}{2r^3} - \frac{\kappa}{6r}\right)\mathbf{L}^2 + \left(\frac{3C_F a}{2r^3} - \frac{\kappa}{2r}\right)\mathbf{L}\cdot\mathbf{S}\right. \\ &+ \left.\frac{4\pi C_F a}{3}\delta^{(3)}(\mathbf{r})\mathbf{S}^2 + \frac{C_F a}{4r^3}\mathbf{S}_{12}(\hat{\mathbf{r}}) + \pi C_F a\delta^{(3)}(\mathbf{r}) - \frac{9\,\zeta_3\,\kappa^2 r}{2\pi^3}\right\}. \end{aligned} \tag{5.18}$$

We have also included the kinematic correction proportional to $1/m^3$ since, as we will see in the next section, it will be of the same parametric size as some of the $1/m^2$ corrections after setting the power counting.
Notice that the $V^{(0)}$ (static) potential corresponds to the Coulomb plus linear potential known as the *Cornell potential* [77]. The potential defined by Eqs. (5.16)-(5.18) depends on the same three parameters as the Cornell potential does, namely, the quark mass m, the string tension κ and the coupling a. From Eqs. (5.16)-(5.18) we can check our argument about the limiting behavior of the potential, for instance, in the static potential we see that in the non-perturbative limit the Coulomb potential is sub-dominant compared to the linear part; the same can be checked for the $1/m$ and $1/m^2$-suppressed potentials. We will consider a, κ and m as free parameters; in order to fix them we will need to account for the relativistic corrections to the potential in the expression of the quarkonium mass $M(n^{2S+1}L_J)$. Using quantum mechanical perturbation theory to include these corrections we have

$$\begin{aligned} M(n^{2S+1}L_J) &= 2m_{c,b} + E^{(0)}_{nl} + \langle nl|V^{\rm NLO}(r)|nl\rangle + \sum_{m\neq n}^{\infty}\frac{|\langle nl|V^{\rm NLO}(r)|ml\rangle|^2}{E^{(0)}_{nl} - E^{(0)}_{ml}} \\ &+ \langle nljs|V^{\rm NNLO}(r)|nljs\rangle, \end{aligned} \tag{5.19}$$

where the explicit shape of $V^{\rm LO}$, $V^{\rm NLO}$ and $V^{\rm NNLO}$ will be given in terms of the expressions in Eqs. (5.16)-(5.18) according to the counting we will specify for a, κ and m. Notice that in Eq. (5.19) we assume that the second order perturbative correction due to the $V^{\rm NLO}$ potential scales as $V^{\rm NNLO}$.

5.2 Power countings

With the power counting adopted in [21] the relativistic NLO corrections to the E1 decay rates are of relative size v^2 (see next chapter). This dictates the size of the relativistic corrections that need to be included in the potential, which in turn will depend on the power counting imposed on its parameters, in our case m, a and κ. For what concerns

the potential, the counting adopted in [21] reads

$$\begin{aligned} |\mathbf{p}| &\sim mv, \\ r &\sim 1/mv. \end{aligned} \tag{5.20}$$

For fitting the potential parameters and later evaluating the rates, we will consider the following three different possibilities for the counting of the potential.

Counting 1

In this counting we assume

$$\begin{aligned} a &\sim v, \\ \kappa &\sim m^2 v^3, \\ |\mathbf{p}| &\sim mv, \\ r &\sim 1/mv, \end{aligned}$$

which implies that, to evaluate Eq. (5.19), we must organize the potential as follows

$$V^{\rm LO} = -C_F \frac{a}{r} + \kappa r, \tag{5.21}$$

$$V^{\rm NLO} = \frac{2\kappa}{m\pi} \log(\sqrt{\kappa} r), \tag{5.22}$$

$$\begin{aligned} V^{\rm NNLO} &= -\frac{\mathbf{p}^4}{4m^3} + \frac{1}{m^2}\left\{ \frac{1}{2}\left\{ \mathbf{p}^2, -\frac{C_F a}{r} \right\} + \left(\frac{C_F a}{2r^3} - \frac{\kappa}{6r} \right) \mathbf{L}^2 + \left(\frac{3C_F a}{2r^3} - \frac{\kappa}{2r} \right) \mathbf{L}\cdot\mathbf{S} \right. \\ &+ \left. \frac{4\pi C_F a}{3} \delta^{(3)}(\mathbf{r}) \mathbf{S}^2 + \frac{C_F a}{4r^3} \mathbf{S}_{12}(\hat{\mathbf{r}}) + \pi C_F a \delta^{(3)}(\mathbf{r}) \right\} - \frac{C_F C_A a^2}{2mr^2}. \end{aligned} \tag{5.23}$$

This counting also implies that the parametric size of the potential is such that $V^{\rm LO} \sim mv^2$, $V^{\rm NLO} \sim v\ln(v) V^{\rm LO}$ and $V^{\rm NNLO} \sim v^2 V^{\rm LO}$. The scaling $a \sim v$ is the natural scaling of the QCD running coupling in the perturbative regime [10]. With the scaling imposed on κ, $V^{\rm LO}$ corresponds to the static potential and it scales homogeneously. The counting of $|\mathbf{p}|$ and r is inherited from Eq. (5.20).

Counting 2

In this case, instead of imposing a counting on the parameters we will just order the potentials according to their size in powers of $1/m$, so in order to evaluate Eq. (5.19) we set

$$V^{\rm LO} = V^{(0)}(r) \tag{5.24}$$

$$V^{\rm NLO} = V^{(1/m)}(r) \tag{5.25}$$

$$V^{\rm NNLO} = -\frac{\mathbf{p}^4}{4m^3} + V^{(1/m^2)}(r, \mathbf{p}, \mathbf{L}, \mathbf{S}). \tag{5.26}$$

We have kept the kinematic correction proportional to $1/m^3$ since it does not originate from a specific regime of the potential. Later we will use the results obtained with this counting to measure the impact of adopting different orderings in the potential.

Counting 3

In this counting for charmonium states we will assume

$$\begin{aligned} a &\sim v^2, \\ \kappa &\sim m^2 v^3, \\ |\mathbf{p}| &\sim mv, \\ r &\sim 1/mv, \end{aligned}$$

which implies that for charmonium the potential is organized as follows

$$V^{\rm LO} = \kappa r, \tag{5.27}$$

$$V^{\rm NLO} = -C_F \frac{a}{r} + \frac{2\kappa}{m\pi} \log(\sqrt{\kappa} r), \tag{5.28}$$

$$V^{\rm NNLO} = -\frac{\mathbf{p}^4}{4m^3} + \frac{1}{m^2} \left\{ -\frac{\kappa}{6r} \mathbf{L}^2 - \frac{\kappa}{2r} \mathbf{L} \cdot \mathbf{S} \right\} \tag{5.29}$$

With this ordering $V^{\rm LO} \sim mv^2$, $V^{\rm NLO} \sim vV^{\rm LO}$ and $V^{\rm NNLO} \sim v^2 V^{\rm LO}$. The motivation for adding an extra v-suppression to a will be clear later in this chapter: it turns out that considering $a \sim v^2$ for charmonium is more consistent than naively adopting Counting 1 for bottomonium and charmonium simultaneously. The extra suppression implies that for charmonium states the perturbative contributions to the potential will be less relevant than long-distance contributions. In this approach, when evaluating bottomonium masses and transitions, we will adopt the expressions of Counting 1.

5.3 Inputs

We will use two different input sources to fix the potential parameters. The first input comes from the charmonium and bottomonium spectra as retrieved from the Particle Data Group (PDG) report [78]; we call this approach *phenomenology input*. The second input source comes from the lattice determination of the $Q\bar{Q}$ static energy done by the HotQCD collaboration reported in [79]; we will refer to this approach as the *lattice input*. In both cases there is more data than parameters so our objective will be to find average values for each parameter based on these redundant data sets; we do this for each of the countings specified earlier. Now we go ahead explaining the details of both procedures.

Phenomenology input

In this approach, in order to get a set of parameters $[a,\, \kappa,\, m_c,\, m_b]$, we solve a system of four equations of the type

$$M_{\rm theo}(n^{2S+1}L_J; a, \kappa, m) - M_{\rm exp}(n^{2S+1}L_J) = 0, \tag{5.30}$$

for four different quarkonium states, where $M_{\rm theo}$ is given by Eq. (5.19) and $M_{\rm exp}$ corresponds to the central value of the mass of the $n^{2S+1}L_J$ state quoted in the PDG report

[78]; explicit values are given in Appendix C.
We proceed by choosing sixteen different combinations of quarkonium states in order to obtain the corresponding sixteen sets of parameters. Three of these sets are obtained by choosing three bottomonium states to fit a, κ and m_b and then solving a fourth equation to fit m_c keeping a and κ fixed. Three more sets are obtained doing the reversed process, fitting a, κ and m_c using three charmonium states and then fitting m_b with a and κ held fixed. The remaining ten sets are obtained solving the equations for two charmonium and two bottomonium states simultaneously. All states used in this approach are below the respective open flavor thresholds, except for the bottomonium $\Upsilon(4S)$, which is slightly above. Details about the method used to solve Eq. (5.30) are given in Chapter 7. The detailed results of the fitting with this input are given in Appendix D, the final averages for each parameter in each of the countings are given in the next section.

Lattice input

In this approach we fit the parameters a and κ of the $V^{(0)}$ potential in Eq. (5.16) using the results of the lattice determination of the $Q\bar{Q}$ static energy reported by the HotQCD collaboration [79]. This procedure gives us twelve pairs $(a_{\text{latt}}, \kappa_{\text{latt}})$ corresponding to each of the twelve data sets for different lattice spacings. Two of the data sets used for the fit are displayed in Fig. 5.1. The full results of the fitting are shown in Table 5.1.

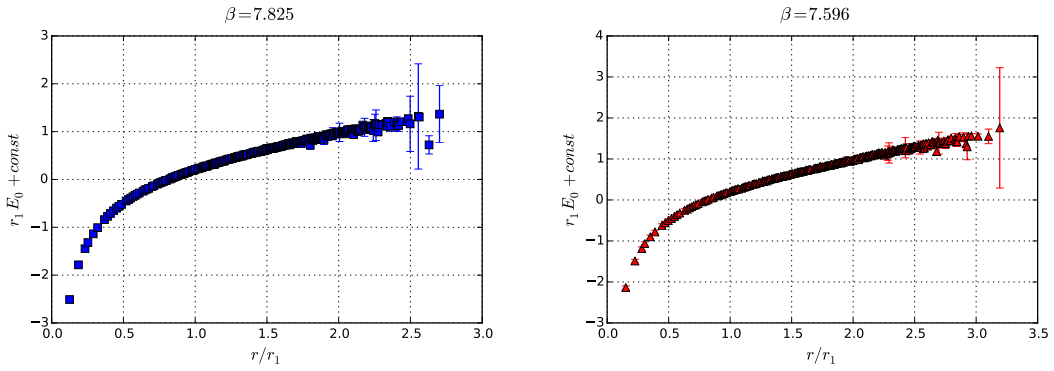

Figure 5.1: Two of the data sets used to fit a and κ in the lattice approach. They are labeled using the gauge parameter β: the larger β is the smaller the lattice spacing is. In the case of $\beta = 7.825$ (left) the lattice spacing is around 0.2 [GeV^{-1}], for $\beta = 7.596$ (right) it is approximately 0.25 [GeV^{-1}]. Both plots are presented in dimensionless units, we have used $r_1 \approx 1.58$ [GeV^{-1}] [79] in order to convert the data to physical units.

The procedure for fitting the masses is the following:

- For each quarkonium state, $n^{2S+1}L_J$, we find twelve m' values solving

$$M_{\text{theo}}(n^{2S+1}L_J; a = a_{\text{latt}}, \kappa = \kappa_{\text{latt}}, m') - M_{\text{exp}}(n^{2S+1}L_J) = 0, \tag{5.31}$$

where M_{theo} is given by Eq. (5.19) assuming one the countings specified in the previous section and the values of a_{latt} and κ_{latt} given in Table 5.1. We take the average of these twelve m' values to extract the quark mass corresponding to each quarkonium state: $m_c(n^{2S+1}L_J)$ and $m_b(n^{2S+1}L_J)$.

- Our final values for the quark masses are obtained by averaging the eight values we get for $m_c(n^{2S+1}L_J)$ and the fourteen values we get for $m_b(n^{2S+1}L_J)$.

The partial results for the fitting of the masses are given in Appendix D. Further technical details about the fitting with lattice input are given in Chapter 7.

Data Set	Spacing (β)	a	σ_a	$\kappa\,[GeV^2]$	$\sigma_\kappa\,[GeV^2]$
1	6.66	0.320	0.009	0.214	0.003
2	6.74	0.346	0.004	0.210	0.001
3	6.8	0.296	0.005	0.227	0.002
4	6.88	0.297	0.004	0.222	0.002
5	6.95	0.296	0.004	0.223	0.002
6	7.03	0.293	0.004	0.220	0.002
7	7.15	0.285	0.003	0.227	0.002
8	7.28	0.278	0.003	0.230	0.002
9	7.37	0.276	0.003	0.233	0.002
10	7.5	0.292	0.005	0.177	0.003
11	7.6	0.263	0.002	0.245	0.002
12	7.83	0.253	0.002	0.246	0.002
Averages	-	0.297	0.015	0.220	0.008

Table 5.1: Results for the fitting of a and κ with lattice input, σ_a and σ_κ are the standard deviations of a and κ respectively. The values are obtained by fitting the dataset of each lattice spacing to a function with the shape of Eq. (5.16). In the case of a and κ the averages are calculated using σ_a and σ_κ as weights. We treat the values of σ_a and σ_κ as the uncertainties in the determination of each parameter, so the quoted average of these quantities is calculated using quadratures.

5.4 Results of the fitting

The final results of the fitting are given in Tables 5.2 and 5.3 for the phenomenology and lattice input respectively. In both inputs we will use these values to generate sixteen new values that distribute normally around their respective mean; in Chapter 8 we will evaluate the decay rates using these randomly generated sets. In this way we expect to cancel possible correlations between the states used to fit the parameters and the states involved in the decays.

Counting	$a\,(\sigma_a)$	$\kappa\,(\sigma_\kappa)\,[\mathrm{GeV}^2]$	$m_c\,(\sigma_{m_c})\,[\mathrm{GeV}]$	$m_b\,(\sigma_{m_b})\,[\mathrm{GeV}]$
1	0.222 (0.070)	0.182 (0.026)	1.345 (0.070)	4.736 (0.061)
2	0.213 (0.073)	0.184 (0.027)	1.346 (0.074)	4.730 (0.065)
3	0.246 (0.074)	0.210 (0.041)	1.123 (0.074)	4.704 (0.086)

Table 5.2: Summary of the fitting with phenomenology input, the standard deviation of each parameter is quoted in brackets.

Counting	$m_c\,(\sigma_{m_c})\,[\mathrm{GeV}]$	$m_b\,(\sigma_{m_b})\,[\mathrm{GeV}]$
1	1.321 (0.115)	4.719 (0.132)
2	1.338 (0.114)	4.725 (0.137)
3	1.130 (0.086)	-

Table 5.3: Summary of the fitting of the masses with lattice input. The values of $a = 0.297$ with $\sigma_a = 0.015$ and $\kappa = 0.220\,[\mathrm{GeV}^2]$ with $\sigma_\kappa = 0.008\,[\mathrm{GeV}^2]$ are the same for all the countings. Notice that we do not quote a value for m_b adopting Counting 3 because the procedure to obtain this value in this counting is equivalent to the one of adopting Counting 1, thus yielding the same result for the three parameters.

5.5 Consistency of Countings 1 and 3

In Tables 5.4 - 5.10 we compare the values obtained for the parameters against their expected size according to Countings 1 and 3. The computation of the expected sizes depends on the quantum numbers of the quarkonium state that is being considered, the comparisons shown in Tables 5.4 - 5.10 are done for all the initial states of the decays that will be evaluated later.
An alternative consistency test is to check if the hierarchy among the LO, NLO and NNLO potentials as dictated by the counting is realized once the parameters have been fixed. The results of this test are shown in Tables D.9 - D.15 of Appendix D for the same initial bottomonium and charmonium states.

State	$a(\sigma_a)$	v	$\kappa(\sigma_\kappa)$ [GeV^2]	m^2v^3 [GeV^2]	$\langle 1/r\rangle^{-1}$ [GeV^{-1}]
1^1P_J	0.22 (0.07)	0.24	0.18 (0.03)	0.31	1.79
2^1P_J	0.22 (0.07)	0.27	0.18 (0.03)	0.46	2.36
2^3S_J	0.22 (0.07)	0.26	0.18 (0.03)	0.41	1.56
3^3S_J	0.22 (0.07)	0.29	0.18 (0.03)	0.56	2.04
3^3P_J	0.22 (0.07)	0.30	0.18 (0.03)	0.62	2.81

Table 5.4: Consistency check in the bottomonium states of the results for the parameter fitting using Counting 1 with phenomenology input. In order to compute the expectation values, the Schrödinger equation is solved numerically using the LO potential with the corresponding values of a, m_b and κ taken from Table 5.2, also quoted here. For more details about the method used to solve the Schrödinger equation see Chapter 7.

State	$a(\sigma_a)$	v	$\kappa(\sigma_\kappa)$ [GeV^2]	m^2v^3 [GeV^2]	$\langle 1/r\rangle^{-1}$ [GeV^{-1}]
1^1P_J	0.22 (0.07)	0.52	0.18 (0.03)	0.25	2.95
2^3S_J	0.22 (0.07)	0.57	0.18 (0.03)	0.33	2.57

Table 5.5: Consistency check in the charmonium states of the results for the parameter fitting using Counting 1 with phenomenology input. The values are computed as in Table 5.4.

State	$a(\sigma_a)$	v	$\kappa(\sigma_\kappa)$ [GeV^2]	m^2v^3 [GeV^2]	$\langle 1/r\rangle^{-1}$ [GeV^{-1}]
1^1P_J	0.30 (0.02)	0.26	0.22 (0.01)	0.41	1.63
2^1P_J	0.30 (0.02)	0.30	0.22 (0.01)	0.59	2.17
2^3S_J	0.30 (0.02)	0.29	0.22 (0.01)	0.54	1.43
3^3S_J	0.30 (0.02)	0.32	0.22 (0.01)	0.71	1.89
3^3P_J	0.30 (0.02)	0.33	0.22 (0.01)	0.77	2.60

Table 5.6: Consistency check in the bottomonium states of the results for the parameter fitting using Counting 1 with lattice input. The values are computed as in Table 5.4.

State	$a(\sigma_a)$	v	$\kappa(\sigma_\kappa)$ [GeV^2]	m^2v^3 [GeV^2]	$\langle 1/r\rangle^{-1}$ [GeV^{-1}]
1^1P_J	0.30 (0.02)	0.56	0.22 (0.01)	0.31	2.75
2^3S_J	0.30 (0.02)	0.62	0.22 (0.01)	0.42	2.40

Table 5.7: Consistency check in the charmonium states of the results for the parameter fitting using Counting 1 with lattice input. The values are computed as in Table 5.4.

State	$a(\sigma_a)$	v	$\kappa(\sigma_\kappa)$ [GeV^2]	m^2v^3 [GeV^2]	$\langle 1/r\rangle^{-1}$ [GeV^{-1}]
1^1P_J	0.25 (0.07)	0.25	0.21 (0.04)	0.37	1.70
2^1P_J	0.25 (0.07)	0.29	0.21 (0.04)	0.54	2.24
2^3S_J	0.25 (0.07)	0.28	0.21 (0.04)	0.48	1.49
3^3S_J	0.25 (0.07)	0.31	0.21 (0.04)	0.65	1.94
3^3P_J	0.25 (0.07)	0.32	0.21 (0.04)	0.72	2.68

Table 5.8: Consistency check in the bottomonium states of the results for the parameter fitting using Counting 3 with phenomenology input. The values are computed as in Table 5.4.

State	$a(\sigma_a)$	v^2	$\kappa(\sigma_\kappa)$ [GeV^2]	m^2v^3 [GeV^2]	$\langle 1/r\rangle^{-1}$ [GeV^{-1}]
1^1P_J	0.25 (0.07)	0.34	0.21 (0.04)	0.25	3.16
2^3S_J	0.25 (0.07)	0.41	0.21 (0.04)	0.33	2.78

Table 5.9: Consistency check in the charmonium states of the results for the parameter fitting using Counting 3 with phenomenology input. The values are computed as in Table 5.4.

State	$a(\sigma_a)$	v^2	$\kappa(\sigma_\kappa)$ [GeV^2]	m^2v^3 [GeV^2]	$\langle 1/r\rangle^{-1}$ [GeV^{-1}]
1^1P_J	0.30 (0.02)	0.35	0.22 (0.01)	0.26	3.11
2^3S_J	0.30 (0.02)	0.42	0.22 (0.01)	0.35	2.73

Table 5.10: Consistency check in the charmonium states of the results for the parameter fitting using Counting 3 with lattice input. The values are computed as in Table 5.4.

Analysis

In the case of bottomonium states we see that the scaling $a \sim v$, imposed on the coupling parameter is fairly fulfilled with both countings in all states. In the case of the string tension parameter, it can be read from the previous tables that the scaling $\kappa \sim m^2 v^3$ appears to be an overestimation of the size of κ, especially in excited states.
Regarding charmonium states, the scaling $a \sim v^2$ of Counting 3 appears to be better realized than $a \sim v$. Also considering Counting 3, we see that the scaling of κ is quantitatively better realized than in Counting 1, especially in the $1P$ states.
In the case of the parametric size of r, notice that the scaling $r \sim 1/mv$ omits any dependence on the quantum numbers, however, such a dependence may be substantial. In the case of a pure Coulombic LO potential, the following exact relation holds

$$\langle 1/r \rangle^{-1} = \frac{n'}{m\langle v \rangle}, \tag{5.32}$$

with n' being the principal quantum number, i.e. $n' = n + l$. Surprisingly, Eq. (5.32) is the scaling that governs the expectation value of $1/r$ also in our evaluations, regardless of whether the LO potential is given by $V^{(0)}$ like in Counting 1 or just a pure linear term like in the Counting 3 for charmonium states. For instance, considering the evaluation of $(m\langle v \rangle)^{-1}$ in $1P$ bottomonium states adopting Counting 1 with phenomenology input, Table 5.4, the RHS of Eq. (5.32) gives $1.76\,[\mathrm{GeV}^{-1}]$, which agrees within 2% with the value of $\langle 1/r \rangle^{-1}$ for $1P$ states quoted in that table. Similar results can be verified for all states regardless of the flavor or the adopted counting.
As mentioned, a complementary test of the realization of the power counting is to check if the expectation values of each term in the $Q\bar{Q}$ potential respect the ordering inherited from the adopted counting. For the sake of clarity we have left the tables of this analysis in Appendix D.
Considering first the bottomonium states, the main conclusion that can be drawn from those tables is that, regardless of the counting (1 or 3) or the input, the potential fulfils

$$|\langle V_i^{\mathrm{LO}} \rangle| > |\langle V^{\mathrm{NLO}} \rangle|, |\langle V_j^{\mathrm{NNLO}} \rangle|, \tag{5.33}$$

where V_i^{LO} is either of the terms of the LO potential, Coulombic or linear, and V_j^{NNLO} is any of the NNLO potentials. The distinction between the NLO and NNLO potentials is more dubious; the general situation is that in both countings we have

$$|\langle V^{\mathrm{NLO}} \rangle| \sim |\langle V_>^{\mathrm{NNLO}} \rangle|. \tag{5.34}$$

where $\langle V_>^{\mathrm{NNLO}} \rangle$ is the largest of the expectation values of the NNLO potentials. Actually, for many states the numerical value of the expectation value of the logarithmic NLO potential, although of the same order, is smaller than the one of the $1/m$-suppressed NNLO potential. Nevertheless, it can be verified that in most of the cases this is due to numerical factors of the potentials that are independent of the adopted counting.
For charmonium states, when adopting Counting 1 we have a similar scaling as in bottomonium, in the case of the Counting 3 the potential fulfils

$$|\langle V^{\mathrm{LO}} \rangle| > |\langle V_>^{\mathrm{NLO}} \rangle| > |\langle V^{\mathrm{NNLO}} \rangle|, \tag{5.35}$$

where $\langle V_>^{\rm NLO}\rangle$ is the largest of the expectation values of the NLO potentials, which for all states turns out to be the one of the Coulombic potential, and $\langle V^{\rm NNLO}\rangle$ is the expectation value of the full NNLO potential. As in the Counting 1, the expectation value of the logarithmic potential appears to be extra-suppressed.

5.6 Summary

The establishment of a power counting is a useful way of ordering the relativistic corrections to a given physical observable. Constructing the $Q\bar{Q}$ potential by adding short and long distance contributions, in this chapter we have studied the numerical impact on the potential parameters from ordering the contributions to the potential in three different ways. In two of them (Countings 1 and 3) the ordering derives from the scaling imposed on the parameters themselves.

Since the analysis of the previous section shows that the counting of the coupling parameter as v is better realized in bottomonium states, and that for the same states the scaling of κ is missed, our consistency test appears to indicate that short-distance physics is dominant in bottomonium. On the other hand, the extra-suppression in v of the coupling parameter, together with the better realization of the scaling of κ, indicate that non-perturbative effects are more relevant in charmonium. This is what one would expect knowing that charmonium is a larger system than bottomonium.

For what concerns the numerical impact of the extra suppression of the logarithmic potential in the evaluation of the decay rates, we consider two possibilities. The first one is that we have underestimated the size of some of the NNLO corrections, so they should be counted as NLO; in such a case, the contribution coming from the second order correction due to the NLO potential in Eq. (5.19) may have been underestimated. It turns out that the leading NNLO correction in Counting 1 comes from the $1/m$-suppressed potential. The counting of this potential as NLO has been considered in Counting 2, which we will use to measure the effect of considering both $1/m$ potentials as NLO in the evaluation of the decay rates.

The second possibility is that, instead of separating the logarithmic potential from the other corrections, one should count all the relativistic corrections homogeneously, in which case there would be no contribution to the decay rates from a second order correction. Since what we get is an extra-suppression of this potential, we expect these second order corrections to be small enough not to alter the qualitative features of our results for the evaluation of the E1 rates.

This chapter ends our construction of the $Q\bar{Q}$ potential, which for the rest of the thesis will be considered, in each of its counting/input combinations, as fixed. The explicit expressions of the relativistic corrections to the E1 decay rates derived from it and their numerical evaluation are the subject of the following chapters.

Chapter 6

The radiative E1 transition

In the first part of this chapter, we give an overview of some of the relevant aspects arising in the study of quarkonium radiative decays in pNRQCD. Then we present the specific formulas necessary for the evaluation of the E1 decay rates. We close this chapter with an overview of the available experimental data that we will use to compare our results in Chapter 9.

6.1 The radiative decays in pNRQCD

By radiative decays we will refer mainly to the electric dipole (E1) and magnetic dipole (M1) decays. The M1 decay differs from the E1 in that the final quarkonium state has the same angular momentum quantum number but the spin has been changed by one. An example of such a decay in charmonium is J/ψ decaying into a photon and an η_c state. The development of EFTs for heavy quarkonium helped to establish a model-independent framework for the study of these radiative transitions. A study of the M1 transitions within the framework of pNRQCD can be found in [80]. Using this framework, a perturbative evaluation of the decay rates has been performed in [81]. In this thesis, we are focusing on the study of the E1 decays, however, at the end of this section we briefly discuss the status of M1 decays in pNRQCD.

6.1.1 The physical landscape

Before giving concrete formulas, let us discuss the physics of the radiative decays and where they locate within the landscape of quarkonium physics at large. In Fig. 6.1 we show part of the charmonium and bottomonium spectrum (mainly below threshold) together with some of the most significant E1 decays that have been observed. The basic kinematics of the decay are displayed in Fig. 6.2. We argued in Chapter 2 that the weakly-coupled regime of pNRQCD is suitable for the study of quarkonium states that lie in the lower half of Fig. 6.1. In this regime the Lagrangian of pNRQCD relevant for radiative transitions can be written as

$$\mathcal{L}_{\rm pNRQCD} = \mathcal{L}_{Q\bar{Q}}(S,O) + \Delta\mathcal{L}_{\rm E1,M1}(S,O,\mathbf{E}^{\rm em},\mathbf{B}^{\rm em}), \tag{6.1}$$

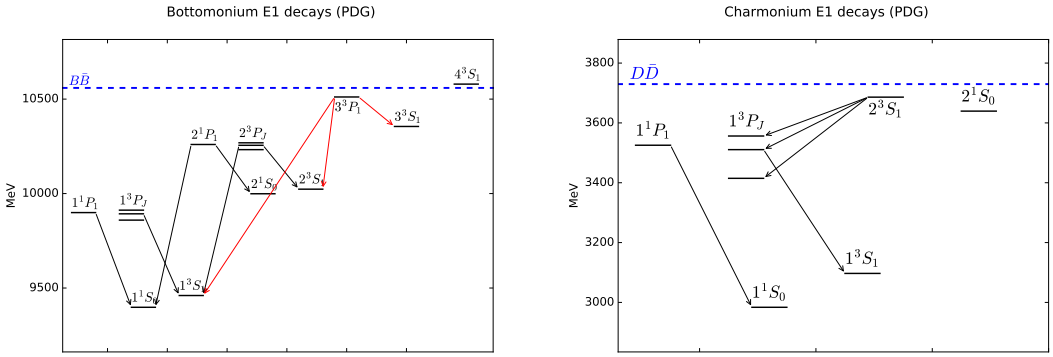

Figure 6.1: Part of the bottomonium and charmonium spectra showing some characteristic E1 decays. The decays in black are those with a large branching fraction, the decays in red have a status of *seen* in the PDG. Explicit values of the masses are given in Appendix C, the values of the available branching fractions of the E1 decays from different experimental sources are given in Sec. 6.2.

where we have separated the part of the Lagrangian that depends only on the quark and antiquark fields and the part that includes the pNRQCD operators responsible for the coupling of the theory to electromagnetism (EM). S and O are the quark-antiquark singlet and octet fields respectively, which were described in Chapter 2. The index of $\delta\mathcal{L}$ indicates if its operators are responsible for the E1 or M1 transitions. In the weakly-coupled regime, the Wilson coefficients of the theory (potentials) are purely perturbative quantities. In the case of the singlet potential its explicit expressions are listed in Eqs. (5.7)-(5.14) of Chapter 5. If we are interested in the physics of states that lie in the upper half of Fig. 6.1, strongly-coupled states, the Lagrangian of pNRQCD reduces to

$$\mathcal{L}_{\rm pNRQCD} = \mathcal{L}_{Q\bar{Q}}(S) + \Delta\mathcal{L}_{\rm E1,M1}(S, \mathbf{E}^{\rm em}, \mathbf{B}^{\rm em}), \tag{6.2}$$

i.e., it includes the singlet field and the EM operators corresponding to ultrasoft photons, $\mathbf{E}^{\rm em}$ and $\mathbf{B}^{\rm em}$. The potentials are now non-perturbative quantities, whose expressions in the EST we calculated in Chapter 4. In our evaluation of the E1 decay rates, we will assume that all initial states are strongly-coupled. From Fig. 6.1 we see that the lowest E1 decay is characterized in terms of quantum numbers as $1P \to 1S\gamma$ in charmonium or bottomonium. Our assumption about the nature of the initial state implies that we are considering $1P$ to be a strongly-coupled state, that is, we assume that the $Q\bar{Q}$ potential for the $1P$ bottomonium state receives seizable non-perturbative contributions[1]. An alternative approach would be to consider the state $1P$ as weakly-coupled; in this case the relevant Lagrangian is given by Eq. (6.1) with a purely perturbative $Q\bar{Q}$ potential. It turns out that if one follows the later approach, the $O(v^2)$ relativistic corrections to the leading E1 decay rate develop non-perturbative contributions originat-

[1]The typical radius of the $1P$ charmonium state is large enough to be considered strongly-coupled.

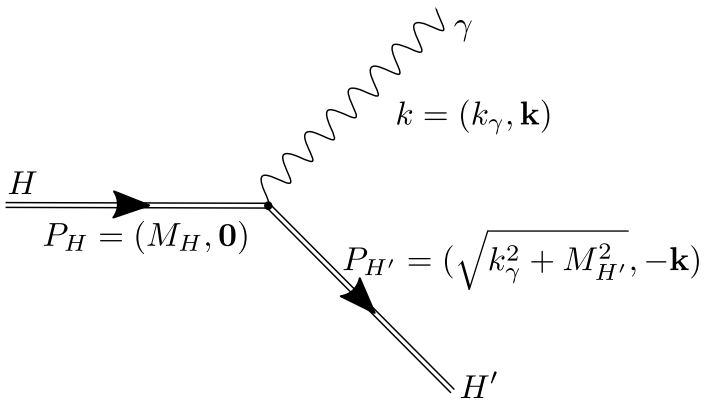

Figure 6.2: Kinematics of the $H \to H'\gamma$ decay. Momenta given in the center-of-mass frame. In the language of pNRQCD, the states H and H' correspond to singlet fields and γ corresponds to an ultrasoft photon.

ing from the presence of the octet field in the Lagrangian [21]. An evaluation of these contributions requires some assumption about the non-perturbative regime of QCD. In our evaluation, we will assume that all non-perturbative contributions to the decay rates are parametrized by the long-range potential that we calculated in the EST, and that the Lagrangian required to describe the decay is given by Eq. (6.2).

Considering now the upper part of Fig. 6.1, wee see that an equivalent scenario arises in the non-perturbative regime, namely, a transition among strongly-coupled states, like $3P \to 3S$, may be studied considering a purely non-perturbative potential. Here we are taking a hybrid approach, in which the potential receives contributions from both regimes. We assume that lower and higher states are eigenstates of the same Hamiltonian whose potential we have constructed in Chapter 5. One could think of a more elaborate approach, in which higher states are eigenstates of a purely non-perturbative potential and lower states eigenstates of a purely perturbative one. Such an approach would change the explicit formulas for the relativistic corrections to the rates that we will present in the following sections and, very likely, complicate the calculation of decay rates of transitions such as $3P \to 1S$. Nevertheless, it would be interesting to see the results of such a study.

In the following we will assume that the Lagrangian describing all the E1 transitions is given by Eq. (6.2) and that the sum of the EST and perturbative potentials, Eqs. (5.1) and (5.6) respectively, with each of the power countings of Chapter 5, describe the physics of all the quarkonium states involved in the transitions.

Let us conclude this section with some words about threshold effects. We have said already that we will only evaluate transitions among states that lie below their respective

open-flavor thresholds. If one wants to evaluate decay rates in which the initial state lies above threshold, the coupling of quarkonium states to B mesons for bottomonium and to D mesons for charmonium should be incorporated in the Lagrangian. For transitions in which the initial state is below but close to threshold, for instance, transitions with an initial state $3P$ in bottomonium, the contributions of these mesons in loops may become important. These effects have been left out of the study performed in [21] and they will not be considered here. We can think of these effects as an additional source of uncertainty that we will assume is small enough to be absorbed in the uncertainty coming from other sources that we will do consider.

6.1.2 The relativistic $O(v^2)$ corrections to the E1 decay rate

The results we present in this section profit from two of the main features of pNRQCD. The first one is that the theory allows a quantum-mechanical description of quarkonium physics that is fully equivalent to QCD when studying the same energy scale. The second one is that the relativistic corrections to some observable can be incorporated systematically as an expansion in powers of the quark-antiquark relative velocity v once the power counting of the relevant Lagrangian operators has been established. In the case of the E1 transitions, the relativistic $O(v^2)$ corrections to the decay rates have been calculated using pNRQCD explicitly in [21]; in this section we present the main results of that paper, whose notation we follow closely.
The general formula for the decay rates is given by

$$\begin{aligned}\Gamma_{H\to H'\gamma} &= \int \frac{d^3P_{H'}}{(2\pi)^3}\frac{d^3k}{(2\pi)^3}\frac{1}{2k}\frac{1}{N_\lambda}\sum_{\lambda,\lambda'\sigma}|A_{H\to H'\gamma}|^2(2\pi)^4\delta^4(P_H-k-P_{H'}) \\ &= \frac{1}{8\pi^2}\left(1-\frac{k_\gamma}{M_H}\right)\int dk k\int d\Omega(\hat{\mathbf{k}})\delta(k-k_\gamma)\frac{1}{N_\lambda}\sum_{\lambda\lambda'\sigma}|A_{H\to H'\gamma}|^2, \quad (6.3)\end{aligned}$$

where $P_H, P_{H'}, k$ are the 4-momenta of the initial state, final state and photon respectively, λ and λ' are the polarization of initial and final state, σ is the photon polarization, M_H is the initial quarkonium state mass and k_γ is the photon energy that, following the kinematics of Fig. 6.2, is given by

$$k_\gamma = |\mathbf{k}| = \frac{M_H^2 - M_{H'}^2}{2M_H}. \quad (6.4)$$

The amplitude $A_{H\to H'\gamma}$ is defined through

$$A_{H\to H'\gamma} = -\langle H'(\mathbf{P}',\lambda')\gamma(\mathbf{k},\sigma)|\int d^3R\{\mathcal{L}_{E1}^{(0)}+\delta\mathcal{L}_{E1}\}|H(\mathbf{P},\lambda)\rangle, \quad (6.5)$$

where $\mathcal{L}_{E1}^{(0)}$ is the leading operator relevant for the E1 decays in the pNRQCD Lagrangian and $\delta\mathcal{L}_{E1}$ accounts for higher order operators. The quarkonium state $|H\rangle$ may include corrections due to relativistic corrections to the $Q\bar{Q}$ potential, explicitly

$$|H\rangle = |H\rangle^{(0)} + |H\rangle^{(1)} + \dots, \quad (6.6)$$

where $|H\rangle^{(0)}$ is the LO quarkonium state given by

$$|H(\mathbf{P},\lambda)\rangle^{(0)} = \int d^3R \int d^3r\, e^{i\mathbf{P}\cdot\mathbf{R}} \mathrm{Tr}\left\{\phi^{(0)}_{H(\lambda)} S^\dagger(\mathbf{r},\mathbf{R})|US\rangle\right\}, \tag{6.7}$$

with S being the singlet operator and $|US\rangle$ the vacuum that only contains ultrasoft gluons and photons. The wavefunctions $\phi^{(0)}_H$ are obtained from solving the Schrödinger equation using the leading order $Q\bar{Q}$ potential, i.e.,

$$\left(\frac{\mathbf{p}^2}{m} + V^{\mathrm{LO}}\right)\phi^{(0)}_H = E_H \phi^{(0)}_H, \tag{6.8}$$

The LO decay rate $\Gamma^{\mathrm{LO}}_{H\to H'\gamma}$ is obtained considering just the LO state $|H\rangle^{(0)}$ and the LO operator $\mathcal{L}^{(0)}_{E1}$ given by[2]

$$\mathcal{L}^{(0)}_{E_1} = e e_Q \int d^3r \mathrm{Tr}\left\{S^\dagger \mathbf{r}\cdot\mathbf{E}^{\mathrm{em}} S\right\}. \tag{6.9}$$

where e is the electron charge, e_Q is the fractional quark electric charge, $\mathbf{r}$ is the quark-antiquark separation vector and $\mathbf{E}^{\mathrm{em}}$ is the electric field operator.
In order to get the LO decay rate we recall the canonical equal-time commutation relation for the singlet field given in Chapter 2

$$\left[S_{ij}(\mathbf{r},\mathbf{R}), S^\dagger_{kl}(\mathbf{r}',\mathbf{R}')\right] = \delta_{il}\delta_{jk}\delta^{(3)}(\mathbf{r}-\mathbf{r}')\delta^{(3)}(\mathbf{R}-\mathbf{R}'), \tag{6.10}$$

where $(i,j),(k,l)$ are the spin indices, $\mathbf{R}$ is the coordinate of the center of mass of the quark-antiquark system, together with the following relations

$$\langle\gamma(\mathbf{k},\sigma)|\mathbf{E}^{\mathrm{em}}(\mathbf{R})|0\rangle = -ik\epsilon^*(\sigma)e^{-i\mathbf{k}\cdot\mathbf{R}}, \tag{6.11}$$

$$\langle H(\mathbf{P}',\lambda')|H(\mathbf{P},\lambda)\rangle = (2\pi)^3\delta^{(3)}(\mathbf{P}-\mathbf{P}')\delta_{\lambda\lambda'}, \tag{6.12}$$

where $\epsilon(\sigma)$ is the photon polarization vector. The first relation is obtained from the usual Lorenz-invariant normalization of the photon field and the second one is the non-relativistic normalization of the quarkonium states. In this last relation also the normalization of $\phi^{(0)}_{H(\lambda)}$ is implicit. The angular parts of $\phi^{(0)}_{H(\lambda)}$ for $L = 0,1,2$ have been calculated in Refs. [21, 80, 82, 83], to which we refer for explicit expressions. Using Eqs. (6.3)-(6.12) the LO decay rates of the transitions we will evaluate read [21]

$$\Gamma^{\mathrm{LO}}_{n\,^3P_J\to n'\,^3S_1\gamma} = \Gamma^{\mathrm{LO}}_{n\,^1P_1\to n'\,^1S_0\gamma} = \Gamma^{(0)}_{nn'}, \tag{6.13}$$

$$\Gamma^{\mathrm{LO}}_{n\,^3S_1\to n'\,^3P_J\gamma} = \frac{2J+1}{3}\Gamma^{(0)}_{nn'}, \tag{6.14}$$

$$\Gamma^{\mathrm{LO}}_{n\,^1S_0\to n'\,^1P_1\gamma} = 3\Gamma^{(0)}_{nn'}, \tag{6.15}$$

[2]Here we use the fact that the Wilson coefficient associated with this operator is found to be equal to 1, for details see [21].

where

$$\Gamma^{(0)}_{nn'} \equiv \frac{4}{9}\alpha_{em} e_Q^2 k_\gamma^3 I_3(n1, n'0)^2, \tag{6.16}$$

α_{em} is the fine structure constant and the integrals I_N are defined as

$$I_N^{(k)}(nL, n'L') \equiv \int_0^\infty dr r^N R_{n'0}(r) \frac{d^k}{dr^k} R_{n1}(r), \tag{6.17}$$

where R_{nl} corresponds to the radial part of the wavefunction $\phi_H(\mathbf{r})$.
The relativistic corrections to the LO decay rate come from considering higher order operators in the pNRQCD Lagrangian, i.e., the term $\delta\mathcal{L}_{E1}$ in Eq. (6.5), and from the inclusion of the relativistic corrections to the $Q\bar{Q}$ potential, i.e., from considering the state corrections $|H\rangle^{(i)}$ in Eq. (6.6). For convenience, let us separate these corrections as[3]

$$\Gamma^{\rm NLO}_{H\to H'\gamma} = \Gamma^{\rm LO}_{H\to H'\gamma}(1 + R_{H\to H'\gamma} + \delta\Gamma_{H\to H'\gamma}), \tag{6.18}$$

where $R_{H\to H'\gamma}$ accounts for the higher order corrections to the quarkonium state and $\delta\Gamma_{H\to H'\gamma}$ accounts for the contributions due to higher order pNRQCD operators. The explicit expression of $R_{H\to H'\gamma}$ is given in the next section. The corrections $\delta\Gamma_{H\to H'\gamma}$ have been calculated in [21] considering the following operators in $\delta\mathcal{L}_{E1}$

$$\begin{aligned}
\delta\mathcal{L}_{E1} = \int d^3r \ {\rm Tr}\Big\{ & \frac{1}{24} V^{(r\nabla)^2 r\cdot E} S^\dagger \mathbf{r}\cdot[(\mathbf{r}\cdot\boldsymbol{\nabla})^2 e e_Q \mathbf{E}^{\rm em}] S \\
& + \frac{i}{4m} V^{\nabla\cdot(r\times B)} S^\dagger \{\boldsymbol{\nabla}\cdot, \mathbf{r}\times e e_Q \mathbf{B}^{\rm em}\} S \\
& + \frac{i}{12m} V^{\nabla_r\cdot(r\times(r\nabla)B)} S^\dagger \{\boldsymbol{\nabla}_r\cdot, \mathbf{r}\times[(\mathbf{r}\cdot\boldsymbol{\nabla}) e e_Q \mathbf{B}^{\rm em}]\} S \\
& + \frac{1}{4m} V^{(r\nabla)\sigma\cdot B} [S^\dagger, \boldsymbol{\sigma}]\cdot[(\mathbf{r}\cdot\boldsymbol{\nabla}) e e_Q \mathbf{B}^{\rm em}] S \\
& - \frac{i}{4m^2} V^{\sigma\cdot(E\times\nabla_r)} [S^\dagger, \boldsymbol{\sigma}]\cdot(e e_Q \mathbf{E}^{\rm em}\times\boldsymbol{\nabla}_r) S \Big\}
\end{aligned} \tag{6.19}$$

where $V^{(r\nabla)^2 r\cdot E}$, $V^{\nabla\cdot(r\times B)}$, $V^{\nabla_r\cdot(r\times(r\nabla)B)}$, $V^{(r\nabla)\sigma\cdot B}$, $V^{\sigma\cdot(E\times\nabla_r)}$ are the Wilson coefficients associated with their respective operators, ∇ acts on the center of mass coordinate

[3] Although, due to the presence of potential corrections that may scale as v in the velocity counting, Eq. (6.18) may correspond to a LO+NLO+NNLO decay rate, in order to keep the notation simple we will refer to the decay rate that includes the full $R_{H\to H'\gamma}$ and $\delta\Gamma_{H\to H'\gamma}$ corrections simply as $\Gamma^{\rm NLO}_{H\to H'\gamma}$. We will never consider decay rates that scale just as v, so it shall be clear that when we refer to the NLO rates we are referring to the expression of Eq. (6.18), and that when we refer to NLO amplitudes (see below) or NLO potential corrections we are referring to terms that scale as v in the case of Counting 1 and 3, or as $1/m$ in the case of Counting 2. It was established in [21] that the first corrections to the decay rates due to higher order operators in the pNRQCD Lagrangian, $\delta\Gamma_{H\to H'\gamma}$, are of order v^2, so Eq. (6.18) accounts for the NLO corrections to the LO decay rate before establishing what is the size (or the shape) of the term $R_{H\to H'\gamma}$, hence the motivation for our notation.

$\mathbf{R}$ and $\nabla_{\mathbf{r}}$ acts on $\mathbf{r}$. These terms are all the v^2-suppressed operators with respect to $\mathcal{L}^{(0)}_{E1}$ if one considers the following power counting

$$\begin{aligned} k_\gamma &\sim mv^2, \\ r &\sim 1/mv, \\ \nabla_{\mathbf{r}} &\sim mv, \\ \nabla &\sim mv^2, \\ \mathbf{E}^{\rm em}, \mathbf{B}^{\rm em} &\sim k_\gamma^2. \end{aligned} \tag{6.20}$$

The Wilson coefficients were calculated matching pNRQCD with NRQCD in [21], they read

$$V^{(r\nabla)^2 r\cdot E} = V^{\nabla\cdot(r\times B)} = V^{\nabla_r\cdot(r\times(r\nabla)B)} = 1\,, \tag{6.21}$$

$$V^{(r\nabla)\sigma\cdot B} = c_F^{\rm em}\,, \tag{6.22}$$

$$V^{\sigma\cdot(E\times\nabla_r)} = c_S^{\rm em}\,, \tag{6.23}$$

where $c_F^{\rm em}$ and $c_S^{\rm em}$ are Wilson coefficients of NRQCD (see Eq. (2.22)), their explicit expressions at order $\alpha_{\rm s}$ read [37, 39]

$$c_F^{\rm em} = 1 + C_F\frac{\alpha_{\rm s}}{2\pi}, \tag{6.24}$$

$$c_S^{\rm em} = 2c_F^{\rm em} - 1. \tag{6.25}$$

The values of the Wilson coefficients in Eqs. (6.21)-(6.23) are found to be valid at all orders in $\alpha_{\rm s}$.
Once we are provided with the Wilson coefficients, the corrections $\delta\Gamma_{H\to H'\gamma}$ can be computed by first inserting $\delta\mathcal{L}_{E1}$ in Eq. (6.5), setting $|H\rangle = |H\rangle^{(0)}$ and then putting the resulting amplitudes into the formula of the decay rates in Eq. (6.3). The final expressions for these corrections are [21]

$$\begin{aligned} \delta\Gamma_{n\,^3P_J\to n'\,^3S_1\gamma} &= -\frac{k_\gamma^2}{60}\frac{I_5(n1,n'0)}{I_3(n1,n'0)} - \frac{k_\gamma}{6m} \\ &+ \left(\frac{J(J+1)}{2} - 2\right)\left(\frac{1}{m^2}\frac{I_2^{(1)}(n1,n'0) + 2I_1(n1,n'0)}{I_3(n1,n'0)} - \frac{k_\gamma}{2m}\right), \end{aligned} \tag{6.26}$$

$$\delta\Gamma_{n\,^1P_1\to n'\,^1S_0\gamma} = -\frac{k_\gamma}{6m} - \frac{k_\gamma^2}{60}\frac{I_5(n1,n'0)}{I_3(n1,n'0)}, \tag{6.27}$$

$$\delta\Gamma_{n\,^3S_1\to n'\,^3P_J\gamma} = \delta\Gamma_{n\,^3P_J\to n'\,^3S_1}(k_\gamma\to -k_\gamma, n\to n', n'\to n), \tag{6.28}$$

$$\delta\Gamma_{n\,^1S_0\to n'\,^1P_1\gamma} = \delta\Gamma_{n\,^1P_1\to n'\,^1S_0}(k_\gamma\to -k_\gamma, n\to n', n'\to n). \tag{6.29}$$

Notice that so far the formula of the decay rates and its relativistic corrections is completely model-independent, it only depends on the power counting assumed for the pNRQCD operators, however, in order to evaluate the rates, a definite expression of

the $Q\bar{Q}$ potential becomes necessary. The choice of the potential defines the explicit shape of $R_{H\to H'\gamma}$ and the numerical values of $\Gamma^{\rm LO}_{H\to H'\gamma}$ and $\delta\Gamma_{H\to H'\gamma}$. Here we will adopt the full-range potential presented in the previous chapter, yet, it is important to recall that this choice is far from unique. We will discuss a little more about alternative evaluations of the decay rates in Chapter 10.

About the M1 transitions

In the case of the radiative M1 transitions, in Ref. [80] all the Wilson coefficients of the relevant pNRQCD operators have been obtained up to order $1/m^2$. When considering weakly-coupled quarkonia, these operators fully determine the $O(v^2)$ relativistic corrections to the M1 decay rates. Moreover, it turns out that for weakly-coupled quarkonia, there are no non-perturbative contributions to the decay rates. As a consequence of this, in contrast to the E1 case, the evaluation of M1 transitions among lower states (e.g. $J/\psi \to \eta_c\gamma$) can be performed in a fully perturbative manner. Such an analysis has been performed in [81], their results agree with the available experimental data.
For strongly-coupled quarkonia one should also consider the contribution of an $1/m^3$ operator in order to obtain the full $O(v^2)$ corrections to the rate. The value of the Wilson coefficient associated with this operator is still missing.
For more details about the study of M1 transitions within a pNRQCD framework we refer the reader to [80] and [81]; for the rest of this section we will focus only on the E1 transitions.

6.1.3 Relativistic corrections to the quarkonium state

In this section we give the explicit expression of $R_{H\to H'\gamma}$ in Eq. (6.18) that follows from adopting the potential of Chapter 5. Before we start, it will be convenient to introduce some notation; for a given amplitude or sum of amplitudes A we define $\bar{A}$ as

$$\bar{A} \equiv \frac{A}{A^{(0)}_{H\to H'\gamma}}, \tag{6.30}$$

where $A^{(0)}_{H\to H'\gamma}$ is the LO amplitude defined as

$$A^{(0)}_{H\to H'\gamma} \equiv -{}^{(0)}\langle H'\gamma| \int d^3R \mathcal{L}^{(0)}_{E_1} |H\rangle^{(0)}, \tag{6.31}$$

with the LO quarkonium states as in Eq. (6.7). Considering the factorization of Eq. (6.18), up to second order corrections to the initial and final quarkonium states, $R_{H\to H'\gamma}$ is given by

$$R_{H\to H'\gamma} = 2\bar{A}_{R_c} + \bar{B}^2_{R_c}, \tag{6.32}$$

where A_{R_c} is given by

$$\begin{aligned} A_{R_c} &\equiv -{}^{(0)}\langle H'\gamma| \int d^3R \mathcal{L}^{(0)}_{E_1} |H\rangle^{(1)} - {}^{(1)}\langle H'\gamma| \int d^3R \mathcal{L}^{(0)}_{E_1} |H\rangle^{(0)} \\ &- {}^{(0)}\langle H'\gamma| \int d^3R \mathcal{L}^{(0)}_{E_1} |H\rangle^{(2)} - {}^{(2)}\langle H'\gamma| \int d^3R \mathcal{L}^{(0)}_{E_1} |H\rangle^{(0)} \\ &- {}^{(1)}\langle H'\gamma| \int d^3R \mathcal{L}^{(0)}_{E_1} |H\rangle^{(1)}. \end{aligned} \tag{6.33}$$

The terms $|H\rangle^{(1)}$, $|H\rangle^{(2)}$ and their final state equivalents are the relativistic corrections to the quarkonium state defined through Eq. (6.6). Notice that since $R_{H\to H'\gamma}$ depends on these corrections and, therefore, on the shape of the NLO and NNLO corrections to the leading $Q\bar{Q}$ potential, $R_{H\to H'\gamma}$ is a counting-depending quantity. This is made explicit by the inclusion of the index c in A_{R_c} and B_{R_c}; later we will label $c = 1, 2$ or 3 to distinguish between the three power countings we considered in Chapter 5. The term B_{R_c} includes the terms of A_{R_c} that scale as the NLO potential, i.e., terms that have only one state correction of first order calculated from $V^{\rm NLO}$. This term would cancel in the case when the relativistic corrections to the potential have a homogeneous size, i.e. there is no distinction between NLO and NNLO contributions.
The first order correction to the state, $|H\rangle^{(1)}$, is given by

$$|H(\mathbf{P})\rangle^{(1)} = \sum_{H'\neq H} {}^{(0)}\langle H'(\mathbf{P})| \int d^3R \int d^3r {\rm Tr}\{S^\dagger \delta h S\} |H(\mathbf{P})\rangle^{(0)} \frac{|H'(\mathbf{P})\rangle^{(0)}}{E_H^{(0)} - E_{H'}^{(0)}}, \tag{6.34}$$

where

$$\delta h = V^{\rm NLO} + V^{\rm NNLO}. \tag{6.35}$$

The second order correction, $|H\rangle^{(2)}$, is given by

$$\begin{aligned} &|H(\mathbf{P})\rangle^{(2)} = \\ &\sum_{\check{H}\neq H} \sum_{\widetilde{H}\neq H} |\check{H}\rangle^{(0)} \frac{{}^{(0)}\langle \check{H}| \int d^3R d^3r {\rm Tr}\{S^\dagger V^{\rm NLO} S\} |\widetilde{H}\rangle^{(0)} \, {}^{(0)}\langle \widetilde{H}| \int d^3R d^3r {\rm Tr}\{S^\dagger V^{\rm NLO} S\} |H\rangle^{(0)}}{(E_H^{(0)} - E_{\check{H}}^{(0)})(E_H^{(0)} - E_{\widetilde{H}}^{(0)})} \\ &- \sum_{\check{H}\neq H} |\check{H}\rangle^{(0)} \frac{{}^{(0)}\langle H| \int d^3R d^3r {\rm Tr}\{S^\dagger V^{\rm NLO} S\} |H\rangle^{(0)} \, {}^{(0)}\langle \check{H}| \int d^3R d^3r {\rm Tr}\{S^\dagger V^{\rm NLO} S\} |H\rangle^{(0)}}{(E_H^{(0)} - E_{\check{H}}^{(0)})^2} \\ &- \frac{1}{2} |H\rangle^{(0)} \sum_{\check{H}\neq H} \frac{{}^{(0)}\langle H| \int d^3R d^3r {\rm Tr}\{S^\dagger V^{\rm NLO} S\} |\check{H}\rangle^{(0)} \, {}^{(0)}\langle \check{H}| \int d^3R d^3r {\rm Tr}\{S^\dagger V^{\rm NLO} S\} |H\rangle^{(0)}}{(E_H^{(0)} - E_{\check{H}}^{(0)})^2}. \end{aligned} \tag{6.36}$$

The expressions for $|H\rangle^{(1)}$ and $|H\rangle^{(2)}$ are obtained using quantum mechanical perturbation theory to account for the relativistic corrections to the LO potential.
Explicitly, the term B_{R_c} is then given by

$$B_{R_c} = {}^{(0)}\langle H'\gamma| \int d^3R \mathcal{L}^{(0)}_{E_1} |H\rangle^{(1)}_{\rm nlo} + {}^{(1)}_{\rm nlo}\langle H'\gamma| \int d^3R \mathcal{L}^{(0)}_{E_1} |H\rangle^{(0)}, \tag{6.37}$$

where $|H\rangle^{(1)}_{\rm nlo}$ is the first order state correction originated from the $V^{\rm NLO}$ potential, that is, it is obtained by replacing δh just with $V^{\rm NLO}$ in Eq. (6.34).
With the previous definitions, the nominal size of $R_{H\to H'\gamma}$ is the same as the NNLO corrections to the potential, which in the case of the Counting 1 and 3 implies that $R_{H\to H'\gamma}$ nominally scales as v^2; the numerical realization of this scaling is studied in Chapter 8.
The calculation of the explicit expressions for A_{R_c} and B_{R_c}, and therefore $R_{H\to H'\gamma}$, is lengthy but straightforward. For a given counting, one starts by solving the Schrödinger equation (Eq. (6.8)) for the LO potential for the initial and final states, this calculation determines the energy eigenvalues $E^{(0)}_H$ and $E^{(0)}_{H'}$ and the expressions for $|H\rangle^{(0)}$ and $|H'\rangle^{(0)}$. Using these results and the expressions for the NLO and NNLO potentials in the considered counting, the expressions for $|H\rangle^{(1)}$ (Eq. (6.34)), $|H\rangle^{(2)}$ (Eq. (6.36)) and the corresponding final state equivalents can be determined in terms of a perturbative sum. What follows is to insert these expressions together with $\mathcal{L}^{(0)}_{E_1}$ (Eq. (6.9)) into the formulas for A_{R_c} (Eq. (6.33)) and B_{R_c} (Eq. (6.37)). Then using the canonical equal-time commutation relation given in Eq. (6.10) together with Eqs. (6.11) and (6.12), one is left with the final expressions for A_{R_c} and B_{R_c} in terms of a sum of amplitudes, each of them written as an infinite perturbative sum, which in turn originates from one of the terms of the NLO and NNLO potentials.
Before giving A_{R_c} and B_{R_c} in each counting, it is convenient to introduce some notation. Let us label the amplitudes on which A_{R_c} and B_{R_c} depend as A^S_P, where the index P (*potential*) labels the term of the NLO or NNLO potential from which the amplitude originates[4] and the index S (*sequence*) denotes if the amplitude corresponds to an initial ($S=i$), final ($S=f$) or initial and final ($S=i\,f$) state correction. In the case of second order corrections, we use the notation $P\equiv(2),c$ where (2) denotes that the amplitude originates from a second order correction and $c=1,2,3$ indicates which counting is being adopted. The exact expressions for all the A^S_P amplitudes will follow shortly, first we list the expressions for A_{R_c} and B_{R_c} in each of the countings.
Adopting Counting 1 for bottomonium and charmonium decays, we get

$$\begin{aligned}
\bar{A}_{R_1} &= \bar{A}^i_{p^4}+\bar{A}^f_{p^4}+\bar{A}^i_{V^{\rm EST}_{(1/m)}}+\bar{A}^f_{V^{\rm EST}_{(1/m)}}+\bar{A}^i_{V^{\rm pert.}_{(1/m)}}+\bar{A}^f_{V^{\rm pert.}_{(1/m)}}+\bar{A}^i_{V_{p^2}}+\bar{A}^f_{V_{p^2}}\\
&+ \bar{A}^i_{V^{\rm pert.}_{L^2}}+\bar{A}^i_{V^{\rm EST}_{L^2}}+\bar{A}^f_{V_{L^2}}+\bar{A}^i_{V^{\rm pert.}_{LS}}+\bar{A}^i_{V^{\rm EST}_{LS}}+\bar{A}^f_{V_{LS}}+\bar{A}^i_{V_{S^2}}+\bar{A}^f_{V_{S^2}}\\
&+ \bar{A}^i_{V_{S_{12}}}+\bar{A}^f_{V_{S_{12}}}+\bar{A}^i_{V_{\delta(r)}}+\bar{A}^f_{V_{\delta(r)}}+\bar{A}^i_{(2),1}+\bar{A}^f_{(2),1}+\bar{A}^{if}_{(2),1}, \qquad (6.38)\\
\bar{B}_{R_1} &= \bar{A}^i_{V^{\rm EST}_{(1/m)}}+\bar{A}^f_{V^{\rm EST}_{(1/m)}}\,. \qquad (6.39)
\end{aligned}$$

[4]In the case of amplitudes originating from the kinetic correction proportional to $\mathbf{p}^4$, we use $P=p^4$. For the other amplitudes, we follow the notation introduced in Sec. 5.1, except in the case when $P=V_{L^2}$ and $P=V_{LS}$, in which case it should be understood that the amplitude is coming from the sum of the perturbative and EST potentials, i.e., from $V_{L^2}=V^{\rm pert.}_{L^2}+V^{\rm EST}_{L^2}$ and $V_{LS}=V^{\rm pert.}_{LS}+V^{\rm EST}_{LS}$ respectively.

Adopting Counting 2 also for both flavors, we have

$$\begin{aligned}
\bar{A}_{R_2} &= \bar{A}^i_{p^4} + \bar{A}^f_{p^4} + \bar{A}^i_{V^{\rm EST}_{(1/m)}} + \bar{A}^f_{V^{\rm EST}_{(1/m)}} + \bar{A}^i_{V^{\rm pert.}_{(1/m)}} + \bar{A}^f_{V^{\rm pert.}_{(1/m)}} + \bar{A}^i_{V_{p^2}} + \bar{A}^f_{V_{p^2}} \\
&+ \bar{A}^i_{V^{\rm pert.}_{L^2}} + \bar{A}^i_{V^{\rm EST}_{L^2}} + \bar{A}^f_{V_{L^2}} + \bar{A}^i_{V^{\rm pert.}_{LS}} + \bar{A}^i_{V^{\rm EST}_{LS}} + \bar{A}^f_{V_{LS}} + \bar{A}^i_{V_{S^2}} + \bar{A}^f_{V_{S^2}} \\
&+ \bar{A}^i_{V_{S_{12}}} + \bar{A}^f_{V_{S_{12}}} + \bar{A}^i_{V_{\delta(r)}} + \bar{A}^f_{V_{\delta(r)}} + \bar{A}^i_{(2),2} + \bar{A}^f_{(2),2} + \bar{A}^{if}_{(2),2} \\
&+ \bar{A}^i_{V^{\rm EST}_{(1/m^2)}} + \bar{A}^f_{V^{\rm EST}_{(1/m^2)}}, \qquad (6.40) \\
\bar{B}_{R_2} &= \bar{A}^i_{V^{\rm EST}_{(1/m)}} + \bar{A}^f_{V^{\rm EST}_{(1/m)}} + \bar{A}^i_{V^{\rm pert.}_{(1/m)}} + \bar{A}^f_{V^{\rm pert.}_{(1/m)}}. \qquad (6.41)
\end{aligned}$$

For Counting 3 in the case of bottomonium decays $\bar{A}_R$ and $\bar{B}_R$ are given by Eqs. (6.38) and (6.39) respectively. For charmonium decays, we have

$$\begin{aligned}
\bar{A}^{\rm charm}_{R_3} &= \bar{A}^i_{p^4} + \bar{A}^f_{p^4} + \bar{A}^i_{V_{\rm Coul.}} + \bar{A}^f_{V_{\rm Coul.}} + \bar{A}^i_{V^{\rm EST}_{(1/m)}} + \bar{A}^f_{V^{\rm EST}_{(1/m)}} + \bar{A}^i_{V^{\rm EST}_{L^2}} + \bar{A}^f_{V_{L^2}} \\
&+ \bar{A}^i_{V^{\rm EST}_{LS}} + \bar{A}^f_{V_{LS}} + \bar{A}^i_{(2),3} + \bar{A}^f_{(2),3} + \bar{A}^{if}_{(2),3}, \qquad (6.42) \\
\bar{B}^{\rm charm}_{R_3} &= \bar{A}^i_{V^{\rm EST}_{(1/m)}} + \bar{A}^f_{V^{\rm EST}_{(1/m)}} + \bar{A}^i_{V_{\rm Coul.}} + \bar{A}^f_{V_{\rm Coul.}}. \qquad (6.43)
\end{aligned}$$

The explicit expression of each A^S_P amplitude will be given in terms of the integrals I_N defined in Eq. (6.17) together with the following definitions:

$$\begin{aligned}
I_{Log}(nL, n'L') &\equiv \int_0^\infty dr\, y_{n'L'}(r) y_{nL}(r) \ln(\sqrt{\kappa} r), \qquad (6.44) \\
I^N_V(nL, n'L') &\equiv \int_0^\infty dr\, y_{n'L'}(r) y_{nL}(r) \left[V^{\rm LO}(r)\right]^N, \qquad (6.45)
\end{aligned}$$

where y_{nL} are the reduced radial wavefunctions obtained after solving the Schrödinger equation for the LO potential, i.e., $R_{nL}(r) = y_{nL}(r)/r$. In the following we will drop the index (0) of the LO eigenvalues; it should be understood that in each counting the eigenvalues E_{nL} are obtained after solving the Schödinger equation with the corresponding LO potential.

Considering $n\,^{2S+1}P_J \to n'\,^{2S+1}S_1$ decays for the momentum-dependent amplitudes, we get

$$\bar{A}^i_{p^4} = -\frac{1}{4m}\sum_{m\neq n}\frac{-(E_{n1}+E_{m1})I^1_V(n1,m1)+I^2_V(n1,m1)}{E_{n1}-E_{m1}}\frac{I_3(m1,n'0)}{I_3(n1,n'0)}, \tag{6.46}$$

$$\bar{A}^f_{p^4} = -\frac{1}{4m}\sum_{m\neq n'}\frac{-(E_{m0}+E_{n'0})I^1_V(m0,n'0)+I^2_V(m0,n'0)}{E_{n'0}-E_{m0}}\frac{I_3(n1,m0)}{I_3(n1,n'0)}, \tag{6.47}$$

$$\bar{A}^i_{V_{p^2}} = -\frac{C_F a}{2m}\sum_{m\neq n}\frac{(E_{n1}+E_{m1})I_1(n1,m1)+2C_F a I_0(n1,m1)}{E_{n1}-E_{m1}}\frac{I_3(m1,n'0)}{I_3(n1,n'0)}, \tag{6.48}$$

$$\bar{A}^f_{V_{p^2}} = -\frac{C_F a}{2m}\sum_{m\neq n'}\frac{(E_{n0}+E_{m0})I_1(m0,n'0)+2C_F a I_0(m0,n'0)}{E_{n'0}-E_{m0}}\frac{I_3(n1,m0)}{I_3(n1,n'0)}. \tag{6.49}$$

For $S=0$ all the spin-dependent amplitudes cancel. For $S=1$, we get

$$\bar{A}^i_{V^{\rm pert.}_{LS}} = \frac{3C_F a}{2m^2}\left[\frac{J(J+1)}{2}-2\right]\sum_{m\neq n}\frac{I_{-1}(n1,m1)}{E_{n1}-E_{m1}}\frac{I_3(m1,n'0)}{I_3(n1,n'0)}, \tag{6.50}$$

$$\bar{A}^i_{V^{\rm EST}_{LS}} = -\frac{\kappa}{2m^2}\left[\frac{J(J+1)}{2}-2\right]\sum_{m\neq n}\frac{I_1(n1,m1)}{E_{n1}-E_{m1}}\frac{I_3(m1,n'0)}{I_3(n1,n'0)}, \tag{6.51}$$

$$\bar{A}^f_{V_{LS}} = 0, \tag{6.52}$$

$$\bar{A}^i_{V_{S^2}} = 0, \tag{6.53}$$

$$\bar{A}^f_{V_{S^2}} = \frac{2C_F a}{3m^2}\sum_{m\neq n'}\frac{R_{n'0}(0)R_{m0}(0)}{E_{n'0}-E_{m0}}\frac{I_3(n1,m0)}{I_3(n1,n'0)}, \tag{6.54}$$

$$\bar{A}^i_{V_{S_{12}}} = -\frac{C_F a}{2m^2}F_{S_{12}}(J)\sum_{m\neq n}\frac{I_{-1}(n1,m1)}{E_{n1}-E_{m1}}\frac{I_3(m1,n'0)}{I_3(n1,n'0)}, \tag{6.55}$$

$$\bar{A}^f_{V_{S_{12}}} = -\frac{C_F a}{2m^2}F_{S_{12}}(J)\sum_{m\neq n'-2}\frac{I_{-1}(m2,n'0)}{E_{n'0}-E_{m2}}\frac{I_3(n1,m2)}{I_3(n1,n'0)}, \tag{6.56}$$

where $F_{S_{12}}(0)=2$, $F_{S_{12}}(1)=-1$, $F_{S_{12}}(2)=1/5$.

For the momentum-independent, spin-independent, amplitudes we obtain

$$\bar{A}^i_{V_{\rm Coul.}} = -C_F a \sum_{m\neq n} \frac{I_1(n1,m1)}{E_{n1}-E_{m1}} \frac{I_3(m1,n'0)}{I_3(n1,n'0)}, \tag{6.57}$$

$$\bar{A}^f_{V_{\rm Coul.}} = -C_F a \sum_{m\neq n'} \frac{I_1(m0,n'0)}{E_{n'0}-E_{m0}} \frac{I_3(n1,m0)}{I_3(n1,n'0)}, \tag{6.58}$$

$$\bar{A}^i_{V^{\rm EST}_{(1/m)}} = \frac{2\kappa}{\pi m} \sum_{m\neq n} \frac{I_{Log}(n1,m1)}{E_{n1}-E_{m1}} \frac{I_3(m1,n'0)}{I_3(n1,n'0)}, \tag{6.59}$$

$$\bar{A}^i_{V^{\rm pert.}_{(1/m)}} = -\frac{C_F C_A a^2}{2m} \sum_{m\neq n} \frac{I_0(n1,m1)}{E_{n1}-E_{m1}} \frac{I_3(m1,n'0)}{I_3(n1,n'0)}, \tag{6.60}$$

$$\bar{A}^f_{V^{\rm EST}_{(1/m)}} = \frac{2\kappa}{\pi m} \sum_{m\neq n'} \frac{I_{Log}(m0,n'0)}{E_{n'0}-E_{m0}} \frac{I_3(n1,m0)}{I_3(n1,n'0)}, \tag{6.61}$$

$$\bar{A}^f_{V^{\rm pert.}_{(1/m)}} = -\frac{C_F C_A a^2}{2m} \sum_{m\neq n'} \frac{I_0(m0,n'0)}{E_{n'0}-E_{m0}} \frac{I_3(n1,m0)}{I_3(n1,n'0)}, \tag{6.62}$$

$$\bar{A}^i_{V^{\rm EST}_{(1/m^2)}} = -\frac{9\zeta_3\kappa^2}{2\pi^3 m^2} \sum_{m\neq n} \frac{I_3(n1,m1)}{E_{n1}-E_{m1}} \frac{I_3(m1,n'0)}{I_3(n1,n'0)}, \tag{6.63}$$

$$\bar{A}^i_{V_{\delta(r)}} = 0, \tag{6.64}$$

$$\bar{A}^f_{V_{\delta(r)}} = \frac{C_F a}{4m^2} \sum_{m\neq n'} \frac{R_{n'0}(0)R_{m0}(0)}{E_{n'0}-E_{m0}} \frac{I_3(n1,m0)}{I_3(n1,n'0)}, \tag{6.65}$$

$$\bar{A}^f_{V^{\rm EST}_{(1/m^2)}} = -\frac{9\zeta_3\kappa^2}{2\pi^3 m^2} \sum_{m\neq n'} \frac{I_3(m0,n'0)}{E_{n'0}-E_{m0}} \frac{I_3(n1,m0)}{I_3(n1,n'0)}, \tag{6.66}$$

$$\bar{A}^i_{V^{\rm pert.}_{L^2}} = \frac{C_F a}{m^2} \sum_{m\neq n} \frac{I_{-1}(n1,m1)}{E_{n1}-E_{m1}} \frac{I_3(m1,n'0)}{I_3(n1,n'0)}, \tag{6.67}$$

$$\bar{A}^i_{V^{\rm EST}_{L^2}} = -\frac{\kappa}{3m^2} \sum_{m\neq n} \frac{I_1(n1,m1)}{E_{n1}-E_{m1}} \frac{I_3(m1,n'0)}{I_3(n1,n'0)}, \tag{6.68}$$

$$\bar{A}^f_{V_{L^2}} = 0. \tag{6.69}$$

For the second order corrections due to the NLO potential, we obtain

$$\begin{aligned}\bar{A}^{i}_{(2),c} &= \sum_{\check{m}\neq n}\sum_{\widetilde{m}\neq n}\frac{I_c^{\rm NLO}(\check{m}1,\widetilde{m}1)I_c^{\rm NLO}(\widetilde{m}1,n1)}{(E_{n1}-E_{\check{m}1})(E_{n1}-E_{\widetilde{m}1})}\frac{I_3(\check{m}1,n'0)}{I_3(n1,n'0)}\\ &- \sum_{\check{m}\neq n}\frac{I_c^{\rm NLO}(n1,n1)I_c^{\rm NLO}(\check{m}1,n1)}{(E_{n1}-E_{\check{m}1})^2}\frac{I_3(\check{m}1,n'0)}{I_3(n1,n'0)}\\ &- \frac{1}{2}\sum_{\check{m}\neq n}\frac{I_c^{\rm NLO}(n1,\check{m}1)I_c^{\rm NLO}(\check{m}1,n1)}{(E_{n1}-E_{\check{m}1})^2},\end{aligned} \tag{6.70}$$

$$\begin{aligned}\bar{A}^{f}_{(2),c} &= \sum_{\check{m}\neq n}\sum_{\widetilde{m}\neq n}\frac{I_c^{\rm NLO}(\check{m}0,\widetilde{m}0)I_c^{\rm NLO}(\widetilde{m}0,n'0)}{(E_{n'0}-E_{\check{m}0})(E_{n'0}-E_{\widetilde{m}0})}\frac{I_3(n1,\check{m}0)}{I_3(n1,n'0)}\\ &- \sum_{\check{m}\neq n}\frac{I_c^{\rm NLO}(n'0,n'0)I_c^{\rm NLO}(\check{m}0,n'0)}{(E_{n'0}-E_{\check{m}0})^2}\frac{I_3(n1,\check{m}0)}{I_3(n1,n'0)}\\ &- \frac{1}{2}\sum_{\check{m}\neq n}\frac{I_c^{\rm NLO}(n'0,\check{m}0)I_c^{\rm NLO}(\check{m}0,n'0)}{(E_{n'0}-E_{\check{m}0})^2},\end{aligned} \tag{6.71}$$

$$\bar{A}^{if}_{(2),c} = \sum_{\check{m}\neq n}\sum_{\widetilde{m}\neq n}\frac{I_c^{\rm NLO}(n'0,\check{m}0)I_c^{\rm NLO}(\widetilde{m}1,n1)}{(E_{n'0}-E_{\check{m}0})(E_{n1}-E_{\widetilde{m}0})}\frac{I_3(\widetilde{m}1,\check{m}0)}{I_3(n1,n'0)}, \tag{6.72}$$

where, for Counting c, the integrals $I_c^{\rm NLO}$ are given by

$$I_1^{\rm NLO}(nL,n'L') = \frac{2\kappa}{\pi m}I_{Log}(nL,n'L'), \tag{6.73}$$

$$I_2^{\rm NLO}(nL,n'L') = \frac{2\kappa}{\pi m}I_{Log}(nL,n'L') - \frac{C_FC_Aa^2}{2m}I_0(nL,n'L'), \tag{6.74}$$

$$I_3^{\rm NLO}(nL,n'L') = \frac{2\kappa}{\pi m}I_{Log}(nL,n'L') - C_FaI_1(nL,n'L'). \tag{6.75}$$

In the case of the $n\,^{2S+1}S_1 \to n'\,^{2S+1}P'_J$ transitions ($n > n'$) the amplitudes correspond to Eqs. (6.46)-(6.72) with $n \leftrightarrow n'$, which is equivalent to exchanging $A^i \leftrightarrow A^f$.
The results of the evaluation of $\delta\Gamma_{H\to H'\gamma}$ and $R_{H\to H'\gamma}$, and therefore the decay rates, are presented in Chapter 8. Details about the numerical evaluation of the relevant formulas are given in Chapter 7.

6.2 Experimental results overview

The experimental landscape of the quarkonium radiative decays has changed dramatically in recent years and it has the prospect to experience further change in the near future.

Experiments like BES, BELLE, BaBar and CLEO have improved the available data in many of the radiative decays, measuring some of them for the first time. Regarding the E1 decays, among the most important results we have:

- The first observation of the $h_c(1P) \to \eta_c(1S)\gamma$ decay reported by the BESIII experiment in [84].

- The first observation of the equivalent bottomonium decay, $h_b(1P) \to \eta_b(1S)\gamma$, reported by the BaBar and BELLE collaborations in [85] and [86] respectively.

- The improved measurements of some of the $\chi_{bJ}(nP) \to \Upsilon\gamma(mS)$ decays reported by the BaBar collaboration in [87].

- The first observation of the $\chi_{bJ}(3P) \to \Upsilon(3S)\gamma$ decay reported by LHCb in [88].

- The measurement of the charmonium $J/\psi, \psi(2S) \to \chi_c(1S)\gamma$ decay branching ratios reported by BELLE in [89].

- A recent improvement in the measurement of the $h_b(1P) \to \eta_b(1S)\gamma$ branching ratio reported by BELLE in [90].

Also we can add to this list the recent estimation of the upper limit for the total width of the $\chi_{b0}(1P)$ state reported by BELLE in [91]. This result is not strictly related to the E1 decay, however, combining our result for the $\chi_{b0}(1P) \to \Upsilon(1S)\gamma$ decay rate and the experimental value of the corresponding branching fraction (see next section), we will be able to estimate the total width of the initial state; the results of this evaluation are given in Chapter 9.
Regarding the M1 decays, the list may be extended by:

- The first observation of the $\Upsilon(2S) \to \eta_b(1S)\gamma$ decay made by BaBar [92]

- The first observation of the $\Upsilon(3S) \to \eta_b(1S)\gamma$ decay made by CLEO [93].

- The measurement of the upper limits of the $\psi(3770) \to \eta_c(1S, 2S)$ branching ratio, which has been reported by BESIII in [94].

Other radiative decays of charmonium have been recently reported by BESIII in [95].
To these experimental results we may add lattice studies of the M1 $J/\psi \to \eta_c(1S)\gamma$, $\eta_c(2S) \to J/\psi\gamma$ and E1 $h_c(1P) \to \eta_c(1S)\gamma$ decays carried out in [96] and [97] and of the M1 $\Upsilon(2S) \to \eta_b(1S)\gamma$ decay performed in [98]. New developments in the evaluation of charmonium radiative transitions on the lattice have been recently reported in [99].
In what is left of this section, we proceed to give the relevant experimental values of the E1 decays that we will use to compare our final results later in Chapter 9.

6.2.1 E1 decays in the PDG

Since many of the experimental results for the radiative transitions have been incorporated into the PDG averages [78], we will use the PDG as our main source of experimental data. In Tables 6.1 and 6.2, we show values quoted in the (by the time of writing) latest PDG report for the E1 branching ratios of bottomonium and charmonium decays respectively. When available, we also quote the PDG value for the total width of the initial state.
In Table 6.3, we display the PDG averages of the total width of the $\eta_b(2S)$ and $\eta_c(2S)$ states. In Chapter 9 we will use these values to estimate the branching ratios of the $\eta_b(2S) \to h_b(1P)$ and $\eta_c(2S) \to h_c(1P)$ decays.

Transition	Γ_H	$\Gamma_{H\to H'\gamma}/\Gamma_H$
$h_b(1P) \to \eta_b(1S)\gamma$	NA	$0.49^{+0.08}_{-0.07}$
$h_b(2P) \to \eta_b(1S)\gamma$	NA	0.22 ± 0.05
$h_b(2P) \to \eta_b(2S)\gamma$	NA	0.48 ± 0.13
$\chi_{b0}(1P) \to \Upsilon(1S)\gamma$	NA	$(1.76 \pm 0.35)\%$
$\chi_{b1}(1P) \to \Upsilon(1S)\gamma$	NA	0.339 ± 0.022
$\chi_{b2}(1P) \to \Upsilon(1S)\gamma$	NA	0.191 ± 0.012
$\chi_{b0}(2P) \to \Upsilon(1S)\gamma$	NA	$(9 \pm 6) \times 10^{-3}$
$\chi_{b1}(2P) \to \Upsilon(1S)\gamma$	NA	$(9.2 \pm 0.8)\%$
$\chi_{b2}(2P) \to \Upsilon(1S)\gamma$	NA	$(7.0 \pm 0.7)\%$
$\chi_{b0}(2P) \to \Upsilon(2S)\gamma$	NA	$(4.6 \pm 2.1)\%$
$\chi_{b1}(2P) \to \Upsilon(2S)\gamma$	NA	0.199 ± 0.019
$\chi_{b2}(2P) \to \Upsilon(2S)\gamma$	NA	0.106 ± 0.026
$\Upsilon(2S) \to \chi_{b0}(1P)\gamma$	31.98 ± 2.63 [keV]	$(3.8 \pm 0.4)\%$
$\Upsilon(2S) \to \chi_{b1}(1P)\gamma$	31.98 ± 2.63 [keV]	$(6.9 \pm 0.4)\%$
$\Upsilon(2S) \to \chi_{b2}(1P)\gamma$	31.98 ± 2.63 [keV]	$(7.15 \pm 0.35)\%$
$\Upsilon(3S) \to \chi_{b0}(1P)\gamma$	20.32 ± 1.85 [keV]	$(2.7 \pm 0.4) \times 10^{-3}$
$\Upsilon(3S) \to \chi_{b1}(1P)\gamma$	20.32 ± 1.85 [keV]	$(9 \pm 5) \times 10^{-4}$
$\Upsilon(3S) \to \chi_{b2}(1P)\gamma$	20.32 ± 1.85 [keV]	$(9.9 \pm 1.3) \times 10^{-3}$
$\Upsilon(3S) \to \chi_{b0}(2P)\gamma$	20.32 ± 1.85 [keV]	$(5.9 \pm 0.6)\%$
$\Upsilon(3S) \to \chi_{b1}(2P)\gamma$	20.32 ± 1.85 [keV]	0.126 ± 0.012
$\Upsilon(3S) \to \chi_{b2}(2P)\gamma$	20.32 ± 1.85 [keV]	0.131 ± 0.016

Table 6.1: Experimental data of bottomonium E1 decays available in the PDG [78]. The total width of the initial state and the branching fraction of the corresponding decay are labeled as Γ_H and $\Gamma_{H\to H'\gamma}/\Gamma_H$ respectively.

Transition	Γ_H	$\Gamma_{H\to H'\gamma}/\Gamma_H$
$h_c(1P) \to \eta_c(1S)\gamma$	$0.7 + 0.4\,[\mathrm{MeV}]$	0.51 ± 0.06
$\chi_{c0}(1P) \to J/\psi\gamma$	$10.5 \pm 0.6\,[\mathrm{MeV}]$	$(1.27 \pm 0.06) \times 10^{-2}$
$\chi_{c1}(1P) \to J/\psi\gamma$	$0.84 \pm 0.04\,[\mathrm{MeV}]$	0.339 ± 0.012
$\chi_{c2}(1P) \to J/\psi\gamma$	$1.93 \pm 0.11\,[\mathrm{MeV}]$	0.192 ± 0.007
$\psi(2S) \to \chi_{c0}(1P)\gamma$	$298 \pm 8\,[\mathrm{keV}]$	$(9.99 \pm 0.27) \times 10^{-2}$
$\psi(2S) \to \chi_{c1}(1P)\gamma$	$298 \pm 8\,[\mathrm{keV}]$	$(9.55 \pm 0.31) \times 10^{-2}$
$\psi(2S) \to \chi_{c2}(1P)\gamma$	$298 \pm 8\,[\mathrm{keV}]$	$(9.11 \pm 0.31) \times 10^{-2}$

Table 6.2: Experimental data of charmonium E1 decays available in the PDG [78], values as in Table 6.1.

State	Γ_H [MeV] (exp.)
$\eta_b(2S)$	< 24
$\eta_c(2S)$	$11.3^{+3.2}_{-2.9}$

Table 6.3: PDG values for the total width of the bottomonium and charmonium $2S$ spin singlets.

6.2.2 Other E1 experimental results

We close this chapter by presenting some of the experimental measurements of E1 decays that have not been incorporated (by the time of writing) to the PDG. The BaBar E1 results reported in [87] are presented in Tables 6.4 - 6.6 as they were presented in that paper, that is, separating the values of the branching fractions obtained from the study of different decay chains. In Table 6.7 we show the result for the $h_c \to \eta_c\gamma$ branching fraction recently reported by the BELLE experiment [90].

Transition	$\Gamma_{H\to H'\gamma}/\Gamma_H$ (exp.)
$\chi_{b0}(1P) \to \Upsilon(1S)\gamma$	0.0206 ± 0.0032
$\chi_{b1}(1P) \to \Upsilon(1S)\gamma$	0.367 ± 0.024
$\chi_{b2}(1P) \to \Upsilon(1S)\gamma$	0.187 ± 0.011
$\Upsilon(2S) \to \chi_{b0}(1P)\gamma$	0.046 ± 0.010
$\Upsilon(2S) \to \chi_{b1}(1P)\gamma$	0.075 ± 0.0054
$\Upsilon(2S) \to \chi_{b2}(1P)\gamma$	0.0706 ± 0.0051

Table 6.4: Branching fractions of E1 bottomonium decays obtained by BaBar from the analysis of the $2S \to 1P \to 1S$ decay chain, for details see [87].

Transition	$\Gamma_{H\to H'\gamma}/\Gamma_H$ (exp.)
$\chi_{b0}(2P) \to \Upsilon(2S)\gamma$	0.0131 ± 0.003
$\chi_{b1}(2P) \to \Upsilon(2S)\gamma$	0.211 ± 0.025
$\chi_{b2}(2P) \to \Upsilon(2S)\gamma$	0.09 ± 0.017
$\Upsilon(3S) \to \chi_{b0}(2P)\gamma$	0.046 ± 0.017
$\Upsilon(3S) \to \chi_{b1}(2P)\gamma$	0.145 ± 0.022
$\Upsilon(3S) \to \chi_{b2}(2P)\gamma$	0.12 ± 0.02

Table 6.5: Branching fractions of E1 bottomonium decays obtained by BaBar from the analysis of the $3S \to 2P \to 2S$ decay chain, for details see [87].

Transition	$\Gamma_{H\to H'\gamma}/\Gamma_H$ (exp.)
$\chi_{b0}(2P) \to \Upsilon(1S)\gamma$	0.0037 ± 0.0017
$\chi_{b1}(2P) \to \Upsilon(1S)\gamma$	0.1078 ± 0.0094
$\chi_{b2}(2P) \to \Upsilon(1S)\gamma$	0.061 ± 0.0069
$\Upsilon(3S) \to \chi_{b0}(2P)\gamma$	0.022 ± 0.016
$\Upsilon(3S) \to \chi_{b1}(2P)\gamma$	0.141 ± 0.014
$\Upsilon(3S) \to \chi_{b2}(2P)\gamma$	0.119 ± 0.014

Table 6.6: Branching fractions of E1 bottomonium decays obtained by BaBar from the analysis of the $3S \to 2P \to 1S$ decay chain, for details see [87].

Transition	$\Gamma_{H\to H'\gamma}/\Gamma_H$ (exp.)
$1^1P_1 \to 1^1S_0\gamma$	0.56 ± 0.09

Table 6.7: Branching fraction of the $h_b \to \eta_b\gamma$ decay reported by BELLE in [90].

Chapter 7

Tools and methods for numerical analysis

In this chapter we briefly review the tools and methods used in the numerical evaluations presented in this thesis. We separate the tools between *primary* and *custom*. The first ones are libraries with a focus on general applications, while the custom tools are the collection of functions developed specifically for the fitting of the $Q\bar{Q}$ potential parameters (Chapter 5) and the evaluation of the E1 decay rates. We close the chapter giving details about the methods used to carry out the numerical evaluations.

7.1 Primary Tools

Python and IPython

`Python` [100] is a general purpose high-level programing language, its design emphasizes code readability meaning that, generally, code written to perform a given task can be understood easier when written in `Python` than when written in other languages. Usually this also means that one needs to write fewer lines of code to implement an equivalent function. Since it is a high-level language, CPU-intensive tasks like numerical calculations under-perform in `Python` when compared to lower-level languages like `C` or `Fortran`. There are various approaches to overcome this problem, one of them is to use wrappers to embed lower-level functions within `Python` code[1].
One of the popular applications of `Python` is as a scripting language, that is, for writing files (scripts) that contain a set of function definitions and a list of commands that can be executed later in a `Python` interpreter. `Python` can also be used within an interactive environment called *console*, in which variables and functions can be defined and executed *on-the-fly*, however, these definitions are lost once the console session is closed.
The interactive environment of the console is useful for quick evaluations or to test new functions, whereas scripts are useful to store functions and instructions that need to be

[1] A popular alternative to the use of wrappers is `Cython` in which, as in lower-level languages, one needs to define variable types, for more information about `Cython` see [101].

called several times. An environment that mixes features of these two frameworks is the *notebook*. The specific notebook environment we have used is called `IPython`[2] [102, 103]; it allows the execution of blocks of code in an interactive way as in the console, but additionally, as the scripts, the notebook file can be stored for later execution.
In recent years `Python` has become one of the most popular scientific scripting languages; the integration of `IPython` with libraries like `NumPy` and `SciPy` (see below) provides a powerful and flexible alternative to commercial software like `Mathematica`, `Matlab` or `Maple`.

NumPy

`NumPy` [104] is an extension to the `Python` language that adds support for the manipulation of large multi-dimensional arrays and matrices, together with a large library of high-level mathematical functions that can operate on these arrays. In our calculations we have used `NumPy` extensively to compute and store the wavefunctions that result from solving the Schrödinger equation numerically. For more info about `NumPy`, see [105].

SciPy and Matplotlib

`SciPy` [106] is an open source `Python` library that contains, among others, modules for optimization, linear algebra, integration, interpolation, special functions and differential equation solvers. The library is extensive, here we will just review the three functions to which we will refer later:

- `scipy.integrate.simps`: this function takes as input an array of the type $[f(x_i), \cdots, f(x_f)]$ and returns the value of the integral $\int_{x_i}^{x_f} f(x)dx$ calculated using the Simpson rule for numerical integration [107].

- `scipy.optimize.fsolve`: it returns the roots of the set of (non-linear) equations defined by $F_i(x) = 0$ given a starting estimate. It corresponds to a wrapper of the `Fortran MINPACK hybrd` [108] and `hybrj` [109] routines, which are based on the Powell method for the solution of non-linear systems [110].

- `scipy.optimize.curve_fit`: it uses non-linear least squares to fit a function to data. Internally it corresponds to an implementation of the Levenberg-Marquardt algorithm [111]. From its output the standard deviation of the fitted parameters can be calculated.

The source code of the implementation of these functions can be directly checked from the `SciPy` website [106]. Together with these functions we have `Matplotlib` [112], that is the plotting library of `SciPy`. It integrates seamlessly with `NumPy` and `SciPy` and it can be integrated in `IPython` to generate and display plots within notebooks. All the plots of this thesis have been generated using Matplotlib.

[2] Now known as the `Jupyter` notebook.

SClib

As we mentioned, embedding code written in other languages is a common approach to boost the speed of `Python` applications. Several alternatives exist to achieve this, such as, `CFFI` [113], `SWIG` [114], `weave` [115], and the aforementioned `Cython`, among others. In our evaluations we used `SClib` [116], a wrapper originally developed for engineering applications [117] but later extended to more general purposes. The aim of `SClib` is to integrate `C` code into a `Python` environment minimizing the intervention of the code. It works mapping `Python` data to `C` compatible data and provides a way to call functions in shared libraries; a schematic explanation of the `SClib` workflow is shown in Fig. 7.3. More details and examples of the usage of `SClib` can be found in [116], the source code is available for download from [118] and [119].

7.2 Custom tools

SChroe.py

There are plenty of scripts/programs that can numerically solve the Schrödinger equation in different contexts. In the context of bound states, the Mathematica script presented in [120] has been a popular choice for some time because it can be easily integrated with the built-in Mathematica functions to manipulate the wavefunctions, however, for numeric-intensive calculations this purely high-level approach presents a very poor performance. In order to perform the calculations in which we need to numerically solve the Schrödinger equation, we have ported the algorithm[3] of [120] to a `Python` script to which we will refer as `SChroe.py`. The first approach we tried was to write a pure `Python` implementation of the algorithm used in [120]; this results in an almost one-to-one correspondence with `SChroe.py` with the main difference being that, while in [120] the resulting wavefunctions are `Mathematica` interpolating functions, in `SChroe.py` these are discrete `NumPy` arrays, so we can profit from the `NumPy` and `SciPy` libraries to manipulate them. Even though `Python` is also a high-level language like Mathematica, this simpler approach results in a 4X speed-up. The reason is that `Mathematica` loops, on which the solution algorithm relies, have a very poor performance. A better Mathematica implementation would require to be written using the built-in Mathematica differential equation solvers, however, in that case we would lose full control over the method, since we are unable to see how these solvers are implemented. These short-comings, poor performance and loses of control, motivate us to abandon the use of `Mathematica` altogether.

[3] This algorithm is known as the *shooting method*, we have outlined it in Appendix E.

n	`schroe.nb` [120]	`SChroe.py` (`Python`)	`SChroe.py` (`SClib`)
1	98.88	25.46	0.66
2	124.14	30.95	0.75
3	135.68	35.32	0.84
21	370.0	88.04	1.99

Table 7.1: Time in seconds taken to compute the eigenvalues and reduced wavefunctions for the potential of Eq. (5.16). The column `Python` corresponds to the implementation of the algorithm in `Python` without `SClib`. All the scripts were tested using the same parameters in the same machine, a notebook with a 2.4 Ghz core i5 processor (dual core) and 8 GB of RAM.

For the fitting of the parameters of the $Q\bar{Q}$ potential presented in Chapter 5, it was necessary to get even higher boosts in speed. We achieved this using `SClib` for porting our `Python` implementation of the script specified in [120] to low-level `C` code but keeping the `Python` interface. As in the pure `Python` implementation, in the `C` flavor of the script the resulting wavefunctions are also `NumPy` arrays, so we can still profit from the functions of the `NumPy` and `SciPy` libraries to manipulate them. The net speed-boost of the `C` version of `SChroe.py` compared to its `Mathematica` counterpart is of more than two orders of magnitude. A basic benchmark comparing the script of [120] with the two versions of `SChroe.py` is shown in Table 7.1.
As a form of summary, Fig. 7.1 presents the full framework in which we have performed the numerical analysis. It shows an example of the usage of the `C` flavor of `SChroe.py` together with `NumPy`, `SciPy` and Matplotlib functions embedded within an `IPython` notebook.

7.3 Methods

7.3.1 Parameter fitting

We already stated in Chapter 5 that the parameters obtained from considering the phenomenology input come from solving four equations of the form

$$M_{\text{theo}}(n\,^{2S+1}L_J; a, \kappa, m) - M_{\text{exp}}(n\,^{2S+1}L_J) = 0, \tag{7.1}$$

for four different quarkonium states $n\,^{2S+1}L_J$, where M_{theo} corresponds to

$$\begin{aligned} M(n\,^{2S+1}L_J) &= 2m_{c,b} + E^{(0)}_{nl} + \langle nl|V^{\text{NLO}}(r)|nl\rangle + \sum_{m\neq n}^{\infty} \frac{|\langle nl|V^{\text{NLO}}(r)|ml\rangle|^2}{E^{(0)}_{nl} - E^{(0)}_{ml}} \\ &+ \langle nljs|V^{\text{NNLO}}(r)|nljs\rangle, \end{aligned} \tag{7.2}$$

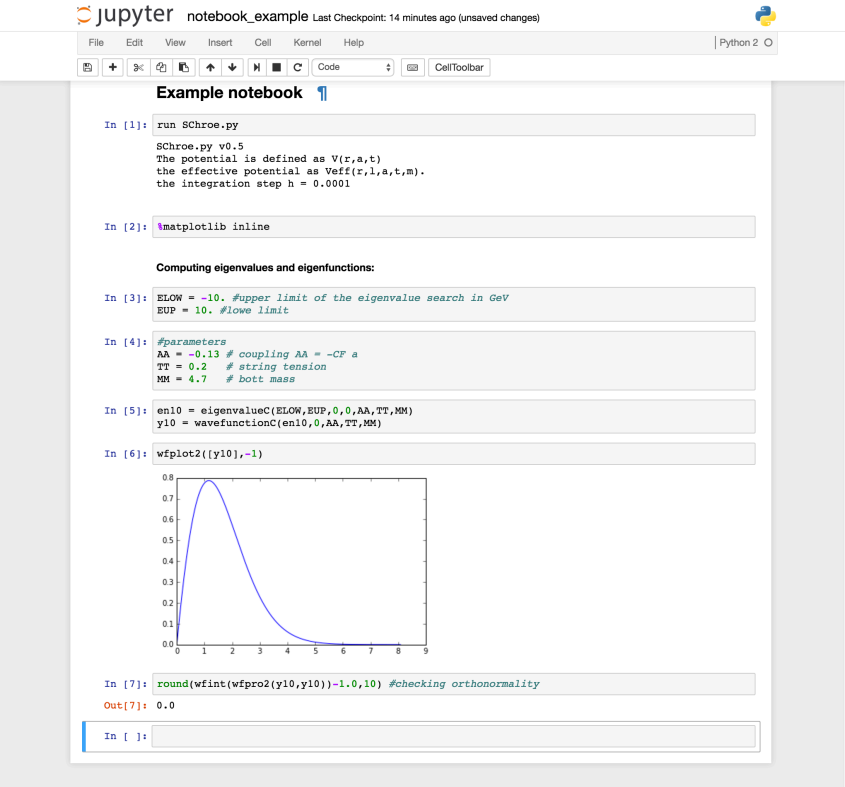

Figure 7.1: The `IPython` notebook (now called `Jupyter`) running the `SChroe.py` script.

for each of the countings, and M_{exp} is a fixed value taken from the PDG report. From a programing point of view, we see that for each probe set of parameters we need to solve the Schrödinger equation for the V^{LO} potential and then evaluate Eq. (7.2) with the resulting eigenvalues and eigenfunctions.

In our implementation, in each call to M_{theo} we use the functions of `SChroe.py` and `SClib` to solve the Schrödinger equation and the other integrations in Eq. (7.2). In order to speed up this evaluation, the sum of the second order correction is evaluated in parallel at the `C` level using `POSIX threads` [121]. The system of equations (7.1) is defined at the `Python` level; this allows us to use the `SciPy` function `fsolve` to solve it. The initial guesses for the parameters required by `fsolve` are $a \sim 0.2$, $\kappa \sim 0.2$, $m_b \sim 4.5\,\text{GeV}$, $m_c \sim 1.2\,\text{GeV}$. These values are motivated by the known values of their physical equivalents determined by experiment, lattice and perturbative calculations. We do not impose a special constraint on the parameters other than the coupling parameter a must satisfy $0 < a < 1$. A simplified diagram of the workflow of a call to `fsolve` and the subsequent call to M_{theo} is shown in Fig. 7.3.

For speed and simplicity, we have fixed the number of terms of the sum in M_{theo} to 20. We have checked that the inclusion of further terms (up to 100) does not affect our final results for the decay rates, although it may alter the value of the parameters beyond the

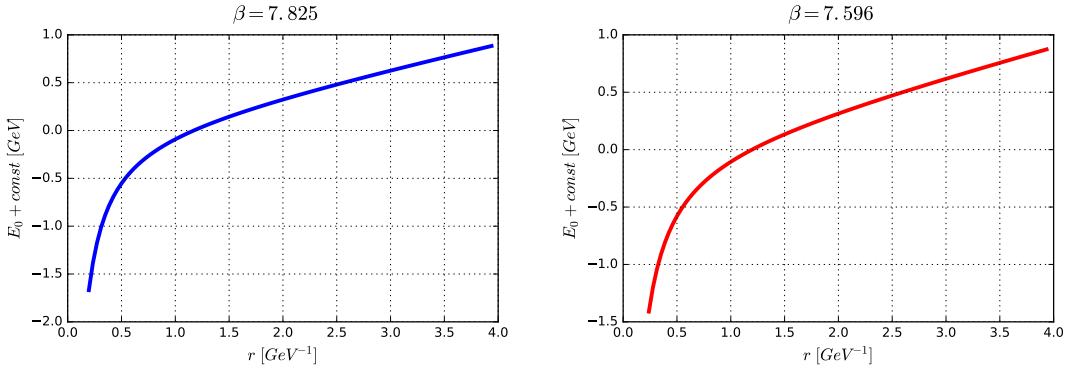

Figure 7.2: Fitted curves from the data of the two lattice spacings showed in Fig. 5.1. We impose a cut-off on the data at $r/r_1 = 2.5$ which is equivalent to $r_{\text{max.}} \approx 4\,[\text{GeV}^{-1}]$ in physical units. The value of $r_{\text{max.}}$ is around $1\,[\text{GeV}^{-1}]$ larger than the $1P$ charmonium state, which is the larger system we are considering in the evaluation of the decay rates.

precision we have quoted in the tables of Chapter 5 and Appendix D.

For the lattice input we use the `curve_fit` function of `SciPy` to fix the parameters a and κ of the $V^{(0)}$ potential in Eq. (5.16). For the two data sets displayed in Fig. 5.1 the fitted curves are displayed in Fig. 7.2. The method to fix the masses was outlined in Chapter 5. From the point of view of the numerical methods, it basically consists in several calls to the `fsolve` function to solve Eq. (7.1) in order to find the mass parameter. For this purpose we have used a simplified version of the same method used in the fitting with phenomenology input.

7.3.2 Evaluation of the amplitudes

The evaluation of the amplitudes in Eqs. (6.46)-(6.72) together with the other NLO corrections in Eqs. (6.26)-(6.29) and the LO decay rates given in Eqs. (6.13)-(6.15) has been performed entirely in `Python`. The numerical integrations are carried out using the aforementioned `integrate.simps` function. The evaluation of the sums can easily be parallelized, so we can considerably speed up the calculation. Due to memory constraints we restrict the number of terms in the sums of all the amplitudes to 20. In the case of the first order corrections, Eqs. (6.46)-(6.56), the effect of adding terms beyond the twentieth leads to a variation of, at most, order 10^{-4} in the value of each amplitude. As we will see in the next chapter, this variation is at least two orders of magnitude smaller than the other relativistic uncertainties we will consider in the decay rates.
In the case of the evaluation of the second order corrections in Eqs. (6.70)-(6.72), except for two cases, they show mostly the same convergence behavior as the first order corrections. The first exception is the evaluation of the $\bar{A}^f_{(2),3}$ amplitude, Eq. (6.71), for which the uncertainty originated from cutting the series (for $\widetilde{m}$ and $\check{m}$) at the twentieth term is at most of order 10^{-3}. The other exception is the evaluation of the same correction

adopting Counting 2, $\bar{A}^f_{(2),2}$, where the effect of adding further terms may have an impact of, at most, order 10^{-2} in the value of the correction. These slower convergences originate from the presence of terms proportional to $1/r$ and $1/r^2$ in the NLO potential of Countings 3 and 2 respectively. Although these effects are larger than in the evaluation of the first order corrections, we will see in the next chapter that they still may be *absorbed* within other uncertainties.

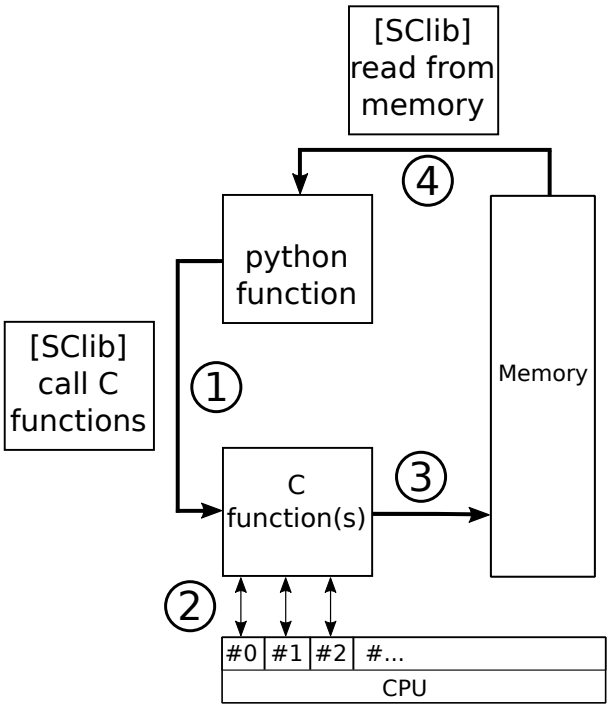

Figure 7.3: Simplified workflow of the execution of a `Python` script using `SClib` to call `C` functions: (1) `C` functions available in a `.so` file are called within a `Python` environment; (2) the computing-intensive task is performed using low level `C` code; (3) the results are stored in memory; (4) `SClib` allows these results to be read back into the `Python` environment. In the case of the parameter fitting, the `SciPy` function `fsolve` calls a definition of the system of equations (7.1), also implemented in `Python`, with some probe parameters; in the first call these correspond to the initial guesses of the values. Then, within the `Python` script, we call the `C`-defined M^{theo} function (Eq. (7.2)), which internally incorporates the Schrödinger equation solver (see Appendix E). The perturbative sum in M^{theo} can be parallelized, so on a machine with many cores the computation is performed faster. The resulting values of M^{theo} corresponding to the probe parameters are written to memory, where they can be accessed by the `fsolve` function controlling the solution algorithm.

Chapter 8

Evaluation of the E1 decay I: Method and partial results

Having spent most of the previous chapters introducing the framework of our evaluations, in this chapter we present the numerical results of the computation of the E1 decay rates. We also present the error assignment and a discussion of our results.

8.1 Evaluation method and error

Considering both fitting inputs, we evaluate the $O(v^2)$ E1 decay rates (Eq. (6.18)) using the randomly-generated set of parameters described in Sec. 5.4; the central value of each decay rate corresponds to the mean of these values. We will also present results for the leading order decay rates given in Eqs. (6.13)-(6.15).
To compute the photon energy, we evaluate Eq. (6.4) using the central values of the PDG masses (given in Appendix C) except in the case of transitions involving the bottomonium $3\,^3P_1$ state ($\chi_{b1}(3P)$), in which case we use the value reported by the LHCb experiment [88][1]

$$M_{\chi_{b1}(3P)} = 10511.3 \pm 1.7 \pm 2.5 \text{ [MeV]}. \tag{8.1}$$

For the error we consider a combination of the sensitivity to the change of parameters with an estimation of the size of the neglected relativistic corrections (see below). Explicitly, the uncertainty ϵ assigned to each decay rate is given by

$$\epsilon \equiv \sqrt{\epsilon_{\text{par}}^2 + \epsilon_{\text{rel}}^2}, \tag{8.2}$$

where in the case of the LO rates ϵ_{par} is given by the standard deviation of the sixteen values obtained after the evaluation of Eqs. (6.13)-(6.15) and ϵ_{rel} is given by the mean

[1] While writing this thesis, the PDG online tables were updated including a value for the mass of the $\chi_{b1}(3P)$ state. The current value quoted in the PDG is 10512.3 ± 2.3 [MeV], which is calculated using the values reported by the LHCb experiment in Refs. [88] and [122]. The difference of order 10^{-3} [GeV] between the value of Eq. (8.1) and the current PDG average is negligible in the evaluation of the E1 decay rates.

of the values obtained after computing

$$\Gamma' = \Gamma^{LO}_{H\to H'\gamma} \times K_{\rm LO} \times v(a,\kappa,m), \tag{8.3}$$

where $v(a,\kappa,m)$ is the quark-antiquark relative velocity given by

$$v(a,\kappa,m) = \left[\frac{1}{m}\left(E^{(0)}_{nl} - \langle nl|V^{LO}|nl\rangle\right)\right]^{1/2}. \tag{8.4}$$

The dependence on a,κ and m must be understood as implicit in the eigenvalues $E^{(0)}_{nl}$ and eigenfunctions $|nl\rangle = \phi^{(0)}_H(\mathbf{r})$ that result from solving the Schrödinger equation (6.8). The constant K_{LO} accounts for the non-parametric (no counting-dependent) coefficients of the next relativistic correction; we expect this factor to scale *naturally* in order not to break the counting of the relativistic expansion. The estimation of the relativistic error comes from the fact that we know the parametric size of the leading amplitude in $R_{H\to H'\gamma}$, which in the case of Countings 1 and 3 includes corrections that are v-suppressed with respect to the LO. We proceed similarly for Counting 2, although in this case the ordering of the potential is in powers of $1/m$.
For what we call the NLO rates, $\epsilon_{\rm par}$ is given by the standard deviation of the values obtained after evaluating Eq. (6.18). In analogy to the LO case, $\epsilon_{\rm rel}$ is the mean of the values obtained after computing

$$\Gamma'' = \Gamma^{LO}_{H\to H'\gamma} \times K_{\rm NLO} \times v(a,\kappa,m)^3 \tag{8.5}$$

for each random set.
The shape of Γ'' comes from considering the size of the next relativistic correction when the relativistic expansion of the rates is factorized as in Eq. (6.18). From [21] we know that the next relativistic correction to Eq. (6.18) will be at least v^3-suppressed with respect to the leading order[2]. For all the following evaluations we set $K_{\rm LO} = K_{\rm NLO} = 1$.
Now we can check the justification given at the end of the previous chapter for truncating the perturbative series of the amplitudes at twenty terms. The minimum value of v^3 in charmonium and bottomonium scale as[3]

$$v_c^3 \sim 0.1,$$
$$v_b^3 \sim 0.01,$$

so a deviation of order 10^{-3} in the amplitudes that contribute to $R_{H\to H'\gamma}$ is still negligible compared to the error coming from neglecting the $O(v^3)$ relativistic correction to the decay rates. In the case of the (Counting 2) $\bar{A}^f_{(2),2}$ amplitude (Eq. (6.71)), where such effects may reach order 10^{-2}, they are comparable to the relativistic uncertainty in the

[2] In [21] it was noticed that some of the (neglected) extra-suppressed operators of the pNRQCD Lagrangian responsible for the E1 transitions were of relative order v^3.

[3] These values depend on the counting/input combination; we have taken the minimum value for both charmonium and bottomonium $1P$ states.

case of bottomonium decays. For the evaluations using the phenomenology input, they still may be neglected in the total uncertainty calculation, since in these evaluations the relativistic uncertainty ϵ_{rel} is always at least one order of magnitude smaller than the uncertainty due to the change of the parameters ϵ_{par}. This scaling between ϵ_{rel} and ϵ_{par} is not replicated in the evaluations performed using Counting 2 with lattice input, where both uncertainties are comparable. In this case it may be necessary to either evaluate the series for the $\bar{A}^f_{(2),2}$ correction until it reaches the desired convergence or re-estimate the relativistic error to account for the effect of the neglected terms, i.e. to consider a value of K_{NLO} larger than one. Later we will see that these changes will no be necessary, since the evaluations using Counting 2 with lattice input will not contribute to our final results for the decay rates.

8.2 Results

Restricted to transitions in which the initial state lies below threshold, we evaluate all the decay rates for which we have experimental input for the initial and final state masses. In Tables 8.1 and 8.3 we show the results for decay rates using the phenomenology input for charmonium and bottomonium decays respectively, the analogous results using the lattice input are shown in Tables 8.2 and 8.4. An expanded version of these tables, where the energy of the photon and the individual contributions of ϵ_{par} and ϵ_{rel} are also displayed, can be found in Appendix F.

	Counting 1				Counting 2				Counting 3			
Decay	$\overline{\Gamma^{\text{LO}}}$ [keV]	$\overline{R}$	$\overline{\delta\Gamma}$	Γ^{NLO} [keV]	$\overline{\Gamma^{\text{LO}}}$ [keV]	$\overline{R}$	$\overline{\delta\Gamma}$	Γ^{NLO} [keV]	$\overline{\Gamma^{\text{LO}}}$ [keV]	$\overline{R}$	$\overline{\delta\Gamma}$	Γ^{NLO} [keV]
$1\,^1P_1 \to 1\,^1S_0\gamma$	1066 ± 564	-0.56	-0.112	363 ± 283	1071 ± 568	-0.53	-0.112	393 ± 254	1346 ± 793	-0.41	-0.131	620 ± 278
$2\,^1S_0 \to 1\,^1P_1\gamma$	0.13 ± 0.08	-0.16	0.0003	0.11 ± 0.04	0.13 ± 0.08	-0.17	0.0003	0.11 ± 0.04	0.05 ± 0.03	-0.33	0.014	0.03 ± 0.01
$1\,^3P_0 \to 1\,^3S_1\gamma$	237 ± 126	-0.31	-0.273	100 ± 50	238 ± 126	-0.29	-0.275	106 ± 46	299 ± 176	-0.41	-0.314	84 ± 67
$1\,^3P_1 \to 1\,^3S_1\gamma$	503 ± 266	-0.39	-0.155	235 ± 111	505 ± 268	-0.36	-0.156	247 ± 101	635 ± 374	-0.41	-0.178	264 ± 136
$1\,^3P_2 \to 1\,^3S_1\gamma$	676 ± 358	-0.38	-0.028	408 ± 136	679 ± 360	-0.35	-0.028	426 ± 126	853 ± 503	-0.41	-0.037	473 ± 175
$2\,^3S_1 \to 1\,^3P_0\gamma$	61 ± 35	-0.57	-0.057	23 ± 14	61 ± 35	-0.57	-0.056	23 ± 14	60 ± 39	-0.23	-0.013	45 ± 17
$2\,^3S_1 \to 1\,^3P_1\gamma$	51 ± 29	-0.31	0.012	36 ± 10	51 ± 30	-0.31	0.013	36 ± 10	50 ± 33	-0.28	0.042	38 ± 14
$2\,^3S_1 \to 1\,^3P_2\gamma$	35 ± 20	-0.27	-0.011	26 ± 7	35 ± 20	-0.27	-0.011	25 ± 7	35 ± 23	-0.38	-0.039	20 ± 10

Table 8.1: Summary of the evaluation of the charmonium decays using the phenomenology input. The central values and their respective uncertainties were calculated as explained in Sec. 8.1. For later reference we have included the average values of the $R_{H\to H'\gamma}$ and $\delta\Gamma_{H\to H'\gamma}$ corrections; these values are calculated as the mean of the values obtained with each of the sixteen random sets of parameters of each counting.

	Counting 1				Counting 2				Counting 3			
Decay	$\overline{\Gamma^{\rm LO}}$ [keV]	$\overline{R}$	$\overline{\delta\Gamma}$	$\overline{\Gamma^{\rm NLO}}$ [keV]	$\overline{\Gamma^{\rm LO}}$ [keV]	$\overline{R}$	$\overline{\delta\Gamma}$	$\overline{\Gamma^{\rm NLO}}$ [keV]	$\overline{\Gamma^{\rm LO}}$ [keV]	$\overline{R}$	$\overline{\delta\Gamma}$	$\overline{\Gamma^{\rm NLO}}$ [keV]
$1\,^1P_1 \to 1\,^1S_0\gamma$	904 ± 524	-0.86	-0.108	30 ± 183	881 ± 496	-0.82	-0.105	65 ± 162	1323 ± 784	-0.43	-0.13	581 ± 273
$2\,^1S_0 \to 1\,^1P_1\gamma$	0.14 ± 0.09	-0.14	-0.004	0.12 ± 0.04	0.14 ± 0.09	-0.14	-0.004	0.12 ± 0.03	0.05 ± 0.03	-0.34	0.014	0.03 ± 0.01
$1\,^3P_0 \to 1\,^3S_1\gamma$	201 ± 117	-0.43	-0.37	38 ± 40	196 ± 110	-0.4	-0.356	47 ± 35	294 ± 174	-0.43	-0.315	73 ± 62
$1\,^3P_1 \to 1\,^3S_1\gamma$	427 ± 247	-0.56	-0.201	102 ± 84	416 ± 234	-0.52	-0.194	118 ± 75	624 ± 370	-0.43	-0.179	242 ± 129
$1\,^3P_2 \to 1\,^3S_1\gamma$	573 ± 332	-0.54	0.021	278 ± 111	559 ± 314	-0.5	0.019	288 ± 101	839 ± 497	-0.43	-0.036	450 ± 175
$2\,^3S_1 \to 1\,^3P_0\gamma$	56 ± 35	-0.8	-0.043	9 ± 15	55 ± 34	-0.79	-0.045	9 ± 13	59 ± 38	-0.24	-0.011	44 ± 16
$2\,^3S_1 \to 1\,^3P_1\gamma$	47 ± 30	-0.4	0.02	29 ± 12	46 ± 29	-0.4	0.018	29 ± 11	50 ± 32	-0.29	0.042	37 ± 14
$2\,^3S_1 \to 1\,^3P_2\gamma$	33 ± 21	-0.29	-0.015	22 ± 8	32 ± 20	-0.29	-0.014	22 ± 8	34 ± 22	-0.39	-0.039	19 ± 9

Table 8.2: Summary of the evaluation of the charmonium decays using the lattice input, values computed as in Table 8.1.

	Counting 1				Counting 2				Counting 3			
Decay	$\overline{\Gamma^{\rm LO}}$ [keV]	$\overline{R}$	$\overline{\delta\Gamma}$	$\overline{\Gamma^{\rm NLO}}$ [keV]	$\overline{\Gamma^{\rm LO}}$ [keV]	$\overline{R}$	$\overline{\delta\Gamma}$	$\overline{\Gamma^{\rm NLO}}$ [keV]	$\overline{\Gamma^{\rm LO}}$ [keV]	$\overline{R}$	$\overline{\delta\Gamma}$	$\overline{\Gamma^{\rm NLO}}$ [keV]
$1\,^1P_1 \to 1\,^1S_0\gamma$	78 ± 26	-0.46	-0.034	44 ± 29	79 ± 24	-0.42	-0.035	46 ± 25	64 ± 20	-0.65	-0.032	24 ± 24
$2\,^1P_1 \to 1\,^1S_0\gamma$	10 ± 4	0.5	0.132	17 ± 6	10 ± 4	0.68	0.131	19 ± 7	11 ± 4	0.64	0.082	18 ± 6
$2\,^1P_1 \to 2\,^1S_0\gamma$	28 ± 9	-0.45	-0.024	16 ± 9	29 ± 9	-0.41	-0.025	17 ± 8	24 ± 8	-0.63	-0.023	9 ± 8
$2\,^1S_0 \to 1\,^1P_1\gamma$	0.07 ± 0.03	0.02	-0.001	0.07 ± 0.02	0.07 ± 0.03	0.01	-0.001	0.07 ± 0.02	0.07 ± 0.03	0.04	-0.002	0.08 ± 0.03
$1\,^3P_0 \to 1\,^3S_1\gamma$	40 ± 13	-0.24	-0.051	30 ± 12	41 ± 13	-0.21	-0.05	31 ± 10	33 ± 10	-0.33	-0.07	21 ± 9
$1\,^3P_1 \to 1\,^3S_1\gamma$	51 ± 17	-0.28	-0.037	36 ± 16	51 ± 16	-0.26	-0.037	37 ± 13	42 ± 13	-0.39	-0.046	25 ± 12
$1\,^3P_2 \to 1\,^3S_1\gamma$	58 ± 19	-0.28	-0.022	42 ± 17	58 ± 18	-0.26	-0.022	43 ± 15	47 ± 15	-0.4	-0.01	30 ± 13
$2\,^3P_0 \to 1\,^3S_1\gamma$	7 ± 3	-0.21	-0.046	6 ± 1	7 ± 3	-0.04	-0.049	7 ± 3	8 ± 3	-0.23	-0.122	5 ± 2
$2\,^3P_1 \to 1\,^3S_1\gamma$	8 ± 3	0.04	0.038	9 ± 2	8 ± 3	0.22	0.036	10 ± 4	8 ± 3	0.07	-0.022	9 ± 3
$2\,^3P_2 \to 1\,^3S_1\gamma$	9 ± 3	0.28	0.186	13 ± 4	9 ± 3	0.46	0.186	14 ± 5	9 ± 4	0.37	0.161	14 ± 4
$2\,^3P_0 \to 2\,^3S_1\gamma$	15 ± 5	-0.17	-0.031	12 ± 3	15 ± 5	-0.14	-0.031	12 ± 3	13 ± 4	-0.23	-0.038	9 ± 2
$2\,^3P_1 \to 2\,^3S_1\gamma$	20 ± 7	-0.24	-0.025	15 ± 5	20 ± 6	-0.21	-0.025	16 ± 4	17 ± 5	-0.33	-0.028	11 ± 4
$2\,^3P_2 \to 2\,^3S_1\gamma$	24 ± 8	-0.29	-0.019	17 ± 6	24 ± 7	-0.26	-0.019	18 ± 5	20 ± 6	-0.4	-0.013	12 ± 5
$3\,^3P_1 \to 1\,^3S_1\gamma$	3 ± 2	0.18	-0.041	4 ± 2	3 ± 2	0.04	-0.044	3 ± 2	4 ± 2	0.28	-0.103	5 ± 3
$3\,^3P_1 \to 2\,^3S_1\gamma$	3 ± 1	-0.002	0.095	3.3 ± 1.0	3 ± 1	-0.13	0.093	2.8 ± 0.7	3 ± 1	0.04	0.047	3 ± 1
$3\,^3P_1 \to 3\,^3S_1\gamma$	11 ± 4	-0.22	-0.021	8 ± 2	11 ± 4	-0.21	-0.021	8 ± 2	9 ± 3	-0.3	-0.023	6 ± 2
$2\,^3S_1 \to 1\,^3P_0\gamma$	1.6 ± 0.4	-0.2	-0.013	1.3 ± 0.1	1.6 ± 0.4	-0.21	-0.013	1.2 ± 0.1	1.5 ± 0.4	-0.25	-0.012	1.1 ± 0.1
$2\,^3S_1 \to 1\,^3P_1\gamma$	2.4 ± 0.7	-0.09	-0.002	2.2 ± 0.2	2.4 ± 0.7	-0.1	-0.002	2.2 ± 0.2	2.2 ± 0.7	-0.1	-0.001	2.0 ± 0.2
$2\,^3S_1 \to 1\,^3P_2\gamma$	2.5 ± 0.7	-0.04	0.004	2.4 ± 0.2	2.5 ± 0.7	-0.05	0.004	2.4 ± 0.2	2.3 ± 0.7	-0.03	0.004	2.2 ± 0.3
$3\,^3S_1 \to 2\,^3P_0\gamma$	1.6 ± 0.5	-0.2	-0.007	1.3 ± 0.1	1.6 ± 0.5	-0.21	-0.007	1.3 ± 0.1	1.5 ± 0.5	-0.23	-0.005	1.1 ± 0.2
$3\,^3S_1 \to 2\,^3P_1\gamma$	2.6 ± 0.8	-0.07	-0.0005	2.4 ± 0.2	2.6 ± 0.8	-0.09	-0.0003	2.4 ± 0.2	2.4 ± 0.8	-0.08	0.0006	2.2 ± 0.3
$3\,^3S_1 \to 2\,^3P_2\gamma$	2.8 ± 0.8	-0.02	-0.0001	2.8 ± 0.3	2.8 ± 0.9	-0.04	-0.0002	2.7 ± 0.3	2.6 ± 0.9	-0.01	-0.0004	2.6 ± 0.4

Table 8.3: Summary of the evaluation of the bottomonium decays using the phenomenology input, values computed as in Table 8.1.

	Counting 1				Counting 2			
Decay	$\overline{\Gamma^{\rm LO}}$ [keV]	$\overline{R}$	$\overline{\delta\Gamma}$	$\overline{\Gamma^{\rm NLO}}$ [keV]	$\overline{\Gamma^{\rm LO}}$ [keV]	$\overline{R}$	$\overline{\delta\Gamma}$	$\overline{\Gamma^{\rm NLO}}$ [keV]
$1\,^1P_1 \to 1\,^1S_0\gamma$	56 ± 15	-0.8	-0.031	10 ± 5	57 ± 15	-0.77	-0.031	11 ± 5
$2\,^1P_1 \to 1\,^1S_0\gamma$	12 ± 3	0.8	0.051	22 ± 1	12 ± 4	1.24	0.052	27 ± 2
$2\,^1P_1 \to 2\,^1S_0\gamma$	22 ± 7	-0.77	-0.022	5 ± 2	22 ± 7	-0.72	-0.023	6 ± 2
$2\,^1S_0 \to 1\,^1P_1\gamma$	0.08 ± 0.02	0.07	-0.002	0.087 ± 0.004	0.08 ± 0.02	0.05	-0.002	0.085 ± 0.005
$1\,^3P_0 \to 1\,^3S_1\gamma$	29 ± 8	-0.4	-0.081	15 ± 2	29 ± 8	-0.37	-0.082	16 ± 2
$1\,^3P_1 \to 1\,^3S_1\gamma$	36 ± 10	-0.48	-0.051	17 ± 3	37 ± 10	-0.45	-0.051	18 ± 3
$1\,^3P_2 \to 1\,^3S_1\gamma$	41 ± 11	-0.48	-0.003	21 ± 3	42 ± 11	-0.46	-0.003	23 ± 3
$2\,^3P_0 \to 1\,^3S_1\gamma$	9 ± 3	-0.2	-0.149	5.6 ± 0.3	9 ± 3	0.23	-0.151	9.2 ± 1.0
$2\,^3P_1 \to 1\,^3S_1\gamma$	9 ± 3	0.14	-0.05	10.1 ± 0.5	9 ± 3	0.57	-0.051	14 ± 1
$2\,^3P_2 \to 1\,^3S_1\gamma$	10 ± 3	0.48	0.134	15.7 ± 0.8	10 ± 3	0.92	0.136	20 ± 2
$2\,^3P_0 \to 2\,^3S_1\gamma$	11 ± 3	-0.27	-0.041	7.9 ± 0.7	12 ± 3	-0.22	-0.042	8.5 ± 0.6
$2\,^3P_1 \to 2\,^3S_1\gamma$	16 ± 5	-0.39	-0.029	9 ± 1	16 ± 5	-0.35	-0.029	9.7 ± 0.9
$2\,^3P_2 \to 2\,^3S_1\gamma$	18 ± 6	-0.48	-0.011	9 ± 1	18 ± 6	-0.44	-0.011	10 ± 1
$3\,^3P_1 \to 1\,^3S_1\gamma$	4 ± 1	0.41	-0.116	5.4 ± 0.5	4 ± 1	0.14	-0.118	4.3 ± 0.4
$3\,^3P_1 \to 2\,^3S_1\gamma$	3 ± 1	0.11	0.026	3.8 ± 0.2	3 ± 1	-0.2	0.026	2.7 ± 0.2
$3\,^3P_1 \to 3\,^3S_1\gamma$	9 ± 3	-0.36	-0.024	5.3 ± 0.5	9 ± 3	-0.35	-0.024	5.5 ± 0.5
$2\,^3S_1 \to 1\,^3P_0\gamma$	1.4 ± 0.4	-0.27	-0.013	1.03 ± 0.05	1.4 ± 0.4	-0.3	-0.013	0.99 ± 0.05
$2\,^3S_1 \to 1\,^3P_1\gamma$	2.2 ± 0.6	-0.11	-0.002	1.95 ± 0.08	2.2 ± 0.6	-0.13	-0.002	1.91 ± 0.08
$2\,^3S_1 \to 1\,^3P_2\gamma$	2.3 ± 0.7	-0.02	0.005	2.22 ± 0.09	2.3 ± 0.7	-0.04	0.005	2.18 ± 0.08
$3\,^3S_1 \to 2\,^3P_0\gamma$	1.5 ± 0.5	-0.25	-0.006	1.08 ± 0.06	1.5 ± 0.5	-0.29	-0.006	1.03 ± 0.06
$3\,^3S_1 \to 2\,^3P_1\gamma$	2.4 ± 0.7	-0.07	0.0001	2.2 ± 0.1	2.4 ± 0.8	-0.11	0.0002	2.12 ± 0.1
$3\,^3S_1 \to 2\,^3P_2\gamma$	2.6 ± 0.8	0.01	0.0003	2.6 ± 0.1	2.6 ± 0.8	-0.03	0.0003	2.5 ± 0.1

Table 8.4: Summary of the evaluation of the bottomonium decays using the lattice input, values computed as in Table 8.1.

8.3 Analysis

8.3.1 Bottomonium

The first conclusion that can be drawn from Tables 8.3 and 8.4 is that, as it may be expected, $R_{H\to H'\gamma}$ is the dominant correction to the decay rates. More than because it contains the contribution coming from the NLO potential, the dominance of $R_{H\to H'\gamma}$ comes from the fact that the amplitudes, although some of them are extra suppressed, may add up to make a sizeable contribution. In general, the largest contributions to $R_{H\to H'\gamma}$ are the ones coming from the $1/m$ potentials and some of the momentum-dependent potentials. In most of the evaluations, the largest momentum-dependent contribution to $R_{H\to H'\gamma}$ comes from the potential containing the $\mathbf{p}^2$ operator, which we have labeled as $\bar{A}^S_{V_{p^2}}$ in Eqs. (6.48) and (6.49) for initial and final state wavefunction corrections respectively. Each of these contributions corresponds actually to two separate series, each of them of parametric order v^2 if we adopt Countings 1 or 3. Moreover, one of these series corresponds to $2C_F/C_A \approx 0.9$ times the series of the $\bar{A}^S_{V_2^{(1/m)}}$ amplitude, which in turn is one of the largest contributions to $R_{H\to H'\gamma}$.

In Chapter 5 it was noticed that the distinction between NLO and NNLO contributions to the potential appears not to be realized numerically when comparing the expectation values of the NLO and NNLO potentials. A similar situation can be observed in the scaling of the contributions to $R_{H\to H'\gamma}$. In Table 8.5 we show the average of the NLO and other leading amplitudes that contribute to $R_{H\to H'\gamma}$ in the $1P \to 1S$ and $2P \to 1S$

decays. From the values of that table we see that some of the NNLO amplitudes, for instance $\bar{A}^f_{V^{\rm pert.}_{(1/m)}}$, are of the same order or even larger than the NLO ones. This result and the scaling of the potentials discussed in Chapter 5 suggest that, rather than separating between NLO and NNLO contributions, one may count them homogeneously. Nevertheless, it can be verified that the numerical impact of the second order contributions coming from the NLO potential is in any case small enough ($\sim 10^{-3}$) not to alter the value of the decay rates calculated with Countings 1 and 3 significantly.
The non-realization of the distinction between NLO and NNLO potentials is also replicated in the results obtained by adopting Counting 2, where to consider the $1/m$ potential as NLO appears to be arbitrary if one compares the values of the amplitudes originated from this and some of the NNLO potentials (e.g. see the values of the NLO and $\bar{A}_{V_{p^2}}$ amplitudes in Table 8.5). Notice that in this counting, however, the second order corrections coming from the NLO potentials are larger than the equivalent contributions in Countings 1 or 3.
We conclude that in our evaluations we cannot distinguish a hierarchy among the corrections to the quark-antiquark potential. However, notice that in the results obtained by adopting Countings 1 and 3, the extra-suppression of the second order corrections makes them numerically closer to an evaluation in which all corrections are considered of the same parametric size, i.e., the second order corrections due to the NLO potential in these countings are negligible.
Even if the ordering inherited from the counting (1 or 3) is not fully realized in the corrections to the decay rates, it is convenient to measure the size of the corrections in terms of their *effective scaling* with respect to the relative velocity v. Let us factorize the contributions as

$$\begin{aligned} \bar{A}_> &\equiv \alpha v, \\ \delta\Gamma &\equiv \beta v^2, \end{aligned} \tag{8.6}$$

where $\bar{A}_>$ is the amplitude with the largest contribution to $R_{H\to H'\gamma}$ in each transition regardless from which potential it originates. The values of α for the three relevant counting/input combinations are shown in Table 8.6. From these values it can be seen that, apart from the $3P \to 1S$ decay, the amplitudes contributing to $R_{H\to H'\gamma}$ scale as some value in the interval $[v_b^2, v_b]$. This is in accordance with the *ideal* realization of the counting, where the contributions to $R_{H\to H'\gamma}$ would scale at most as the relative velocity. Moreover, these values appear to support our claim that in our evaluations all corrections to the potential should be considered as scaling homogeneously. For the $3P \to 1S$ transition $\alpha \sim 2$, which still may be considered as a factor that does not break the scaling dictated by the non-relativistic expansion.

In the case of the scaling of the $\delta\Gamma_{H\to H'\gamma}$ corrections, we have that for most of the decays the scaling $\delta\Gamma_{H\to H'\gamma} \sim v^2$ appears to be an overestimation of its size, specially

Decay	Counting 1	Counting 2	Counting 3
$1P \to 1S$	$\bar{A}^f_{\rm NLO} = -0.03(4\%)$ $\bar{A}^f_{V_{p^2}} = -0.12(64\%)$ $\bar{A}^f_{V^{\rm pert.}_{(1/m)}} = -0.1(79\%)$	$\bar{A}^f_{\rm NLO} = -0.12(49\%)$ $\bar{A}^f_{V_{p^2}} = -0.11(54\%)$	$\bar{A}^f_{\rm NLO} = -0.03(8\%)$ $\bar{A}^f_{V_{p^2}} = -0.17(59\%)$ $\bar{A}^f_{V^{\rm pert.}_{(1/m)}} = -0.15(74\%)$
$2P \to 1S$	$\bar{A}^f_{\rm NLO} = 0.15(48\%)$ $\bar{A}^f_{V_{p^2}} = 0.31(23\%)$ $\bar{A}^f_{V^{\rm pert.}_{(1/m)}} = 0.22(42\%)$	$\bar{A}^f_{\rm NLO} = -0.37(11\%)$ $\bar{A}^f_{V_{p^2}} = 0.31(22\%)$	$\bar{A}^i_{\rm NLO} = 0.15(48\%)$ $\bar{A}^f_{V_{p^2}} = 0.31(23\%)$ $\bar{A}^f_{V^{\rm pert.}_{(1/m)}} = 0.22(42\%)$

Table 8.5: Mean values of the parametric NLO and other leading amplitudes that contribute to the $R_{H\to H'\gamma}$ corrections in the $1P \to 1S$ and $2P \to 1S$ bottomonium decays using phenomenology input. In Countings 1 and 3 $\bar{A}^f_{\rm NLO} = \bar{A}^f_{V^{\rm EST}_{(1/m)}}$, in Counting 2 $\bar{A}^f_{\rm NLO}$ is the sum of the two $1/m$ final wave correction amplitudes, i.e., $\bar{A}^f_{\rm NLO} = \bar{A}^f_{V^{\rm EST}_{(1/m)}} + \bar{A}^f_{V^{\rm pert.}_{(1/m)}}$. In brackets we show the relative (to the mean) value of the standard deviation of each mean amplitude.

in decays among excited states. A feature of these corrections is that in many of the evaluations, they result in a contribution that is smaller than the uncertainty associated with neglecting the $O(v^3)$ relativistic corrections (8.5). This may also be the case for some of the amplitudes that contribute to $R_{H\to H'\gamma}$, which may scale in the same way as $\delta\Gamma_{H\to H'\gamma}$ does. For clarity, we have left the tables displaying the β factors in the Appendix F.2.

Decay	Count. 1 (phen.)	Count. 1 (latt.)	Count. 3 (phen.)
$1P \to 1S$	0.4	0.7	0.6
$2S \to 1P$	0.2	0.3	0.2
$2P \to 1S$	0.8	1.2	1.0
$2P \to 2S$	0.4	0.6	0.5
$3S \to 2P$	0.2	0.3	0.2
$3P \to 1S$	1.2	1.8	1.9
$3P \to 2S$	0.7	1.1	1.5
$3P \to 3S$	0.3	0.5	0.6

Table 8.6: Values of the scaling factor α in bottomonium decays. Any value in this table that is less than one means that, in the corresponding decay, the largest amplitude that contribute to $R_{H\to H'\gamma}$ has a value that is less than a power of the relative velocity. In each counting/input combination the relative velocity has been calculated using the relevant mean values of the parameters (Tables 5.2 and 5.3).

Regarding the uncertainties, in the evaluations with phenomenology input we see that for most of the decays the relative (to $\overline{\Gamma^{\rm NLO}}$) value of $\epsilon^{\rm NLO}$ is smaller than the relative (to $\overline{\Gamma^{\rm LO}}$) value of $\epsilon^{\rm LO}$. For decays in which this does not occur[4], the origin of this behaviour can be traced down to the large dispersion among the values obtained after evaluating $R_{H\to H'\gamma}$. The source of these large dispersions are the *accidental* cancellations among the amplitudes that contribute to $R_{H\to H'\gamma}$, which occur in the evaluation with some of the parameter sets. Since the dispersion among the parameters in the lattice approach is smaller, we have that in the evaluations with lattice input only the singlet $1P\to 1S$ and $2P\to 2S$ decays present this issue. We recognize these accidental cancellations as one of the limitations of the method we have adopted for the evaluation of the rates, however, we recall that for most of the decays the total NLO uncertainty is less than 40%. Remarkable are the results for the $3S\to 2P$ transitions, where the total uncertainty is around 10%.

Although we cannot control accidental cancellations, we made sure to keep the series of the amplitudes that contribute to $R_{H\to H'\gamma}$ under control. Explicitly, we have required that all the amplitudes $\bar{A}_P^S$ in Eqs. (6.46)-(6.72) of Chapter 6 fulfill $|\bar{A}_P^S|<1$. Considering this condition, we left out a preliminary evaluation of the $3S\to 1P$ decays in which the series of some amplitudes diverges; the origin of these divergences is studied in Appendix G. Nevertheless, as it can be seen from the results for the $2\,^1P_1\to 1\,^1S_0\gamma$ bottomonium decay adopting Counting 2 with lattice input (displayed in Table 8.4), the condition that $|\bar{A}_P^S|<1$ alone does not guarantee that the absolute value of $R_{H\to H'\gamma}$ is less than one. In this case, although all amplitudes fulfill $|\bar{A}_P^S|<1$, they add up to make $|R_{H\to H'\gamma}|>1$. We have left the value of this rate in the tables as an illustration of the limitations of our method, however, this decay will not be considered in further analyses.

The incompatibility among the results for the fitting of the coupling parameter with different input and, to a lesser extent, the stress among the analogous results for the string tension (see tables in Sec. 5.4) indicate that we cannot expect agreement among the results of the evaluation of the rates with different inputs.

If we now consider the same input source, an inspection of the results with phenomenology input with Countings 1 and 3 shows that the values of the NLO decay rates are compatible within the quoted uncertainty. We recall that in the case of evaluations using the lattice input, the evaluations with Countings 1 and 3 are equivalent.

8.3.2 Charmonium

In contrast to bottomonium, in some charmonium decays[5] the relative value of the uncertainty due to the neglected relativistic corrections is larger for the NLO rates than for the LO ones. This occurs when the LO and NLO rates are such that $\Gamma^{\rm LO}\gg\Gamma^{\rm NLO}$ due to large relativistic corrections, that is, large values of $R_{H\to H'\gamma}$ and $\delta\Gamma_{H\to H'\gamma}$. Considering

[4]Five transitions in Countings 1 and 2 and eight in Counting 3. The specific transitions can be read from the tables of Appendix F.

[5]See for instance the results for the $1\,^3P_0\to 1\,^3S_1\gamma$ decay in Table F.10 of Appendix F.

Eqs. (8.3) and (8.5), we note that in these cases it may occur that $\Gamma^{\rm LO} \times v^3 \sim \Gamma^{\rm NLO}$, making the value of $\epsilon_{\rm rel}$ comparable to $\Gamma^{\rm NLO}$.
As in bottomonium, in charmonium there are also decays in which the relative value of $\epsilon^{\rm NLO}$ is larger than the relative value of $\epsilon^{\rm LO}$, but in contrast to the bottomonium case, where the larger error is always due to the sensitivity to parameters, in charmonium the dominant error may also come from neglecting the $O(v^3)$ relativistic corrections.
In general, the poor realization of the separation of scales in charmonium makes its study with non-relativistic EFTs challenging. For instance, in the case of $1P$ states adopting Counting 3, we have the following values for the scaling of increasing powers of the relative velocity

$$\begin{aligned} v_c &\sim 0.6, \\ v_c^2 &\sim 0.3, \\ v_c^3 &\sim 0.2, \\ v_c^4 &\sim 0.1. \end{aligned} \tag{8.7}$$

So if we expect that the largest amplitudes that contribute to $R_{H\to H'\gamma}$ scale like v, we have to consider that just a factor $1/3$ in front of the of sum will make it effectively scale as v^3, even if the expected scaling is fully realized in the counting-dependent coefficients, and the size of the amplitude without the factor $1/3$ is indeed v. The value v^3 is the scale we have assigned to the neglected relativistic corrections, and therefore, one of the uncertainty sources of our evaluations. Then it should not come as a surprise that many of the contributions we have computed are *absorbed* within the uncertainty, since its *effective scaling* is v^3 or smaller. Notice that from Table 8.6 it can be seen that in bottomonium the largest suppression on the leading amplitude occurs in the $3S \to 2P$ and $2S \to 1P$ decays in which the leading amplitude contributing to $R_{H\to H'\gamma}$ scales as $0.2 \times v \sim v^2$, so even in this case $R_{H\to H'\gamma}$ contains significant corrections to the decay rate.
In Table 8.7 we display the NLO and other leading contributions to $R_{H\to H'\gamma}$ of the evaluation of the $1P \to 1S$ and $2S \to 1P$ decays with phenomenology input. The effective scaling of the largest amplitude in terms of v is shown in Table 8.8 for phenomenology and lattice input. From Table 8.7 it appears as we may have left out a sizeable contribution from the $\mathbf{p}^2$-dependent potential in evaluations with Counting 3, since this amplitude is the dominant one in the evaluations with the other countings. An estimation of the size of $\bar{A}^f_{V_{p^2}}$ using the parameters of this counting shows that its effective size is v^4, therefore its contribution may be considered as *absorbed* in the uncertainty[6]. The same contribution is also useful to illustrate the problem with the *prefactors*: the global factor $C_F/2 \approx 0.67$ in front of the sum in $\bar{A}^f_{V_{p^2}}$ (Eq. (6.49)) counts as an effective extra

[6]This estimation of the size of $\bar{A}^f_{V_{p^2}}$ should be handled with care: since the values of the parameters in Counting 3 are obtained neglecting the contribution of the $\mathbf{p}^2$-dependent potential, it is not entirely consistent to evaluate this amplitude with these parameters. Our estimation of the value $\bar{A}^f_{V_{p^2}}$ assumes that the values of the parameters are not largely affected if we consider the $\mathbf{p}^2$-dependent potential in the parameter fitting.

suppression of order v, so the value of the series without this factor is actually v^3, which is precisely the scaling dictated by Counting 3. This apparent extra suppression occurs in other contributions to $R_{H\to H'\gamma}$ in charmonium and bottomonium, but because the separation of scales is badly realized, the effect of these factors in the effective scaling is more dramatic in charmonium. Moreover, the values of the effective scaling factor α displayed in Table 8.8 show that, regardless of the counting/input combination, the leading amplitude contributing to $R_{H\to H'\gamma}$ scales at most as v^3, hence the significance of our evaluation of charmonium decays is drastically reduced.
In the case of the $\delta\Gamma_{H\to H'\gamma}$ corrections, using the same factorization as in the bottomonium case, Eq. (8.6), we see that the scaling factor β is such that $|\beta| \in [0.001, 1.1]$. In this case, these corrections are significant only for $|\beta| > v$; this criterion is only fulfilled in the $1\,^3P_{J=0,1} \to 1\,^3S_1\gamma$ decays. Explicit values of β for each decay are given in Appendix F.2.

Decay	Counting 1	Counting 2	Counting 3
$1P \to 1S$	$\bar{A}^f_{\rm NLO} = -0.07(5\%)$ $\bar{A}^f_{V_{p^2}} = -0.13(49\%)$ $\bar{A}^f_{p^4} = -0.09(20\%)$	$\bar{A}^f_{\rm NLO} = -0.13(29\%)$ $\bar{A}^f_{V_{p^2}} = -0.13(43\%)$ $\bar{A}^f_{p^4} = -0.09(18\%)$	$\bar{A}^f_{\rm NLO} = -0.19(17\%)$ $\bar{A}^f_{p^4} = -0.07(17\%)$ $\bar{A}^{if}_{(2),3} = 0.04(32\%)$
$2S \to 1P$	$\bar{A}^f_{\rm NLO} = -0.09(7\%)$ $\bar{A}^f_{p^4} = -0.14(10\%)$ $\bar{A}^f_{V_{p^2}} = -0.09(36\%)$	$\bar{A}^i_{\rm NLO} = 0.11(21\%)$ $\bar{A}^f_{p^4} = -0.14(8\%)$ $\bar{A}^f_{\rm NLO} = -0.10(7\%)$	$\bar{A}^f_{\rm NLO} = -0.21(13\%)$ $\bar{A}^f_{p^4} = -0.18(17\%)$ $\bar{A}^i_{\rm NLO} = 0.21(17\%)$

Table 8.7: Mean values of the parametric NLO and other leading amplitudes that contribute to the $R_{H\to H'\gamma}$ corrections in the $1P \to 1S$ and $2S \to 1P$ charmonium decays using phenomenology input. In Counting 3 $\bar{A}^S_{\rm NLO} = \bar{A}^S_{V_{\rm Coul.}} + \bar{A}^S_{V^{\rm EST}_{(1/m)}}$, the other values as in Table 8.5.

Decay	Count. 1 (phen.)	Count. 1 (latt.)	Count. 3 (phen.)	Count. 3 (latt.)
$1P \to 1S$	0.2	0.3	0.3	0.3
$2S \to 1P$	0.1	0.2	0.3	0.4

Table 8.8: Values of the scaling factor α in charmonium decays. The values here illustrate the problem with the poorly realization of the separation of scales in charmonium. For instance, considering the powers of the velocity in Eq. (8.7), we see that for the $1P \to 1S$ decay, the effective scaling of the leading amplitude in $R_{H\to H'\gamma}$ is v^3, which is the size of the relativistic uncertainty. In each counting/input combination, the relative velocity has been calculated using the relevant mean values of the parameters (Tables 5.2 and 5.3).

With regard to the impact of the adopted power counting on the value of the decay rate, we see that when considering the same input source, the results for Countings 1 and 2 are compatible with each other within just a fraction of their respective uncertainties. This does not occur if we compare the results of Counting 1 (or 2) with the results of Counting 3. This difference can be explained by the different shape of the series for $R_{H\to H'\gamma}$ (Eqs. (6.38)-(6.43)), in fact, the variation of the values of $\delta\Gamma_{H\to H'\gamma}$ across all countings is small, which means that for the evaluation of the rate, the values of the parameters are less relevant than the shape of $R_{H\to H'\gamma}$.

8.4 Summary

It would be natural to expect the $Q\bar{Q}$ potential to have a different counting for different states, lower or excited, or at least a different counting for bottomonium and charmonium, since the nature of their physics may be different due to the different sizes of the systems. Originally, we introduced Counting 3 as a way to overcome the apparent inconsistency in the numerical results of the parameter fitting when considering the scaling of Counting 1 for the $Q\bar{Q}$ potential in bottomonium and charmonium states. However, since charmonium is larger than bottomonium, the extra v suppression in the coupling parameter for charmonium can be understood as a way to give less weight to the short distance physics within a larger system. Since the ordering of the potential for bottomonium states is the same in Countings 1 and 3, the numerical impact of changing the counting on the decay rates is small. In the case of charmonium, we have seen that the different ordering implies also a big variation in the values of the contributions to $R_{H\to H'\gamma}$, thus the variation in the final value of the rate is more pronounced.
In order to select the results for our final evaluation we make two observations. First, we have that the realization of the counting in the parameters is better accomplished in Counting 3, so, as it may be expected, it appears that to have different countings for bottomonium and charmonium systems represents a more realistic picture of the physics of the $Q\bar{Q}$ bound states. The second observation is that, as we have mentioned previously in this chapter, the distinction between NLO and NNLO contributions to $R_{H\to H'\gamma}$ appears to not be realized, so the inclusion of a second order perturbative correction coming to the NLO potential is not well justified. Nevertheless, in Counting 1 and Counting 3, the contribution of this second order correction is negligible, so the results with these countings are closer to effectively count homogeneously all the corrections to the potential. Based on these observations, in order to compute our final results in the next chapter, we will select the results corresponding to evaluations with phenomenology input adopting Counting 3 for bottomonium and charmonium decays and the results of the evaluation with lattice input using Counting 1 for bottomonium and Counting 3 for charmonium decays.
It may look like we have done some unnecessary work in evaluating the decay rates with Counting 2. However, notice that in evaluations of decays in which the second order

correction of the $1/m$ potential is small, for instance the $2S \to 1P$ decays, the main difference between Countings 1 and 2 is that in Counting 2 we are also incorporating the $1/m^2$ momentum and spin independent long-range corrections to the potential computed in Chapter 4. Our results for the parameter fitting and the evaluation of the decay rates show that the numerical impact of incorporating this contribution is small. Looking at the long-range spectrum in Figs. 4.3 and 4.4, it is not immediately obvious that the long-range $1/m^2$ corrections are negligible, moreover, these plots show that they are not negligible at all, if we just consider long-range contributions. What we have shown with the results of Counting 2 is that, using a full-range $Q\bar{Q}$ potential like the one constructed in Chapter 5 for the evaluation of the rates, the contribution of this long-range relativistic correction is negligible. Nevertheless, one could think of an alternative construction of the potential in which the long-range and short-range contributions are separated by a cut-off; in such a case, one may expect all the $1/m^2$ long-range corrections to have a sizeable numerical impact in the evaluation of the E1 decay rates.

Chapter 9

Evaluation of the E1 decay II: Final results and comparison with experiments

Based on the outcome of the previous chapter, we present here the final results of the evaluation of the E1 decay rates. We call these our primary results, since they come purely from the theoretical framework we have presented along the thesis.
Additionally we also estimate the total width of all the initial states for which the experimental value of the E1 decay branching fraction is available. We also give predictions for the branching fractions of some transitions for which only the data for the width of the initial state is available. We call these evaluations our secondary results since they depend on our theoretical predictions and experimental input. When the available data allows it, we compare our results with the experimental results from the PDG and other sources.

9.1 Primary results

9.1.1 Decay rates

As stated at the end of the previous chapter, in the case of bottomonium decays we will consider the results of adopting Counting 1 with lattice input and Counting 3 with phenomenology input. For charmonium transitions we will consider the results with phenomenology and lattice input adopting Counting 3. The central value of each rate corresponds to the average of the central values for each input. The error assigned to each decay rate corresponds to $\mathrm{Max}(\epsilon_{\mathrm{phen.}}, \epsilon_{\mathrm{latt.}})$ where $\epsilon_{\mathrm{phen.}}$ and $\epsilon_{\mathrm{latt.}}$ are the full uncertainties (Eq. (8.2)) obtained with each approach. The final results for the decay rates are shown in Tables 9.1 and 9.2 for charmonium and bottomonium respectively. Since the aim of this chapter is also to compare our results with the ones of experiments, we switch to the notation for quarkonia usually found in the experimental literature, a full translation between the spectroscopy notation we have used so far and the one used

here can be found in the tables of Appendix C.

Decay	LO [keV]	NLO [keV]
$h_c(1P) \to \eta_c(1S)\gamma$	1334 ± 793	601 ± 278
$\eta_c(2S) \to h_c(1P)\gamma$	0.05 ± 0.03	0.03 ± 0.01
$\chi_{c0}(1P) \to J/\psi\gamma$	297 ± 176	79 ± 67
$\chi_{c1}(1P) \to J/\psi\gamma$	630 ± 374	253 ± 136
$\chi_{c2}(1P) \to J/\psi\gamma$	846 ± 503	461 ± 175
$\psi(2S) \to \chi_{c0}(1P)\gamma$	59 ± 39	44 ± 17
$\psi(2S) \to \chi_{c1}(1P)\gamma$	50 ± 33	38 ± 14
$\psi(2S) \to \chi_{c2}(1P)\gamma$	34 ± 23	20 ± 10

Table 9.1: Final results for the charmonium decays.

Decay	LO [keV]	NLO [keV]
$h_b(1P) \to \eta_b(1S)\gamma$	60 ± 20	17^{+24}_{-17}
$h_b(2P) \to \eta_b(1S)\gamma$	11 ± 4	20 ± 6
$h_b(2P) \to \eta_b(2S)\gamma$	23 ± 8	7^{+8}_{-7}
$\eta_b(2S) \to h_b(1P)\gamma$	0.08 ± 0.03	0.08 ± 0.03
$\chi_{b0}(1P) \to \Upsilon(1S)\gamma$	31 ± 10	18 ± 9
$\chi_{b1}(1P) \to \Upsilon(1S)\gamma$	39 ± 13	21 ± 12
$\chi_{b2}(1P) \to \Upsilon(1S)\gamma$	44 ± 15	25 ± 13
$\chi_{b0}(2P) \to \Upsilon(1S)\gamma$	8 ± 3	5 ± 2
$\chi_{b1}(2P) \to \Upsilon(1S)\gamma$	9 ± 3	9 ± 3
$\chi_{b2}(2P) \to \Upsilon(1S)\gamma$	9 ± 4	15 ± 4
$\chi_{b0}(2P) \to \Upsilon(2S)\gamma$	12 ± 4	9 ± 2
$\chi_{b1}(2P) \to \Upsilon(2S)\gamma$	16 ± 5	10 ± 4
$\chi_{b2}(2P) \to \Upsilon(2S)\gamma$	19 ± 6	11 ± 5
$\chi_{b1}(3P) \to \Upsilon(1S)\gamma$	4 ± 2	5 ± 3
$\chi_{b1}(3P) \to \Upsilon(2S)\gamma$	3 ± 1	4 ± 1
$\chi_{b1}(3P) \to \Upsilon(3S)\gamma$	9 ± 3	6 ± 2
$\Upsilon(2S) \to \chi_{b0}(1P)\gamma$	1.4 ± 0.4	1.1 ± 0.1
$\Upsilon(2S) \to \chi_{b1}(1P)\gamma$	2.2 ± 0.7	2.0 ± 0.2
$\Upsilon(2S) \to \chi_{b2}(1P)\gamma$	2.3 ± 0.7	2.2 ± 0.3
$\Upsilon(3S) \to \chi_{b0}(2P)\gamma$	1.5 ± 0.5	1.1 ± 0.2
$\Upsilon(3S) \to \chi_{b1}(2P)\gamma$	2.4 ± 0.8	2.2 ± 0.3
$\Upsilon(3S) \to \chi_{b2}(2P)\gamma$	2.6 ± 0.9	2.6 ± 0.4

Table 9.2: Final results for the bottomonium decays.

9.1.2 Comparison with experiments

In Figs. 9.1 - 9.5 we compare our results with experimental data available from the PDG [78]. In Fig. 9.5 we also include a lattice determination of the charmonium singlet $1P \to 1S$ decay. The experimental values of the rates are calculated using the values of the branching fraction and the total width given in Sec. 6.2 assuming that the uncertainties of both quantities are not correlated. In Figs. 9.6 - 9.8 we use the branching fraction of the $\Upsilon(2S) \to \chi_{bJ}(1P)\gamma$ and $\Upsilon(3S) \to \chi_{bJ}(2P)\gamma$ decays reported by the BaBar collaboration [87] to calculate the experimental values of the decay rates. At the time of writing, these values have not been included in the PDG averages.

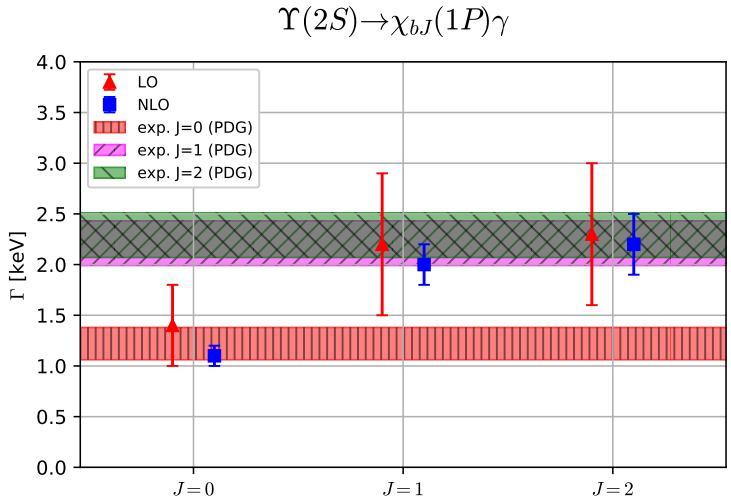

Figure 9.1: Comparison of our results for the bottomonium $\Upsilon(2S) \to \chi_{bJ}(1P)\gamma$ transition with the experiment. The experimental data (total width and branching fractions) have been taken from the PDG report [78].

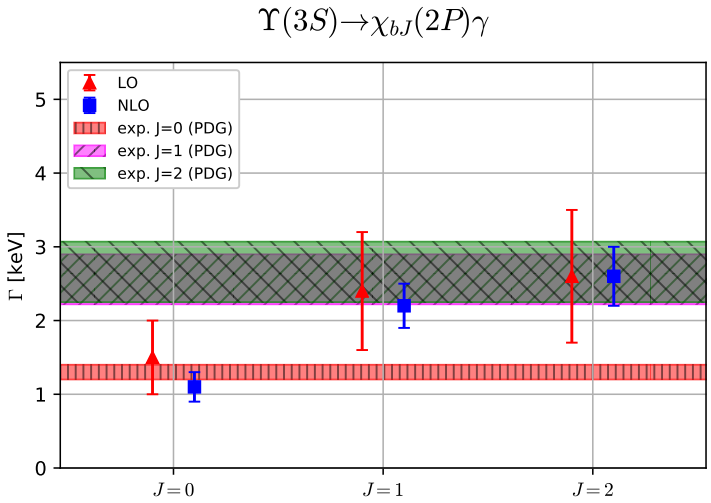

Figure 9.2: Comparison of our results for bottomonium $\Upsilon(3S) \to \chi_{bJ}(2P)\gamma$ transition with the experiment. The experimental data (total width and branching fractions) have been taken from the PDG report [78].

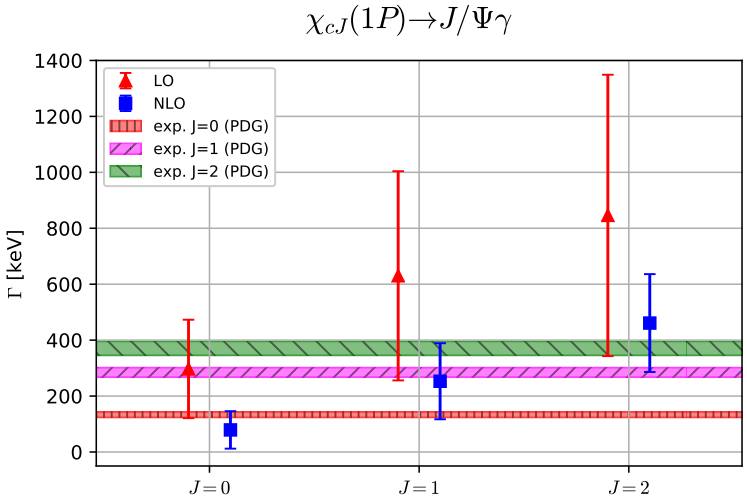

Figure 9.3: Comparison of our results for charmonium $\chi_{cJ}(1P) \to J/\psi\gamma$ transition with the experiment. The experimental data have been taken from the PDG report [78].

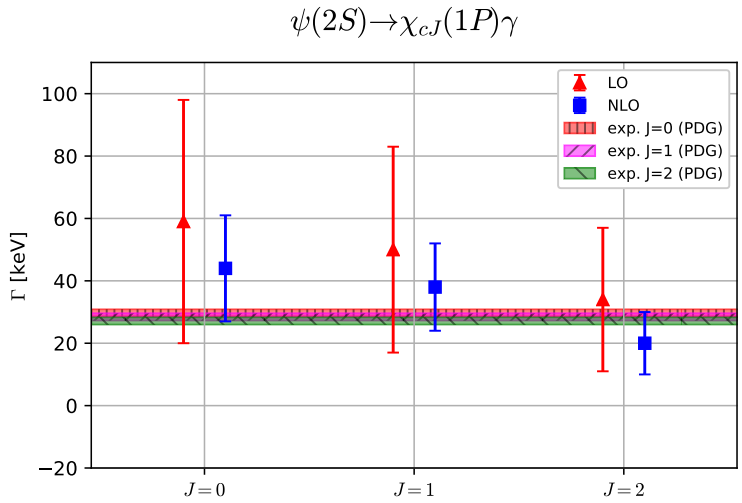

Figure 9.4: Comparison of our results for charmonium $\psi(2S) \to \chi_{cJ}(1P)\gamma$ transition with the experiment. The experimental data have been taken from the PDG report [78].

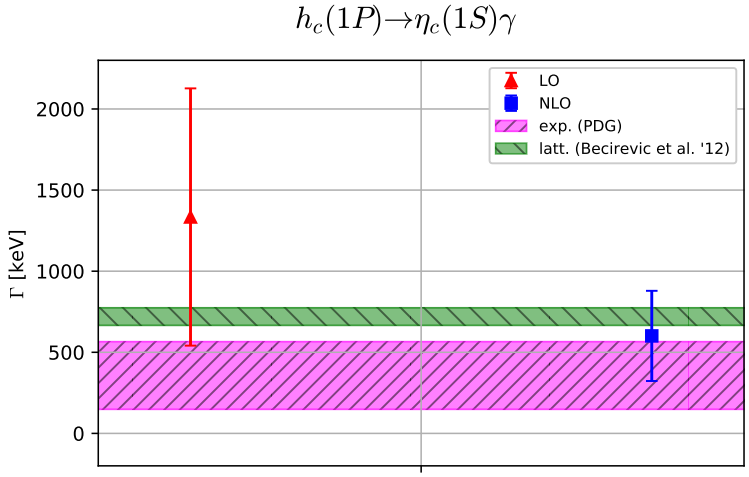

Figure 9.5: Comparison of our results for the charmonium $1P \to 1S$ singlet transition with PDG data [78] and a lattice evaluation reported in [96].

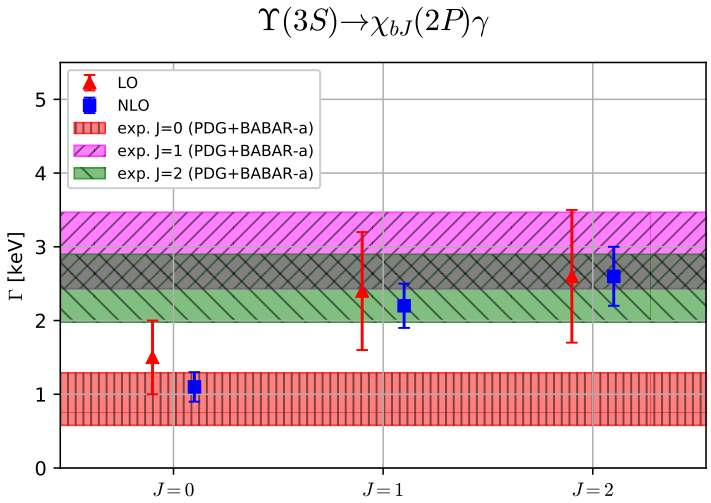

Figure 9.6: Comparison of our results for the bottomonium $\Upsilon(2S) \to \chi_{bJ}(1P)\gamma$ transition with experiment. The experimental data for the width have been taken from the PDG report [78] and the branching fractions obtained from [87] considering the decay chain $3S \to 2P \to 2S$; explicit values of both quantities are given in Sec. 6.2.

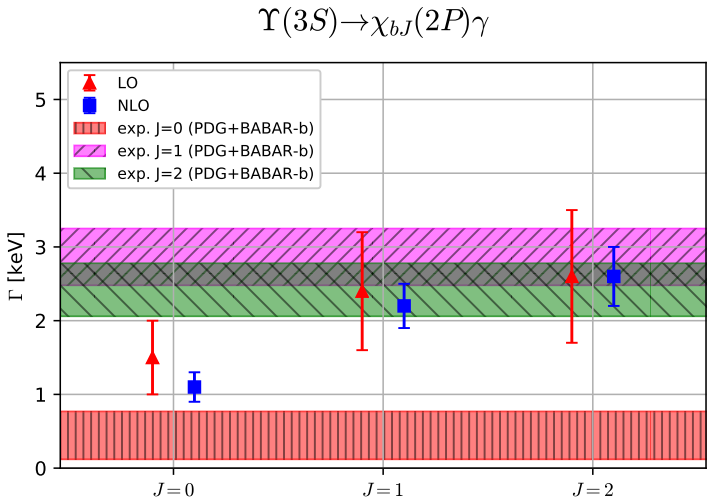

Figure 9.7: Comparison of our results for the bottomonium $\Upsilon(2S) \to \chi_{bJ}(1P)\gamma$ transition with experiment. The experimental data for the width have been taken from the PDG report [78] and the branching fractions obtained from [87] considering the decay chain $3S \to 2P \to 1S$; explicit values of both quantities are given in Sec. 6.2.

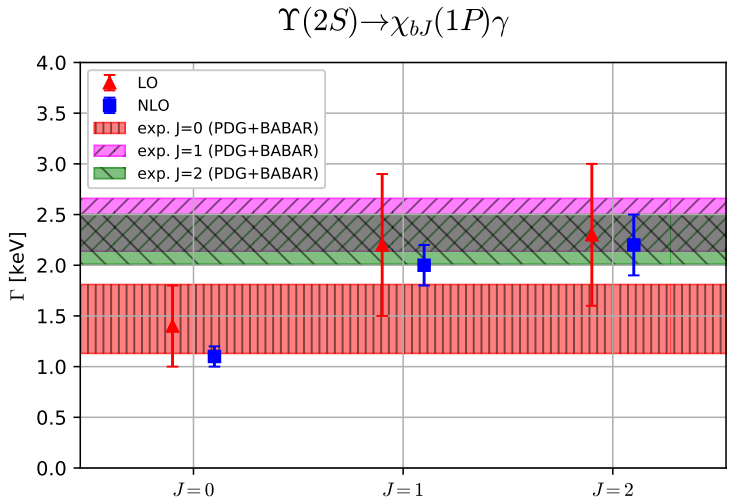

Figure 9.8: Comparison of our results for the bottomonium $\Upsilon(2S) \to \chi_{bJ}(1P)\gamma$ transition with experiment. The experimental value of the width has been taken from the PDG report [78] and the branching fractions from [87], explicit values of both quantities are given in Sec. 6.2.

9.2 Secondary results

9.2.1 Total width and branching fractions

Using experimental input of the branching fractions and our results for the decay rates we can estimate the total width of the initial states. The results for the widths using input from the PDG are presented in Tables 9.3 and 9.4 for bottomonium and charmonium states respectively. In Tables 9.5, 9.6 and 9.7 we use input from BaBar [87] to estimate the widths. In Table 9.8 we compute the total width of the $h_b(1P)$ state using the branching fraction of the $h_b(1P) \to \eta_b(1S)\gamma$ transition reported by the BELLE experiment [90]. Using the values of the widths from the PDG, in Table 9.9 we estimate the branching fraction of the singlet $2S \to 1P$ transition in bottomonium and charmonium.

State	Decay	Γ_H [keV] (theo. + exp.)	Γ_H [keV] (PDG)
$h_b(1P)$	$h_b(1P) \to \eta_b(1S)\gamma$	35 ± 35	NA
$h_b(2P)$	$h_b(2P) \to \eta_b(1S)\gamma$	91 ± 34	NA
$h_b(2P)$	$h_b(2P) \to \eta_b(2S)\gamma$	15 ± 15	NA
$\chi_{b0}(1P)$	$\chi_{b0}(1P) \to \Upsilon(1S)\gamma$	1023 ± 550	NA
$\chi_{b1}(1P)$	$\chi_{b1}(1P) \to \Upsilon(1S)\gamma$	62 ± 36	NA
$\chi_{b2}(1P)$	$\chi_{b2}(1P) \to \Upsilon(1S)\gamma$	131 ± 69	NA
$\chi_{b0}(2P)$	$\chi_{b0}(2P) \to \Upsilon(1S)\gamma$	556 ± 432	NA
$\chi_{b1}(2P)$	$\chi_{b1}(2P) \to \Upsilon(1S)\gamma$	98 ± 34	NA
$\chi_{b2}(2P)$	$\chi_{b2}(2P) \to \Upsilon(1S)\gamma$	214 ± 61	NA
$\chi_{b0}(2P)$	$\chi_{b0}(2P) \to \Upsilon(2S)\gamma$	196 ± 99	NA
$\chi_{b1}(2P)$	$\chi_{b1}(2P) \to \Upsilon(2S)\gamma$	50 ± 21	NA
$\chi_{b2}(2P)$	$\chi_{b2}(2P) \to \Upsilon(2S)\gamma$	104 ± 54	NA
$\Upsilon(2S)$	$\Upsilon(2S) \to \chi_{b0}(1P)\gamma$	29 ± 4	31.98 ± 2.63
$\Upsilon(2S)$	$\Upsilon(2S) \to \chi_{b1}(1P)\gamma$	29 ± 3	31.98 ± 2.63
$\Upsilon(2S)$	$\Upsilon(2S) \to \chi_{b2}(1P)\gamma$	31 ± 4	31.98 ± 2.63
$\Upsilon(3S)$	$\Upsilon(3S) \to \chi_{b0}(2P)\gamma$	19 ± 4	20.32 ± 1.85
$\Upsilon(3S)$	$\Upsilon(3S) \to \chi_{b1}(2P)\gamma$	17 ± 3	20.32 ± 1.85
$\Upsilon(3S)$	$\Upsilon(3S) \to \chi_{b2}(2P)\gamma$	20 ± 4	20.32 ± 1.85

Table 9.3: Estimation of the total widths of bottomonium states using PDG input for the branching fractions.

State	Decay	Γ_H [keV] (theo. + exp.)	Γ_H [keV] (PDG)
$h_c(1P)$	$h_c(1P) \to \eta_c(1S)\gamma$	1178 ± 562	700 ± 400
$\chi_{c0}(1P)$	$\chi_{c0}(1P) \to J/\psi\gamma$	6220 ± 5284	10500 ± 600
$\chi_{c1}(1P)$	$\chi_{c1}(1P) \to J/\psi\gamma$	746 ± 402	840 ± 40
$\chi_{c2}(1P)$	$\chi_{c2}(1P) \to J/\psi\gamma$	2401 ± 916	1930 ± 110
$\psi(2S)$	$\psi(2S) \to \chi_{c0}(1P)\gamma$	444 ± 172	298 ± 8
$\psi(2S)$	$\psi(2S) \to \chi_{c1}(1P)\gamma$	398 ± 147	298 ± 8
$\psi(2S)$	$\psi(2S) \to \chi_{c2}(1P)\gamma$	220 ± 110	298 ± 8

Table 9.4: Estimation of the total widths of charmonium states using PDG input for the branching fractions.

State	Decay	Γ_H [keV] (theo. + exp.)	Γ_H [keV] (PDG)
$\chi_{b0}(1P)$	$\chi_{b0}(1P) \to \Upsilon(1S)\gamma$	874 ± 457	NA
$\chi_{b1}(1P)$	$\chi_{b1}(1P) \to \Upsilon(1S)\gamma$	57 ± 33	NA
$\chi_{b2}(1P)$	$\chi_{b2}(1P) \to \Upsilon(1S)\gamma$	134 ± 70	NA
$\Upsilon(2S)$	$\Upsilon(2S) \to \chi_{b0}(1P)\gamma$	24 ± 6	NA
$\Upsilon(2S)$	$\Upsilon(2S) \to \chi_{b1}(1P)\gamma$	27 ± 3	NA
$\Upsilon(2S)$	$\Upsilon(2S) \to \chi_{b2}(1P)\gamma$	31 ± 5	NA

Table 9.5: Estimation of the total widths of bottomonium states using input from the BaBar experiment for the branching fractions. The branching fractions used to compute the values in this table were obtained by BaBar analysing the $2S \to 1P \to 1S$ decay process, for more details see [87].

State	Decay	Γ_H [keV] (theo. + exp.)	Γ_H [keV] (PDG)
$\chi_{b0}(2P)$	$\chi_{b0}(2P) \to \Upsilon(2S)\gamma$	687 ± 219	NA
$\chi_{b1}(2P)$	$\chi_{b1}(2P) \to \Upsilon(2S)\gamma$	47 ± 20	NA
$\chi_{b2}(2P)$	$\chi_{b2}(2P) \to \Upsilon(2S)\gamma$	122 ± 60	NA
$\Upsilon(3S)$	$\Upsilon(3S) \to \chi_{b0}(2P)\gamma$	24 ± 10	20.32 ± 1.85
$\Upsilon(3S)$	$\Upsilon(3S) \to \chi_{b1}(2P)\gamma$	15 ± 3	20.32 ± 1.85
$\Upsilon(3S)$	$\Upsilon(3S) \to \chi_{b2}(2P)\gamma$	22 ± 5	20.32 ± 1.85

Table 9.6: Estimation of the widths of bottomonium states using input from the BaBar experiment for the branching fractions. The branching fractions used to compute the values in this table were obtained by BaBar analysing the $3S \to 2P \to 2S$ decay process, for more details see [87].

State	Decay	Γ_H [keV] (theo. + exp.)	Γ_H [keV] (PDG)
$\chi_{b0}(2P)$	$\chi_{b0}(2P) \to \Upsilon(1S)\gamma$	1351 ± 823	NA
$\chi_{b1}(2P)$	$\chi_{b1}(2P) \to \Upsilon(1S)\gamma$	83 ± 29	NA
$\chi_{b2}(2P)$	$\chi_{b2}(2P) \to \Upsilon(1S)\gamma$	246 ± 71	NA
$\Upsilon(3S)$	$\Upsilon(3S) \to \chi_{b0}(2P)\gamma$	50 ± 37	20.32 ± 1.85
$\Upsilon(3S)$	$\Upsilon(3S) \to \chi_{b1}(2P)\gamma$	16 ± 3	20.32 ± 1.85
$\Upsilon(3S)$	$\Upsilon(3S) \to \chi_{b2}(2P)\gamma$	22 ± 4	20.32 ± 1.85

Table 9.7: Estimation of the total widths of bottomonium states using input from the BaBar experiment for the branching fractions. The branching fractions used to compute the values in this table were obtained by BaBar analysing the $3S \to 2P \to 1S$ decay process, for more details see [87].

State	Decay	Γ_H [keV] (theo. + exp.)	Γ_H [keV] (PDG)
$h_b(1P)$	$h_b(1P) \to \eta_b(1S)\gamma$	30 ± 30	NA

Table 9.8: Estimation of the total width of the bottomonium $h_b(1P)$ state using input from the BELLE experiment [90] for the branching fraction.

Decay	$\Gamma_{H \to H'\gamma}/\Gamma_H$ (theo. + exp.)
$\eta_b(2S) \to h_b(1P)\gamma$	$> 2 \times 10^{-6}$
$\eta_c(2S) \to h_c(1P)\gamma$	$(3 \pm 1) \times 10^{-6}$

Table 9.9: Predictions for the branching fraction of the singlet $2S \to 1P$ transition in bottomonium and charmonium. The data of the width has been retrieved from the PDG.

9.3 Summary

The large uncertainty of the $h_b(1P) \to \eta_b(1S)\gamma$ and $h_b(2P) \to \eta_b(2S)\gamma$ bottomonium decays comes from the accidental cancellation of the contributions to $R_{H \to H'\gamma}$ discussed in Chapter 8; for the other bottomonium evaluations we get an error that is typically less than 40% the central value. In general, our results agree with the experiments within the

assigned uncertainties. Since there are no more free parameters to fit after the parameters of the potential have been determined, our agreement with experiment is not a trivial result, especially in the case of the bottomonium decays where the theoretical uncertainty is small. Especially remarkable are our results for the bottomonium $2S \to 1P$ and the $3S \to 2P$ decays, where the theoretical uncertainty is competitive with the experimental one.

The only decay for which we do not have agreement with the experiment is the $\Upsilon(3S) \to \chi_{b1}(2P)\gamma$ decay when compared to the BaBar result obtained from the analysis of the $3S \to 2P \to 1S$ decay chain (Fig. 9.7). In the case of the BaBar result for the same decay obtained from the analysis of the $3S \to 2P \to 2S$ chain (Fig. 9.6), we see that there is no such disagreement, moreover, there seems to be tension among the two BaBar results. For transparency reasons, we have kept the BaBar results as they were reported in [87], however, one may expect that a consistent determination of the $\Upsilon(3S) \to \chi_{bJ}(2P)\gamma$ branching fractions from BaBar would correspond to the average of the values obtained from the analysis of the two decay chains. In this case, our results would agree with BaBar, as they do with the PDG value for the same decay.

Due to the poor convergence of the non-relativistic expansion, the uncertainties of our results for charmonium decays are in general larger than the experimental uncertainties, except in the case of the singlet $1P \to 1S$ transition (Fig. 9.5), where theoretical and experimental uncertainties are comparable.

From our results for the total width of the bottomonium states $h_b(2P)$, $\chi_{b1}(2P)$ and $\chi_{b2}(2P)$, we see that there is some tension among the predictions coming from different transitions. The source of this tension may be attributed to our results for the decay rates or to the experimental values of the branching fractions. One may expect that further experimental measurements will move the values of their respective branching fractions. For instance, in the case of the $h_b(2P)$ state, we have that the branching fractions of the $2P \to 1S$ and $2P \to 2S$ transitions quoted in the PDG come from only one experiment [86]; it would be interesting to see if the current PDG values for these transitions will be altered by further measurements. The values of the branching fractions of the $\chi_b(2P) \to \Upsilon(1S), \Upsilon(2S)\gamma$ decays appear to be better established with three experiments quoted in the computation of the PDG average [123–125], however, for these transitions our estimations of the width of the initial state show some tension but are still compatible within errors. Finally let us point out that the upper limit of our estimation for the width of the $\chi_{b0}(1P)$ bottomonium state, $\sim 1.5\,[\mathrm{MeV}]$, is compatible with the upper limit of $\sim 2.4\,[\mathrm{MeV}]$ recently reported by the BELLE experiment in [91]. It would be interesting to see if further analysis by BELLE or other experiment can narrow the experimental uncertainty and provide a more rigorous test of our prediction.

Chapter 10

Conclusions and outlook

10.1 Regarding the EST potential

We have seen that the unambiguous expression for the $Q\bar{Q}$ potential up to $\mathcal{O}(1/m^2)$ is provided by the EFTs for heavy quarkonium, in particular pNRQCD, in terms of QCD correlators that are independent of the distance between the quark and antiquark, but whose evaluation is constrained by the distance regime that is being considered. In the first part of the thesis, we have evaluated these correlators using a mapping between the QCD and EST degrees of freedom. This mapping has been constructed under the assumption that the symmetry properties of the $Q\bar{Q}$ system are the same in both theories. Our main results regarding the EST are the expressions for the relativistic corrections to the $Q\bar{Q}$ string potential given in Eqs. (4.27)-(4.37). In particular, we have obtained a new $1/m^2$-suppressed, momentum- and spin-independent contribution that may be interpreted as a relativistic correction to the string tension.

We have shown that if only the leading terms are considered, the EST potential depends only on two parameters: the string tension and the quark mass. Evaluating the EST $Q\bar{Q}$ spectrum from this potential, we have seen that in some circumstances the contribution of the $1/m^2$-suppressed corrections are as significant as the $1/m$-suppressed one.

The relativistic corrections to the EST potential have been obtained assuming the LO string action (Eq. (4.4)) and the LO mapping between the EST and QCD (Eq. (4.16)). We argued that the expressions listed in Eqs. (4.27)-(4.37) correspond to the leading corrections to the potential even if NLO terms in the mapping are taken into account. The incorporation of these terms in the calculation may lead to new subleading contributions or to a change in the coefficients of the leading potentials, but they will not alter their dependence on r. A study of the EST potential beyond the LO, in the action and the mapping, can be found in [126].

The most relevant aspect of our results has to do with the quark-antiquark interaction at long distances. Since the computation of the correlators in the $Q\bar{Q}$ potential derived from EFTs cannot be performed perturbatively, the EST provides an analytical alternative for their evaluation. The results of this evaluation can be compared to lattice determinations of the correlators and, eventually, be used to parametrize the results

of these lattice computations. So far, the available lattice evidence is compatible with the EST hypothesis for large distances. We have found that the momentum and spin-independent $1/m^2$ potential shows a behavior rising linearly with the distance; this is a prediction that can be tested once lattice determinations of the relevant correlators are performed. Existing lattice data for the spin-spin potentials are so far consistent with zero in the long range [127]. It would be interesting to produce more accurate data able to detect a long-distance signal since the EST predicts a sharp fall off proportional to $1/r^5$.
Another relevant aspect is the application of our results to other topics of quarkonium phenomenology. Possible applications of the EST potential may include spectroscopy or other decays different from the E1.

10.2 Regarding the E1 transitions

In the general case, the E1 heavy quarkonium transitions involve at least one excited state, therefore, the evaluation of the E1 decay rates at order v^2 in the relative quark-qntiquark velocity expansion, which have been obtained in the framework of pNRQCD, requires input for the quark-antiquark potential in the whole distance regime. In our approach for the evaluation of these rates, we have developed a framework in which the long-range of the potential is given by the LO results of our the evaluation of the relevant QCD correlators in the EST, which, as we stated before, only depend on the string tension and on the quark mass.
For the evaluation of the short-distance contribution, we have used the expressions that result from the perturbative evaluation of these correlators. In order to have a smooth transition between both distance regimes without the addition of a cut-off parameter, the potential is constructed by adding the expressions of both regimes. One of the trade-offs of this approach is that the QCD running coupling, appearing in the perturbative expressions, must be converted into a fixed parameter, since now the evaluation of the potential goes into the non-perturbative regime, where the value of the coupling diverges. The resulting $Q\bar{Q}$ potential has three free parameters, namely, the quark mass, the fixed coupling, and the string tension. We considered three possible orderings of the potential based on three different power countings that can be imposed on its parameters. We took a statistical approach to fit these parameters: using input from redundant experimental data for the bottomonium and charmonium spectrums and redundant lattice data for the static energy, we found a range of values for each parameter.
The evaluation of the E1 rates is carried out using points that distribute normally in the range of each parameter, thus leading to a set of values for each of the considered decay rates in each of the input and counting combinations. The mean and standard deviation of these sets is what we consider the central value and associated uncertainty of our evaluations respectively.
Our intermediate results show how the ordering of the potential affects the evaluation of the rates. Also, they provide results for the two different data inputs we have used to fit the parameters.

Our final results for the E1 decay rates are obtained by combining the results from both inputs, adopting the countings we considered to be closer to representing the differences between charmonium and bottomonium states. These evaluations are summarized in Tables 9.1 and 9.2 of Chapter 9; they compare favorably with the available experimental data. In particular for the triplet $3S \to 2P$ and $2S \to 1P$ transitions in bottomonium and the singlet $1P \to 1S$ transition in charmonium, we get errors that are comparable to the experimental ones.
Using our results for the decays and experimental input in Tables 9.3 - 9.8, we computed predictions for the total width of some quarkonium states. Our prediction for the $\chi_{b0}(1P)$ is compatible with the latest experimental limits.
In Table 9.9, we use our results together with experimental input for the total width to estimate the branching fraction of the singlet $2S \to 1P$ transition in bottomonium and charmonium. There is some tension among our predictions for the total width when these are computed from different transitions. We expect that further experimental data can conciliate this tension.
The results reported here may be seen as a first evaluation of the $\mathcal{O}(v^2)$ E1 decay rates within an EFT framework. A possible next step may be to include the full perturbative expressions of the potential in the short-distance regime. Provided an estimation of the non-perturbative effects that still appear (octet effects) and ignoring contributions from the long-range regime of the potential, this approach may be sufficient for transitions among lower states. In this approach, the mass and coupling may be evaluated in a specific renormalization scheme rather than the fixed parameters of our approach. Such a study has been carried out in the case of the M1 transitions in [81] and a preliminary evaluation of some E1 transitions can be found in [128].
For transitions involving excited states, still some parametrization of the long-range potential will be necessary as well as a cut-off to separate both distance regimes. It would be interesting to see if a more sophisticated evaluation can account for the $3S \to 1P$ bottomonium transition, since in our approach this transition suffers from a large instability. The origin of this instability (see Appendix G) seems to indicate that precise fine-tuned values of the potential parameters are necessary for getting stable relativistic corrections.
The results presented here may be relevant for current and future experiments like BELLE II, BESIII and quarkonium-related LHC experiments.

10.3 Concluding remarks

We have presented an evaluation of the quarkonium electromagnetic dipole transitions that uses some of the accumulated results from the EFTs for quarkonium, in particular from pNRQCD. This represents a novel approach to the study of a process that in the past has been treated using models that did not have a solid justification in terms of QCD. Although in the construction of the potential we had to give some rigor away, we believe that our evaluation is a step forward with respect to these older approaches.

To conduct this evaluation, it was required to complete the calculation of the relativistic corrections to the EST potential at $\mathcal{O}(1/m^2)$, a calculation that by itself is important, since it provides some predictions for the quark-antiquark interaction that may be testable in future lattice studies. These results together with some of the tools developed for the numerical analysis may be relevant for applications other than those presented in this thesis.

The research we have detailed here has also been reported in [129], [58], [130], [131], and [116].

Appendices

Appendix A

Further details on the calculation of the pNRQCD $1/m$ potential

In this section we give some details on the calculation of the $1/m$ potential in Sec. 3.2 based on [18].

The spin-dependent term in Eq. (3.41) has been eliminated using time reversal:

$$\langle \mathbf{B}(t)\rangle_\Box = -\langle \mathbf{B}(-t)\rangle_\Box. \tag{A.1}$$

In order to expand $G^{(1,0)}_{\rm NRQCD}$ in Eq. (3.41) and obtain the expression of (3.43), the following identities are necessary

$$\begin{aligned}
\mathbf{D}(\mathbf{x},t)\phi(t,\mathbf{x},t',\mathbf{x}) &= \phi(t,\mathbf{x},t',\mathbf{x})\mathbf{D}(\mathbf{x},t') \\
&+ ig\int_{t'}^{t} dt''\phi(t,\mathbf{x},t'',\mathbf{x})\mathbf{E}(\mathbf{x},t'')\phi(t'',\mathbf{x},t',\mathbf{x}), \qquad \text{(A.2)}\\
\mathbf{D}(\mathbf{x}_1,t)\phi(\mathbf{x}_1,\mathbf{x}_2;t) &= ig\mathbf{r}\times\int_0^1 ds\, s\,\phi(\mathbf{x}_1,\mathbf{x}'(s);t)\mathbf{B}(\mathbf{x}'(s),t)\phi(\mathbf{x}'(s),\mathbf{x}_2;t) \\
&+ \phi(\mathbf{x}_1,\mathbf{x}_2;t)\nabla_{\mathbf{x}_1}, \qquad \text{(A.3)}
\end{aligned}$$

where

$$\begin{aligned}
\phi(t,\mathbf{x},t',\mathbf{x}) &\equiv P\exp\left\{-ig\int_{t'}^{t} dt'' A_0(\mathbf{x},t'')\right\}, \qquad \text{(A.4)}\\
\mathbf{x}'(s) &= s\mathbf{x}_1 + (1-s)\mathbf{x}_2, \qquad \text{(A.5)}
\end{aligned}$$

and $\phi(\mathbf{x}_1,\mathbf{x}_2;t)$ was defined in Eq. (3.28) as

$$\phi(\mathbf{x}_1,\mathbf{x}_2;t) \equiv \mathrm{P}\exp\left[ig\int_0^1 ds(\mathbf{x}_1-\mathbf{x}_2)\cdot\mathbf{A}(\mathbf{x}_2-s(\mathbf{x}_2-\mathbf{x}_1),t)\right]. \tag{A.6}$$

From identities (A.2) and (A.3) the following relation can be obtained

$$\nabla_{\mathbf{x}_1}\langle W_\Box\rangle = ig\int_{-T/2}^{T/2} dt\langle \mathbf{E}(t)\rangle_\Box + \langle \mathbf{O}_1(-T/2)\rangle_\Box - \langle \mathbf{O}_2(T/2)\rangle_\Box, \tag{A.7}$$

where $\mathbf{O}_1$ and $\mathbf{O}_2$ are given in Eqs. (3.44) and (3.45) respectively.

The method for going from Eq. (3.50) to (3.53) and from (3.68) to (3.67) was outlined in Ref. [18]; it reads:

1. Inserting the identity operator $I = \sum |n\rangle^{(0)\,(0)}\langle n|$ into the Wilson loop averages one obtains Eq. (3.51).

2. Doing the same for $\langle \mathbf{E}(t)\rangle_\Box$ one gets

$$\langle \mathbf{E}(t)\rangle_\Box = \sum_n e^{-iE_n^{(0)}T} a_n^2\, {}^{(0)}\langle n|\mathbf{E}|n\rangle^{(0)} + \sum_{n\neq m} e^{-i(E_n^{(0)}+E_m^{(0)})\frac{T}{2}+i(E_n^{(0)}-E_m^{(0)})t} a_n a_m\, {}^{(0)}\langle n|\mathbf{E}|m\rangle^{(0)}. \tag{A.8}$$

3. End-point strings containing $\mathbf{O}_2$ and $\mathbf{O}_1$ select intermediate states with quantum numbers different from the ones of the singlet. As a consequence of this, correlators containing $\mathbf{O}_2$ and $\mathbf{O}_1$ vanish when taking the limit $T \to \infty$.

4. Consider the following two results

$$-(\nabla V_0) = {}^{(0)}\langle 0|g\mathbf{E}|0\rangle^{(0)}, \tag{A.9}$$

$$(\nabla Z_0) = 2\sum_{n\neq 0} a_0 a_n \frac{{}^{(0)}\langle 0|g\mathbf{E}|n\rangle^{(0)}}{E_n - E_0}, \tag{A.10}$$

   which can be proven using Eq. (A.7) together with time-inversion invariance of the chromoelectric field.

5. Inserting the identity operator in the correlator $\langle \mathbf{E}(t)\cdot\mathbf{E}(t')\rangle_\Box$, one obtains for $t > t'$:

$$\langle \mathbf{E}(t)\cdot\mathbf{E}(t')\rangle_\Box = \sum_{n,m,s} a_n a_m\, {}^{(0)}\langle n|\mathbf{E}|s\rangle^{(0)\,(0)}\langle s|\mathbf{E}|m\rangle^{(0)} e^{-i(E_n^{(0)}+E_m^{(0)})\frac{T}{2}} e^{i(E_n^{(0)}-E_s^{(0)})t} e^{i(E_s^{(0)}-E_m^{(0)})t}. \tag{A.11}$$

This method also provides the steps to prove that the expressions involving the correlators (Eqs. (3.50) and (3.68)) are finite when taking the limit $T \to \infty$.

Appendix B

The EST two-field correlator

For the sake of completeness, in this section we show the explicit derivation of Eq. (4.11). The following derivation has been presented previously in [132].

Let the position of the quark and antiquark be $\pm\mathbf{r}/2 \equiv (0, 0, \pm r/2)$ meaning that the $Q\bar{Q}$ system is located along the z-axis and symmetric with respect to the x-y plane. We want to calculate the correlator given by

$$G_F^{lm}(t, z; t', z') = \langle \xi^l(t, z)\xi^m(t', z')\rangle \equiv \frac{1}{Z}\int \mathcal{D}\xi^1\mathcal{D}\xi^2\, \xi^l\xi^m e^{iS_{string}(\xi^1,\xi^2)}, \tag{B.1}$$

with Z being the normalization, and $G_F^{lm}(t, z; t', z')$ the Feynman propagator that can be obtained from the equations of motion

$$\frac{\partial\mathcal{L}}{\partial\xi^l} - \partial_\mu\frac{\partial\mathcal{L}}{\partial(\partial_\mu\xi^l)} = \partial_\mu\partial^\mu\xi^l = 0. \tag{B.2}$$

Because ξ only depends on z and t, the equations of motion simplify to

$$\frac{\partial^2\xi^l}{\partial t^2} - \frac{\partial^2\xi^l}{\partial z^2} = 0. \tag{B.3}$$

It is much more convenient to work in Euclidean space-time; performing a Wick rotation $t \to it$, the equations of motion reduce to a Laplacian in two dimensions

$$\frac{\partial^2\xi^l}{\partial t^2} + \frac{\partial^2\xi^l}{\partial z^2} = 0 \quad \text{and} \quad \xi^l(it, \pm r/2) = \xi^l(\pm i\infty, z) = 0. \tag{B.4}$$

Now we can compute the Green function defined by

$$\left(\frac{\partial^2}{\partial t^2} + \frac{\partial^2}{\partial z^2}\right) G_F^{lm}(it, z; it', z') = -\frac{\delta_{lm}}{\kappa}\delta(z - z')\delta(t - t'). \tag{B.5}$$

Dropping the Kroenecker delta in (B.5), we get

$$\left(\frac{\partial^2}{\partial t^2} + \frac{\partial^2}{\partial z^2}\right) \tilde{G}(t, z; t', z') = -\frac{1}{\kappa}\delta(z - z')\delta(t - t'). \tag{B.6}$$

Note that the Green function introduced in (B.6) also has to satisfy the boundary conditions of (B.4). Hence it is useful to translate the coordinate system in the z direction:

$$z \to z + r/2 \ , \ z' \to z' + r/2,$$
$$\tilde{G}(t, r; t', z') = \tilde{G}(t, 0; t', z') = \tilde{G}(\pm\infty, r; t', z') = 0.$$

To handle Eq. (B.6), the first step is to express the Green function as a Fourier transformation $\tilde{g}(\eta, z; t', z')$ namely

$$\tilde{g}(\eta, z; t', z') = \frac{1}{\sqrt{2\pi}} \int dt \ e^{i\eta t} \tilde{G}(t, z; t', z') \tag{B.7}$$

and

$$\tilde{G}(t, z; t', z') = \frac{1}{\sqrt{2\pi}} \int d\eta \ e^{-i\eta t} \tilde{g}(\eta, z; t', z'). \tag{B.8}$$

Multiplying Eq. (B.6) with $e^{i\eta t}$ and performing an integration over the whole time axis yields

$$\int dt \ e^{i\eta t} \frac{\partial^2 \tilde{G}}{\partial t^2} + \int dt \ e^{i\eta t} \frac{\partial^2 \tilde{G}}{\partial z^2} = -\frac{1}{\kappa} \int dt \ e^{i\eta t} \delta(z - z') \delta(t - t').$$

Assuming that the Green function and its first derivative vanishes when $t \to \pm\infty$, one obtains after two integrations by parts

$$\int dt \ e^{i\eta t} \frac{\partial^2 \tilde{G}}{\partial t^2} = -\eta^2 \sqrt{2\pi} \ \tilde{g}.$$

Moreover the second integral reads

$$\int dt \ e^{i\eta t} \frac{\partial^2 \tilde{G}}{\partial z^2} = \frac{d^2}{dz^2} \int dt \ e^{i\eta t} \tilde{G} = \sqrt{2\pi} \ \frac{d^2 \tilde{g}}{dz^2}.$$

Altogether the remaining equation which has to be solved is given by

$$\frac{d^2 \tilde{g}}{dz^2} - \eta^2 \tilde{g} = -\frac{1}{\sqrt{2\pi}\kappa} e^{i\eta t'} \delta(z - z') \text{ and } \tilde{g}(\eta, 0) = \tilde{g}(\eta, r) = 0. \tag{B.9}$$

The solution of Eq. (B.9) can be expanded in terms of a complete system of orthonormal functions which fulfill the boundary conditions. This expansion gets simpler if one uses eigenfunctions defined by $\left(\frac{d^2}{dz^2} + \lambda_n^2\right) \psi_n(z) = 0$ and $\psi_n(0) = \psi_n(r) = 0$. A complete system ($\sum_n \psi_n(z) \psi_n^*(z') = \delta(z - z')$) respecting also the boundary conditions is $\psi_n(z) = \sqrt{\frac{2}{r}} \sin(\lambda_n z)$ and $\lambda_n = \frac{n\pi}{r}$ and $\int_0^r dz \ \psi_n(z) \psi_m^*(z) = \delta_{mn}$.
The expansion then becomes

$$\tilde{g}(\eta, z; t', z') = \frac{e^{i\eta t'}}{\sqrt{2\pi}\kappa} \frac{2}{r} \sum_{n=1}^{\infty} \frac{\sin(\lambda_n z) \sin(\lambda_n z')}{\eta^2 + \lambda_n^2}. \tag{B.10}$$

To get the sought Green function combine Eq. (B.10) and (B.8):

$$\tilde{G}(t,z;t',z') = \frac{1}{\pi\kappa r}\sum_{n=1}^{\infty}\sin(\lambda_n z)\sin(\lambda_n z')\int d\eta\; e^{-i\eta(t-t')}\frac{1}{\eta^2+\lambda_n^2}. \tag{B.11}$$

Computing the integral with the residue theorem, the correlator reads

$$\tilde{G}(t,z;t',z') = \frac{1}{\pi\kappa}\sum_{n=1}^{\infty}\frac{1}{n}\sin(\lambda_n z)\sin(\lambda_n z')\; e^{-\lambda_n|t-t'|}. \tag{B.12}$$

This relation may be written as the real part of a complex function:

$$\tilde{G}(t,z;t',z') = \frac{1}{2\pi\kappa}\Re\left[\sum_{n=1}^{\infty}\frac{1}{n}e^{i\lambda_n((z'-z)+i|t-t'|)} - \sum_{n=1}^{\infty}\frac{1}{n}e^{i\lambda_n((z'+z)+i|t-t'|)}\right].$$

With $\sum_{n=1}^{\infty}\frac{Z^n}{n} = -\ln(1-Z)$ and $\ln(Z) = \ln|Z| + i\arg(Z)$, the sum can be rewritten as a logarithm with a complex argument

$$\begin{aligned}\tilde{G}(t,z;t',z') &= \frac{1}{2\pi\kappa}\Re\;\ln\left(\frac{1-e^{i\frac{\pi}{r}((z'+z)+i|t-t'|)}}{1-e^{i\frac{\pi}{r}((z'-z)+i|t-t'|)}}\right)\\ &= \frac{1}{4\pi\kappa}\;\ln\left(\frac{\cosh(\frac{\pi}{r}(t-t'))-\cos(\frac{\pi}{r}(z+z'))}{\cosh(\frac{\pi}{r}(t-t'))-\cos(\frac{\pi}{r}(z-z'))}\right).\end{aligned} \tag{B.13}$$

Coming back to the original coordinates, we have

$$\begin{aligned}&z\to z-r/2\;,\;\; z'\to z'-r/2\\ &\cos\left(\frac{\pi}{r}(z+z')\right)\to-\cos\left(\frac{\pi}{r}(z+z')\right).\end{aligned}$$

Putting back the Kroenecker delta, we get

$$G_F^{lm}(it,z;it',z') = \frac{\delta_{lm}}{4\pi\kappa}\;\ln\left(\frac{\cosh(\frac{\pi}{r}(t-t'))+\cos(\frac{\pi}{r}(z+z'))}{\cosh(\frac{\pi}{r}(t-t'))-\cos(\frac{\pi}{r}(z-z'))}\right), \tag{B.14}$$

which is the desired result.

Appendix C

Quarkonium spectrum from the PDG

In Tables C.1 and C.2 we display the values of the masses used for the parameter fitting and the calculation of the photon energy as they were retrieved from [78]. These values may change in future PDG reports.

State $(^{2S+1}L_J)$	Mass [MeV]
$\eta_c(1S)$ $(1\,^1S_0)$	2983.7 ± 0.7
J/ψ $(1\,^3S_1)$	3096.916 ± 0.011
$h_c(1P)$ $(1\,^1P_1)$	3525.38 ± 0.11
$\chi_{c0}(1P)$ $(1\,^3P_0)$	3414.75 ± 0.31
$\chi_{c1}(1P)$ $(1\,^3P_1)$	3510.66 ± 0.07
$\chi_{c2}(1P)$ $(1\,^3P_2)$	3556.2 ± 0.09
$\eta_c(2S)$ $(2\,^1S_0)$	3639.4 ± 1.3
$\psi(3686)$ $(2\,^3S_1)$	3686.109 ± 0.013

Table C.1: Experimental values of the charmonium masses retrieved from the PDG report [78].

State ($^{2S+1}L_J$)	Mass [MeV]
$\eta_b(1S)$ ($1\,^1S_0$)	9398.0 ± 3.2
$\Upsilon(1S)$ ($1\,^3S_1$)	9460.30 ± 0.26
$h_b(1P)$ ($1\,^1P_1$)	9899.3 ± 1.0
$\chi_{b0}(1P)$ ($1\,^3P_0$)	9859.44 ± 0.73
$\chi_{b1}(1P)$ ($1\,^3P_1$)	9892.78 ± 0.57
$\chi_{b2}(1P)$ ($1\,^3P_2$)	9912.21 ± 0.57
$\eta_b(2S)$ ($2\,^1S_0$)	9999 ± 4
$\Upsilon(2S)$ ($2\,^3S_1$)	10023.26 ± 0.31
$h_b(2P)$ ($2\,^1P_1$)	10259.8 ± 1.2
$\chi_{b0}(2P)$ ($2\,^3P_0$)	10232.5 ± 0.9
$\chi_{b1}(2P)$ ($2\,^3P_1$)	10255.46 ± 0.77
$\chi_{b2}(2P)$ ($2\,^3P_2$)	10268.65 ± 0.77
$\Upsilon(3S)$ ($3\,^3S_1$)	10355.2 ± 0.5
$\Upsilon(4S)$ ($4\,^3S_1$)	10579.4 ± 1.2

Table C.2: Experimental values of the bottomonium masses retrieved from the PDG report [78].

Appendix D

Detailed results of the parameter fitting

In the first part of this section we show the detailed partial results of the parameter fitting that lead to the values of Tables 5.2 and 5.3. In the second part we present further details of the analysis of the scaling of the potential with Countings 1 and 3.

D.1 Partial results of the fitting

The results of the fitting with phenomenology input are summarized in Tables D.1 - D.3. The fitting of m_b and m_c with lattice input is shown in Tables D.4 - D.8. We only quote up to three decimals in each parameter although the precision of the experimental input requires that the parameters must be fitted at a precision of at least six decimals.

Set	Bottomonium	Charmonium	a	$\kappa\,[\mathrm{GeV}^2]$	$m_c\,[\mathrm{GeV}]$	$m_b\,[\mathrm{GeV}]$
1	$1\,^3S_1, 2\,^3S_1, 3\,^3S_1$	$2\,^1S_0$	0.309	0.172	1.435	4.803
2	$1\,^3S_1$	$1\,^3S_1, 2\,^3S_1, 1\,^1P_1$	0.251	0.186	1.357	4.714
3	$1\,^1S_0, 2\,^1S_0, 4\,^3S_1$	$1\,^3P_0$	0.328	0.14	1.428	4.864
4	$2\,^1P_1$	$1\,^3S_1, 1\,^3P_1, 2\,^1S_0$	0.209	0.191	1.318	4.717
5	$1\,^3S_1, 2\,^3P_1, 4\,^3S_1$	$1\,^3S_1$	0.301	0.165	1.421	4.794
6	$1\,^3S_1$	$1\,^3S_1, 1\,^1P_1, 2\,^1S_0$	0.243	0.19	1.346	4.702
7	$2\,^1P_1, 3\,^3S_1$	$1\,^1S_0, 2\,^1S_0$	0.242	0.215	1.297	4.693
8	$2\,^1P_1, 3\,^3S_1$	$1\,^3S_1, 2\,^1S_0$	0.206	0.191	1.316	4.716
9	$2\,^1S_0, 3\,^3S_1$	$1\,^3S_1, 2\,^1S_0$	0.238	0.19	1.341	4.733
10	$2\,^1S_0, 3\,^3S_1$	$1\,^3S_1, 2\,^3S_1$	0.246	0.187	1.352	4.744
11	$2\,^3P_1, 3\,^3S_1$	$1\,^3S_1, 2\,^3S_1$	0.201	0.194	1.309	4.708
12	$2\,^3P_1, 3\,^3S_1$	$1\,^1S_0, 2\,^3S_1$	0.233	0.212	1.29	4.693
13	$2\,^1S_0, 3\,^3S_1$	$1\,^1S_0, 2\,^1S_0$	0.117	0.234	1.157	4.597
14	$3\,^3S_1, 4\,^3S_1$	$1\,^3P_1, 2\,^3S_1$	0.039	0.159	1.313	4.708
15	$3\,^3S_1, 4\,^3S_1$	$1\,^1P_1, 2\,^3S_1$	0.154	0.149	1.386	4.771
16	$3\,^3S_1, 4\,^3S_1$	$1\,^3P_2, 2\,^3S_1$	0.238	0.14	1.449	4.826
mean	-	-	0.222	0.182	1.345	4.736
σ	-	-	0.07	0.026	0.07	0.061

Table D.1: Parameter fitting using Counting 1 with phenomenology input. We quote the states used to fit each parameter set, the experimental values for their masses can be found in Appendix C.

Set	Bottomonium	Charmonium	a	$\kappa\,[\mathrm{GeV}^2]$	$m_c\,[\mathrm{GeV}]$	$m_b\,[\mathrm{GeV}]$
1	$1\,^3S_1, 2\,^3S_1, 3\,^3S_1$	$2\,^1S_0$	0.293	0.175	1.428	4.792
2	$1\,^3S_1$	$1\,^3S_1, 2\,^3S_1, 1\,^1P_1$	0.236	0.188	1.353	4.701
3	$1\,^1S_0, 2\,^1S_0, 4\,^3S_1$	$1\,^3P_0$	0.313	0.143	1.42	4.851
4	$2\,^1P_1$	$1\,^3S_1, 1\,^3P_1, 2\,^1S_0$	0.2	0.193	1.318	4.712
5	$1\,^3S_1, 2\,^3P_1, 4\,^3S_1$	$1\,^3S_1$	0.29	0.165	1.427	4.79
6	$1\,^3S_1$	$1\,^3S_1, 1\,^1P_1, 2\,^1S_0$	0.233	0.19	1.349	4.696
7	$2\,^1P_1, 3\,^3S_1$	$1\,^1S_0, 2\,^1S_0$	0.238	0.216	1.306	4.69
8	$2\,^1P_1, 3\,^3S_1$	$1\,^3S_1, 2\,^1S_0$	0.205	0.192	1.323	4.714
9	$2\,^1S_0, 3\,^3S_1$	$1\,^3S_1, 2\,^1S_0$	0.237	0.19	1.353	4.735
10	$2\,^1S_0, 3\,^3S_1$	$1\,^3S_1, 2\,^3S_1$	0.247	0.186	1.366	4.747
11	$2\,^3P_1, 3\,^3S_1$	$1\,^3S_1, 2\,^3S_1$	0.201	0.196	1.316	4.706
12	$2\,^3P_1, 3\,^3S_1$	$1\,^1S_0, 2\,^3S_1$	0.231	0.214	1.299	4.69
13	$2\,^1S_0, 3\,^3S_1$	$1\,^1S_0, 2\,^1S_0$	0.08	0.244	1.127	4.563
14	$3\,^3S_1, 4\,^3S_1$	$1\,^3P_1, 2\,^3S_1$	0.021	0.161	1.31	4.699
15	$3\,^3S_1, 4\,^3S_1$	$1\,^1P_1, 2\,^3S_1$	0.145	0.15	1.386	4.766
16	$3\,^3S_1, 4\,^3S_1$	$1\,^3P_2, 2\,^3S_1$	0.229	0.141	1.448	4.82
mean	-	-	0.213	0.184	1.346	4.73
σ	-	-	0.073	0.027	0.074	0.065

Table D.2: Parameter fitting using Counting 2 with phenomenology input.

Set	Bottomonium	Charmonium	a	$\kappa\,[\mathrm{GeV}^2]$	$m_c\,[\mathrm{GeV}]$	$m_b\,[\mathrm{GeV}]$
1	$1\,^3S_1, 2\,^3S_1, 3\,^3S_1$	$2\,^1S_0$	0.309	0.172	1.204	4.803
2	$1\,^1S_0, 2\,^1S_0, 4\,^3S_1$	$1\,^3P_0$	0.328	0.14	1.251	4.864
3	$1\,^3S_1, 2\,^3P_1, 4\,^3S_1$	$1\,^3S_1$	0.301	0.165	1.164	4.794
4	$2\,^1P_1, 3\,^3S_1$	$1\,^1S_0, 2\,^1S_0$	0.283	0.254	1.024	4.654
5	$2\,^1P_1, 3\,^3S_1$	$1\,^3S_1, 2\,^1S_0$	0.225	0.203	1.141	4.705
6	$2\,^1S_0, 3\,^3S_1$	$1\,^3S_1, 2\,^1S_0$	0.209	0.202	1.145	4.698
7	$2\,^1S_0, 3\,^3S_1$	$1\,^3S_1, 2\,^3S_1$	0.159	0.22	1.133	4.641
8	$2\,^3P_1, 3\,^3S_1$	$1\,^3S_1, 2\,^3S_1$	0.254	0.226	1.116	4.68
9	$2\,^3P_1, 3\,^3S_1$	$1\,^1S_0, 2\,^3S_1$	0.309	0.278	1.0	4.633
10	$2\,^1S_0, 3\,^3S_1$	$1\,^1S_0, 2\,^1S_0$	0.084	0.243	1.053	4.567
mean	-	-	0.246	0.21	1.123	4.704
σ	-	-	0.074	0.041	0.074	0.086

Table D.3: Parameter fitting using Counting 3 with phenomenology input. In this case only 10 sets fulfill the condition $0 < a < 1$.

State	$m_b(n\,^{2S+1}L_J)\,[GeV]$	$\sigma_{m_b}\,[GeV]$
$1\,^1S_0$	4.767	0.051
$1\,^3S_1$	4.757	0.042
$1\,^1P_1$	4.715	0.026
$1\,^3P_0$	4.709	0.027
$1\,^3P_1$	4.715	0.026
$1\,^3P_2$	4.718	0.025
$2\,^1S_0$	4.744	0.036
$2\,^3S_1$	4.734	0.033
$2\,^1P_1$	4.702	0.033
$2\,^3P_0$	4.701	0.033
$2\,^3P_1$	4.703	0.033
$2\,^3P_2$	4.703	0.032
$3\,^3S_1$	4.709	0.039
$4\,^3S_1$	4.664	0.045
Average	4.719	0.132

Table D.4: Results for the fitting of the bottom mass parameter m_b with the lattice input adopting Counting 1; σ_{m_b} corresponds to the standard deviation of the twelve values obtained after solving Eq. (5.31). The average is calculated using the values σ_{m_b} as weights. The average of the σ_{m_b} values is calculated using quadratures.

State	$m_c(n\,^{2S+1}L_J)\,[GeV]$	$\sigma_{m_c}\,[GeV]$
$1\,^1S_0$	1.354	0.041
$2\,^1S_0$	1.329	0.048
$1\,^3S_1$	1.361	0.036
$2\,^3S_1$	1.310	0.047
$1\,^3P_0$	1.271	0.041
$1\,^3P_1$	1.303	0.039
$1\,^1P_1$	1.314	0.037
$1\,^3P_2$	1.328	0.035
Average	1.321	0.115

Table D.5: Results for m_c with Counting 1 and lattice input. The values are computed as in Table D.4.

State	$m_b(n\,^{2S+1}L_J)\,[GeV]$	$\sigma_{m_b}\,[GeV]$
$1\,^1S_0$	4.783	0.058
$1\,^3S_1$	4.773	0.049
$1\,^1P_1$	4.716	0.026
$1\,^3P_0$	4.710	0.027
$1\,^3P_1$	4.716	0.026
$1\,^3P_2$	4.719	0.025
$2\,^1S_0$	4.748	0.037
$2\,^3S_1$	4.738	0.034
$2\,^1P_1$	4.703	0.033
$2\,^3P_0$	4.702	0.033
$2\,^3P_1$	4.703	0.033
$2\,^3P_2$	4.704	0.032
$3\,^3S_1$	4.711	0.039
$4\,^3S_1$	4.666	0.045
Average	4.725	0.137

Table D.6: Results for m_b with Counting 2 and lattice input. The values are computed as in Table D.4.

State	$m_c(n\,^{2S+1}L_J)\,[GeV]$	$\sigma_{m_c}\,[GeV]$
$1\,^1S_0$	1.376	0.044
$2\,^1S_0$	1.347	0.047
$1\,^3S_1$	1.384	0.039
$2\,^3S_1$	1.328	0.046
$1\,^3P_0$	1.282	0.039
$1\,^3P_1$	1.315	0.037
$1\,^1P_1$	1.324	0.035
$1\,^3P_2$	1.338	0.033
Average	1.338	0.114

Table D.7: Results for m_c with Counting 2 and lattice input. The values are computed as in Table D.4.

State	$m_c(n\,^{2S+1}L_J)\,[GeV]$	$\sigma_{m_c}\,[GeV]$
$1\,^1S_0$	1.053	0.015
$2\,^1S_0$	1.094	0.038
$1\,^3S_1$	1.115	0.014
$2\,^3S_1$	1.122	0.038
$1\,^3P_0$	1.083	0.037
$1\,^3P_1$	1.159	0.033
$1\,^1P_1$	1.183	0.03
$1\,^3P_2$	1.215	0.028
Average	1.130	0.086

Table D.8: Results for m_c with Counting 3 and lattice input. The values are computed as in Table D.4.

D.2 Consistency of the potential

D.2.1 Counting 1

For reading convenience, let us recall the definition of the potential adopting Counting 1 with the following notation

$$V^{\rm LO} = V_1^{\rm LO} + V_2^{\rm LO} \sim mv^2, \tag{D.1}$$

$$V^{\rm NLO} = \frac{2\kappa}{m\pi}\log(\sqrt{\kappa}r) \sim mv^3, \tag{D.2}$$

$$V^{\rm NNLO} = V_2^{(1/m)} + V^{\rm NNLO'} \sim mv^4, \tag{D.3}$$

where

$$V_1^{\rm LO} \equiv -C_F\frac{a}{r}, \tag{D.4}$$

$$V_2^{\rm LO} \equiv \kappa r, \tag{D.5}$$

$$V_2^{(1/m)} \equiv -\frac{C_F C_A a^2}{2mr^2}, \tag{D.6}$$

$$\begin{aligned} V^{\rm NNLO'} \equiv & -\frac{\mathbf{p}^4}{4m^3} + \frac{1}{m^2}\left\{\frac{1}{2}\left\{\mathbf{p}^2, -\frac{C_F a}{r}\right\} + \left(\frac{C_F a}{2r^3} - \frac{\kappa}{6r}\right)\mathbf{L}^2 + \left(\frac{3C_F a}{2r^3} - \frac{\kappa}{2r}\right)\mathbf{L}\cdot\mathbf{S}\right. \\ & + \left.\frac{4\pi C_F a}{3}\delta^{(3)}(\mathbf{r})\mathbf{S}^2 + \frac{C_F a}{4r^3}\mathbf{S}_{12}(\hat{\mathbf{r}}) + \pi C_F a\delta^{(3)}(\mathbf{r})\right\}. \end{aligned} \tag{D.7}$$

In this counting the potential has the same shape for both bottomonium and charmonium states. Using the values of a, κ, m_b and m_c obtained from for the parameter fitting, in Tables D.9 - D.12 we compare the expectation values of $V^{\rm LO}$, $V^{\rm NLO}$ and $V^{\rm NNLO}$ calculated in all initial states of the E1 decays we are evaluating.

State	$\lvert\langle V_1^{\rm LO}\rangle\rvert$	$\lvert\langle V_2^{LO}\rangle\rvert$	$\lvert\langle V^{\rm NLO}\rangle\rvert(\lvert\sqrt{\kappa\langle r\rangle}\rvert)$	$\lvert\langle V_2^{(1/m)}\rangle\rvert$	$\lvert\langle V^{\rm NNLO'}\rangle\rvert$
$1\,^1P_1$	0.17	0.38	0.005 (0.89)	0.008	0.02
$2\,^1P_1$	0.13	0.58	0.005 (1.37)	0.006	0.02
$1\,^3P_0$	0.17	0.38	0.005 (0.89)	0.008	0.03
$1\,^3P_1$	0.17	0.38	0.005 (0.89)	0.008	0.02
$1\,^3P_2$	0.17	0.38	0.005 (0.89)	0.008	0.01
$2\,^3P_0$	0.13	0.58	0.005 (1.37)	0.006	0.04
$2\,^3P_1$	0.13	0.58	0.005 (1.37)	0.006	0.03
$2\,^3P_2$	0.13	0.58	0.005 (1.37)	0.006	0.02
$2\,^3S_1$	0.19	0.47	0.002 (1.09)	0.025	0.02
$3\,^3S_1$	0.15	0.66	0.006 (1.55)	0.019	0.03
$3\,^3P_1$	0.11	0.76	0.011 (1.78)	0.005	0.04

Table D.9: Consistency test of the ordering of the potential in the initial bottomonium states adopting Counting 1 with phenomenology input. We show the expectation value of the NLO potential together with the expectation value of the argument of the logarithm. The suppression of the NLO potential was noticed also in Chapter 4, where considering just the long-distance potential, for some states the NLO logarithmic potential turned out to be more suppressed than some of the NNLO contributions. We also display the expectation values of the NNLO $1/m$-suppressed corrections, which turn out to be larger than the NLO ones. All energy values in GeV.

State	$\lvert\langle V_1^{\rm LO}\rangle\rvert$	$\lvert\langle V_2^{LO}\rangle\rvert$	$\lvert\langle V^{\rm NLO}\rangle\rvert(\lvert\sqrt{\kappa\langle r\rangle}\rvert)$	$\lvert\langle V_2^{(1/m)}\rangle\rvert$	$\lvert\langle V^{\rm NNLO'}\rangle\rvert$
$1\,^1P_1$	0.24	0.42	0.005 (0.89)	0.017	0.03
$2\,^1P_1$	0.18	0.65	0.006 (1.39)	0.013	0.04
$1\,^3P_0$	0.24	0.42	0.005 (0.89)	0.017	0.05
$1\,^3P_1$	0.24	0.42	0.005 (0.89)	0.017	0.03
$1\,^3P_2$	0.24	0.42	0.005 (0.89)	0.017	0.02
$2\,^3P_0$	0.18	0.65	0.006 (1.39)	0.013	0.06
$2\,^3P_1$	0.18	0.65	0.006 (1.39)	0.013	0.04
$2\,^3P_2$	0.18	0.65	0.006 (1.39)	0.013	0.03
$2\,^3S_1$	0.28	0.51	0.002 (1.1)	0.056	0.03
$3\,^3S_1$	0.21	0.74	0.008 (1.57)	0.042	0.04
$3\,^3P_1$	0.15	0.85	0.013 (1.82)	0.011	0.05

Table D.10: Consistency test of the potential in the initial bottomonium states adopting Counting 1 with lattice input. Values as in Table D.9.

State	$\lvert\langle V_1^{\rm LO}\rangle\rvert$	$\lvert\langle V_2^{LO}\rangle\rvert$	$\lvert\langle V^{\rm NLO}\rangle\rvert(\lvert\sqrt{\kappa\langle r\rangle}\rvert)$	$\lvert\langle V_2^{(1/m)}\rangle\rvert$	$\lvert\langle V^{\rm NNLO'}\rangle\rvert$
$1\,^1P_1$	0.1	0.62	0.027 (1.45)	0.01	0.07
$1\,^3P_0$	0.1	0.62	0.027 (1.45)	0.01	0.09
$1\,^3P_1$	0.1	0.62	0.027 (1.45)	0.01	0.07
$1\,^3P_2$	0.1	0.62	0.027 (1.45)	0.01	0.07
$2\,^3S_1$	0.12	0.76	0.035 (1.77)	0.029	0.09

Table D.11: Consistency test of the potential in the initial charmonium states adopting Counting 1 with phenomenology input. Values as in Table D.9.

State	$\lvert\langle V_1^{\rm LO}\rangle\rvert$	$\lvert\langle V_2^{LO}\rangle\rvert$	$\lvert\langle V^{\rm NLO}\rangle\rvert(\lvert\sqrt{\kappa\langle r\rangle}\rvert)$	$\lvert\langle V_2^{(1/m)}\rangle\rvert$	$\lvert\langle V^{\rm NNLO'}\rangle\rvert$
$1\,^1P_1$	0.14	0.7	0.035 (1.49)	0.021	0.1
$1\,^3P_0$	0.14	0.7	0.035 (1.49)	0.021	0.14
$1\,^3P_1$	0.14	0.7	0.035 (1.49)	0.021	0.1
$1\,^3P_2$	0.14	0.7	0.035 (1.49)	0.021	0.1
$2\,^3S_1$	0.17	0.85	0.046 (1.82)	0.063	0.13

Table D.12: Consistency test of the potential evaluated in the initial charmonium states adopting Counting 1 with lattice input. Values as in Table D.9.

D.2.2 Counting 3

We repeat the analysis of the previous section now for Counting 3. For the evaluations of the expectation values of the bottomonium states, the potential has the same shape as in Counting 1, so we adopt the same notation. In the case of the evaluations in charmonium states, the potential is given by

$$V^{\rm LO} = \kappa r \sim mv^2, \tag{D.8}$$

$$V^{\rm NLO} = V_1^{\rm NLO} + V_2^{\rm NLO} \sim mv^3, \tag{D.9}$$

$$V^{\rm NNLO} = -\frac{\mathbf{p}^4}{4m^3} + \frac{1}{m^2}\left\{-\frac{\kappa}{6r}\mathbf{L}^2 - \frac{\kappa}{2r}\mathbf{L}\cdot\mathbf{S}\right\} \sim mv^4, \tag{D.10}$$

where

$$V_1^{\rm NLO} \equiv \frac{2\kappa}{m\pi}\log(\sqrt{\kappa}r). \tag{D.11}$$

$$V_2^{\rm NLO} \equiv -C_F\frac{a}{r}. \tag{D.12}$$

The results of the study of the realization of this ordering in the potential are shown in Tables D.13 - D.15.

State	$\|\langle V_1^{\rm LO}\rangle\|$	$\|\langle V_2^{LO}\rangle\|$	$\|\langle V^{\rm NLO}\rangle\|(\|\sqrt{\kappa\langle r\rangle}\|)$	$\|\langle V_2^{(1/m)}\rangle\|$	$\|\langle V^{\rm NNLO'}\rangle\|$
$1\,^1P_1$	0.19	0.42	0.005 (0.91)	0.011	0.02
$2\,^1P_1$	0.15	0.64	0.006 (1.4)	0.008	0.03
$1\,^3P_0$	0.19	0.42	0.005 (0.91)	0.011	0.04
$1\,^3P_1$	0.19	0.42	0.005 (0.91)	0.011	0.02
$1\,^3P_2$	0.19	0.42	0.005 (0.91)	0.011	0.01
$2\,^3P_0$	0.15	0.64	0.006 (1.4)	0.008	0.05
$2\,^3P_1$	0.15	0.64	0.006 (1.4)	0.008	0.03
$2\,^3P_2$	0.15	0.64	0.006 (1.4)	0.008	0.03
$2\,^3S_1$	0.22	0.51	0.001 (1.12)	0.035	0.02
$3\,^3S_1$	0.17	0.72	0.008 (1.58)	0.026	0.04
$3\,^3P_1$	0.12	0.83	0.013 (1.82)	0.007	0.05

Table D.13: The same as Table D.9, but using the results of the fitting adopting the Counting 3 with phenomenology input.

State	$\|\langle V^{\rm LO}\rangle\|$	$\|\langle V_1^{\rm NLO}\rangle\|(\|\sqrt{\kappa\langle r\rangle}\|)$	$\|\langle V_2^{\rm NLO}\rangle\|$	$\|\langle V^{\rm NNLO}\rangle\|$
$1\,^1P_1$	0.76	0.05 (1.66)	0.1	0.07
$1\,^3P_0$	0.76	0.05 (1.66)	0.1	0.01
$1\,^3P_1$	0.76	0.05 (1.66)	0.1	0.04
$1\,^3P_2$	0.76	0.05 (1.66)	0.1	0.09
$2\,^3S_1$	0.93	0.06 (2.02)	0.12	0.09

Table D.14: Consistency test of the potential for initial charmonium states using Counting 3 with phenomenology input. All energy values in GeV.

State	$\|\langle V^{\rm LO}\rangle\|$	$\|\langle V_1^{\rm NLO}\rangle\|(\|\sqrt{\kappa\langle r\rangle}\|)$	$\|\langle V_2^{\rm NLO}\rangle\|$	$\|\langle V^{\rm NNLO}\rangle\|$
$1\,^1P_1$	0.78	0.06 (1.67)	0.13	0.07
$1\,^3P_0$	0.78	0.06 (1.67)	0.13	0.01
$1\,^3P_1$	0.78	0.06 (1.67)	0.13	0.04
$1\,^3P_2$	0.78	0.06 (1.67)	0.13	0.1
$2\,^3S_1$	0.95	0.07 (2.03)	0.14	0.09

Table D.15: The same as Table D.14, now with lattice input.

Appendix E

The `SChroe.py` script

In this section we describe the method used to solve the Schrödinger equation together with a basic example of the usage of the script where this method has been implemented.

Problem set-up and solution method

The time-independent Schrödinger equation for two particles interacting through a potential $V(\mathbf{r})$ is given by

$$\left(-\frac{\nabla_{\mathbf{r}}^2}{2\mu} + V(\mathbf{r})\right)\psi(\mathbf{r}) = E\psi(\mathbf{r}), \tag{E.1}$$

where $\psi(\mathbf{r})$ is the wavefunction, E is the eigenvalue and μ is the reduced mass given by

$$\mu = \frac{m_1 m_2}{m_1 + m_2}, \tag{E.2}$$

with m_i being the masses of the particles. If we consider the equal mass case with a spherically symmetric potential $V(r)$, the equation reduces to

$$\left[-\frac{1}{m}\frac{d^2}{dr^2} + \frac{l(l+1)}{mr^2} + V(r)\right] y_{n,l}(r) = E_{n,l} y_{n,l}(r), \tag{E.3}$$

where $y_{n,l}$ is the *reduced radial wavefunction* defined through

$$\psi(\mathbf{r})_{n,l} \equiv \frac{y_{n,l}(r)}{r}\mathcal{Y}(\theta,\phi), \tag{E.4}$$

where the pair (n, l) are the radial and angular momentum quantum numbers respectively and $\mathcal{Y}(\theta,\phi)$ are the spherical harmonics.
The fundamental computational problem related to Eq. (E.3) is to find $E_{n,l}$ for a given n and l. The standard method to solve this problem is called the *shooting method*, which consists of applying two known constraints to the reduced wavefunction $y_{n,l}$:

- The number of nodes (number of times the wavefunction crosses the x axis) of $y_{n,l}(r)$ must be equal to $n - 1$. This result is called the *nodal theorem*.

- $y_{n,l}(r)$ has to be normalizable:

$$\int_0^\infty dr[y_{n,l}(r)]^2 = 1. \tag{E.5}$$

In general $y_{n,l}(r)$ will diverge except when $E_{n,l}$ corresponds to an eigenvalue. The procedure to find the eigenvalues consists in performing a scan of values of $E_{n,l}$ until $y_{n,l}(r)$ has $n-1$ nodes and converges for a large enough value of r, see Fig. E.1. This implies that for each test value of $E_{n,l}$ Eq. (E.3) must be solved.
The algorithm to solve (E.3) for a given pair $n = N, l = L$ can be summarized as follows:

- A lower and an upper bound E_{low} and E_{up} of the interval in which the eigenvalue is expected to lie must be specified in the input. Also the precision P of the calculation must be specified.
- There will be two loops running: the *solver loop*, that computes the eigenfunction for a given probe eigenvalue and the *global loop* in which the eigenvalue that the solver loop receives is modified.
- In our implementation we solve Eq. (E.3) with $E_{n,l} \equiv \epsilon = (E_{\text{low}} + E_{\text{up}})/2$ using the Runge-Kutta (RK) method. In each step of the RK loop, the solver loop, we compare the sign of $y_{n,l}$ with respect to its sign in the previous step; if it is different, we have that $y_{n,l}$ has crossed the x axis, so we increase the node counter that initially has been set to zero.
- In each step of the solver loop the following conditionals are analysed:
  - If the number of nodes is larger than $N-1$, the solver loop stops and then we call again the global loop, now with $E_{\text{up}} = \epsilon$ while E_{low} remains the same.
  - If $y_{n,l}$ starts to diverge, the solver loop stops and for the next step in the global loop $E_{\text{low}} = \epsilon$ while E_{up} remains the same.
  - The asymptotic behavior of $y_{n,l}$ can be determined by looking at its derivative, which is calculated in each step of the solver loop: if the derivative and the function have the same sign, then the function diverges [120].
- The global loop stops when $E_{\text{up}} - E_{\text{low}} < P$; then ϵ corresponds to the eigenvalue $E_{N,L}$ at the given precision P.

In our implementation, the wavefunctions (arrays) that result from this method have the following structure:

$$y = [[(x_0, y(x_0)], [x_1, y(x_1)], \ldots, [x_{\max}, y(x_{\max})]]. \tag{E.6}$$

In general, the smaller the value of P, the larger the value of $x_{\max}$ and the smaller the value of $y(x_{\max})$. For different wavefunctions, the value of $x_{\max}$ will be in general also different. We must account for this difference when computing the integrals of the matrix

elements, which will be defined up to the smaller of the two $x_{\max}$ values.
For more details about the solution method we refer the reader to [120] and to [133], where the code of `SChroe.py` is available.

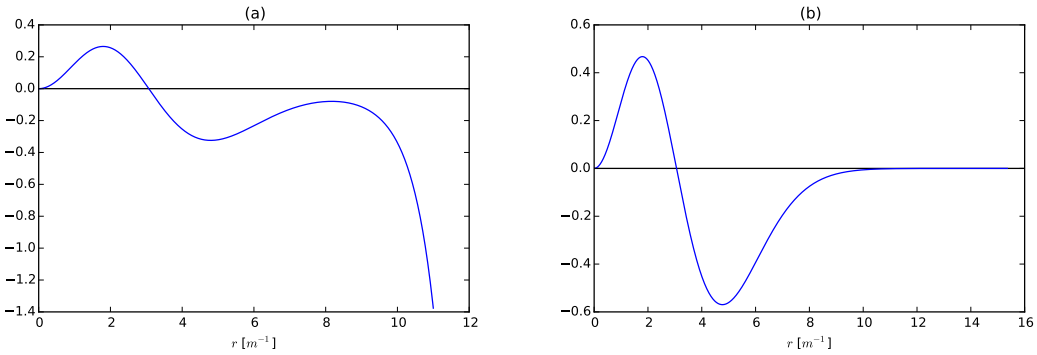

Figure E.1: `SChroe.py` algorithm: (a) if the probe value is not an eigenvalue of the Hamiltonian the wavefunction will not converge for large r; (b) the eigenvalue is found when the wavefunction has the right number of nodes and converges for large r.

Usage

Before running the script, the potential must be specified in the `potential.h` file for the `C` solver, or in the `SChroe.py` file if one wants to use the pure `Python` solver. In the case of the potential of Eq. (5.16), the definition in `C` reads

```
long double V(long double r, long double k, long double sig){
    return -4.*k/(3.*r)+sig*r;
}
```

The user must take care that the inputs of the potential are accounted for in the Python code when calling the `C` functions, see the accompanying example in [133]. Once the potential is defined, the operation of `SChroe.py` is very simple:

```
>> run SChroe.py
>> E = eigenvalueC(ELOW,EUP,n,l,a,t,m)
>> Y = eigenfunctionC(E,l,a,t,m)
```

In the above block of code, `E` stores the eigenvalue of the potential with quantum numbers `n` and `l`, which must lie in the interval spanned between `ELOW` and `EUP`. In this specific example, we should also specify the parameters of the potential `a,t,m` as an additional input, the shape of the input depends on the definition of the potential. In the next line, using the value `E`, the array corresponding to the reduced radial wavefunction is calculated and stored in the variable `Y`.
Together with these basic functions, the script provides some useful aliases of `SciPy` functions in order to manipulate the wavefunctions. For instance, assuming the user has calculated two wavefunctions `Y` and `Yp`, some of the provided functions are

```
>> def F(r):
>>     return r**2
>> I = wfpro(F,Y,Yp)
>> K = wfint(I)
```

In this example, the function $F(r) = r^2$ is first defined, then the variable K stores the result of $\int_0^\infty dr Y_p(r) r^2 Y(r)$ calculated with the `SChroe.py` function `wfint`. The intermediate step defines the integrand `I` through the SChroe.py function `wfpro`, which returns the array that corresponds to the product of two arrays and one function. The integral is computed using the `SciPy` function `integrate.simps` described in Chapter 7. The script also provides plotting functions that can easily be integrated within a notebook environment; an example is displayed in Fig. 7.1.
`SChroe.py` is useful in cases where the functional shape of the potential is fixed, like in the case of Eq. (5.16), however, for applications in which one needs to change the potential the script is not so useful, since for each potential the code needs to be modified.

Appendix F

Detailed partial results for the decay rates

F.1 Further details of the evaluation of the decay rates

The following tables provide further details of the partial results of the numerical evaluation of the E1 decay rates.

Decay	k_γ [GeV]	$\overline{\Gamma^{\rm LO}}$ [keV]	$\epsilon^{\rm LO}_{\rm par}$ (%) [keV]	$\epsilon^{\rm LO}_{\rm rel}$ (%) [keV]	$\overline{R}$	$\overline{\delta\Gamma}$	$\overline{\Gamma^{\rm NLO}}$ [keV]	$\epsilon^{\rm NLO}_{\rm par}$ (%) [keV]	$\epsilon^{\rm NLO}_{\rm rel}$ (%) [keV]
$1^1P_1 \to 1^1S_0\gamma$	0.5	1065.52	124.34(11.7)	550.55(51.7)	-0.56	-0.112	363.04	241.38(66.5)	148.17(40.8)
$2^1S_0 \to 1^1P_1\gamma$	0.11	0.13	0.03(24.2)	0.07(57.0)	-0.16	0.0003	0.11	0.03(29.9)	0.02(22.0)
$1^3P_0 \to 1^3S_1\gamma$	0.3	237.13	27.67(11.7)	122.53(51.7)	-0.31	-0.273	100.34	37.29(37.2)	32.98(32.9)
$1^3P_1 \to 1^3S_1\gamma$	0.39	502.98	58.7(11.7)	259.89(51.7)	-0.39	-0.155	234.7	85.88(36.6)	69.94(29.8)
$1^3P_2 \to 1^3S_1\gamma$	0.43	675.7	78.85(11.7)	349.13(51.7)	-0.38	-0.028	407.95	98.51(24.1)	93.96(23.0)
$2^3S_1 \to 1^3P_0\gamma$	0.26	60.69	4.39(7.2)	34.53(56.9)	-0.57	-0.057	22.65	8.34(36.8)	11.27(49.7)
$2^3S_1 \to 1^3P_1\gamma$	0.17	51.23	3.71(7.2)	29.15(56.9)	-0.31	0.012	36.04	3.53(9.8)	9.51(26.4)
$2^3S_1 \to 1^3P_2\gamma$	0.13	35.32	2.56(7.2)	20.1(56.9)	-0.27	-0.011	25.56	2.55(10.0)	6.56(25.7)

Table F.1: Summary of the results obtained from the evaluation of the charmonium decay rates using Counting 1 with phenomenology input. The photon energy k_γ is computed using Eq. (6.4), the values of $\overline{\Gamma^{\rm LO}}$ and $\overline{\Gamma^{\rm NLO}}$ and the uncertainties are computed as explained in Sec. 8.1. For further reference, we include also the mean value of the two kinds of relativistic corrections: $\overline{R}$ and $\overline{\delta\Gamma}$. For each uncertainty, in brackets we display its percent value relative to $\overline{\Gamma^{\rm LO}}$ or $\overline{\Gamma^{\rm NLO}}$.

Decay	k_γ [GeV]	$\overline{\Gamma^{\rm LO}}$ [keV]	$\epsilon^{\rm LO}_{\rm par}$ (%) [keV]	$\epsilon^{\rm LO}_{\rm rel}$ (%) [keV]	$\overline{R}$	$\overline{\delta\Gamma}$	$\overline{\Gamma^{\rm NLO}}$ [keV]	$\epsilon^{\rm NLO}_{\rm par}$ (%) [keV]	$\epsilon^{\rm NLO}_{\rm rel}$ (%) [keV]
$1^1P_1 \to 1^1S_0\gamma$	0.49	78.43	18.6(23.7)	18.58(23.7)	-0.46	-0.034	44.08	29.03(65.8)	1.05(2.4)
$2^1P_1 \to 1^1S_0\gamma$	0.83	10.28	2.82(27.4)	2.82(27.5)	0.5	0.132	17.14	5.63(32.8)	0.21(1.2)
$2^1P_1 \to 2^1S_0\gamma$	0.26	28.48	4.95(17.4)	7.75(27.2)	-0.45	-0.024	16.04	9.21(57.4)	0.58(3.6)
$2^1S_0 \to 1^1P_1\gamma$	0.1	0.07	0.02(27.4)	0.02(26.5)	0.02	-0.001	0.07	0.02(30.8)	0.001(1.8)
$1^3P_0 \to 1^3S_1\gamma$	0.39	40.21	9.53(23.7)	9.53(23.7)	-0.24	-0.051	29.89	12.22(40.9)	0.54(1.8)
$1^3P_1 \to 1^3S_1\gamma$	0.42	50.9	12.07(23.7)	12.06(23.7)	-0.28	-0.037	36.24	15.78(43.5)	0.68(1.9)
$1^3P_2 \to 1^3S_1\gamma$	0.44	57.91	13.73(23.7)	13.72(23.7)	-0.28	-0.022	41.88	17.16(41.0)	0.78(1.9)
$2^3P_0 \to 1^3S_1\gamma$	0.74	7.5	2.06(27.4)	2.06(27.5)	-0.21	-0.046	5.51	1.36(24.7)	0.16(2.8)
$2^3P_1 \to 1^3S_1\gamma$	0.76	8.16	2.24(27.4)	2.24(27.5)	0.04	0.038	8.84	2.47(27.9)	0.17(1.9)
$2^3P_2 \to 1^3S_1\gamma$	0.78	8.56	2.35(27.4)	2.35(27.5)	0.28	0.186	12.72	3.94(31.0)	0.18(1.4)
$2^3P_0 \to 2^3S_1\gamma$	0.21	14.82	2.58(17.4)	4.03(27.2)	-0.17	-0.031	12.06	3.15(26.1)	0.3(2.5)
$2^3P_1 \to 2^3S_1\gamma$	0.23	20.19	3.51(17.4)	5.5(27.2)	-0.24	-0.025	15.22	4.83(31.7)	0.41(2.7)
$2^3P_2 \to 2^3S_1\gamma$	0.24	23.78	4.13(17.4)	6.47(27.2)	-0.29	-0.019	16.93	6.04(35.7)	0.48(2.8)
$3^3P_1 \to 1^3S_1\gamma$	1.0	3.29	1.37(41.5)	1.0(30.3)	0.18	-0.041	3.94	2.03(51.7)	0.09(2.3)
$3^3P_1 \to 2^3S_1\gamma$	0.48	2.95	0.77(26.2)	0.89(30.3)	-0.002	0.095	3.26	0.97(29.7)	0.08(2.5)
$3^3P_1 \to 3^3S_1\gamma$	0.15	10.82	1.58(14.6)	3.26(30.1)	-0.22	-0.021	8.34	2.21(26.6)	0.3(3.6)
$2^3S_1 \to 1^3P_0\gamma$	0.16	1.6	0.12(7.2)	0.42(26.2)	-0.2	-0.013	1.26	0.13(10.7)	0.03(2.3)
$2^3S_1 \to 1^3P_1\gamma$	0.13	2.43	0.18(7.2)	0.64(26.2)	-0.09	-0.002	2.21	0.17(7.7)	0.04(2.0)
$2^3S_1 \to 1^3P_2\gamma$	0.11	2.51	0.18(7.2)	0.66(26.2)	-0.04	0.004	2.42	0.18(7.6)	0.05(1.9)
$3^3S_1 \to 2^3P_0\gamma$	0.12	1.6	0.12(7.3)	0.47(29.1)	-0.2	-0.007	1.27	0.11(8.8)	0.04(3.1)
$3^3S_1 \to 2^3P_1\gamma$	0.1	2.59	0.19(7.3)	0.75(29.1)	-0.07	-0.0005	2.4	0.19(7.7)	0.06(2.7)
$3^3S_1 \to 2^3P_2\gamma$	0.09	2.82	0.2(7.3)	0.82(29.1)	-0.02	-0.0001	2.75	0.24(8.8)	0.07(2.5)

Table F.2: Summary of the results obtained from the evaluation of the bottomonium decay rates using Counting 1 with phenomenology input. Values as in Table F.1.

Decay	k_γ [GeV]	$\overline{\Gamma^{\rm LO}}$ [keV]	$\epsilon^{\rm LO}_{\rm par}$ (%) [keV]	$\epsilon^{\rm LO}_{\rm rel}$ (%) [keV]	$\overline{R}$	$\overline{\delta\Gamma}$	$\overline{\Gamma^{\rm NLO}}$ [keV]	$\epsilon^{\rm NLO}_{\rm par}$ (%) [keV]	$\epsilon^{\rm NLO}_{\rm rel}$ (%) [keV]
$1^1P_1 \to 1^1S_0\gamma$	0.49	55.88	3.49(6.2)	14.78(26.4)	-0.8	-0.031	9.65	4.94(51.2)	1.03(10.7)
$2^1P_1 \to 1^1S_0\gamma$	0.83	11.7	0.45(3.9)	3.47(29.7)	0.8	0.051	21.69	1.03(4.8)	0.31(1.4)
$2^1P_1 \to 2^1S_0\gamma$	0.26	21.9	1.11(5.1)	6.5(29.7)	-0.77	-0.022	4.65	1.71(36.9)	0.57(12.3)
$2^1S_0 \to 1^1P_1\gamma$	0.1	0.08	0.003(3.9)	0.02(28.9)	0.07	-0.002	0.09	0.004(4.5)	0.002(2.3)
$1^3P_0 \to 1^3S_1\gamma$	0.39	28.65	1.79(6.2)	7.58(26.4)	-0.4	-0.081	15.01	2.06(13.8)	0.53(3.5)
$1^3P_1 \to 1^3S_1\gamma$	0.42	36.27	2.27(6.2)	9.59(26.4)	-0.48	-0.051	17.16	2.65(15.4)	0.67(3.9)
$1^3P_2 \to 1^3S_1\gamma$	0.44	41.26	2.58(6.2)	10.91(26.4)	-0.48	-0.003	21.27	3.01(14.2)	0.76(3.6)
$2^3P_0 \to 1^3S_1\gamma$	0.74	8.53	0.33(3.9)	2.53(29.7)	-0.2	-0.149	5.57	0.26(4.7)	0.22(4.0)
$2^3P_1 \to 1^3S_1\gamma$	0.76	9.28	0.36(3.9)	2.75(29.7)	0.14	-0.05	10.12	0.44(4.3)	0.24(2.4)
$2^3P_2 \to 1^3S_1\gamma$	0.78	9.73	0.38(3.9)	2.89(29.7)	0.48	0.134	15.74	0.71(4.5)	0.25(1.6)
$2^3P_0 \to 2^3S_1\gamma$	0.21	11.4	0.58(5.1)	3.38(29.7)	-0.27	-0.041	7.89	0.64(8.1)	0.3(3.8)
$2^3P_1 \to 2^3S_1\gamma$	0.23	15.52	0.79(5.1)	4.6(29.7)	-0.39	-0.029	8.96	0.93(10.4)	0.41(4.5)
$2^3P_2 \to 2^3S_1\gamma$	0.24	18.29	0.93(5.1)	5.42(29.7)	-0.48	-0.011	9.26	1.15(12.4)	0.48(5.2)
$3^3P_1 \to 1^3S_1\gamma$	1.0	4.2	0.25(6.0)	1.37(32.5)	0.41	-0.116	5.44	0.45(8.3)	0.14(2.7)
$3^3P_1 \to 2^3S_1\gamma$	0.48	3.32	0.13(3.9)	1.08(32.5)	0.11	0.026	3.77	0.19(5.0)	0.11(3.0)
$3^3P_1 \to 3^3S_1\gamma$	0.15	8.61	0.4(4.6)	2.8(32.5)	-0.36	-0.024	5.34	0.46(8.6)	0.3(5.5)
$2^3S_1 \to 1^3P_0\gamma$	0.16	1.44	0.05(3.4)	0.41(28.9)	-0.27	-0.013	1.03	0.04(3.7)	0.03(3.4)
$2^3S_1 \to 1^3P_1\gamma$	0.13	2.19	0.07(3.4)	0.63(28.9)	-0.11	-0.002	1.95	0.06(3.3)	0.05(2.7)
$2^3S_1 \to 1^3P_2\gamma$	0.11	2.25	0.08(3.4)	0.65(28.9)	-0.02	0.005	2.22	0.07(3.2)	0.05(2.4)
$3^3S_1 \to 2^3P_0\gamma$	0.12	1.46	0.05(3.2)	0.46(31.6)	-0.25	-0.006	1.08	0.03(3.2)	0.05(4.3)
$3^3S_1 \to 2^3P_1\gamma$	0.1	2.36	0.08(3.2)	0.75(31.6)	-0.07	0.0	2.2	0.07(3.1)	0.07(3.4)
$3^3S_1 \to 2^3P_2\gamma$	0.09	2.58	0.08(3.2)	0.81(31.6)	0.01	0.0	2.61	0.08(3.1)	0.08(3.1)

Table F.3: Summary of the results obtained from the evaluation of the bottomonium decay rates using Counting 1 with lattice input. Values as in Table F.1.

Decay	k_γ [GeV]	$\overline{\Gamma^{\rm LO}}$ [keV]	$\epsilon^{\rm LO}_{\rm par}$ (%) [keV]	$\epsilon^{\rm LO}_{\rm rel}$ (%) [keV]	$\overline{R}$	$\overline{\delta\Gamma}$	$\overline{\Gamma^{\rm NLO}}$ [keV]	$\epsilon^{\rm NLO}_{\rm par}$ (%) [keV]	$\epsilon^{\rm NLO}_{\rm rel}$ (%) [keV]
$1^1P_1 \to 1^1S_0\gamma$	0.5	904.33	82.34(9.1)	517.01(57.2)	-0.86	-0.108	29.95	65.12(217.4)	171.14(571.5)
$2^1S_0 \to 1^1P_1\gamma$	0.11	0.14	0.01(4.9)	0.09(62.6)	-0.14	-0.004	0.12	0.01(5.3)	0.04(28.9)
$1^3P_0 \to 1^3S_1\gamma$	0.3	201.26	18.33(9.1)	115.06(57.2)	-0.43	-0.37	38.37	13.7(35.7)	38.09(99.3)
$1^3P_1 \to 1^3S_1\gamma$	0.39	426.89	38.87(9.1)	244.05(57.2)	-0.56	-0.201	102.22	22.81(22.3)	80.79(79.0)
$1^3P_2 \to 1^3S_1\gamma$	0.43	573.48	52.22(9.1)	327.86(57.2)	-0.54	0.021	277.54	22.74(8.2)	108.53(39.1)
$2^3S_1 \to 1^3P_0\gamma$	0.26	56.03	4.06(7.2)	35.17(62.8)	-0.8	-0.043	8.7	3.87(44.5)	14.04(161.4)
$2^3S_1 \to 1^3P_1\gamma$	0.17	47.3	3.43(7.2)	29.69(62.8)	-0.4	0.02	29.42	1.01(3.4)	11.85(40.3)
$2^3S_1 \to 1^3P_2\gamma$	0.13	32.61	2.36(7.2)	20.47(62.8)	-0.29	-0.015	22.39	0.83(3.7)	8.17(36.5)

Table F.4: Summary of the results obtained from the evaluation of the charmonium decay rates using Counting 1 with lattice input. Values as in Table F.1.

Decay	k_γ [GeV]	$\overline{\Gamma^{\rm LO}}$ [keV]	$\epsilon^{\rm LO}_{\rm par}$ (%) [keV]	$\epsilon^{\rm LO}_{\rm rel}$ (%) [keV]	$\overline{R}$	$\overline{\delta\Gamma}$	$\overline{\Gamma^{\rm NLO}}$ [keV]	$\epsilon^{\rm NLO}_{\rm par}$ (%) [keV]	$\epsilon^{\rm NLO}_{\rm rel}$ (%) [keV]
$1^1P_1 \to 1^1S_0\gamma$	0.49	79.07	15.6(19.7)	18.87(23.9)	-0.42	-0.035	45.92	25.15(54.8)	1.08(2.4)
$2^1P_1 \to 1^1S_0\gamma$	0.83	10.23	2.98(29.1)	2.82(27.5)	0.68	0.131	19.16	7.47(39.0)	0.22(1.1)
$2^1P_1 \to 2^1S_0\gamma$	0.26	28.68	4.09(14.2)	7.86(27.4)	-0.41	-0.025	16.87	7.66(45.4)	0.59(3.5)
$2^1S_0 \to 1^1P_1\gamma$	0.1	0.07	0.02(29.1)	0.02(26.5)	0.01	-0.001	0.07	0.02(31.7)	0.001(1.8)
$1^3P_0 \to 1^3S_1\gamma$	0.39	40.54	8.0(19.7)	9.67(23.9)	-0.21	-0.05	30.7	10.33(33.6)	0.55(1.8)
$1^3P_1 \to 1^3S_1\gamma$	0.42	51.31	10.12(19.7)	12.24(23.9)	-0.26	-0.037	37.29	13.42(36.0)	0.7(1.9)
$1^3P_2 \to 1^3S_1\gamma$	0.44	58.38	11.52(19.7)	13.93(23.9)	-0.26	-0.022	43.12	14.62(33.9)	0.8(1.9)
$2^3P_0 \to 1^3S_1\gamma$	0.74	7.46	2.17(29.1)	2.06(27.5)	-0.04	-0.049	7.02	2.75(39.2)	0.16(2.2)
$2^3P_1 \to 1^3S_1\gamma$	0.76	8.12	2.36(29.1)	2.24(27.5)	0.22	0.036	10.48	3.96(37.8)	0.17(1.6)
$2^3P_2 \to 1^3S_1\gamma$	0.78	8.51	2.48(29.1)	2.35(27.5)	0.46	0.186	14.41	5.41(37.6)	0.18(1.2)
$2^3P_0 \to 2^3S_1\gamma$	0.21	14.92	2.13(14.2)	4.09(27.4)	-0.14	-0.031	12.42	2.5(20.1)	0.31(2.5)
$2^3P_1 \to 2^3S_1\gamma$	0.23	20.32	2.9(14.2)	5.57(27.4)	-0.21	-0.025	15.73	3.9(24.8)	0.42(2.7)
$2^3P_2 \to 2^3S_1\gamma$	0.24	23.94	3.41(14.2)	6.56(27.4)	-0.26	-0.019	17.56	4.92(28.0)	0.5(2.8)
$3^3P_1 \to 1^3S_1\gamma$	1.0	3.24	1.38(42.6)	0.98(30.4)	0.04	-0.044	3.32	1.6(48.3)	0.09(2.7)
$3^3P_1 \to 2^3S_1\gamma$	0.48	2.93	0.81(27.6)	0.89(30.4)	-0.13	0.093	2.8	0.71(25.4)	0.08(2.9)
$3^3P_1 \to 3^3S_1\gamma$	0.15	10.89	1.3(12.0)	3.3(30.3)	-0.21	-0.021	8.47	1.83(21.6)	0.3(3.6)
$2^3S_1 \to 1^3P_0\gamma$	0.16	1.6	0.13(8.1)	0.42(26.3)	-0.21	-0.013	1.25	0.13(10.5)	0.03(2.4)
$2^3S_1 \to 1^3P_1\gamma$	0.13	2.44	0.2(8.1)	0.64(26.3)	-0.1	-0.002	2.19	0.19(8.4)	0.04(2.0)
$2^3S_1 \to 1^3P_2\gamma$	0.11	2.52	0.2(8.1)	0.66(26.3)	-0.05	0.004	2.4	0.21(8.8)	0.05(1.9)
$3^3S_1 \to 2^3P_0\gamma$	0.12	1.6	0.14(8.6)	0.47(29.2)	-0.21	-0.007	1.25	0.13(10.0)	0.04(3.2)
$3^3S_1 \to 2^3P_1\gamma$	0.1	2.59	0.22(8.6)	0.76(29.2)	-0.09	-0.0003	2.37	0.21(9.1)	0.07(2.7)
$3^3S_1 \to 2^3P_2\gamma$	0.09	2.83	0.24(8.6)	0.83(29.2)	-0.04	-0.0002	2.71	0.27(10.0)	0.07(2.6)

Table F.5: Summary of the results obtained from the evaluation of the bottomonium decay rates using Counting 2 with phenomenology input. Values as in Table F.1.

Decay	k_γ [GeV]	$\overline{\Gamma^{\rm LO}}$ [keV]	$\epsilon^{\rm LO}_{\rm par}$ (%) [keV]	$\epsilon^{\rm LO}_{\rm rel}$ (%) [keV]	$\overline{R}$	$\overline{\delta\Gamma}$	$\overline{\Gamma^{\rm NLO}}$ [keV]	$\epsilon^{\rm NLO}_{\rm par}$ (%) [keV]	$\epsilon^{\rm NLO}_{\rm rel}$ (%) [keV]
$1^1P_1 \to 1^1S_0\gamma$	0.5	1070.74	113.85(10.6)	556.04(51.9)	-0.53	-0.112	393.04	204.22(52.0)	150.78(38.4)
$2^1S_0 \to 1^1P_1\gamma$	0.11	0.13	0.03(25.4)	0.07(57.2)	-0.17	0.0003	0.11	0.03(29.5)	0.02(22.4)
$1^3P_0 \to 1^3S_1\gamma$	0.3	238.29	25.34(10.6)	123.75(51.9)	-0.29	-0.275	105.59	30.77(29.1)	33.56(31.8)
$1^3P_1 \to 1^3S_1\gamma$	0.39	505.44	53.74(10.6)	262.48(51.9)	-0.36	-0.156	246.85	71.71(29.0)	71.18(28.8)
$1^3P_2 \to 1^3S_1\gamma$	0.43	679.01	72.2(10.6)	352.61(51.9)	-0.35	-0.028	425.88	82.41(19.4)	95.62(22.5)
$2^3S_1 \to 1^3P_0\gamma$	0.26	60.8	5.46(9.0)	34.75(57.2)	-0.57	-0.056	22.56	7.68(34.0)	11.41(50.6)
$2^3S_1 \to 1^3P_1\gamma$	0.17	51.32	4.61(9.0)	29.33(57.2)	-0.31	0.013	35.93	3.94(11.0)	9.63(26.8)
$2^3S_1 \to 1^3P_2\gamma$	0.13	35.39	3.18(9.0)	20.22(57.2)	-0.27	-0.011	25.37	3.05(12.0)	6.64(26.2)

Table F.6: Summary of the results obtained from the evaluation of the charmonium decay rates using Counting 2 with phenomenology input. Values as in Table F.1.

Decay	k_γ [GeV]	$\overline{\Gamma^{\rm LO}}$ [keV]	$\epsilon^{\rm LO}_{\rm par}$ (%) [keV]	$\epsilon^{\rm LO}_{\rm rel}$ (%) [keV]	$\overline{R}$	$\overline{\delta\Gamma}$	$\overline{\Gamma^{\rm NLO}}$ [keV]	$\epsilon^{\rm NLO}_{\rm par}$ (%) [keV]	$\epsilon^{\rm NLO}_{\rm rel}$ (%) [keV]
$1^1P_1 \to 1^1S_0\gamma$	0.49	56.56	3.31(5.9)	15.05(26.6)	-0.77	-0.031	11.26	4.97(44.2)	1.07(9.5)
$2^1P_1 \to 1^1S_0\gamma$	0.83	11.74	0.56(4.8)	3.5(29.8)	1.24	0.052	26.95	1.98(7.3)	0.31(1.2)
$2^1P_1 \to 2^1S_0\gamma$	0.26	22.13	0.98(4.4)	6.61(29.9)	-0.72	-0.023	5.64	1.6(28.4)	0.59(10.5)
$2^1S_0 \to 1^1P_1\gamma$	0.1	0.08	0.004(4.8)	0.02(29.1)	0.05	-0.002	0.09	0.004(5.3)	0.002(2.4)
$1^3P_0 \to 1^3S_1\gamma$	0.39	29.0	1.7(5.9)	7.72(26.6)	-0.37	-0.082	15.95	1.95(12.3)	0.55(3.4)
$1^3P_1 \to 1^3S_1\gamma$	0.42	36.7	2.15(5.9)	9.77(26.6)	-0.45	-0.051	18.34	2.54(13.9)	0.69(3.8)
$1^3P_2 \to 1^3S_1\gamma$	0.44	41.75	2.45(5.9)	11.11(26.6)	-0.46	-0.003	22.67	2.93(12.9)	0.79(3.5)
$2^3P_0 \to 1^3S_1\gamma$	0.74	8.56	0.41(4.8)	2.55(29.8)	0.23	-0.151	9.25	0.94(10.1)	0.23(2.5)
$2^3P_1 \to 1^3S_1\gamma$	0.76	9.32	0.44(4.8)	2.78(29.8)	0.57	-0.051	14.19	1.17(8.2)	0.25(1.7)
$2^3P_2 \to 1^3S_1\gamma$	0.78	9.77	0.47(4.8)	2.92(29.8)	0.92	0.136	20.09	1.48(7.4)	0.26(1.3)
$2^3P_0 \to 2^3S_1\gamma$	0.21	11.52	0.51(4.4)	3.44(29.9)	-0.22	-0.042	8.48	0.52(6.1)	0.31(3.6)
$2^3P_1 \to 2^3S_1\gamma$	0.23	15.69	0.69(4.4)	4.69(29.9)	-0.35	-0.029	9.74	0.79(8.1)	0.42(4.3)
$2^3P_2 \to 2^3S_1\gamma$	0.24	18.48	0.81(4.4)	5.52(29.9)	-0.44	-0.011	10.16	1.01(9.9)	0.49(4.9)
$3^3P_1 \to 1^3S_1\gamma$	1.0	4.21	0.32(7.7)	1.38(32.7)	0.14	-0.118	4.28	0.37(8.7)	0.15(3.4)
$3^3P_1 \to 2^3S_1\gamma$	0.48	3.33	0.16(4.9)	1.09(32.7)	-0.2	0.026	2.75	0.11(3.9)	0.12(4.3)
$3^3P_1 \to 3^3S_1\gamma$	0.15	8.69	0.33(3.8)	2.85(32.7)	-0.35	-0.024	5.46	0.4(7.3)	0.31(5.6)
$2^3S_1 \to 1^3P_0\gamma$	0.16	1.45	0.04(2.6)	0.42(29.1)	-0.3	-0.013	0.99	0.03(3.4)	0.04(3.6)
$2^3S_1 \to 1^3P_1\gamma$	0.13	2.2	0.06(2.6)	0.64(29.1)	-0.13	-0.002	1.91	0.05(2.8)	0.05(2.9)
$2^3S_1 \to 1^3P_2\gamma$	0.11	2.27	0.06(2.6)	0.66(29.1)	-0.04	0.005	2.18	0.06(2.6)	0.06(2.6)
$3^3S_1 \to 2^3P_0\gamma$	0.12	1.47	0.04(2.6)	0.47(31.8)	-0.29	-0.006	1.03	0.03(3.2)	0.05(4.6)
$3^3S_1 \to 2^3P_1\gamma$	0.1	2.38	0.06(2.6)	0.76(31.8)	-0.11	0.0	2.12	0.06(2.7)	0.08(3.6)
$3^3S_1 \to 2^3P_2\gamma$	0.09	2.6	0.07(2.6)	0.82(31.8)	-0.03	0.0	2.53	0.07(2.8)	0.08(3.3)

Table F.7: Summary of the results obtained from the evaluation of the bottomonium decay rates using Counting 2 with lattice input. Values as in Table F.1.

Decay	k_γ [GeV]	$\overline{\Gamma^{\rm LO}}$ [keV]	$\epsilon^{\rm LO}_{\rm par}$ (%) [keV]	$\epsilon^{\rm LO}_{\rm rel}$ (%) [keV]	$\overline{R}$	$\overline{\delta\Gamma}$	$\overline{\Gamma^{\rm NLO}}$ [keV]	$\epsilon^{\rm NLO}_{\rm par}$ (%) [keV]	$\epsilon^{\rm NLO}_{\rm rel}$ (%) [keV]
$1^1P_1 \to 1^1S_0\gamma$	0.5	881.08	53.05(6.0)	492.93(55.9)	-0.82	-0.105	64.87	47.73(73.6)	154.99(238.9)
$2^1S_0 \to 1^1P_1\gamma$	0.11	0.14	0.01(5.4)	0.09(61.4)	-0.14	-0.004	0.12	0.01(7.1)	0.03(27.0)
$1^3P_0 \to 1^3S_1\gamma$	0.3	196.09	11.81(6.0)	109.7(55.9)	-0.4	-0.356	47.23	7.41(15.7)	34.49(73.0)
$1^3P_1 \to 1^3S_1\gamma$	0.39	415.91	25.04(6.0)	232.69(55.9)	-0.52	-0.194	117.99	15.48(13.1)	73.16(62.0)
$1^3P_2 \to 1^3S_1\gamma$	0.43	558.73	33.64(6.0)	312.59(55.9)	-0.5	0.019	288.07	24.04(8.3)	98.29(34.1)
$2^3S_1 \to 1^3P_0\gamma$	0.26	55.0	2.55(4.6)	33.8(61.5)	-0.79	-0.045	9.11	2.12(23.3)	12.83(140.8)
$2^3S_1 \to 1^3P_1\gamma$	0.17	46.43	2.15(4.6)	28.53(61.5)	-0.4	0.018	28.85	1.04(3.6)	10.83(37.5)
$2^3S_1 \to 1^3P_2\gamma$	0.13	32.01	1.48(4.6)	19.67(61.5)	-0.29	-0.014	22.12	0.92(4.2)	7.47(33.8)

Table F.8: Summary of the results obtained from the evaluation of the charmonium decay rates using Counting 2 with lattice input. Values as in Table F.1.

Decay	k_γ [GeV]	$\overline{\Gamma^{\rm LO}}$ [keV]	$\epsilon_{\rm par}^{\rm LO}$ (%) [keV]	$\epsilon_{\rm rel}^{\rm LO}$ (%) [keV]	$\overline{R}$	$\overline{\delta\Gamma}$	$\overline{\Gamma^{\rm NLO}}$ [keV]	$\epsilon_{\rm par}^{\rm NLO}$ (%) [keV]	$\epsilon_{\rm rel}^{\rm NLO}$ (%) [keV]
$021^1P_1 \to 1^1S_0\gamma$	0.49	63.96	11.48(17.9)	16.43(25.7)	-0.65	-0.032	24.12	24.11(99.9)	1.09(4.5)
$2^1P_1 \to 1^1S_0\gamma$	0.83	10.57	3.0(28.4)	3.07(29.0)	0.64	0.082	18.44	5.7(30.9)	0.26(1.4)
$2^1P_1 \to 2^1S_0\gamma$	0.26	24.05	3.06(12.7)	7.01(29.2)	-0.63	-0.023	9.22	8.16(88.6)	0.6(6.5)
$2^1S_0 \to 1^1P_1\gamma$	0.1	0.07	0.02(28.4)	0.02(28.2)	0.04	-0.002	0.08	0.03(32.4)	0.002(2.1)
$1^3P_0 \to 1^3S_1\gamma$	0.39	32.79	5.88(17.9)	8.42(25.7)	-0.33	-0.07	20.79	9.02(43.4)	0.56(2.7)
$1^3P_1 \to 1^3S_1\gamma$	0.42	41.51	7.45(17.9)	10.66(25.7)	-0.39	-0.046	24.71	11.9(48.1)	0.71(2.9)
$1^3P_2 \to 1^3S_1\gamma$	0.44	47.22	8.47(17.9)	12.13(25.7)	-0.4	-0.01	29.59	13.37(45.2)	0.81(2.7)
$2^3P_0 \to 1^3S_1\gamma$	0.74	7.71	2.18(28.4)	2.24(29.0)	-0.23	-0.122	5.02	1.72(34.3)	0.19(3.8)
$2^3P_1 \to 1^3S_1\gamma$	0.76	8.39	2.38(28.4)	2.44(29.0)	0.07	-0.022	8.88	2.69(30.3)	0.21(2.3)
$2^3P_2 \to 1^3S_1\gamma$	0.78	8.79	2.49(28.4)	2.55(29.0)	0.37	0.161	13.58	4.05(29.8)	0.22(1.6)
$2^3P_0 \to 2^3S_1\gamma$	0.21	12.51	1.59(12.7)	3.65(29.2)	-0.23	-0.038	9.35	2.36(25.2)	0.31(3.3)
$2^3P_1 \to 2^3S_1\gamma$	0.23	17.04	2.17(12.7)	4.97(29.2)	-0.33	-0.028	11.27	3.8(33.7)	0.43(3.8)
$2^3P_2 \to 2^3S_1\gamma$	0.24	20.08	2.56(12.7)	5.86(29.2)	-0.4	-0.013	12.19	4.93(40.4)	0.5(4.1)
$3^3P_1 \to 1^3S_1\gamma$	1.0	3.65	1.61(44.2)	1.16(31.8)	0.28	-0.103	4.53	2.6(57.3)	0.12(2.6)
$3^3P_1 \to 2^3S_1\gamma$	0.48	3.03	0.88(29.1)	0.97(31.9)	0.04	0.047	3.35	1.18(35.2)	0.1(3.0)
$3^3P_1 \to 3^3S_1\gamma$	0.15	9.28	1.01(10.8)	2.98(32.1)	-0.3	-0.023	6.39	1.76(27.5)	0.31(4.8)
$2^3S_1 \to 1^3P_0\gamma$	0.16	1.46	0.16(10.7)	0.41(28.2)	-0.25	-0.012	1.08	0.13(11.9)	0.03(3.0)
$2^3S_1 \to 1^3P_1\gamma$	0.13	2.22	0.24(10.7)	0.62(28.2)	-0.1	-0.001	1.98	0.22(11.0)	0.05(2.5)
$2^3S_1 \to 1^3P_2\gamma$	0.11	2.29	0.25(10.7)	0.64(28.2)	-0.03	0.004	2.22	0.28(12.5)	0.05(2.3)
$3^3S_1 \to 2^3P_0\gamma$	0.12	1.47	0.18(12.0)	0.46(31.0)	-0.23	-0.005	1.12	0.15(13.1)	0.04(3.9)
$3^3S_1 \to 2^3P_1\gamma$	0.1	2.38	0.29(12.0)	0.74(31.0)	-0.08	0.001	2.21	0.3(13.6)	0.07(3.2)
$3^3S_1 \to 2^3P_2\gamma$	0.09	2.6	0.31(12.0)	0.8(31.0)	-0.01	-0.0004	2.57	0.4(15.6)	0.08(3.0)

Table F.9: Summary of the results obtained from the evaluation of the bottomonium decay rates using Counting 3 with phenomenology input. Values as in Table F.1.

Decay	k_γ [GeV]	$\overline{\Gamma^{\rm LO}}$ [keV]	$\epsilon_{\rm par}^{\rm LO}$ (%) [keV]	$\epsilon_{\rm rel}^{\rm LO}$ (%) [keV]	$\overline{R}$	$\overline{\delta\Gamma}$	$\overline{\Gamma^{\rm NLO}}$ [keV]	$\epsilon_{\rm par}^{\rm NLO}$ (%) [keV]	$\epsilon_{\rm rel}^{\rm NLO}$ (%) [keV]
$1^1P_1 \to 1^1S_0\gamma$	0.5	1345.67	135.94(10.1)	781.24(58.1)	-0.41	-0.131	620.35	69.87(11.3)	269.31(43.4)
$2^1S_0 \to 1^1P_1\gamma$	0.11	0.05	0.005(10.1)	0.03(64.0)	-0.33	0.014	0.03	0.01(15.4)	0.01(39.2)
$1^3P_0 \to 1^3S_1\gamma$	0.3	299.48	30.25(10.1)	173.87(58.1)	-0.41	-0.314	83.95	30.11(35.9)	59.93(71.4)
$1^3P_1 \to 1^3S_1\gamma$	0.39	635.22	64.17(10.1)	368.78(58.1)	-0.41	-0.178	263.58	48.65(18.5)	127.12(48.2)
$1^3P_2 \to 1^3S_1\gamma$	0.43	853.36	86.21(10.1)	495.42(58.1)	-0.41	-0.037	472.9	39.02(8.3)	170.78(36.1)
$2^3S_1 \to 1^3P_0\gamma$	0.26	59.71	6.03(10.1)	38.23(64.0)	-0.23	-0.013	44.86	4.04(9.0)	16.03(35.7)
$2^3S_1 \to 1^3P_1\gamma$	0.17	50.4	5.09(10.1)	32.27(64.0)	-0.28	0.042	38.24	4.41(11.5)	13.53(35.4)
$2^3S_1 \to 1^3P_2\gamma$	0.13	34.75	3.51(10.1)	22.25(64.0)	-0.38	-0.039	20.27	3.92(19.3)	9.33(46.0)

Table F.10: Summary of the results obtained from the evaluation of the charmonium decay rates using Counting 3 with phenomenology input. Values as in Table F.1.

Decay	k_γ [GeV]	$\overline{\Gamma^{\rm LO}}$ [keV]	$\epsilon^{\rm LO}_{\rm par}$ (%) [keV]	$\epsilon^{\rm LO}_{\rm rel}$ (%) [keV]	$\overline{R}$	$\overline{\delta\Gamma}$	$\overline{\Gamma^{\rm NLO}}$ [keV]	$\epsilon^{\rm NLO}_{\rm par}$ (%) [keV]	$\epsilon^{\rm NLO}_{\rm rel}$ (%) [keV]
$1^1P_1 \to 1^1S_0\gamma$	0.5	1322.88	92.38(7.0)	778.24(58.8)	-0.43	-0.13	581.05	20.71(3.6)	272.05(46.8)
$2^1S_0 \to 1^1P_1\gamma$	0.11	0.05	0.003(7.0)	0.03(64.9)	-0.34	0.014	0.03	0.001(3.6)	0.01(41.1)
$1^3P_0 \to 1^3S_1\gamma$	0.3	294.41	20.56(7.0)	173.2(58.8)	-0.43	-0.315	73.13	12.09(16.5)	60.54(82.8)
$1^3P_1 \to 1^3S_1\gamma$	0.39	624.46	43.61(7.0)	367.37(58.8)	-0.43	-0.179	242.47	11.57(4.8)	128.42(53.0)
$1^3P_2 \to 1^3S_1\gamma$	0.43	838.9	58.58(7.0)	493.52(58.8)	-0.43	-0.036	450.07	26.62(5.9)	172.52(38.3)
$2^3S_1 \to 1^3P_0\gamma$	0.26	58.7	4.1(7.0)	38.08(64.9)	-0.24	-0.011	43.75	2.11(4.8)	16.19(37.0)
$2^3S_1 \to 1^3P_1\gamma$	0.17	49.55	3.46(7.0)	32.15(64.9)	-0.29	0.042	37.15	1.71(4.6)	13.67(36.8)
$2^3S_1 \to 1^3P_2\gamma$	0.13	34.16	2.39(7.0)	22.17(64.9)	-0.39	-0.039	19.41	0.79(4.1)	9.42(48.5)

Table F.11: Summary of the results obtained from the evaluation of the charmonium decay rates using Counting 3 with lattice input. Values as in Table F.1.

F.2 β scaling factors

In the following tables, we show the average values of the effective scaling factor β defined through $\delta\Gamma_{H\to H'} \equiv \beta v^2$.

Decay	Count. 1 (phen.)	Count. 3 (phen.)	Count. 1 (latt.)	Count. 3 (latt.)
$1\,^1P_1 \to 1\,^1S_0\gamma$	0.4	0.4	0.3	0.4
$2\,^1S_0 \to 1\,^1P_1\gamma$	0.002	0.04	0.01	0.03
$1\,^3P_0 \to 1\,^3S_1\gamma$	1.0	0.9	1.1	0.9
$1\,^3P_1 \to 1\,^3S_1\gamma$	0.6	0.5	0.6	0.5
$1\,^3P_2 \to 1\,^3S_1\gamma$	0.1	0.1	0.06	0.1
$2\,^3S_1 \to 1\,^3P_0\gamma$	0.2	0.04	0.1	0.03
$2\,^3S_1 \to 1\,^3P_1\gamma$	0.04	0.1	0.05	0.1
$2\,^3S_1 \to 1\,^3P_2\gamma$	0.03	0.1	0.04	0.1

Table F.12: Average value of the scaling factor $|\beta|$ for charmonium decays. In analogy to how the averages of the $\delta\Gamma_{H\to H'\gamma}$ corrections are calculated in Tables 8.1 - 8.4, in each decay the values correspond to the mean of the sixteen values obtained in each counting/input combination.

Decay	Count. 1 (phen.)	Count. 3 (phen.)	Count. 1 (latt.)
$1\,^1P_1 \to 1\,^1S_0\gamma$	0.6	0.5	0.4
$2\,^1P_1 \to 1\,^1S_0\gamma$	1.8	1.0	0.6
$2\,^1P_1 \to 2\,^1S_0\gamma$	0.3	0.3	0.3
$2\,^1S_0 \to 1\,^1P_1\gamma$	0.015	0.024	0.028
$1\,^3P_0 \to 1\,^3S_1\gamma$	0.9	1.0	1.2
$1\,^3P_1 \to 1\,^3S_1\gamma$	0.6	0.7	0.7
$1\,^3P_2 \to 1\,^3S_1\gamma$	0.4	0.2	0.04
$2\,^3P_0 \to 1\,^3S_1\gamma$	0.5	1.4	1.7
$2\,^3P_1 \to 1\,^3S_1\gamma$	0.6	0.25	0.6
$2\,^3P_2 \to 1\,^3S_1\gamma$	2.5	1.9	1.5
$2\,^3P_0 \to 2\,^3S_1\gamma$	0.4	0.4	0.5
$2\,^3P_1 \to 2\,^3S_1\gamma$	0.3	0.3	0.3
$2\,^3P_2 \to 2\,^3S_1\gamma$	0.26	0.16	0.13
$3\,^3P_1 \to 1\,^3S_1\gamma$	0.42	0.97	1.1
$3\,^3P_1 \to 2\,^3S_1\gamma$	1.1	0.5	0.2
$3\,^3P_1 \to 3\,^3S_1\gamma$	0.2	0.2	0.2
$2\,^3S_1 \to 1\,^3P_0\gamma$	0.2	0.1	0.2
$2\,^3S_1 \to 1\,^3P_1\gamma$	0.03	0.01	0.02
$2\,^3S_1 \to 1\,^3P_2\gamma$	0.05	0.05	0.06
$3\,^3S_1 \to 2\,^3P_0\gamma$	0.1	0.05	0.06
$3\,^3S_1 \to 2\,^3P_1\gamma$	0.006	0.005	0.001
$3\,^3S_1 \to 2\,^3P_2\gamma$	0.001	0.003	0.003

Table F.13: Average value of the scaling factor $|\beta|$ for bottomonium decays. Values as in Table F.12.

Appendix G

The $3S \to 1P$ bottomonium decay

In this section we will discuss the unstable behavior of our results for the evaluation of the $3\,^3S_1 \to 1\,^3P_J\gamma$ bottomonium decay.

In Table G.1 we show the values obtained for the $3\,^3S_1 \to 1\,^3P_J\gamma$ bottomonium decay using Counting 1 with lattice input and Counting 3 with phenomenology input[1]. Apart from the case $J = 0$ in the lattice input evaluation, in all other evaluations we have that $R_{H\to H'\gamma} > 1$. The values for $\delta\Gamma$ are also large compared to the same corrections in the other decays reported in Chapter 8, although still below one.

	Counting 1 (Lattice)			Counting 3 (Phenomenology)		
Decay	$\overline{\Gamma^{\rm LO}}$ [keV]	$\overline{R}$	$\overline{\delta\Gamma}$	$\overline{\Gamma^{\rm LO}}$ [keV]	$\overline{R}$	$\overline{\delta\Gamma}$
$3\,^3S_1 \to 1\,^3P_0\gamma$	0.03 ± 0.01	0.24	-0.48	0.03 ± 0.04	6.25	-0.85
$3\,^3S_1 \to 1\,^3P_1\gamma$	0.08 ± 0.03	2.93	-0.44	0.07 ± 0.09	9.32	-0.77
$3\,^3S_1 \to 1\,^3P_2\gamma$	0.12 ± 0.04	4.65	-0.49	0.1 ± 0.1	11.19	-0.82

Table G.1: Summary of the evaluation of the relativistic corrections to the bottomonium $3S \to 1P$ decay rate; values computed as in Table 8.1. Notice that R has the same shape in both countings. In each of these evaluations, there are amplitudes that contribute to R that are larger than one. In the case of the evaluation of the $3\,^3S_1 \to 1\,^3P_0\gamma$ decay with lattice input, the small value of R results from the cancellation of large (> 1) amplitudes.

In order to track down the source of this behavior, let us compare the values we get from evaluating $R_{H\to H'\gamma}$ for the $3S \to 2P$ decay, which is stable, with the values of $R_{H\to H'\gamma}$ obtained for the $3S \to 1P$ decay. For this purpose, let us consider the mean values of the parameters of the phenomenology input[2] given in Table 5.2.

[1] Evaluations considering the other counting and input combinations show the same unstable results.
[2] A similar analysis with the lattice input yields the same conclusions.

First, it is convenient to recall the formula for $R_{H\to H'\gamma}$ given in Eq. (6.32), which here we rewrite as

$$R(nS \to n'P) = 2\bar{A}_R(nS \to n'P) + \bar{B}_R^2(nS \to n'P). \tag{G.1}$$

In order to give concrete numbers, let us focus on the $3\,^3S_1 \to 1\,^3P_{J=2}$ decay, although, as it will become clear, our conclusions apply for any value of J. For this specific transition, we get

$$R(3S \to 1P) = 7.82. \tag{G.2}$$

This large value comes from the large values of $\bar{A}_R$ and $\bar{B}_R$

$$\bar{A}_R(3S \to 1P) = \frac{0.08}{I_3(3S,1P)} = 2.32, \tag{G.3}$$

$$\bar{B}_R(3S \to 1P) = \frac{0.06}{I_3(3S,1P)} = 1.79. \tag{G.4}$$

Comparing them with the equivalent quantities in the case of the $3\,^3S_1 \to 2\,^3P_{J=2}$ decay given by

$$R(3S \to 2P) = -0.02, \tag{G.5}$$

$$\bar{A}_R(3S \to 2P) = \frac{0.03}{I_3(3S,2P)} = -0.01, \tag{G.6}$$

$$\bar{B}_R(3S \to 2P) = \frac{-0.08}{I_3(3S,2P)} = 0.03, \tag{G.7}$$

we see that the large value of the amplitudes in the $3S \to 1P$ transition comes from the small value of the $I_3(3S,1P)$ integral

$$I_3(3S,1P) = \int_0^\infty dr\, r\, y_{3S}(r) y_{1P}(r) = 0.03\,[\mathrm{GeV}^{-1}], \tag{G.8}$$

compared to the equivalent integral in the $3S \to 2P$ case

$$I_3(3S,2P) = \int_0^\infty dr\, r\, y_{3S}(r) y_{2P}(r) = -2.61\,[\mathrm{GeV}^{-1}]. \tag{G.9}$$

Plotting the integrands of both integrals in Fig. (G.1), it is clear that there is a large cancellation in the integrand of $I_3(3S,1P)$ that does not occur in $I_3(3S,2P)$.
We conclude that in the case of the $3S \to 1P$ decay the unstable values of the contributions to $R_{H\to H'\gamma}$ and the $\delta\Gamma_{H\to H'\gamma}$ correction come from the large cancellation in the integrand of $I_3(3S,1P)$. Moreover, an inspection of the values obtained for the amplitudes that contribute to $R_{H\to H'\gamma}$ with some of the random parameter sets, shows that a small variation of the parameters leads to a large difference among the values for the same amplitudes; this suggests that a convergent evaluation of the relativistic corrections to the $3S \to 1P$ decay rate may require *fine tuned* values of the parameters rather than the statistical approach we have taken.

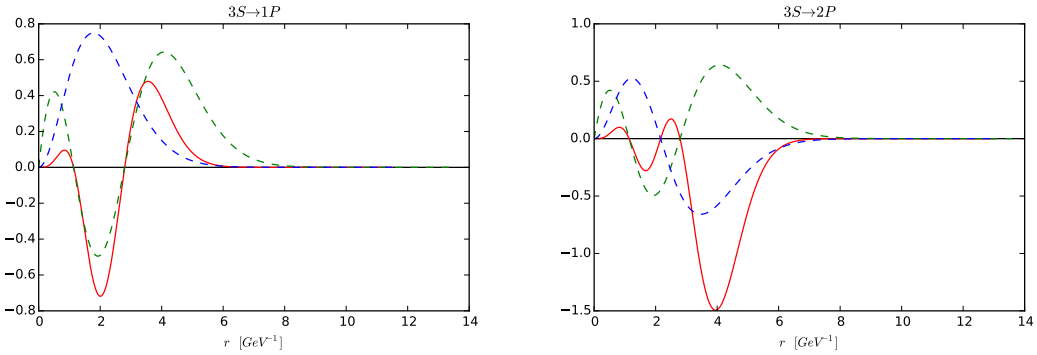

Figure G.1: Left: The integrand of $I_3(3S, 1P)$ (continuous red); the dashed blue and green lines correspond to the $y_{1P}(r)$ and $y_{3S}(r)$ reduced radial wavefunctions. Right: The integrand of $I_3(3S, 2P)$ (continuous red); the dashed blue and green lines correspond to the $y_{2P}(r)$ and $y_{3S}(r)$ reduced radial wavefunctions.

Bibliography

[1] I. Newton, *Philosophiae naturalis principia mathematica*. J. Societatis Regiae ac Typis J. Streater, 1687.

[2] A. Einstein, "Die Grundlage der allgemeinen Relativitätstheorie," *Annalen Phys.*, vol. 49, pp. 769–822, 1916. [Annalen Phys.14,517(2005)].

[3] S. L. Glashow, "Partial Symmetries of Weak Interactions," *Nucl. Phys.*, vol. 22, pp. 579–588, 1961.

[4] S. Weinberg, "A Model of Leptons," *Phys. Rev. Lett.*, vol. 19, pp. 1264–1266, 1967.

[5] A. Salam, "Weak and Electromagnetic Interactions," *Conf. Proc.*, vol. C680519, pp. 367–377, 1968.

[6] A useful bibliography on the topic can be found in the SLAC archive's page dedicated to it `http://www.slac.stanford.edu/history/revolution.shtml`. Accessed: 2016-06-24.

[7] W. Lucha, F. F. Schoberl, and D. Gromes, "Bound states of quarks," *Phys. Rept.*, vol. 200, pp. 127–240, 1991.

[8] N. Brambilla and A. Vairo, "Quark confinement and the hadron spectrum," in *Strong interactions at low and intermediate energies. Proceedings, 13th Annual Hampton University Graduate Studies, HUGS'98, Newport News, USA, May 26-June 12, 1998*, pp. 151–220, 1999.

[9] W. E. Caswell and G. P. Lepage, "Effective Lagrangians for Bound State Problems in QED, QCD, and Other Field Theories," *Phys. Lett.*, vol. B167, pp. 437–442, 1986.

[10] G. T. Bodwin, E. Braaten, and G. P. Lepage, "Rigorous QCD analysis of inclusive annihilation and production of heavy quarkonium," *Phys. Rev.*, vol. D51, pp. 1125–1171, 1995. [Erratum: Phys. Rev.D55,5853(1997)].

[11] A. Pineda and J. Soto, "Effective field theory for ultrasoft momenta in NRQCD and NRQED," *Nucl. Phys. Proc. Suppl.*, vol. 64, pp. 428–432, 1998.

[12] N. Brambilla, A. Pineda, J. Soto, and A. Vairo, "Potential NRQCD: An Effective theory for heavy quarkonium," *Nucl.Phys.*, vol. B566, p. 275, 2000.

[13] N. Brambilla *et al.*, "Heavy quarkonium: progress, puzzles, and opportunities," *Eur. Phys. J.*, vol. C71, p. 1534, 2011.

[14] N. Brambilla, S. Eidelman, P. Foka, S. Gardner, A. Kronfeld, *et al.*, "QCD and Strongly Coupled Gauge Theories: Challenges and Perspectives," *Eur.Phys.J.*, vol. C74, no. 10, p. 2981, 2014.

[15] R. Aaij *et al.*, "Observation of $J/\Psi p$ Resonances Consistent with Pentaquark States in $\Lambda_b^0 \to J/\Psi K^- p$ Decays," *Phys. Rev. Lett.*, vol. 115, p. 072001, 2015.

[16] F.-K. Guo, U.-G. Meißner, W. Wang, and Z. Yang, "How to reveal the exotic nature of the $P_c(4450)$," *Phys. Rev.*, vol. D92, no. 7, p. 071502, 2015.

[17] T. Matsui and H. Satz, "J/ψ Suppression by Quark-Gluon Plasma Formation," *Phys. Lett.*, vol. B178, pp. 416–422, 1986.

[18] N. Brambilla, A. Pineda, J. Soto, and A. Vairo, "The QCD potential at O(1/m)," *Phys.Rev.*, vol. D63, p. 014023, 2001.

[19] A. Pineda and A. Vairo, "The QCD potential at O (1 / m^2) : Complete spin dependent and spin independent result," *Phys.Rev.*, vol. D63, p. 054007, 2001.

[20] Y. Nambu, "QCD and the String Model," *Phys.Lett.*, vol. B80, p. 372, 1979.

[21] N. Brambilla, P. Pietrulewicz, and A. Vairo, "Model-independent Study of Electric Dipole Transitions in Quarkonium," *Phys.Rev.*, vol. D85, p. 094005, 2012.

[22] N. Brambilla, A. Pineda, J. Soto, and A. Vairo, "Effective field theories for heavy quarkonium," *Rev.Mod.Phys.*, vol. 77, p. 1423, 2005.

[23] A. Pich, "Effective field theory: Course," in *Probing the standard model of particle interactions. Proceedings, Summer School in Theoretical Physics, NATO Advanced Study Institute, 68th session, Les Houches, France, July 28-September 5, 1997. Pt. 1, 2*, pp. 949–1049, 1998.

[24] H. Fritzsch and M. Gell-Mann, "Current algebra: Quarks and what else?," *eConf*, vol. C720906V2, pp. 135–165, 1972.

[25] H. Fritzsch, M. Gell-Mann, and H. Leutwyler, "Advantages of the Color Octet Gluon Picture," *Phys. Lett.*, vol. B47, pp. 365–368, 1973.

[26] M. E. Peskin and D. V. Schroeder, *An Introduction to quantum field theory*. 1995.

[27] K. G. Chetyrkin, B. A. Kniehl, and M. Steinhauser, "Strong coupling constant with flavor thresholds at four loops in the MS scheme," *Phys. Rev. Lett.*, vol. 79, pp. 2184–2187, 1997.

[28] T. van Ritbergen, J. A. M. Vermaseren, and S. A. Larin, "The Four loop beta function in quantum chromodynamics," *Phys. Lett.*, vol. B400, pp. 379–384, 1997.

[29] M. Czakon, "The Four-loop QCD beta-function and anomalous dimensions," *Nucl. Phys.*, vol. B710, pp. 485–498, 2005.

[30] P. A. Baikov, K. G. Chetyrkin, and J. H. Kühn, "Five-Loop Running of the QCD coupling constant," 2016.

[31] H. D. Politzer, "Reliable Perturbative Results for Strong Interactions?," *Phys. Rev. Lett.*, vol. 30, pp. 1346–1349, 1973.

[32] D. J. Gross and F. Wilczek, "Ultraviolet Behavior of Nonabelian Gauge Theories," *Phys. Rev. Lett.*, vol. 30, pp. 1343–1346, 1973.

[33] T. Appelquist and J. Carazzone, "Infrared Singularities and Massive Fields," *Phys. Rev.*, vol. D11, p. 2856, 1975.

[34] S. Bethke, "The 2009 World Average of alpha(s)," *Eur. Phys. J.*, vol. C64, pp. 689–703, 2009.

[35] N. Brambilla, D. Gromes, and A. Vairo, "Poincare invariance and the heavy quark potential," *Phys. Rev.*, vol. D64, p. 076010, 2001.

[36] N. Brambilla, D. Gromes, and A. Vairo, "Poincare invariance constraints on NRQCD and potential NRQCD," *Phys. Lett.*, vol. B576, pp. 314–327, 2003.

[37] A. V. Manohar, "The HQET / NRQCD Lagrangian to order α/m^3," *Phys. Rev.*, vol. D56, pp. 230–237, 1997.

[38] C. W. Bauer and A. V. Manohar, "Renormalization group scaling of the $1/m^2$ HQET Lagrangian," *Phys. Rev.*, vol. D57, pp. 337–343, 1998.

[39] M. E. Luke and A. V. Manohar, "Reparametrization invariance constraints on heavy particle effective field theories," *Phys. Lett.*, vol. B286, pp. 348–354, 1992.

[40] J. Heinonen, R. J. Hill, and M. P. Solon, "Lorentz invariance in heavy particle effective theories," *Phys. Rev.*, vol. D86, p. 094020, 2012.

[41] N. Brambilla, M. Berwein, S. Hwang, and A. Vairo, "Poincaré Invariance in NRQCD and pNRQCD,"

[42] A. Pineda and J. Soto, "Matching at one loop for the four quark operators in NRQCD," *Phys. Rev.*, vol. D58, p. 114011, 1998.

[43] A. Vairo, "A Theoretical review of heavy quarkonium inclusive decays," *Mod. Phys. Lett.*, vol. A19, pp. 253–269, 2004.

[44] A. S. Kronfeld, "Heavy quarks and lattice QCD," *Nucl. Phys. Proc. Suppl.*, vol. 129, pp. 46–59, 2004. [,46(2003)].

[45] G. P. Lepage, "High-precision nonperturbative QCD," *Annals Phys.*, vol. 315, pp. 193–212, 2005.

[46] N. Brambilla, M. A. Escobedo, J. Ghiglieri, J. Soto, and A. Vairo, "Heavy Quarkonium in a weakly-coupled quark-gluon plasma below the melting temperature," *JHEP*, vol. 09, p. 038, 2010.

[47] N. Brambilla, J. Ghiglieri, A. Vairo, and P. Petreczky, "Static quark-antiquark pairs at finite temperature," *Phys. Rev.*, vol. D78, p. 014017, 2008.

[48] N. Brambilla, M. A. Escobedo, J. Ghiglieri, and A. Vairo, "Thermal width and gluo-dissociation of quarkonium in pNRQCD," *JHEP*, vol. 12, p. 116, 2011.

[49] N. Brambilla, M. A. Escobedo, J. Ghiglieri, and A. Vairo, "Thermal width and quarkonium dissociation by inelastic parton scattering," *JHEP*, vol. 05, p. 130, 2013.

[50] J. Ghiglieri, *Effective Field Theories of QCD for Heavy Quarkonia at Finite Temperature*. PhD thesis, Munich, Tech. U., 2011.

[51] M. Berwein, N. Brambilla, J. Tarrus Castella, and A. Vairo, "Quarkonium Hybrids with Nonrelativistic Effective Field Theories," *Phys. Rev.*, vol. D92, no. 11, p. 114019, 2015.

[52] C. Peset, A. Pineda, and M. Stahlhofen, "Potential NRQCD for unequal masses and the B_c spectrum at NNNLO," 2015.

[53] E. Eichten and F. Feinberg, "Spin Dependent Forces in QCD," *Phys. Rev.*, vol. D23, p. 2724, 1981.

[54] K. Melnikov and A. Yelkhovsky, "Top quark production at threshold with O(alpha-s**2) accuracy," *Nucl. Phys.*, vol. B528, pp. 59–72, 1998.

[55] A. H. Hoang, "Bottom quark mass from Upsilon mesons," *Phys. Rev.*, vol. D59, p. 014039, 1999.

[56] J. B. Kogut and G. Parisi, "Long Range Spin Spin Forces in Gauge Theories," *Phys.Rev.Lett.*, vol. 47, p. 1089, 1981.

[57] G. Perez-Nadal and J. Soto, "Effective string theory constraints on the long distance behavior of the subleading potentials," *Phys.Rev.*, vol. D79, p. 114002, 2009.

[58] N. Brambilla, M. Groher, H. E. Martinez, and A. Vairo, "Effective string theory and the long-range relativistic corrections to the quark-antiquark potential," *Phys.Rev.*, vol. D90, p. 114032, Dec 2014.

[59] M. Baker, "New constraint on effective field theories of the QCD flux tube," *Phys. Rev.*, vol. D93, no. 5, p. 054012, 2016.

[60] M. Luscher, "Symmetry Breaking Aspects of the Roughening Transition in Gauge Theories," *Nucl.Phys.*, vol. B180, p. 317, 1981.

[61] M. Luscher and P. Weisz, "Quark confinement and the bosonic string," *JHEP*, vol. 0207, p. 049, 2002.

[62] M. Baker and R. Steinke, "Effective string theory of vortices and Regge trajectories," *Phys. Rev.*, vol. D63, p. 094013, 2001.

[63] M. Baker and R. Steinke, "Semiclassical quantization of effective string theory and Regge trajectories," *Phys. Rev.*, vol. D65, p. 094042, 2002.

[64] M. Luscher and P. Weisz, "String excitation energie in SU(N) gauge theories beyond the free-string approximation," *JHEP*, vol. 0407, p. 014, 2004.

[65] O. Aharony and M. Field, "On the effective theory of long open strings," *JHEP*, vol. 1101, p. 065, 2011.

[66] O. Aharony and Z. Komargodski, "The Effective Theory of Long Strings," *JHEP*, vol. 1305, p. 118, 2013.

[67] Y. Koma and M. Koma, "Heavy quarkonium spectroscopy in pNRQCD with lattice QCD input," *PoS*, vol. LATTICE2012, p. 140, 2012.

[68] G. S. Bali, H. Neff, T. Duessel, T. Lippert, and K. Schilling, "Observation of string breaking in QCD," *Phys. Rev.*, vol. D71, p. 114513, 2005.

[69] M. Luscher, K. Symanzik, and P. Weisz, "Anomalies of the Free Loop Wave Equation in the WKB Approximation," *Nucl.Phys.*, vol. B173, p. 365, 1980.

[70] D. Gromes, "Spin Dependent Potentials in QCD and the Correct Long Range Spin Orbit Term," *Z. Phys.*, vol. C26, p. 401, 1984.

[71] A. Barchielli, N. Brambilla, and G. M. Prosperi, "Relativistic Corrections to the Quark - anti-Quark Potential and the Quarkonium Spectrum," *Nuovo Cim.*, vol. A103, p. 59, 1990.

[72] W. Buchmuller, Y. J. Ng, and S. Tye, "Hyperfine Splittings in Heavy Quark Systems," *Phys.Rev.*, vol. D24, p. 3003, 1981.

[73] S. Gupta and S. Radford, "Quark Quark and Quark - Anti-quark Potentials," *Phys.Rev.*, vol. D24, pp. 2309–2323, 1981.

[74] S. Gupta and S. Radford, "REMARKS ON QUARK QUARK AND QUARK - ANTI-QUARK POTENTIALS," *Phys.Rev.*, vol. D25, pp. 3430–3432, 1982.

[75] J. T. Pantaleone, S. H. Tye, and Y. J. Ng, "Spin Splittings in Heavy Quarkonia," *Phys.Rev.*, vol. D33, p. 777, 1986.

[76] S. Titard and F. Yndurain, "Rigorous QCD evaluation of spectrum and ground state properties of heavy q anti-q systems: With a precision determination of m(b) M(eta(b))," *Phys.Rev.*, vol. D49, pp. 6007–6025, 1994.

[77] E. Eichten, K. Gottfried, T. Kinoshita, K. D. Lane, and T.-M. Yan, "Charmonium: The Model," *Phys. Rev.*, vol. D17, p. 3090, 1978. [Erratum: Phys. Rev.D21,313(1980)].

[78] K. Olive *et al.*, "Review of Particle Physics," *Chin.Phys.*, vol. C38, p. 090001, 2014.

[79] A. Bazavov *et al.*, "Equation of state in (2+1)-flavor QCD," *Phys.Rev.*, vol. D90, no. 9, p. 094503, 2014.

[80] N. Brambilla, Y. Jia, and A. Vairo, "Model-independent study of magnetic dipole transitions in quarkonium," *Phys.Rev.*, vol. D73, p. 054005, 2006.

[81] A. Pineda and J. Segovia, "Improved determination of heavy quarkonium magnetic dipole transitions in potential nonrelativistic QCD," *Phys.Rev.*, vol. D87, no. 7, p. 074024, 2013.

[82] Y. Jia, W.-L. Sang, and J. Xu, "Is the $J^P = 2^-$ assignment for the $X(3872)$ compatible with the radiative transition data?," 2010.

[83] P. Pietrulewicz, "Effective field theory for electromagnetic transitions of heavy quarkonium," Master's thesis, Munich, Tech. U., 2011.

[84] M. Ablikim *et al.*, "Measurements of $h_c(^1P_1)$ in psi' Decays," *Phys.Rev.Lett.*, vol. 104, p. 132002, 2010.

[85] J. Lees *et al.*, "Evidence for the $h_b(1P)$ meson in the decay $\Upsilon(3S) \to \pi^0 h_b(1P)$," *Phys.Rev.*, vol. D84, p. 091101, 2011.

[86] R. Mizuk *et al.*, "Evidence for the $\eta_b(2S)$ and observation of $h_b(1P) \to \eta_b(1S)\gamma$ and $h_b(2P) \to \eta_b(1S)\gamma$," *Phys. Rev. Lett.*, vol. 109, p. 232002, 2012.

[87] J. Lees *et al.*, "Bottomonium spectroscopy and radiative transitions involving the $\chi_b J(1P, 2P)$ states at BABAR," *Phys.Rev.*, vol. D90, no. 11, p. 112010, 2014.

[88] R. Aaij *et al.*, "Study of $\chi_{\rm b}$ meson production in p p collisions at $\sqrt{s} = 7$ and 8 TeV and observation of the decay $\chi_{\rm b}(3{\rm P}) \to \Upsilon(3{\rm S})\gamma$," *Eur. Phys. J.*, vol. C74, no. 10, p. 3092, 2014.

[89] Y. L. Han *et al.*, "Measurement of $e^+e^- \to \gamma\chi_{cJ}$ via initial state radiation at Belle," *Phys. Rev.*, vol. D92, no. 1, p. 012011, 2015.

[90] U. Tamponi *et al.*, "First observation of the hadronic transition $\Upsilon(4S) \to \eta h_b(1P)$ and new measurement of the $h_b(1P)$ and $\eta_b(1S)$ parameters," 2015.

[91] A. Abdesselam *et al.*, "Study of $\chi_{bJ}(1P)$ Properties in the Radiative $\Upsilon(2S)$ Decays," 2016.

[92] B. Aubert *et al.*, "Evidence for the eta(b)(1S) Meson in Radiative Upsilon(2S) Decay," *Phys.Rev.Lett.*, vol. 103, p. 161801, 2009.

[93] G. Bonvicini *et al.*, "Measurement of the eta(b)(1S) mass and the branching fraction for Upsilon(3S) to gamma eta(b)(1S)," *Phys.Rev.*, vol. D81, p. 031104, 2010.

[94] M. Ablikim *et al.*, "Search for the radiative transitions $\psi(3770) \to \gamma\eta_c$ and $\gamma\eta_c(2S)$," *Phys. Rev.*, vol. D89, no. 11, p. 112005, 2014.

[95] M. Ablikim *et al.*, "Measurement of higher-order multipole amplitudes in $\psi(3686) \to \gamma\chi_{c1,2}$ with $\chi_{c1,2} \to \gamma J/\psi$ and search for the transition $\eta_c(2S) \to \gamma J/\psi$," 2017.

[96] D. Becirevic and F. Sanfilippo, "Lattice QCD study of the radiative decays $J/\psi \to \eta_c\gamma$ and $h_c \to \eta_c\gamma$," *JHEP*, vol. 1301, p. 028, 2013.

[97] D. Becirevic, M. Kruse, and F. Sanfilippo, "Lattice QCD estimate of the $\eta_c(2S) \to J/\psi\gamma$ decay rate," 2014.

[98] C. Hughes, R. J. Dowdall, C. T. H. Davies, R. R. Horgan, G. von Hippel, and M. Wingate, "Hindered M1 Radiative Decay of $\Upsilon(2S)$ from Lattice NRQCD," *Phys. Rev.*, vol. D92, p. 094501, 2015.

[99] C. O'Hara, S. M. Ryan, G. Moir, and C. E. Thomas, "Towards Radiative Transitions in Charmonium," *PoS*, vol. Lattice2016, p. 120, 2016.

[100] "Python software foundation." `http://www.python.org`. Accessed: 2016-05-02.

[101] "Cython, c extensions for python." `http://www.cython.org`. Accessed: 2016-05-02.

[102] "Project jupyter." `http://www.jupyter.org`. Accessed: 2016-05-02.

[103] F. Pérez and B. E. Granger, "IPython: a system for interactive scientific computing," *Computing in Science and Engineering*, vol. 9, pp. 21–29, May 2007.

[104] S. v. d. Walt, S. C. Colbert, and G. Varoquaux, "The numpy array: A structure for efficient numerical computation," *Computing in Science and Engg.*, vol. 13, pp. 22–30, Mar. 2011.

[105] "Numpy." `http://www.numpy.org`. Accessed: 2016-05-02.

[106] E. Jones, T. Oliphant, P. Peterson, *et al.*, "SciPy: Open source scientific tools for Python," 2001–. [Online; accessed 2016-05-02].

[107] E. W. Weisstein, "Simpsons rule. From MathWorld—A Wolfram Web Resource." `http://mathworld.wolfram.com/SimpsonsRule.html`. Accessed: 2016-05-02.

[108] http://www.math.utah.edu/software/minpack/minpack/hybrd.html. Accessed: 2016-05-02.

[109] http://www.math.utah.edu/software/minpack/minpack/hybrj.html. Accessed: 2016-05-02.

[110] M. J. D. Powell, "An efficient method for finding the minimum of a function of several variables without calculating derivatives," *The Computer Journal*, vol. 7, no. 2, pp. 155–162, 1964.

[111] E. W. Weisstein, "Levenberg-marquardt method. From MathWorld—A Wolfram Web Resource." http://mathworld.wolfram.com/Levenberg-MarquardtMethod.html. Accessed: 2016-05-02.

[112] J. D. Hunter, "Matplotlib: A 2d graphics environment," *Computing In Science & Engineering*, vol. 9, no. 3, pp. 90–95, 2007.

[113] http://cffi.readthedocs.io/en/latest/. Accessed: 2016-05-02.

[114] http://swig.org. Accessed: 2016-05-02.

[115] https://github.com/scipy/weave. Accessed: 2016-05-02.

[116] E. Fuentes and H. E. Martinez, "Sclib, a hack for straightforward embedded C functions in python," *CoRR*, vol. abs/1412.6395, 2014.

[117] E. J. F. Henríquez, *Quasi-Time-Optimal Controllers for Electrical Drives*. PhD thesis, Universitätsbibliothek der TU München, 2015.

[118] https://github.com/drestebon/SClib. Accessed: 2016-05-02.

[119] https://pypi.python.org/pypi/SClib/1.0.0. Accessed: 2016-05-02.

[120] W. Lucha and F. F. Schoberl, "Solving the Schrodinger equation for bound states with Mathematica 3.0," *Int. J. Mod. Phys.*, vol. C10, pp. 607–620, 1999.

[121] https://computing.llnl.gov/tutorials/pthreads/. Accessed: 2016-05-02.

[122] R. Aaij *et al.*, "Measurement of the $\chi_b(3P)$ mass and of the relative rate of $\chi_{b1}(1P)$ and $\chi_{b2}(1P)$ production," *JHEP*, vol. 10, p. 88, 2014.

[123] J. P. Lees *et al.*, "Study of radiative bottomonium transitions using converted photons," *Phys. Rev.*, vol. D84, p. 072002, 2011.

[124] U. Heintz *et al.*, "b anti-b spectroscopy from the Upsilon (3S) state," *Phys. Rev.*, vol. D46, pp. 1928–1940, 1992.

[125] G. D. Crawford *et al.*, "Exclusive chi (2P) production in upsilon (3S) decay," *Phys. Lett.*, vol. B294, pp. 139–144, 1992.

[126] N. Brambilla, S. Hwang, and A. Vairo, "In preparation." 2017.

[127] Y. Koma and M. Koma, "Spin-dependent potentials from lattice QCD," *Nucl. Phys.*, vol. B769, pp. 79–107, 2007.

[128] S. Steinbeißer and J. Segovia, "pNRQCD determination of E1 radiative transitions," *EPJ Web Conf.*, vol. 137, p. 06026, 2017.

[129] H. E. Martinez, "Relativistic corrections to the quark-antiquark potential from the effective string theory," *PoS*, vol. ConfinementX, p. 161, 2012.

[130] H. E. Martinez, "Phenomenology of heavy quarkonium radiative E1 transitions," *AIP Conf. Proc.*, vol. 1701, p. 050008, 2016.

[131] N. Brambilla, H. E. Martinez, and A. Vairo, "In preparation." 2017.

[132] M. Groher, *BSc. Thesis*. Available at `http://einrichtungen.ph.tum.de/T30f/Theses/thesis_mgroher.pdf`.

[133] `https://github.com/heedmane/schroepy`. Accessed: 2016-05-02.